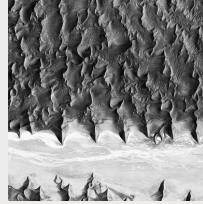
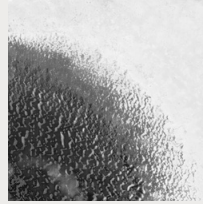
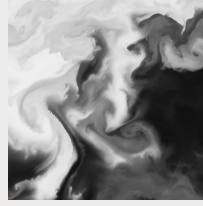
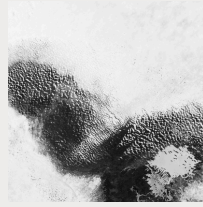
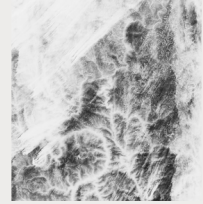
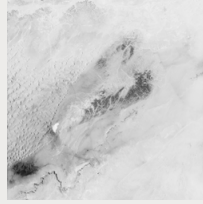
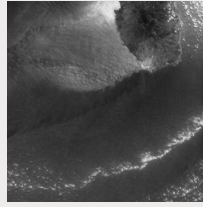
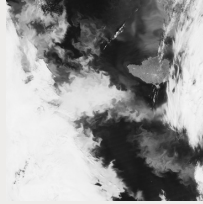


Modelling the atmospheric iron cycle in a changing climate

Elisa Bergas Massó

PhD Thesis



Modelling the atmospheric iron cycle in a changing climate

Memòria presentada per optar al grau de doctor
per la Universitat Politècnica de Catalunya.

Programa de doctorat en Enginyeria Ambiental

Departament d'Enginyeria Civil i Ambiental

Autora: Elisa Bergas Massó

Directors: Maria Gonçalves Ageitos
Carlos Pérez García-Pando



UNIVERSITAT POLITÈCNICA
DE CATALUNYA
BARCELONATECH

Modelling the atmospheric iron cycle in a changing climate.

PhD Thesis

Barcelona, 2025

Author: Elisa Bergas Massó

Copyright: Reproduction of this publication in whole or in part must include the customary bibliographic citation, including author attribution, thesis title, etc.

The research leading to this PhD Thesis has been carried out at the Earth Sciences department of the **Barcelona Supercomputing Center-Centro Nacional de Supercomputación (BSC-CNS)**.



The author acknowledges funding support from the Spanish Ministerio de Economía y Competitividad under the NUTRIENT (grant agreement No. CGL2017-88911-R) and BIOTA (grant agreement No. PID2022-139362OB-I00) projects, the European Space Agency under the DOMOS (grant agreement No. ESA AO/1-10546/20/I-NB) project, the European Research Council under the Horizon 2020 research and innovation programme through the ERC Consolidator Grant FRAGMENT (grant agreement No. 773051) and the AXA Research Fund (grant no. AXA Chair on Sand and Dust Storms).

Cover photos:

NASA, MODIS-Aqua. Natural-color image of a bloom southwest of Nunivak Island and the coast of Alaska, captured on September 4, 2014. Accessed from NASA Earth Observatory:

<https://earthobservatory.nasa.gov/images/84361>.

Copernicus Sentinel-2A. Satellite image of wildfires in the Russian Federation, taken on September 28, 2016. Image: ESA/CC BY-SA 3.0 IGO.

Korea Aerospace Research Institute (KARI), Kompsat-2. Satellite image of the Namib Desert, including the Tsauchab river bed and Dune 45, captured on January 7, 2012. Accessed from European Space Agency:

https://www.esa.int/Applications/Observing_the_Earth/Earth_from_Space/Namib_Dune_45.

NASA Earth Observatory. Phytoplankton swirling off the U.S. Mid-Atlantic coast in spring 2023. Image by Lauren Dauphin, using Landsat data from the U.S. Geological Survey. Accessed from the NASA Earth Observatory story "Bloomin' Atlantic": <https://visibleearth.nasa.gov/images/151261/bloomin-atlantic>.

Copernicus Sentinel-2 Mission, processed by ESA. Satellite image of Barcelona, Spain, taken in July 2022. Contains modified Copernicus Sentinel data (2022). Licensed under CC BY-SA 3.0 IGO or ESA Standard Licence. Accessed from the European Space Agency:

https://www.esa.int/ESA_Multimedia/Search?SearchText=barcelona&result_type=images.

Copernicus Sentinel-2A Mission, processed by ESA. Satellite image of Shanghai, China, taken on December 16, 2015. Contains modified Copernicus Sentinel data (2015). Licensed under CC BY-SA 3.0 IGO or ESA Standard Licence. Accessed from the European Space Agency:

https://www.esa.int/ESA_Multimedia/Search?SearchText=shanghai&result_type=images.

Copernicus Sentinel-2 Mission, processed by ESA. Satellite image of the Donnie Creek wildfire, British Columbia, taken on May 18, 2023. Contains modified Copernicus Sentinel data (2023). Licensed under CC BY-SA 3.0 IGO or ESA Standard Licence. Accessed from the European Space Agency:

https://www.esa.int/ESA_Multimedia/Images/2023/06/Donnie_Creek_fire.

JAXA/ESA. Satellite image of New York City, including Manhattan, Brooklyn, Queens, the Bronx, and Staten Island, taken on June 18, 2010. Captured by Japan's ALOS satellite. Licensed under ESA Standard Licence. Accessed from the European Space Agency:

https://www.esa.int/ESA_Multimedia/Search?SearchText=new+york+city&result_type=images.

Copernicus Sentinel-2A Mission, processed by ESA. Satellite image of a plankton bloom in the Barents Sea, taken on June 30, 2016. Contains modified Copernicus Sentinel data (2016). Licensed under CC BY-SA 3.0 IGO or ESA Standard Licence. Accessed from the European Space Agency:

https://www.esa.int/ESA_Multimedia/Search?SearchText=barents+bloom&result_type=images.

JAXA/ESA. Satellite image of southeastern Algeria in the Sahara Desert, 28 January 2011. Captured by Japan's ALOS satellite. Licensed under ESA Standard Licence. Accessed from the European Space Agency:

https://www.esa.int/ESA_Multimedia/Search?SearchText=sahara+desert&result_type=images.

USGS/NASA. Detailed view of the McKay Creek fire, June 30, 2021. Captured by the Operational Land Imager (OLI) on Landsat 8. Natural-color image overlaid with shortwave-infrared light to highlight the active fire. Accessed from NASA Earth Observatory:

<https://earthobservatory.nasa.gov/images/148530/blazes-rage-in-british-columbia#:~:text=So%20far%20in%202021%2C%20British,200%20kilometers%20northeast%20of%20Vancouver>.

USGS/ESA. Satellite image of Lake Chad, West Africa, 4 July 2014. Captured by Landsat-8. Licensed under ESA Standard Licence. Accessed from the European Space Agency:

https://www.esa.int/ESA_Multimedia/Search?SearchText=lake+chad&result_type=images.

EMIT Mission, NASA. Set of satellite images collected by Elisa Bergas. Accessed from NASA:

<https://search.earthdata.nasa.gov/search?q=%22EMIT%22&lat=-53.22730879086007&long=-85.7109375&zoom=3>.

Acknowledgements

Agradezco en primer lugar a mis supervisores, María y Carlos, por confiar en mí desde el principio de esta tesis y saberme transmitir esa confianza cuando lo he necesitado. Habéis sido unos guías envidiables y, sin duda, he aprendido mucho de vosotros durante el camino, tanto en lo académico como en los valores a la hora de trabajar, que se quedarán conmigo para siempre.

Me siento también muy agradecida por haber tenido el placer de trabajar en un equipo como el departamento de Earth Sciences del BSC-CNS. Es realmente una suerte contar con todo el equipo de personas que lo conforman, tanto aquellos que siguen aquí como aquellos que he visto pasar a lo largo de estos años. Es difícil sentirse solo con un equipo así. Muchos han hecho posible esta tesis, incluyendo compañeros de los grupos de Atmospheric Composition, Computational Earth Sciences y Climate Variability and Change. Especial mención al Joan, que m'ha sabut contagiar la seva passió i sempre ha volgut impulsar-me en tot el que he fet durant la tesi.

This thesis has brought many adventures, including my research stay at NC State University with Douglas Hamilton. I'm grateful for his warm welcome and for making me feel valued and part of his team. My thanks also extend to all external collaborators, especially Stelios Myriokefalitakis, whose contributions have been crucial to this work's success.

Acknowledgements

Beyond work, I have made many travel companions in the department who have become important friends both inside and outside the office. Thanks to them, my everyday life has been much more meaningful (An-Chi, Carla, Jaume, Saskia, Victoria). Some of them have also shared their own PhD journeys with me, and sharing this experience with them has made the path easier (Alba, Aleks, Andrea, Bala, Bianca, Carlos, Cristina, Dani, Eneko, Lluís, Paloma, Pep, Ruben).

La xarxa creada amb companys i doctorands d'altres departaments del BSC-CNS (Ana, Yassine, Migue, Winona, Jose, Sergio, Sergi, Roc,...) ha estat molt important per a mi durant aquests anys i han sigut essencials a l'hora de desconectar. També vull donar les gràcies a les Young IT Girls que han estat un motor de confiança en mi mateixa, en especial a l'Ana i a l'Alejandra les meves referents particulars. I a l'Helena que desde la distancia ha estat molt aprop durant aquest proces. Tots vosaltres m'heu demostrat que el camí és molt millor si és compartit.

Gracias a mis amigas Julia y Laura por seguir acompañándome en esta etapa y vivir mis alegrías y no tan alegrías como si fueran las vuestras propias.

Thanks to Stephen for giving me a boost in the final years of the thesis, cheering me on from the distance, and giving me the space, time, and peace of mind I so much needed.

Finalmente quiero agradecer a mi familia que me hacen sentir muy afortunada cada día. Agradezco a mis padres por apoyarme siempre en todo lo que me propongo y ayudarme en todo lo que está en sus manos, y a mi hermano por ser el mejor modelo a seguir que una puede tener.

Contents

List of Figures	xiii
List of Tables	xix
List of Symbols	xxi
Acronyms	xxiii
Summary	xxix
Resum	xxxiii
Resumen	xxxvii

I Introduction and framework

1 The relevance of iron in the Earth system	1
1.1 Iron in the Earth System	1
1.1.1 Iron: the chemical element	1
1.1.2 The Earth System	3
1.1.3 The iron cycle	4
1.1.4 The iron hypothesis	8
1.2 Sources of atmospheric iron	10
1.2.1 Iron in dust aerosols	11
1.2.2 Iron from fossil fuels	20
1.2.3 Iron from biomass burning	23
1.2.4 Iron from volcanic eruptions	26
1.3 Atmospheric Dissolution of Iron	28
1.4 Atmospheric Deposition	31

Contents

1.5	Ocean response to aerosol iron deposition	33
1.6	The iron cycle in the anthropocene	38
1.6.1	Human-induced changes to aerosol iron sources	39
1.6.2	Changes in global atmospheric chemistry	48
1.6.3	Changes in global ocean biogeochemistry	49
1.7	Constraining the atmospheric iron cycle	51
2	Objectives	55
3	Framework	57
3.1	Thesis structure	57
3.2	Framework within the Earth Sciences Department at the BSC-CNS	59
 II Methods		
4	General methodology	65
4.1	The EC-Earth Earth System Model	65
4.1.1	Tropospheric chemistry in EC-Earth	68
4.2	EC-Earth3-Iron	69
4.2.1	Fe-dust representation	70
4.2.2	Fe-combustion representation	72
4.2.3	The iron solubilization scheme	74
4.3	Model evaluation	77
4.3.1	Observations	78
4.3.2	Statistical analysis for evaluation	80
4.4	Socio-economic Development, Scenarios, and Pathways	82
4.5	Simulations Protocol	86

4.5.1	Nudged experiments	86
4.5.2	Time-slice experiments	87
4.5.3	Sensitivity experiments	90
4.6	Use of HPC systems	91
III Results and discussion		
5	A reconstruction of soluble iron deposition	99
5.1	Introduction	99
5.2	Methods	100
5.3	Results & discussion	102
5.3.1	Evaluation of the iron deposition reconstruction	102
5.3.2	Climatological atmospheric iron cycle	105
5.3.3	Seasonality of soluble iron deposition	109
5.3.4	Long-term trends in soluble iron deposition . . .	113
5.4	Conclusions	117
6	Impact of Soluble Iron Deposition Events on Subseasonal Chlorophyll Dynamics	121
6.1	Introduction	121
6.2	Methods	125
6.2.1	Temporal decomposition	127
6.2.2	Ocean Color Data	130
6.2.3	Statistical analysis	132
6.3	Results & discussion	134
6.3.1	The episodic nature of soluble iron deposition .	134
6.3.2	SChl responses to high soluble iron deposition events	137

Contents

6.3.3	Timing and duration of SChI responses across regions	141
6.3.4	SChI responses to lower soluble iron deposition events	143
6.3.5	Strong deposition events characterization	145
6.4	Conclusions	148
7	Pre-Industrial, Present and Future Atmospheric Soluble Iron Deposition Under CMIP6 Emissions	153
7.1	Introduction	153
7.2	Methods	155
7.2.1	Experimental setup	155
7.3	Results & discussion	157
7.3.1	Iron emissions	157
7.3.2	OXL concentrations and aerosol acidity	161
7.3.3	Atmospheric Fe solubilization	166
7.3.4	Soluble iron deposition and solubility	170
7.4	Conclusions	176
8	Impact of future climate-driven fires on soluble iron deposition and oceanic productivity	181
8.1	Introduction	181
8.2	Methods	185
8.2.1	A new future fires dataset	185
8.2.2	Models	188
8.2.3	Simulations	191
8.2.4	Source contributions to relative changes	192
8.2.5	Fe-limited regions	193

8.2.6	Net primary productivity estimates	194
8.2.7	Sensitivity assessment	195
8.3	Results & discussion	197
8.3.1	The importance of climate-driven fires on future atmospheric fire iron	197
8.3.2	Interplay of fires and fossil fuel emissions on future iron deposition changes	201
8.3.3	Impacts on Fe-limited oceanic regions: the North Atlantic stands out	204
8.3.4	Assessing regional sensitivity: model uncertainty vs. socioeconomic emission scenarios	208
8.4	Conclusions	211
 IV Conclusions and future perspectives		
9	Conclusions and future perspectives	219
9.1	Conclusions	219
9.2	Future work	225
 V Appendices		
A	Supplementary material	235
B	List of publications & Outreach activities	289
C	List of contributions to projects	295
	References	302

Contents

List of Figures

Figure 1.1	Surface ocean nitrate and chlorophyll concentrations . . .	6
Figure 1.2	Schematics of the Fe cycle	7
Figure 1.3	Global arid regions and main dust transport patterns	13
Figure 1.4	Fe content in soil minerals	16
Figure 1.5	PSD of disturbed soil versus emitted dust	19
Figure 1.6	Interplay of dust and fire aerosol sources	24
Figure 1.7	Burned area and transport pathways	26
Figure 1.8	Atmospheric processing of Fe	30
Figure 1.9	Global synthesis of nutrient limitation	35
Figure 1.10	Schematics of the BCP	36
Figure 1.11	Schematic of natural and anthropogenic feedbacks of the Fe cycle in the climate system	40
Figure 1.12	Climate model representations of historical changes in dust loading	42
Figure 1.13	Emissions trajectories for sulfur and BC	44
Figure 1.14	Geographical shifts in forest burned area and fire carbon emissions from 2001 to 2023	47
Figure 4.1	Observation sites used for evaluation.	79
Figure 4.2	Fe and SFe observations.	81
Figure 4.3	Summary schematic of the CMIP6 scenarios used in this Thesis.	85
Figure 5.1	Evaluation of Fe surface concentrations.	104
Figure 5.2	Mean annual Fe emission and deposition fluxes	106

List of Figures

Figure 5.3	Fractions of accumulation vs. coarse mode and wet vs. dry SFe deposition	108
Figure 5.4	Seasonal SFe deposition.	110
Figure 5.5	Seasonal SFe deposition source contribution.	111
Figure 5.6	Seasonal Fe solubility at deposition.	112
Figure 5.7	Long term changes in SFe and Fe solubility at deposition	114
Figure 5.8	Long term changes in SFe deposition by source	115
Figure 6.1	Percentage of SChl data in time series	131
Figure 6.2	Variance of SFe deposition and SChl levels	135
Figure 6.3	SChl response to high SFe deposition events	138
Figure 6.4	Timeline of SChl response to top SFe deposition events	142
Figure 6.5	SChl response to SFe deposition events by percentile	144
Figure 6.6	Regional SFe source contribution by deposition percentiles	146
Figure 6.7	Regional SFe wet vs dry and accumulation vs coarse mode deposition by deposition percentiles	147
Figure 7.1	Mean annual Fe emissions by source, region and scenario	158
Figure 7.2	Net primary production of OXL and SO_4^{2-} across scenarios	163
Figure 7.3	Aerosol pH and OXL surface concentrations across scenarios	165
Figure 7.4	Fe solubilization budgets across scenarios	168
Figure 7.5	Global Fe and SFe deposition across scenarios	169
Figure 7.6	SFe deposition and Fe solubility at deposition across scenarios	171

Figure 7.7	Source contribution of SFe deposition across scenarios and ocean basins	174
Figure 7.8	Changes in SFe deposition due to shifts in dust emission	175
Figure 8.1	Future changes in fire Fe emissions	199
Figure 8.2	Contribution of climate and anthropogenic-driven fires to SFe deposition.	201
Figure 8.3	Future changes in SFe deposition compared to present-day	203
Figure 8.4	Future atmospheric Fe-induced changes in NPP	206
Figure 8.5	Model uncertainty versus socioeconomic scenarios	209
Figure 9.1	Summary schematic of the expertise and topics requiring investigation to further understand aerosol nutrient—ocean biogeochemistry links	229
Figure A.1	Fe and SFe emissions distribution and trends	239
Figure A.2	Fe emissions distribution and trends by source	240
Figure A.3	Seasonal SFe deposition.	241
Figure A.4	Seasonal Fe deposition.	241
Figure A.5	Seasonal Fe emission.	242
Figure A.6	Seasonal OXL surface concentration.	242
Figure A.7	Seasonal SO ₄ surface concentration.	243
Figure A.8	Seasonal dust deposition.	243
Figure A.9	Seasonal percentage of wet SFe deposition	244
Figure A.10	Seasonal percentage of SFe deposition in the accumulation mode	244
Figure A.11	Trends in size mode deposition and deposition type	245

List of Figures

Figure A.12	Comparison of ocean biogeochemistry inputs: control vs. EC-Earth3-Iron reconstruction	246
Figure A.13	Ocean biomes	248
Figure A.14	Modelled SFe deposition and satellite-derived SChl from 1998 to 2014 in a region of the upwelling Pacific	250
Figure A.15	Modelled SFe deposition and satellite-derived SChl from 1998 to 2014 in a region of the equatorial Indian ocean	251
Figure A.16	Modelled SFe deposition and satellite-derived SChl from 1998 to 2014 in a region of the mid-high-latitudes of the NH Atlantic	252
Figure A.17	Modelled SFe deposition and satellite-derived SChl from 1998 to 2014 in a region of the oligotrophic NH Atlantic	253
Figure A.18	SChl response to high dust and SFe by source deposition events	254
Figure A.19	Timeline of SChl response to top dust deposition events.	255
Figure A.20	C_{phyto} and $SChl : C_{phyto}$ response to top SFe deposition events.	256
Figure A.21	Percentage of bbp443 data in time serie.	257
Figure A.22	SChl response to dust deposition events by percentile	258
Figure A.23	Region definition	261
Figure A.24	Dust, SO ₂ and OXL emissions	262
Figure A.25	Dust emission and surface winds	263
Figure A.26	Surface concentrations of nitrate and SO ₄	264
Figure A.27	Fe dissolution rates by Fe source	265

Figure A.28	Fe solubilization budgets for perturbed-dust scenarios	266
Figure A.29	Evaluation of Fe surface concentrations.	270
Figure A.30	Modeled dust surface concentration against observations	275
Figure A.31	Fire-Fe emissions	276
Figure A.32	Summary of simulations	277
Figure A.33	Future seasonal changes in fire Fe emissions	278
Figure A.34	Fire Fe deposition	279
Figure A.35	Fire SFe deposition	280
Figure A.36	EC-Earth3-Iron projected future changes in SFe deposition compared to present-day by source	281
Figure A.37	Changes in Fe limited areas	282
Figure A.38	Future seasonal Fe-induced changes in NPP compared to present-day	283
Figure A.39	Fractional change in the Fe:N deposition ratio from 2010 to 2100	284
Figure A.40	Mean and uncertainty in end-of-the-century SFe deposition changes	284
Figure A.41	Model uncertainty versus socioeconomic scenarios in June, July, and August	285
Figure A.42	Latitudinal SFe deposition by source	285
Figure A.43	CAM6-MIMI projected future changes in SFe deposition compared to present-day	286
Figure A.44	Present day BC and OC fire emissions	287
Figure A.45	Fine vs coarse distribution of deposited fire Fe	287
Figure A.46	Fire Fe solubility at deposition	288

List of Figures

List of Tables

Table 4.1	Modeled Fe content in minerals	71
Table 4.2	Dissolution scheme for Fe-containing combustion and mineral dust aerosols.	76
Table 7.1	List of simulations for Chapter 7	156
Table A.1	Model evaluation statistics across regions of SFe surface concentrations	237
Table A.2	Model evaluation statistics across regions of Fe surface concentrations	238
Table A.3	Fe deposition budgets	262
Table A.4	Fe emission budgets	267
Table A.5	Model evaluation statistics across regions of SFe surface concentrations	271
Table A.6	Model evaluation statistics across regions of Fe surface concentrations	272
Table A.7	Differences between CAM6-MIMI and EC-Earth3-Iron	273

List of Tables

List of Symbols

Symbol	Description
CH_4	Methane.
CO_2	Carbon dioxide.
Fe	Iron.
$Fe^{2+}/Fe(II)$	Ferrous cation.
$Fe^{3+}/Fe(III)$	Ferric cation.
N	Nitrogen.
NO_3	.
N_2O	Nitrous oxide.
P	Phosphorus.
pH	A measure of the acidity or alkalinity of a solution, defined as the negative logarithm of the hydrogen ion concentration.
Si	Silica.
SO_2	Sulfur dioxide.
SO_4^{2-}	Sulfate.
O_3	Ozone.

List of Symbols

Acronyms

AC Atmospheric Composition.

AeroCom Aerosol Comparisons between Observations and Models.

AERONET Aerosol Robotic Network.

AMIP Atmospheric Model Intercomparison Project.

AMMA African Monsoon Multidisciplinary Analysis (dust observations).

AOD Aerosol Optical Depth.

Auto-EC-Earth EC-Earth-specific extension of Autosubmit.

Autosubmit Open-source Python-based workflow manager.

BB4CMIP6 Biomass Burning Emissions Dataset for CMIP6.

bbp Particulate Backscattering Coefficient.

BC Black Carbon.

BCP Biological Carbon Pump.

BFT Brittle Fragmentation Theory.

BSC-CNS Barcelona Supercomputing Center - Centro Nacional de Supercomputación.

CAM6 Community Atmosphere Model Version 6.

Acronyms

Carb Carbonaceous.

CESM Community Earth System Model.

CLM5 Community Land Model Version 5.

CMIP6 Coupled Model Intercomparison Project Phase 6.

Cphyto Phytoplankton Carbon Biomass.

CPU Central Processing Unit.

CV Coefficient of Variation.

DMS Dimethyl Sulfide.

DOD Dust Optical Depth.

EC-Earth European Community Earth System Model.

EC-Earth3-AerChem European Community Earth System Model,
Aerosol Chemistry version.

EC-Earth3-Iron European Community Earth System Model, Iron
Chemistry version.

ECMWF European Centre for Medium-Range Weather Forecasts.

EMIT Earth Surface Mineral Dust Source Investigation.

ENSO El Niño–Southern Oscillation.

EP Export Production.

ERA5 fifth generation ECMWF atmospheric reanalysis of the global
climate.

ERC European Research Council.

ES Earth Sciences.

ESA European Space Agency.

ESGF Earth System Grid Federation.

ESM Earth System Model.

FeA Slow iron dissolution pool.

FeB Aerosol Iron from Biomass-burning Sources.

FeC Aerosol Iron from Combustion Sources.

FeD Aerosol Iron from Dust Sources.

FeF Aerosol Iron from Fossil Fuel Sources.

FeO Intermediate iron dissolution pool that considers nano-sized Fe.

FRAGMENT FRontiers in dust minerAloGical coMposition and its Effects upoN climaTe, ERC Consolidator Grant.

GCM General Circulation Model.

GFED Global Fire Emissions Database.

GFED4s Global Fire Emissions Database Version 4 with small fires.

GHG Greenhouse Gas.

GLADE GLobally Accessible Data Environment.

GPP Gross Primary Production.

GPU Graphics Processing Unit.

HNLC High Nutrient Low Chlorophyll.

Acronyms

- HPC** High Performance Computing.
- HTAP** Hemispheric Transport of Air Pollution.
- IAM** Integrated Assessment Models.
- IFS** Integrated Forecast System.
- IPCC** Intergovernmental Panel on Climate Change.
- ITCZ** Inter-Tropical Convergence Zone.
- LIM** Louvain-la-Neuve Sea Ice Model.
- LNLC** Low-Nutrient, Low-Chlorophyll.
- LPJ-Guess** Lund-Potsdam-Jena General Ecosystem Simulator
(dynamic vegetation model).
- M7** Modal Aerosol Module version 7.
- MAM4** Modal Aerosol Module-4.
- MERIS** Medium Resolution Imaging Spectrometer.
- MIMI** Mechanism of Intermediate complexity for Modelling Iron.
- MLD** Mixed Layer Depth.
- MODIS** Moderate Resolution Imaging Spectroradiometer.
- MPI-ESM** Max Planck Institute Earth System Model.
- NASA** National Aeronautics and Space Administration.
- NCAR** National Center for Atmospheric Research.
- NEMO** Nucleus for European Modeling of the Ocean.

NH Northern Hemisphere.

nMB Normalized Mean Bias.

NPP Net Primary Production.

nRMSE Normalized Root Mean Square Error.

NTCF Near-Term Climate Forcers.

OA Organic Aerosols.

OASIS3 Ocean Atmosphere Sea Ice Soil version 3.

OC Organic Carbon.

OC-CCI Ocean Color Climate Change Initiative.

OIF Ocean Iron Fertilization.

OLCI Ocean and Land Colour Instrument.

OXL Oxalate.

PISCES Pelagic Interactions Scheme for Carbon and Ecosystem
Studies.

POM Particulate Organic Matter.

PP Primary Production.

PSD Particle Size Distribution.

RF Radiative forcing.

RSMAS Rosenstiel School of Marine and Atmospheric Science (dust
observations).

Acronyms

SChl Surface Chlorophyll.

SeaWiFS Sea-viewing Wide Field-of-view Sensor.

SFe Soluble Iron.

SH Southern Hemisphere.

SIC Sea Ice Concentration.

SO Southern Ocean.

SPEW Speciated Particulate Emission Wizar.

SSP Socioeconomic Sceario and Pathway.

SST Sea Surface Temperature.

TM5-MP Tracer Model version 5, massively parallel version.

UPC Universitat Politècnica de Catalunya.

VIIRS Visible Infrared Imaging Radiometer Suite.

WACCM Whole Atmosphere Community Climate Model.

WCRP World Climate Research Programme.

WMO Wolrd Meteorological Organization.

Summary

Iron is a ubiquitous element that plays a critical role in the Earth system. It is an essential micronutrient required by most organisms for vital processes such as respiration, photosynthesis, and nitrogen fixation. Consequently, iron bioavailability is crucial, particularly in aquatic ecosystems, where approximately one-third of open ocean waters are iron-limited, restricting the biological activity of microorganisms. This shapes ocean productivity and affects the ocean's ability to capture atmospheric carbon dioxide. Understanding and quantifying the atmospheric supply of bioavailable iron to the ocean is critical, especially in the context of human-induced climate change.

Despite its significance, knowledge gaps remain regarding the atmospheric iron cycle and its implications for ocean biogeochemistry. Uncertainties persist, for instance, in the contributions of key sources such as dust, biomass burning, and fossil fuel combustion to bioavailable iron deposition, the influence of anthropogenic activities on future iron supply, and the interactions between atmospheric iron deposition and marine ecosystems.

This Thesis seeks to address these gaps by proposing the following objectives: (1) to evaluate the relative contributions of different sources and processes to soluble iron deposition under the present climate; (2) to characterize the extent and magnitude of bioavailable iron's effects on surface ocean ecosystems; (3) to quantify changes in soluble iron

Summary

deposition across past, present, and future climates; and (4) to constrain the impacts of future fire activity, underrepresented in commonly used emission datasets, on soluble iron deposition and ocean biogeochemistry.

To achieve these objectives, the EC-Earth3-Iron model is used; an Earth System Model that incorporates advanced iron emission and solubilization mechanisms, as well as the latest emission inventories. Conducted simulations across pre-industrial, present-day, and future climates quantify soluble iron deposition and explore its sensitivity to uncertainties in future socioeconomic pathways and dust and fire emissions. Additionally, comparisons between present-day modeled deposition fields and satellite observations provide insights into the links between atmospheric iron deposition and surface ocean productivity.

This work's findings provide novel insights into the atmospheric iron cycle and its implications for ocean biogeochemistry. This includes a detailed description of present-day soluble iron fluxes and their spatial distribution. This analysis reveals that non-dust sources, such as biomass burning and fossil fuel combustion, contribute over 75% of soluble iron deposition in iron-limited regions like the Southern Ocean and equatorial Pacific during certain seasons. These present-day estimates are further analyzed to highlight the impact of pulsed deposition events on global ocean biogeochemistry, with widespread positive responses in satellite-derived surface chlorophyll concentrations observed in the days following major iron input events. Another key finding is the sensitivity of soluble iron deposition to aerosol acidity and organic ligands, with simulations showing that socioeconomic trends have significantly altered deposition fluxes since the Industrial Revolution and will likely continue to do so until the century's end.

Additionally, improved estimates of future wildfire emissions indicate significant changes in the patterns of soluble iron deposition, suggesting an approximate 20% increase in the North Atlantic under certain future scenarios.

This work enhances the community's understanding of the atmospheric iron cycle and its role in regulating ocean productivity. It also underscores the importance of improving the representation of atmospheric iron processes in Earth System Models to better predict future climate scenarios, while outlining pathways for future research.

Resum

El ferro és un element ubicu que desempeña un paper crític en el sistema terrestre. És un micronutrient essencial requerit per la majoria d'organismes per a processos vitals com la respiració, la fotosíntesi i la fixació de nitrogen. En conseqüència, la biodisponibilitat del ferro és crucial, especialment en els ecosistemes marins, on aproximadament un terç de l'oceà està limitat pel ferro. Això modela la productivitat oceànica i afecta la seva capacitat per capturar diòxid de carboni atmosfèric. Comprendre i quantificar l'aport atmosfèric de ferro biodisponible a l'oceà és crític, especialment en el context actual de canvi climàtic accelerat.

Malgrat la seva importància, persisteixen llacunes en el coneixement sobre el cicle atmosfèric del ferro i les seves implicacions biogeoquímiques. Aquestes inclouen les incertes contribucions de fonts clau com la pols, els focs i la combustió de combustibles fòssils a la deposició de ferro biodisponible, la influència de les activitats antropogèniques en l'aport futur de ferro i les interaccions entre el ferro atmosfèric i els ecosistemes marins.

Aquesta Tesi aborda aquests punts amb els següents objectius: (1) avaluar les contribucions relatives de diferents fonts i processos a la deposició de ferro soluble; (2) caracteritzar la magnitud i l'abast dels efectes del ferro biodisponible en els ecosistemes marins; (3) quantificar canvis en la deposició de ferro soluble al llarg de climes passats, presents

Resum

i futurs; i (4) entendre millor els impactes de l'activitat futura d'incendis, infrarrepresentada en les dades d'emissions comunament utilitzades, a la deposició de ferro soluble i la biogeoquímica oceànica.

Per a això, s'utilitza el model EC-Earth3-Iron; un Model del Sistema Terrestre que incorpora mecanismes avançats d'emissió i solubilització de ferro, així com els inventaris d'emissions més recents. Diferents simulacions realitzades amb condicions de climes preindustrials, actuals i futurs quantifiquen la deposició de ferro soluble i exploren la seva sensibilitat a les incerteses en les trajectòries socioeconòmiques futures, així com en les emissions de pols i focs. A més, comparacions amb observacions satel·litals proporcionen informació sobre els vincles entre l'aport atmosfèric de ferro i la productivitat a la superfície de l'oceà.

Els resultats d'aquest treball proporcionen nous coneixements sobre el cicle atmosfèric del ferro i les seves implicacions per a la biogeoquímica oceànica, incloent una descripció detallada dels fluxos de ferro soluble actuals i la seva distribució espacial. Aquestes estimacions s'analitzen més a fons per ressaltar l'impacte de grans esdeveniments de deposició puntual en la biogeoquímica global de l'oceà, observant-se respostes positives generalitzades en les concentracions de clorofil·la superficial derivades de satèl·lits els dies posteriors a grans esdeveniments d'entrada de ferro. Un altre descobriment clau és la gran sensibilitat de la deposició de ferro soluble a l'acidesa dels aerosols i els lligands orgànics, amb simulacions que mostren que les tendències socioeconòmiques han alterat significativament aquests nivells i els fluxos de ferro des de la Revolució Industrial, i que continuaran fent-ho fins a finals d'aquest segle. Finalment, estimacions millorades de les emissions futures d'incendis indiquen canvis significatius en els patrons

de la deposició de ferro soluble, suggerint un augment aproximat del 20% a l'Atlàntic Nord en certs escenaris futurs.

Aquest treball millora la comprensió sobre el cicle atmosfèric del ferro i el seu paper en la regulació de la productivitat oceànica, subratlla la importància de millorar la representació dels processos atmosfèrics del ferro en els Models del Sistema Terrestre per predir millor els escenaris climàtics futurs i descriu possibles línies d'investigació futura.

Resumen

El hierro es un elemento ubicuo que desempeña un papel crítico en el sistema terrestre. Es un micronutriente esencial requerido por la mayoría de los organismos para procesos vitales como la respiración, la fotosíntesis y la fijación de nitrógeno. En consecuencia, la biodisponibilidad del hierro es crucial, particularmente en los ecosistemas marinos, donde aproximadamente un tercio del océano está limitado por el hierro. Esto moldea la productividad oceánica y afecta su capacidad para capturar dióxido de carbono atmosférico. Comprender y cuantificar el aporte atmosférico de hierro biodisponible al océano es crítico, especialmente en el contexto actual de cambio climático acelerado.

A pesar de su importancia, persisten brechas en el conocimiento sobre el ciclo atmosférico del hierro y sus implicaciones biogeoquímicas. Estas incluyen las inciertas contribuciones de fuentes clave como el polvo, los fuegos y la combustión de combustibles fósiles a la deposición de hierro biodisponible, la influencia de las actividades antropogénicas en el aporte futuro de hierro y las interacciones entre el hierro atmosférico y los ecosistemas marinos.

Esta Tesis aborda estos puntos con los siguientes objetivos: (1) evaluar las contribuciones relativas de diferentes fuentes y procesos a la deposición de hierro soluble; (2) caracterizar la magnitud y el alcance de los efectos del hierro biodisponible en los ecosistemas marinos; (3)

Resumen

cuantificar cambios en la deposición de hierro soluble a lo largo de climas pasados, presentes y futuros; y (4) entender mejor los impactos de la actividad futura de incendios, subrepresentada en los datos de emisiones comúnmente utilizados, a la deposición de hierro soluble y la biogeoquímica oceánica.

Para ello, se utiliza el modelo EC-Earth3-Iron; un Modelo del Sistema Terrestre que incorpora mecanismos avanzados de emisión y solubilización de hierro, así como los inventarios de emisiones más recientes. Diferentes simulaciones realizadas con condiciones de climas preindustriales, actuales y futuros cuantifican la deposición de hierro soluble y exploran su sensibilidad a las incertidumbres en las trayectorias socioeconómicas futuras, así como en las emisiones de polvo e incendios. Además, comparaciones con observaciones satelitales proporcionan información sobre los vínculos entre el aporte atmosférico de hierro y la productividad en la superficie del océano.

Los hallazgos de este trabajo proporcionan nuevos conocimientos sobre el ciclo atmosférico del hierro y sus implicaciones para la biogeoquímica oceánica, incluyendo una descripción detallada de los flujos de hierro soluble en la actualidad y su distribución espacial. Estas estimaciones se analizan más a fondo para resaltar el impacto de grandes eventos de deposición puntual en la biogeoquímica global del océano, observándose respuestas positivas generalizadas en las concentraciones de clorofila superficial derivadas de satélites en los días posteriores a grandes eventos de entrada de hierro. Otro hallazgo clave es la alta sensibilidad de la deposición de hierro soluble a la acidez de los aerosoles y los ligandos orgánicos, con simulaciones que muestran que las tendencias socioeconómicas han alterado significativamente estos niveles y los flujos

de hierro desde la Revolución Industrial, y que continuaran haciendolo hasta finales de este siglo. Finalmente, estimaciones mejoradas de las emisiones futuras de incendios indican cambios significativos en los patrones de la deposición de hierro soluble, sugiriendo un aumento aproximado del 20% en el Atlántico Norte en ciertos escenarios futuros.

Este trabajo mejora la comprensión sobre el ciclo atmosférico del hierro y su papel en la regulación de la productividad oceánica, subraya la importancia de mejorar la representación de los procesos atmosféricos del hierro en los Modelos del Sistema Terrestre para predecir mejor los escenarios climáticos futuros y describe posibles líneas de investigación futura.

Resumen



4



1

**Introduction
& Framework**

CHAPTER 1

The relevance of iron in the Earth system

Iron (Fe) is a ubiquitous element within the Earth system impacting many processes within it. In this Chapter, journey of Fe from land to the ocean is traced. To begin, the Earth system and the role of Fe within it is described. This is followed by a review of atmospheric Fe emissions, a comprehensive summary of its atmospheric life cycle, and a discussion of its deposition in the open ocean, where it ultimately impacts ocean biogeochemistry. Finally, the potential influence of anthropogenic activities and human-induced climate change on the Fe cycle is explored, along with the scientific challenges associated with constraining this.

1.1. Iron in the Earth System

1.1.1 Iron: the chemical element

The nucleus of Fe is composed of 26 protons and 30 neutrons. Formed in the heart of stars and dispersed into interstellar space by supernova explosions, Fe plays a central role in cosmic processes (Clayton, 1983).

Chapter 1. The relevance of iron in the Earth system

Within the Fe nucleus, the binding forces between protons and neutrons balance the repulsive forces between protons, resulting in one of the most stable nucleus in the universe (Krane and Halliday, 1987).

The Fe atom can exist in several states or ions. Two or three out of the 26 electrons of the electronic cloud of the Fe atom are easily exchanged during chemical reactions, leading to the formation of ferrous Fe(II) or Fe^{2+} and ferric Fe(III) or Fe^{3+} ions. In its pure state, Fe is a reactive metal that readily oxidizes in the presence of oxygen (Atkins, 2010).

The formation of Earth 4.6 billion years ago resulted in a significant accumulation of Fe, driven by its high stability. Fe constitutes more than 30% of Earth's mass, primarily concentrated in the core, though it is also the fourth most abundant element in the Earth's crust (McDonough and s. Sun, 1995).

The evolution of life on Earth is intricately linked to Fe, as it is essential for countless cellular processes and metabolic pathways in both eukaryotic and prokaryotic organisms (Frey and Reed, 2012). Despite its abundance, Fe can be scarce for growing organisms due to changes in its chemical form, which dictate its availability in biological systems.

All in all, Fe's pervasive presence across the atmosphere, biosphere, lithosphere, and hydrosphere influences a vast array of physical, chemical, and biological processes essential for sustaining life and supporting Earth's environmental balance (Schlesinger and Bernhardt, 2013; Frey and Reed, 2012).

1.1.2 The Earth System

The Earth System is an intricate network of life and elements that interact constantly through a complex exchange of energy and matter. This complex and dynamic network comprises five major components: the atmosphere, the hydrosphere, the cryosphere, the land surface, and the biosphere. These components interact with each other and are influenced by external forces, such as solar radiation.

Each component of the Earth System contributes uniquely to the Earth's climate. The atmosphere, being the most dynamic component, plays a crucial role in regulating the Earth's energy balance through the presence of greenhouse gases and aerosols, which interact with both incoming solar radiation and outgoing infrared radiation, ultimately influencing global temperatures. The hydrosphere, dominated by the oceans, acts as a massive heat reservoir, regulating temperature fluctuations and influencing weather patterns through oceanic circulation. The cryosphere, comprising reflective ice surfaces, affects the Earth's albedo and plays a critical role in ocean circulation. Vegetation and soil dynamics influence the uptake and release of greenhouse gases, while the marine and terrestrial biosphere closely interact with the atmosphere, affecting energy exchanges and the carbon cycle. Together, these interconnected components regulate and modify the Earth's climate, responding to both natural fluctuations and human-induced changes within the system (NASA, 1986; Jacobson et al., 2000).

Anthropogenic activities have increasingly become a key external force within the Earth System, particularly since the Industrial Revolution.

The burning of fossil fuels, deforestation, and other human activities have significantly increased the concentrations of greenhouse gases, such as carbon dioxide (CO_2), methane (CH_4) and nitrous oxide (N_2O), in the atmosphere. Atmospheric greenhouse gas levels are now higher than at any point in the past several thousand years and are the dominant cause of human-induced climate change (IPCC, 2023a; Zhang et al., 2013). Despite this, only about 40% of the carbon released through these activities remains in the atmosphere, with the oceans and the land biosphere absorbing the rest (IPCC, 2023b).

Understanding the global carbon cycle within the interconnected Earth System is a critical research challenge and key to managing future climate change. The World Climate Research Programme (WCRP) highlights this by identifying carbon feedbacks in the climate system as one of its seven Grand Challenges (Ilyina and Friedlingstein, 2016). This underscores the need for targeted research, advanced modeling, and detailed observations in this field in the coming decade.

1.1.3 The iron cycle

About a quarter of the CO_2 emitted to the atmosphere since the Industrial Revolution has been captured by the ocean (IPCC, 2023a; Falkowski et al., 2000). CO_2 is diffused from the atmosphere into the ocean's surface waters, where it dissolves and becomes part of the ocean carbon cycle. A fraction of this carbon is sequestered from the surface into the deep ocean, where it can remain stored for hundreds of years. The ocean carbon cycle is driven by three key pumps (Duan and Sun, 2003): the biological carbon pump (BCP), the production of organic carbon (OC) by phytoplankton in the surface ocean and its sinking and

1.1. Iron in the Earth System

rem mineralization (Emerson and Hedges, 2008); the carbonate pump, where calcifying plankton sequester carbon while releasing CO_2 (Smith and Key, 1975; Neukermans et al., 2023); and the physical pump, where physio-chemical processes transport surface carbon into the ocean’s interior for centuries (Ito and Follows, 2003).

While physical drivers such as warming and wind stress currently regulate the ocean’s uptake of anthropogenic carbon, biological processes are primarily responsible for the vertical gradient in dissolved inorganic carbon in the water column (Canadell et al., 2021). BCP is critical for long-term CO_2 storage (IPCC, 2023b). This biological contribution to CO_2 sequestration is expected to grow in significance as climate change progresses (Hauck et al., 2015; Siegel et al., 2023).

Marine biological processes, including the BCP, are fueled by primary production (PP), the chemical synthesis of organic compounds from atmospheric or dissolved CO_2 in the ocean. PP depends on the availability of light and nutrients such as nitrogen (N), phosphorus (P), Fe, and silica (Si) (Moore et al., 2013; Behrenfeld et al., 2006). In open-ocean regions far from coastal nutrient sources, and with limited nutrient supply from deeper waters, atmospheric deposition provides the dominant source of essential nutrients (Jickells et al., 2005; Mahowald et al., 2018). In particular, high-nutrient-low-chlorophyll (HNLC) regions are repleted with macronutrients, such as N, but experience limited Fe availability. In these regions, Fe acts as the primary limiting factor for phytoplankton growth and, consequently, PP (Jickells et al., 2005). The main HNLC regions are the Southern Ocean (SO), the equatorial Pacific, and the high-latitude North Pacific and North Atlantic (Fig. 1.1). Additionally, N-fixing organisms in

oligotrophic regions extend the ocean's sensitivity to Fe availability (Jickells et al., 2005; Mahowald et al., 2018). As a result, atmospheric Fe deposition can influence PP across roughly one-third of the global ocean.

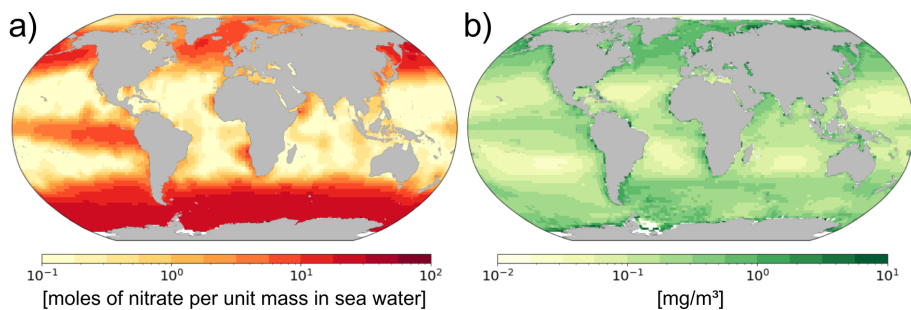


Figure 1.1: **Surface ocean nitrate and chlorophyll concentrations.** Mean observed surface ocean nitrate concentrations in moles of nitrate per unit mass in sea water as in the World Ocean Atlas 2023 (Garcia et al., 2024) (a) and mean 1998-2014 surface chlorophyll-a levels in mg per m^3 based on satellite data as in the ESA OC-CCI version 6 dataset (Sathyendranath et al., 2023) (b).

The dominant input of Fe to the atmosphere is mineral dust emitted from arid and semiarid areas of the world, with an estimated present-day contribution of 95%. Another contributor to atmospheric Fe supply is combustion, particularly from anthropogenic activities and biomass burning, which are thought to account for the remaining 5% (Luo et al., 2008) (see Section 1.2, Fig. 1.2).

However, only a small fraction of Fe is bioavailable to marine organisms. The definition of bioavailability remains elusive and is an active area of research, as Fe utilization by organisms involves complex biochemical pathways (Jickells et al., 2005; Lis et al., 2015; Baker and Croot, 2010). However, soluble Fe (SFe) is widely considered a reasonable

1.1. Iron in the Earth System

proxy for bioavailable Fe (Baker et al., 2006). Although SFe is generally considered to be Fe in the Fe(II) oxidation state, this may not always be the case, as other forms of Fe could also be bioavailable (Barbeau et al., 2001). Furthermore, Fe(II) itself is not universally bioavailable (Visser et al., 2003), adding complexity to our understanding of iron's role in marine ecosystems. SFe is operationally defined as the fraction of Fe in aerosol leachates that can pass through filters with pore sizes ranging from 0.02 to 0.45 μm (Meskhidze et al., 2016). Solubility at emission is reported to be low for freshly emitted Fe. However, experimental, observational, and modeling studies indicate that the solubility of Fe increases downwind of its sources due to various atmospheric processes (Rizzolo et al., 2017; Zhuang et al., 1992b), as described in Section 1.3.

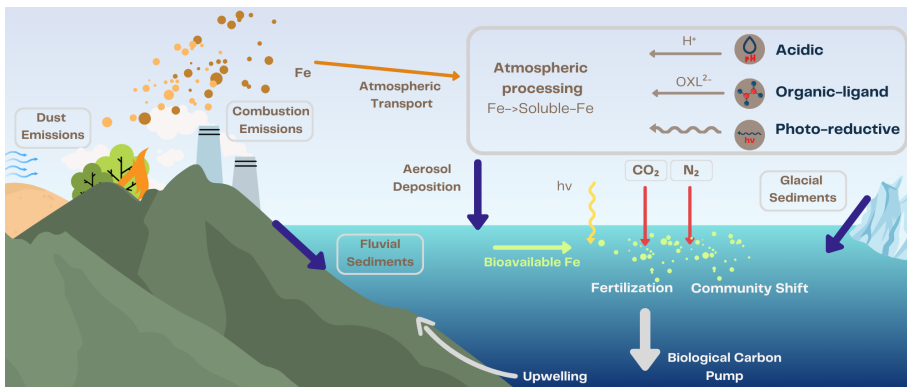


Figure 1.2: **Schematics of the Fe cycle.** Diagram illustrating the journey of atmospheric iron (Fe) sourcing from dust, fire, and anthropogenic fossil fuel combustion. Aerosol iron is transported through the atmosphere, where it undergoes solubilization processes (acidic, organic ligand, and photoreductive dissolution), before being deposited over the open ocean, where its bioavailable fraction serves as a nutrient for marine biota.

Understanding the flux, spatial distribution, and bioavailability of SFe to the ocean is essential for constraining models of marine

biogeochemical cycles and improving climate projections. The importance of these processes has been acknowledged since the publication of the Intergovernmental Panel on Climate Change (IPCC) Fifth Assessment Report (IPCC, 2014), which highlighted the need to address large biogeochemical-climate feedbacks as a key research priority. Insights into Fe cycling can help reduce uncertainties in predicting the ocean's role in mitigating climate change and assessing the effectiveness of carbon sequestration strategies.

1.1.4 The iron hypothesis

The influence of Fe in the Earth System extends far beyond present and future climate. Fe has long been recognized as a key factor in shaping climate conditions well before human-induced changes.

Over the past 800.000 years, CO_2 levels have fluctuated in step with global climate patterns, and it is widely recognized that CO_2 serves as a primary mediator in translating the effects of Milankovitch cycles, Earth's orbital variations, into glacial-interglacial climate transitions (Shakun et al., 2012).

The SO was identified as a potential driver of glacial/interglacial CO_2 variations as it ventilates large volumes of the ocean interior (Kohfeld et al., 2005). In the modern SO, deeply sequestered CO_2 is released into the atmosphere. This observation led to the hypothesis that during ice ages, this release was significantly reduced, causing an increase in oceanic CO_2 storage (Kumar et al., 1995). Evidence also emerged suggesting that phytoplankton growth in the SO is limited by Fe availability (Martin, 1990).

1.1. Iron in the Earth System

The magnitude of Fe-rich dust aerosol deposition also varied dramatically between glacial and interglacial periods. For instance, studies suggest that dust deposition during the Last Glacial Maximum ($\approx 21,000$ years ago) was between 2 and 10 times greater than in the current period (Lambert et al., 2015; Mahowald et al., 2006).

The convergence of all these findings led to the development of the "iron hypothesis" (Martin, 1990). This hypothesis posited that increased dust-borne Fe fertilization of SO phytoplankton during ice ages boosted ocean productivity. This, in turn, enhanced the BCP, where OC was sequestered in deep ocean waters via phytoplankton production and export.

Subsequent sediment reconstructions revealed that productivity during ice ages was not uniform across the SO. Productivity increased in the Subantarctic Zone, located in the northern part of the SO, but decreased in the Antarctic Zone, closer to the Antarctic continent (Jaccard et al., 2013; Mortlock et al., 1991). This heterogeneous pattern of productivity changes casts doubt on the Fe hypothesis explaining glacial-interglacial CO_2 variations. Instead, other processes such as increased sea-ice extent (Stephens and Keeling, 2000), reduced deep-water ventilation (Huang et al., 2020), and enhanced water column stratification (Francois et al., 1997) were proposed to explain the regulation of air-sea CO_2 (Weber et al., 2022).

Recent advances, however, have revived interest in the role of Fe in the SO in regulating glacial-interglacial CO_2 changes. It is now recognized that the marine BCP was likely more efficient during ice ages, which facilitated greater CO_2 partitioning into the ocean's interior (Vollmer

et al., 2022). Although the relative contributions of various mechanisms remain debated, recent Earth System Model (ESM) simulations suggest that air-sea disequilibrium, cooling, and Fe fertilization collectively amplified glacial carbon storage (Weber et al., 2022).

Climate-carbon cycle model assessments from the IPCC's Assessment Reports (IPCC, 2023b) underscore the SO as a pivotal region for oceanic carbon uptake in the present day and near future. However, the variability of this carbon sink and its response to future climate changes remain poorly understood and inadequately captured in current models. Even small shifts in atmospheric SFe inputs in this region could have disproportionate global impacts (Jickells et al., 2005).

1.2. Sources of atmospheric iron

The first step towards unraveling the Fe cycle is to identify the sources of Fe that impact the open ocean, how those are globally distributed, and their physicochemical nature.

Fe is known to be primarily supplied to the oceans through rivers and continental shelves, delivered as suspended sediment (Lam and Bishop, 2008; Lam et al., 2012). However, the transport of continental and glacial particulate Fe is largely confined to near-coastal regions. As a result, the primary source of Fe for the open ocean surface is the deposition of atmospheric aerosol Fe (Duce and Tindale, 1991).

Mineral dust, generated by wind erosion in arid and semi-arid regions, serves as the main contributor of Fe in the atmosphere, accounting for approximately 95% of total atmospheric Fe emissions (Hamilton et al.,

2020b). The remaining approximately 5% is emitted by combustion sources, including wildfires and anthropogenic fossil fuel combustion (Luo et al., 2008; Bergas-Massó et al., 2023). Furthermore, volcanic eruptions have been shown to be important episodic and regional sources of atmospheric Fe (Olgun et al., 2011; Duggen et al., 2010). Each source of atmospheric Fe has unique physical and chemical traits crucial for understanding its impact on ocean biogeochemistry; these characteristics are described in detail in the following subsections. For instance, freshly emitted Fe-dust is mostly insoluble, while combustion Fe, though less abundant, may be more soluble (Ito, 2015).

1.2.1 Iron in dust aerosols

Airborne dust is one of the most abundant aerosols in the atmosphere, representing the largest aerosol type by mass and serving as a fundamental component of the Earth system (Knippertz and Stuut, 2014). Mineral dust is thus the primary source of Fe in the atmosphere, currently accounting for around 95% of the total Fe emitted by mass (Hamilton et al., 2020b). Mineral aerosols consist of soil particles that are lifted into the atmosphere when high winds occur over erodible surfaces. Its entrainment requires dry, unvegetated, and easily erodible soils (Mahowald et al., 2005) (Fig. 1.3). Recent estimates constrained by global observations of dust aerosol optical depth and size-resolved concentrations suggest that every year between 3400 and 9100 Tg yr⁻¹ are emitted globally (Kok et al., 2021a,b).

The largest source region on Earth is the Sahara Desert, which hosts what is thought to be the most prolific dust source of the planet: the Bodélé Depression, located in the northern Lake Chad Basin (Prospero

et al., 2002; Ginoux et al., 2012). Recent estimates suggest that North African source regions contribute around 50% of the total global loading of dust (Kok et al., 2021b). Other major dust source regions, representing around 40% of the total global loading of dust (Kok et al., 2021b), are the Middle East (Pease et al., 1998; Hamidi et al., 2013) and the Asian continent, with the Taklamakan Desert and the Gobi Desert as the main hotspots in the region (Chen et al., 2017). All these sources constitute the so-called “global dust belt” in the Northern Hemisphere (NH), extending from the west coast of North Africa, over the Middle East, Central and South Asia, to China (Prospero et al., 2002). Dust aerosols are also emitted, but to a lesser extent, from arid regions in Australia, South Africa, South America and North America (Ginoux et al., 2012). In addition, it is increasingly recognized that dust emitted in high latitudes is also a non-negligible source of dust, and consequently, Fe, to high-latitude oceans (Bullard et al., 2016; Anderson et al., 2017; Meinander et al., 2022).

Once emitted, aerosol dust is transported through the atmosphere following the main wind currents. As depicted in Fig. 1.3, dust from North Africa primarily travels along four routes: (1) southward to the Sahel and Gulf of Guinea, (2) westward to the North Atlantic, (3) northward to Europe and the Mediterranean, and (4) eastward to the Middle East (Shao et al., 2011). Dust from the Middle East and Central Asia is driven by the Indian monsoon towards the Indian Ocean (Shao et al., 2011; Di Biagio et al., 2021), while in East Asia, it typically moves southeast and northeast, sometimes reaching North America’s west coast. Australian dust mainly travels southeast to the Southern Pacific or northwest to the Indian Ocean (Shao et al., 2011). South

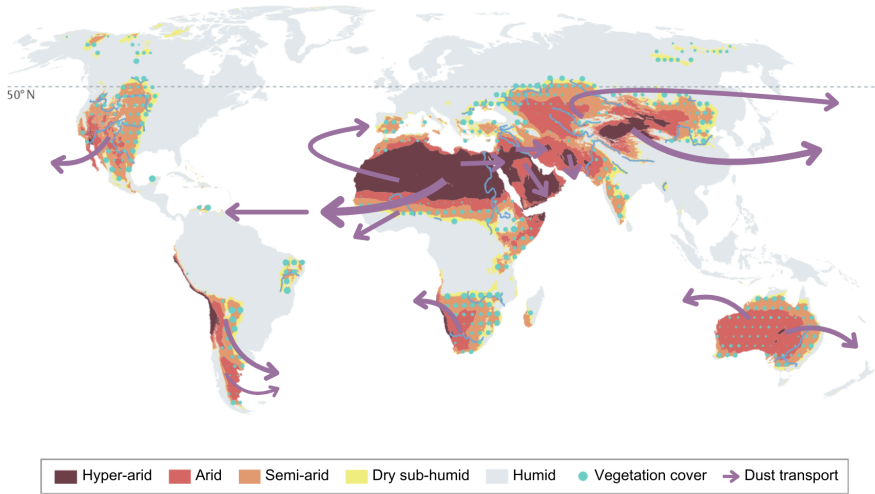


Figure 1.3: **Global arid regions and main dust transport patterns.** The extent and classification of aridity-index-defined drylands for 1961–1990, based on the TerraClimate dataset with high (≈ 4 km) spatial resolution. The cyan dots illustrate the density of vegetation cover for 1982–1990 (based on the GIMMS normalized difference vegetation index), with larger dots indicating denser vegetation cover. Purple arrows reflect the main dust transport patterns as described in Shao et al. (2011). *Modified from Lian et al. (2021).*

American dust often crosses the South Atlantic, occasionally reaching Antarctica (Li et al., 2010; Johnson et al., 2011), and in North America, Santa Ana winds carry dust to the eastern Pacific (Muhs et al., 2007). Limited research on high-latitude dust pathways includes evidence of Icelandic dust transport to the Northern Atlantic and sub-Arctic oceans (Baddock et al., 2017).

1.2.1.1 Key dust microphysical properties

Dust is present in soils and in the atmosphere as a complex mixture of minerals with diverse physicochemical properties that exhibit

significant regional variability, rather than a homogeneously mixed species. Understanding these variations is then essential for accurately estimating Fe dust emissions.

Dust consists of a mixture of different minerals including feldspars, quartz, clay minerals (mica/illite, kaolinite, palygorskite, chlorite and smectite), carbonate minerals (mainly calcite and dolomite), salts (mainly halite and gypsum), Fe oxides and hydroxides (mostly goethite and hematite) and other oxides or hydroxides of titanium, magnesium and aluminium (Formenti et al., 2008; Kandler et al., 2007; Scheuven et al., 2013; Baldo et al., 2020). However, our knowledge of soil mineralogy at the global scale has traditionally relied on a scarce set of soil descriptions. These measurements are particularly rare in the arid and semi-arid regions prone to dust emission, and usually provide only a crude representation of the size distribution. Building on this information, previous studies (Claquin et al., 1999; Nickovic et al., 2012; Journet et al., 2014; Ito and Wagai, 2017) have developed soil mineralogy maps aimed at atmospheric and climate modeling. These maps detail the mineral mass fractions within the clay (<0.002 mm) and silt (0.002–0.05 mm) size ranges (Blott and Pye, 2012). They are built upon soil descriptions usually obtained through experimental techniques that break the aggregates originally present in the soil (i.e., wet sieving). As a result, phyllosilicates, which are usually emitted as aggregates, are overemphasized in the finer soil fractions compared to what is observed in airborne dust. Moreover, wet sieving has the effect of wetting the surface of the aerosol/dust and removes the most soluble and labile Fe fraction from the samples (Shi et al., 2012b).

These minerals have varying Fe content, chemical structures, and typical

1.2. Sources of atmospheric iron

grain sizes, which vary significantly based on geographic origin and particle size, thus affecting the total Fe emitted and its susceptibility to dissolution (Claquin et al., 1999; Hand et al., 2004; Journet et al., 2008; Shi et al., 2012b). The type of Fe is mineral dependent: aluminosilicates contain Fe inclusions as well as surface coatings of nanohematite and ferrihydrite (Shi et al., 2009, 2012b; Ito and Xu, 2014). Fe associated with hematite and goethite is tightly bound to oxygen in Fe oxides or hydroxides, is typically larger in size and is less soluble.

Soil Fe content in both fine and coarse grain sizes ranges from 1% to 15% (Fig. 1.4), but it remains poorly constrained and varies across different soil mineralogical maps (Gonçalves Ageitos et al., 2023) (Fig. 1.4). Despite these uncertainties, certain patterns are consistent across datasets, for example, the total Fe content in Sahelian soils is higher than in other North African dust source regions, such as in the Bodélé Depression, where typically Fe content is lower ($\approx 1\%$) (Go et al., 2022). The proportion of the different minerals such as Fe oxides within total Fe also varies geographically. Saharan dust contains 25%–40% Fe as oxides, while Sahelian dust can reach up to 60% (Shi and Baldo, 2023). On the other hand, high-latitude dust is known to have very different mineralogy than low-latitude dust (Shi and Baldo, 2023). For example, Icelandic dust particles are distinguished by the fact that most of them consist primarily of amorphous basaltic materials, the total Fe content is usually very high (9%–13%) (González-Romero et al., 2024), magnetite is abundant and hematite and goethite contribute only 1%–6% of the total Fe, which is significantly lower than in low-latitude dust.

All these geographic variations in Fe content and mineralogy composition underscore the complexity of understanding Fe dust

emissions, making this a challenging topic of study. Early models aimed at representing the contribution of dust sources to the atmospheric Fe cycle neglected this complexity, using a constant Fe content from dust instead (Luo et al., 2008). This simplification is still assumed in most biogeochemical ocean models, which commonly apply dust climatologies with a fixed Fe ratio (e.g., 3.5%; Aumont et al. (2015)). The solubility of Fe-dust at emissions is as well uncertain but it is thought to be generally low, $\approx 0.1\%$ (Hand et al., 2004; Ito and Shi, 2016).

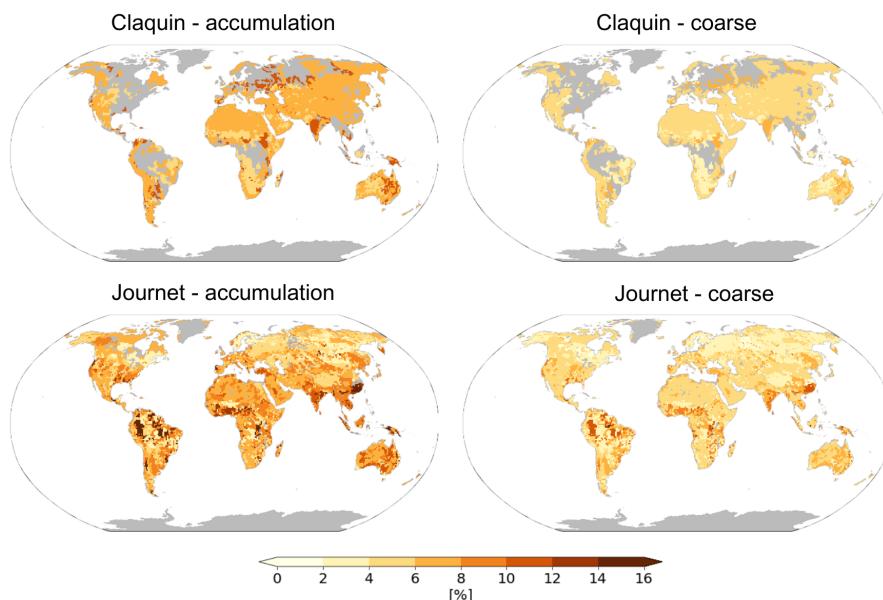


Figure 1.4: **Fe content in soil minerals.** Iron (Fe) content in % in soil minerals for Claquin et al. (1999) mineralogy (upper figures) and Journet et al. (2014) mineralogy (bottom figures) for the accumulation size mode (left column) and the coarse size mode (right column).

As mentioned above, mineralogy of dust is known to have an important role in Fe dissolution in the atmosphere. Alkaline elements present in

dust (e.g., calcite, potassium) alter the acidity of aerosols and hence their efficiency to dissolve in the atmosphere (Journet et al., 2008). Fe sourcing from different minerals shows different susceptibility to dissolve (Cwiertny et al., 2008; Shi et al., 2011b; Journet et al., 2008; Crusius et al., 2009; Fu et al., 2010). Despite this, several early modelling studies on atmospheric Fe assumed that Fe existed only as hematite and applied one or a series of dissolution rates (Meskhidze et al., 2005; Luo et al., 2005; Solmon et al., 2009). This contrasts with experimental studies showing that Fe dissolves very fast initially and then slower and Fe dissolution rates are strongly pH dependent (Spokes et al., 1994; Spokes and Jickells, 1996; Desboeufs et al., 1999, 2005; Mackie, 2005; Cwiertny et al., 2008; Fu et al., 2010; Deguillaume et al., 2010). In Shi et al. (2011a) a three-stage kinetic approach was proposed to fit the pH- and time-dependant Fe dissolution experimental data. In the first stage, a rapid dissolution of hydrous ferric oxide coatings on the mineral particle surfaces is given, resulting in a swift increase in SFe concentrations. This is followed by a slower, intermediate phase where nano-sized Fe oxides present on the surface of the dust particles dissolve. The third and final stage involves the gradual release of Fe from fine-grained materials internally mixed with aluminosilicate particles. This phase is characterized by a sustained but low rate of Fe release due to the slow dissolution of the mineral matrix. Such approach has been used recently to better represent in models the mineralogy-dependent Fe emissions and dissolution from dust sources such the EC-Earth3-Iron model (Myriokefalitakis et al., 2015, 2022) that will be used in this Thesis (see Section 4.2.1).

Additionally, soil mineralogy determines the size distribution of

emitted particles, which is a crucial factor in Fe dissolution processes. Smaller particles have longer atmospheric lifetimes and surface area, providing more opportunities for dissolution (Shi et al., 2011b). The size-dependent composition of the parent soil determines the mineralogy of the emitted dust. During emission, the original, undisturbed aggregates are fragmented, but only partially (Pérez García-Pando et al., 2016). This results in differences in the particle size distribution (PSD), mineralogy, and mixing state between the emitted particles derived from the undisturbed soil versus the disturbed (wet-sieved) soil (Fig. 1.5; Perlwitz et al. (2015a); Panta et al. (2023)). It has been shown that Brittle Fragmentation Theory (BFT) (Kok, 2011) provides a valuable framework to predict the emitted PSD in terms of its constituent minerals (Perlwitz et al., 2015a,b; Pérez García-Pando et al., 2016). BFT predicts that the emitted PSD is shifted toward larger diameters compared to the PSD of the dispersed soil (Fig. 1.5). Despite the crude size-dependence of the mineral fractions derived from the soil type atlas, the emitted PSD derived using BFT significantly improves the ability to predict global measurements of the dust mineral composition (Perlwitz et al., 2015b). Recent Fe modelling studies (Scanza et al., 2018; Ito and Shi, 2016) include BFT to describe the emitted PSD of individual minerals.

The diameter of aerosol mineral dust particles containing Fe ranges from less than $0.1 \mu\text{m}$ to over $100 \mu\text{m}$ (Mahowald et al., 2014; Liu et al., 2022a). This wide range in sizes spanning more than three orders of magnitude is a particular characteristic of dust aerosols. Aerosols have historically been divided into two size categories in atmospheric sciences: fine and coarse (Seinfeld and Pandis, 2016). The fine mode is further

1.2. Sources of atmospheric iron

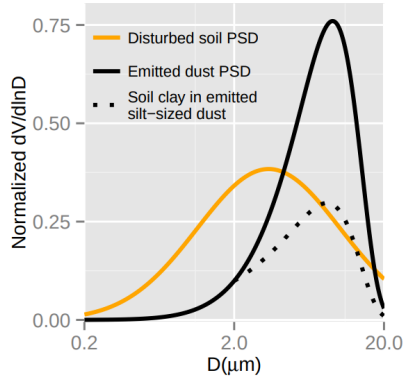


Figure 1.5: **PSD of disturbed soil versus emitted dust.** Example of emitted particle size distribution (PSD) computed with Brittle Fragmentation Theory (black solid line) in comparison of average soil dispersed PSD (orange solid line). The dotted line represents the contribution of dispersed soil clay particles to silt sized dust aggregates. *Modified from Perchwitz et al. (2015a).*

separated into three submodes: nucleation, Aitken, and accumulation (Seinfeld and Pandis, 2016). Prior studies linked dust particles to the coarse mode, but more recent studies have shown that they are also present in the fine mode. Additionally, it has been shown that coarser particles than initially thought can be transported thousands of km (Pérez García-Pando et al., 2016; Jeong et al., 2014). To standardize the boundaries between aerosol modes and the upper limit of the coarser mode, Adebisi et al. (2023) has recently proposed this classification in terms of the geometric diameter (D): (1) Fine dust $D < 2.5 \mu\text{m}$, (2) Coarse dust $2.5 < D < 10 \mu\text{m}$, (3) Super-coarse dust $10 < D < 62.5 \mu\text{m}$, and (4) Giant dust $D > 62.5 \mu\text{m}$.

1.2.2 Iron from fossil fuels

Aeolian dust sources were the primary focus of early research on the impacts of Fe on ocean biogeochemistry (Hand et al., 2004; Luo et al., 2003; Gregg et al., 2003; Moore et al., 2004; Mahowald et al., 2005; Fan et al., 2006). However, the models that simulated the atmospheric transport, chemical processing, and deposition of Fe in aerosols failed to adequately reflect the observed amounts of SFe (Hand et al., 2004; Luo et al., 2005; Fan et al., 2006), indicating the presence of alternative sources. It was reported by Chuang et al. (2005) that even during dust storms, SFe measured at an atmospheric deposition site in Korea was not dominated by mineral sources. Additionally, Sedwick et al. (2007) suggested that the atmospheric supply of bioavailable Fe to the Atlantic Ocean's surface was significantly influenced by emissions of Fe from fossil fuel combustion. However, due to significant uncertainty regarding the origins and chemical forms of Fe from combustion, few early global models took into account the impact of this element on the open-ocean biogeochemistry (Krishnamurthy et al., 2009; Okin et al., 2011).

The primary anthropogenic sources of fossil fuel-Fe include the combustion of coal, wood, and oil (e.g., heavy fuel oil, gasoline, diesel, and natural gas), with heavy fuel oil combustion in boilers and ships being particularly significant. Industrial emissions from smelting processes are also major contributors, encompassing the production of Fe and steel, copper, aluminum, zinc, and lead through both smelting and sintering activities (Rathod et al., 2020). While coal and smelting dominate total Fe emissions, oil and wood combustion

1.2. Sources of atmospheric iron

are the main sources of SFe (Rathod et al., 2020; Ito and Miyakawa, 2023; Rathod et al., 2024). Improved source apportionment is needed to refine regional contributions more accurately (Miyakawa et al., 2023). The first estimate of Fe emissions from fossil fuels and biomass burning was 1.7 Tg yr^{-1} , calculated using the Speciated Particulate Emission Wizard (SPEW) (Luo et al., 2008). Because there are limited observations of Fe emissions from such sources, this software calculates emissions of Fe from black (BC) and OC aerosol emission estimates by combining fuel consumption data provided by the International Energy Agency (2008, 2012) and specific emission factors for individual fuel-use categories (Bond et al., 2004). Ito and Feng (2010) later revised this estimate to 1.2 Tg yr^{-1} for year 2001. In such early modeling estimates, solubility at emission of fossil fuel combustion sources was set at 4%. Building on previous research and accounting for high Fe emissions from ships as well as from oil fly ash, Ito (2013) also estimated fossil-fuel combustion-related Fe emissions at 1.2 Tg yr^{-1} for the year 2001. The study also emphasized that the high solubility of Fe in shipping emissions (80%) significantly improved model accuracy over the northern Pacific and East China Sea regions. The majority of Fe from coal combustion is in the coarse particle size range (Luo et al., 2008; Ito, 2013), while oil combustion aerosols are shown to be predominantly in the fine mode (Ito, 2013).

More recent modeling work of the atmospheric Fe cycle that takes into account Fe aerosols originating from fossil fuels in addition to dust and fires (Hamilton et al., 2019; Ito and Xu, 2014; Myriokefalitakis et al., 2018; Scanza et al., 2018) agrees within an order of magnitude with observations of atmospheric total and soluble surface Fe concentrations

over marine regions. In the SO however, models still underestimate observations between 2 and 4 orders of magnitude. Underestimated combustion sources have been proposed as a contributing factor to a low model bias in the SO (Hamilton et al., 2019; Ito et al., 2019; Myriokefalitakis et al., 2018), based on observed high Fe solubilities. To address this, anthropogenic emissions should be five to ten times higher than in the majority of current inventories (Conway et al., 2019; Hamilton et al., 2019; Ito et al., 2019). Recent studies have primarily focused on developing a more comprehensive mineralogy-based emission inventory of anthropogenic combustion Fe from residential, transportation, and industrial activities (Rathod et al., 2020). Rathod et al. (2020) integrated total Fe emissions with available fuel- and mineral-specific Fe solubility data, revealing that anthropogenic combustion-Fe emissions in the fine fraction are approximately 10–20 times higher than previously reported. This significant increase is largely attributed to the inclusion of smelting activities, which, as Rathod et al. (2020) demonstrates, account for about 75% of fine Fe anthropogenic emissions for the 2010 year.

Fossil fuel combustion Fe sources have different geographic distributions. Combustion Fe sources from industrialized processes are concentrated in East Asia, Europe, and the east coast of North America. Shipping emissions are of particular interest in the context of ocean biogeochemistry, as these emissions often occur in the open ocean. All in all, a lack of long-term total and SFe observations, especially near sources currently limits the ability to constrain such kind of emissions. Detailed inventories are typically developed using bottom-up approaches, which combine activity data with emission factors, but

these methods are time-intensive and challenging to implement on a global scale. In contrast, top-down emission inventories are less time-intensive; however, the scarcity of specific data on Fe emissions significantly hinders the development of such approaches.

1.2.3 Iron from biomass burning

While fire-derived Fe contributes relatively little to global emission budgets compared to major sources such as desert dust, its regional impacts may be as significant as those from fossil fuel Fe emissions (see Section 1.2.2) (Guieu et al., 2005; Ito, 2011; Perron et al., 2022). Recent advancements in atmospheric Fe modeling have sought to include fire-derived Fe alongside fossil fuel emissions, driven by observational data supporting its significant regional effects (Ito et al., 2019).

However, the episodic and unpredictable nature of wildfires poses challenges to obtaining globally representative aerosol samples. This unpredictability complicates both the analysis of smoke plume composition and constraining those emissions in modeling systems. Atmospheric sampling on the western coast of the United States of America reported a 75% increase, on average, in total atmospheric Fe loadings during fire events compared to pre-fire atmospheric conditions (Schlosser et al., 2017).

Although biomass itself contains limited Fe, the observed increase in Fe loadings raises questions about the mechanisms by which fires entrain Fe-bearing particles into smoke plumes. When estimating Fe emissions from fires, it is hard to distinguish what fraction of this Fe comes from the combusted plant material and how much Fe is contributed from soil

suspended in uplifting currents. Studies have attempted to isolate the foliage fraction. A field study on a reed combustion fire found that most of the Fe liberated during the event was derived from soil suspension, not from the plant material itself (Kurisu and Takahashi, 2019).

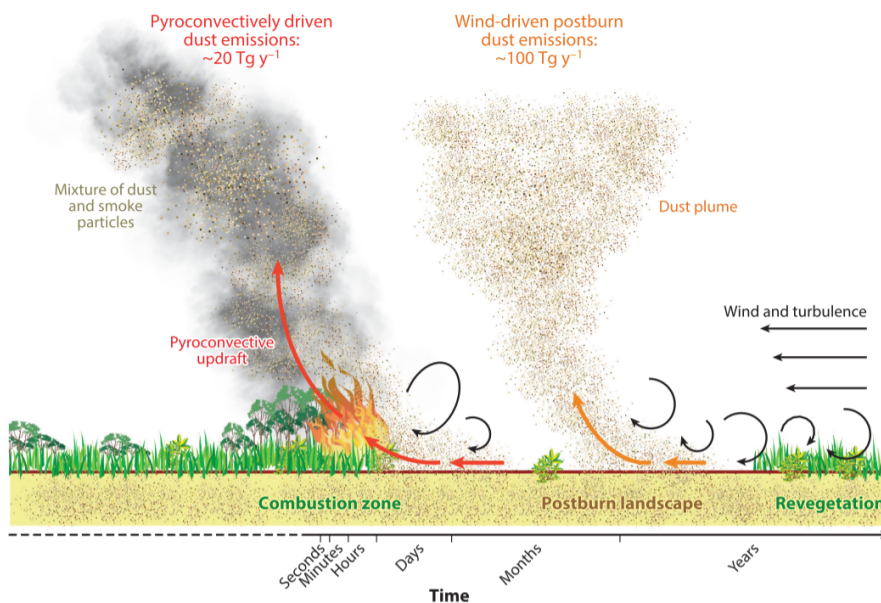


Figure 1.6: **Interplay of dust and fire aerosol sources.** Properties and estimated magnitudes of dust emissions during and after a fire as a function of time starting with an active fire. *Extracted from Hamilton et al. (2022).*

Further insights into fire-driven dust emissions have emerged from studies examining the interplay between fires and near-surface wind patterns. Using an idealized model, Wagner et al. (2018) demonstrated that agricultural fires create aerodynamic conditions conducive to dust emissions (Fig. 1.6). Subsequent research estimated pyroconvectively driven dust emissions by combining fire-modulated wind simulations with dust emission parameterizations, yielding fluxes of $1.0\text{--}5.0\text{ g m}^{-2}\text{ h}^{-1}$ (Wagner et al., 2021). Scaled globally, these emissions could

1.2. Sources of atmospheric iron

account for up to 20 Tg yr^{-1} , contributing an additional 6% to the global dust burden (Wu et al., 2020), especially in regions outside the dust belt.

Postburn landscapes have also been identified as potentially significant dust sources. Regional studies report enhanced dust fluxes following wildfires due to reduced vegetation cover and soil moisture (Wagenbrenner et al., 2013, 2017; Jeanneau et al., 2019). A recent global analysis by Yu and Ginoux (2022) using satellite data showed that 54% of approximately 150,000 large wildfires were followed by substantial dust emissions, persisting for days to weeks over typically dust-free regions.

The solubility of Fe in biomass burning emissions, although thought to be higher than for dust Fe emissions from arid areas (Bowie et al., 2009; Winton et al., 2016), is not well constrained and exhibits a wide range, from 2% (Paris et al., 2010) to 46% (Oakes et al., 2012). This high solubility enhances the bioavailability of Fe in marine environments, underscoring the importance of fire-derived Fe in ocean biogeochemistry.

Active fires occur worldwide, with particularly high activity in tropical regions such as Central Africa, South America, and Southeast Asia, alongside significant contributions from high-latitude sources in Boreal Eurasia and North America. In tropical regions, fire-emitted aerosols are transported westward by trade winds; for example, aerosols from tropical African fires are carried across the equatorial Atlantic, while those from South American forests traverse the equatorial Pacific. At higher latitudes, fire aerosols are transported by westerlies and can reach remote regions such as the SO and the Arctic Ocean (Fig. 1.7).

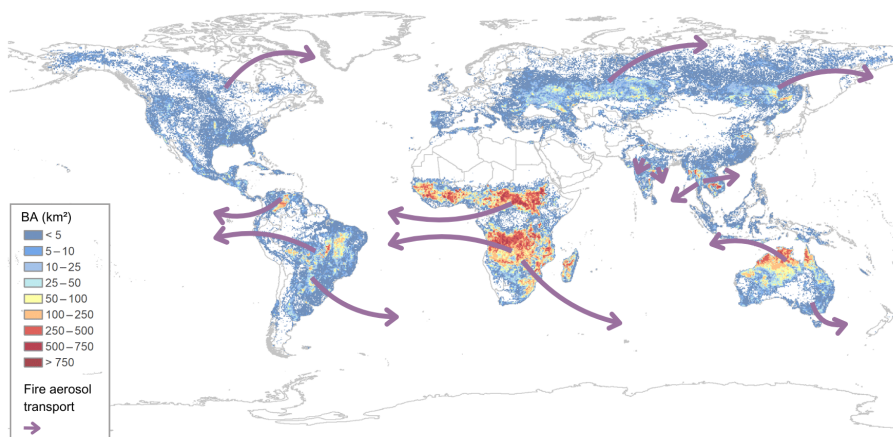


Figure 1.7: **Burned area and transport pathways.** Average global annual burned area (km²) from the FireCCI50 product, based on MERIS satellite images. Typical transport pathways of fire aerosols are represented in purple. *Modified from Chuvieco et al. (2018).*

Fire-driven (pyroconvective) Fe emissions are notable for their ability to reach higher altitudes compared to dust or fossil fuel emissions. Aerosols entrained in the free troposphere can travel longer distances, undergoing atmospheric processing. For instance, smoke from the 2020 Australian megafires circumnavigated the Southern Hemisphere (SH) (Khaykin et al., 2020). These unprecedented megafires boosting ocean productivity in the SO have spurred case studies examining the Fe content in smoke plumes and its impact on open waters (Tang et al., 2021; Perron et al., 2022).

1.2.4 Iron from volcanic eruptions

Volcanic eruptions release large volumes of volcanic ash and aerosols into the atmosphere, making them an important natural nutrient

1.2. Sources of atmospheric iron

source to the open ocean, especially on local to regional scales. The physicochemical properties and depositional patterns of volcanic aerosols differ from those of mineral dust, wildfires, or anthropogenic sources (Langmann, 2013). Their PSD goes from submicron to a few millimeters particle diameters (Stohl et al., 2011); such a large particle size range affects settling velocities and hence the nutrient flux to the ocean.

The chemical composition, surface salt coatings, and PSD of volcanic ashes vary widely, as does the array of nutrients (Duggen et al., 2007; Olgun et al., 2013) and trace metals (Hoffmann et al., 2012; Mahowald et al., 2018) released. Volcanic ash is constituted of 45–75 wt% Si and 1.0–11.0 wt% Fe, depending mainly on the chemistry of the lava and eruption type. The Fe solubility of volcanic ash varies significantly, with the highest solubilities measured in acidic (pH 1–5) solutions (22%) and lower solubilities measured in buffered seawater (0.001–1.8%) (Duggen et al., 2010).

The volcanic ash supply to marine environments can reach as high as 100 g m^{-2} near the volcano, decreasing exponentially to $0.1\text{--}0.3 \text{ g m}^{-2}$ several hundred kilometers away in open ocean regions (Olgun et al., 2013). The most significant volcanic ash deposition areas are in the Pacific Ocean near continental shelves. Remote volcanic hotspots, such as Iceland and Hawaii, also serve as notable nutrient sources to the North Atlantic and North Pacific (Hamilton et al., 2022).

The episodic and highly variable nature of volcanic eruptions, combined with the difficulty of quantifying their contributions to nutrient fluxes and the inherent unpredictability of future emissions, makes their

inclusion in current and long-term Fe estimates highly challenging. Additionally, the localized and short-term impact of volcanic ash deposition contrasts with the more continuous and widespread sources, such as mineral dust, that are the focus of this study. As a result, volcanic eruptions are not accounted for in most Fe estimates and models.

1.3. Atmospheric Dissolution of Iron

Once Fe aerosols are emitted, aerosol transport pathways and distance traveled are determined by a particle's properties (size, composition, and density), atmospheric conditions (particle uplift and buoyancy and wind speed and direction), and travel altitude. The smaller the particle is and the higher its altitude of travel is, the greater chance there is for long atmospheric residence times and for reaching remote marine ecosystems in its soluble form (Baker and Croot, 2010). Most of the SFe being deposited in the ocean has been shown to solubilize in the atmosphere rather than being freshly emitted as soluble. Recent multimodel estimates suggest a global SFe production rate of $0.56 \pm 0.29 \text{ Tg yr}^{-1}$, underscoring substantial uncertainty in these processes (Ito et al., 2019; Myriokefalitakis et al., 2018).

Fe solubility at emission varies widely across aerosol sources as seen in Section 1.2. Anthropogenic combustion-related Fe-containing aerosols, particularly those from oil fly ash in industries and shipping, often exhibit significantly higher solubilities, primarily due to the presence of ferric sulfates (Chen et al., 2012; Ito, 2013; Rathod et al., 2020; Crusius et al., 2009; Desboeufs et al., 2005). In contrast, Fe-dust

1.3. Atmospheric Dissolution of Iron

aerosols typically exhibit lower solubilities, though still heterogeneous. This variability in Fe solubility at emission is reflected in modeling studies, with some models assuming relatively high solubility at emission based on aerosol size (Hamilton et al., 2019; Myriokefalitakis et al., 2011), while others consider Fe to be largely insoluble at emission, with solubility enhanced during transport via atmospheric processing (Ito, 2015; Ito et al., 2021).

Although solubilities of freshly emitted Fe tend to be low, observational and experimental evidence point towards an increase in Fe solubility downwind of the sources (Rizzolo et al., 2017; Rodríguez et al., 2021; Zhuang et al., 1992a). This increase in solubility can only be explained via the atmospheric processing of Fe-containing aerosols. It is specially evident with finer particles showcasing higher solubilities (Siefert et al., 1999) as longer lifetimes and increased surface area make atmospheric processing more efficient (Hand et al., 2004).

Atmospheric solubilization of Fe is known to be driven by three primary pathways: (i) acidic dissolution, (ii) organic ligand-promoted dissolution, and (iii) photoreductive processes (Ito and Shi, 2016), each of which is described below.

- Acidic dissolution: Mineral aerosols can undergo chemical transformation when coated with strong inorganic acids during atmospheric transport. Sulfates (SO_4^{2-}), a dominant species in atmospheric aerosols, control liquid water content and acidity, facilitating Fe dissolution at low pH. This process destabilizes Fe-O bonds in mineral lattices, converting insoluble Fe to bioavailable forms such as ferrous ions, inorganic soluble Fe, and

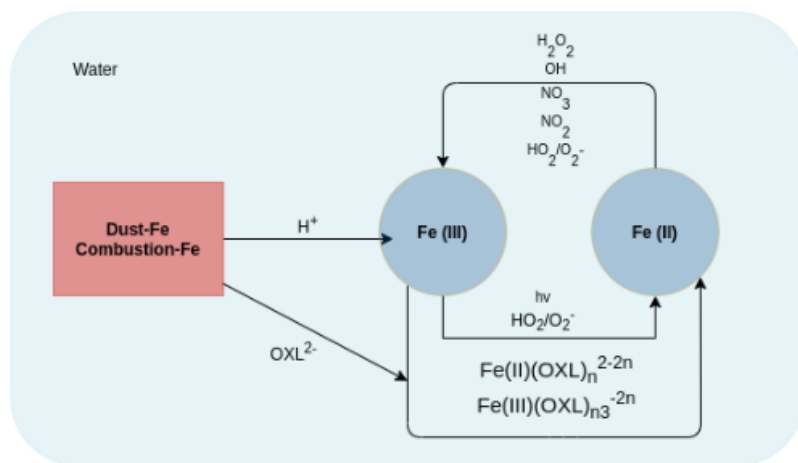


Figure 1.8: **Atmospheric processing of Fe.** Schematics of main atmospheric processing pathways of aerosol iron (Fe). *Modified from Myriokefalitakis et al. (2015).*

Fe-organic complexes (Zhu et al., 1992; Spokes and Jickells, 1996; Mackie, 2005).

- Organic ligand dissolution: Organic ligands, particularly oxalate (OXL), enhance Fe solubility by forming stable complexes with Fe species. Laboratory studies reveal a linear correlation between Fe solubility and OXL concentrations, driven by ligand adsorption and electron-donor properties (Paris and Desboeufs, 2013). Oxalic acid, derived from anthropogenic combustion, ozonolysis, and hydrocarbon photooxidation, is prevalent in cloud water (Warneck, 1999). Three sub-mechanisms underlie ligand-mediated dissolution: i) adsorption of ligands onto mineral surfaces, ii) non-reductive dissolution, and iii) reductive dissolution involving ligand-electron transfer (Paniyas et al., 1996;

Stumm and Morgan, 2012).

- **Photoreductive Processes:** Photochemical reactions involving Fe play a significant role in increasing Fe solubility, particularly via the reduction of Fe(III) to Fe(II). These reactions are driven by light-induced interactions with hydrogen peroxide, organic compounds, and trace metals in deliquesced aerosols.

As discussed in Section 1.2.1.1, Fe in mineral dust exists in various forms, and its solubility depends on the type of chemical bonding or compositional form (e.g., iron oxides versus aluminosilicate inclusions) (Lafon et al., 2004; Journet et al., 2008), as well as on particle size (Baker et al., 2006). Experimental studies show that Fe-dust solubilization occurs in distinct stages: an initial rapid phase, a slower intermediate phase, and a final sustained release from the mineral matrix (Spokes et al., 1994; Spokes and Jickells, 1996; Desboeufs et al., 1999, 2005; Mackie, 2005; Cwiertny et al., 2008; Fu et al., 2010; Deguillaume et al., 2010). Moreover, Fe from combustion sources exhibits solubilization patterns distinct from those of dust sources, with faster solubilization rates (Chen and Grassian, 2013; Baldo et al., 2022). To accurately estimate atmospheric solubilization, modeling systems must account for both the different solubilization mechanisms and the varying responses of different Fe sources.

1.4. Atmospheric Deposition

During transport, aerosol Fe particles are subject to removal through deposition processes, which strongly influence their atmospheric lifetime and subsequent geochemical impacts. The lifetimes of aerosols

in the atmosphere range from a few days to weeks (Textor et al., 2006). The atmospheric journey of Fe aerosol particles concludes when they are removed either by dry deposition, primarily governed by gravity, impaction, and diffusion, or by wet deposition, where particles are scavenged by water in clouds and subsequently removed through precipitation (Bergametti and Forêt, 2014). All deposition processes are highly size-dependent, with coarser particles having shorter lifetimes and therefore depositing closer to their sources (Seinfeld and Pandis, 2016; Gao et al., 2019).

Wet deposition by precipitation scavenging has been proposed to be more efficient than dry deposition in supplying SFe to the ocean. Modeling and observational studies suggests that wet deposition of atmospheric Fe over the open ocean far from main dust sources accounts for the majority of total deposition and contains a greater fractional Fe solubility than dry deposition of atmospheric Fe (Gao et al., 2003; Hand et al., 2004; Gao et al., 2013; Chance et al., 2015). In other regions close to main dust sources like the Mediterranean or the equatorial Atlantic, Fe deposition is found to be of comparable importance in both wet and dry deposition modes (Theodosi et al., 2010; Baker et al., 2007).

Theoretical models have been developed to describe these processes, and parameterizations have been derived to represent as precisely as possible the deposition of aerosols in 3D models. However, direct measurements, especially for dry deposition, are difficult to perform and consequently, data are sparse, limiting our capability to test the accuracy of the simulations of the aerosol deposition and thus to effectively constrain the Fe aerosol mass budget simulated by these models. Accurate quantification of this deposition, although challenging, is crucial for

constraining aerosol Fe transport models and understanding the overall impact.

1.5. Ocean response to aerosol iron deposition

Once in the ocean, Fe is a fundamental micronutrient for phytoplankton used to transfer electrons in key processes including photosynthesis, respiration, chlorophyll production, and carbon and N fixation (Raven et al., 1999). Though Fe is the fourth most abundant element in the Earth's crust, its concentration in seawater is extremely low. The scarcity of bioavailable Fe stems from its chemistry. Once in seawater, Fe rapidly oxidizes to form insoluble ferric hydroxides, which precipitate and become biologically unavailable (Liu and Millero, 2002). This limited bioavailability is a key factor in shaping the productivity of Fe-limited marine ecosystems.

Phytoplankton communities require access to sunlight for photosynthesis, and macronutrients, including nitrates, phosphates, silicates, and trace elements like Fe for their metabolic functions. Additionally, stable temperature and salinity conditions, alongside sufficient CO₂ levels, support their physiological needs. Phytoplankton growth limitation has traditionally been interpreted in the context of Liebig's Law of the Minimum, which states that plant growth will be as great as allowed by the least available resource, the "limiting nutrient" that sets the productivity of the system (De Baar, 1994). While this view is powerful, interactions among nutrients and between

nutrients and light can also control productivity leading to the concept of co-limitation (Browning and Moore, 2023).

The cycling and distribution of dissolved Fe in the ocean is then regulated by chemical, physical, and biological processes. Fe, which enters the biological cycle through phytoplankton uptake, is then transferred within the food web and is remineralized by heterotrophic organisms at depth. Vertical export of biogenic material removes dissolved Fe from the water column (Balistrieri et al., 1981). Dissolved Fe is additionally removed by scavenging, which is the term coined by Turekian (1977) for the loss of Fe from the dissolved phase through adsorption or precipitation on particle surfaces. The influence of Fe on carbon and N fixation rates is then fundamentally linked to the process of Fe acquisition by the biota.

The BCP is the ensemble of processes that transfer the organic matter produced by plankton in the sunlit ocean surface to deeper layers (Volk and Hoffert, 1985). Only a fraction of the organic matter produced in the surface ocean (typically much less than 1%) has the fate of being exported to the deep ocean (e.g., Export Production (EP)). Of the organic matter produced by phytoplankton (NPP), most is respired back to dissolved inorganic forms within the surface ocean and thus recycled for use by phytoplankton (Eppley and Peterson, 1979) (Fig. 1.10). Most phytoplankton cells are too small to sink individually, so sinking occurs only once they aggregate into larger particles or are packaged into "fecal pellets" by zooplankton. The remains of zooplankton are also adequately large to sink.

Dissolved Fe, has been seen shown to correlate well with ocean

1.5. Ocean response to aerosol iron deposition

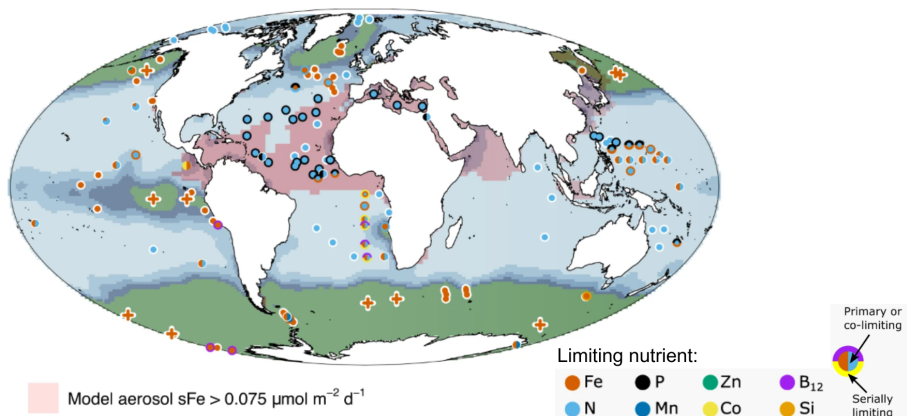


Figure 1.9: **Global synthesis of nutrient limitation.** Experimental locations presented on a global map as coloured symbols. Legend indicates the identities of (co-)limiting nutrient(s). The central symbol colour(s) on the map indicate the primary limiting nutrient. Colors of the annulus indicate serial limiting nutrient(s). Split colours for inner or outer symbol indicate nutrients that were co-limiting. Co-limitation can either be at the primary (split central circle) or serial (split annulus) level. Background colors on the map indicate annual average surface nitrate concentrations. Regions of elevated soluble aerosol Fe deposition predicted by a model are highlighted in red. *Modified from Browning and Moore (2023).*

productivity, chlorophyll concentration, and carbon export in HNLC regions (Johnson et al., 1997; Okin et al., 2011; Boyd et al., 2012; Moore et al., 2001; Twining and Baines, 2013). Spatially, Fe regulates ocean net primary production (NPP) (i.e., the total rate of OC production by autotrophs minus the autotrophs' own rate of respiration) in more than 25% (de Baar et al., 2005) and possibly in up to 50% (Moore et al., 2001; Boyd et al., 2012; Browning and Moore, 2023) of the world's oceans (Fig. 1.9).

While most research has focused on detecting NPP increases, aerosol deposition also influences the BCP in other ways. For instance,

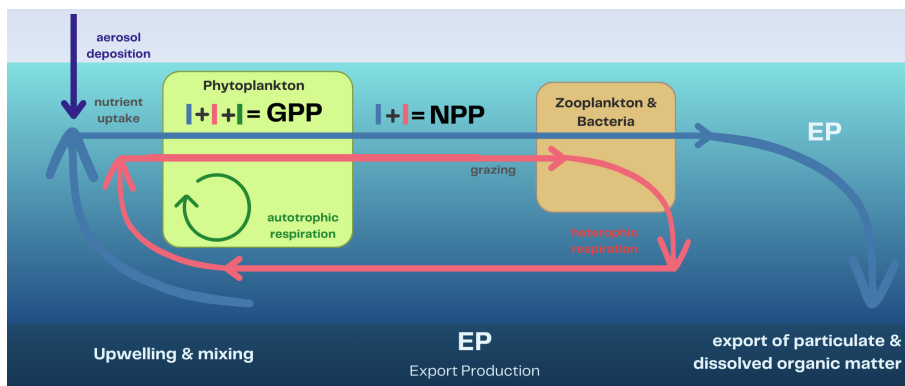


Figure 1.10: **Schematics of the biological carbon pump (BCP)**. Surface ocean productivity, its definitions, and connections to nutrient cycling. The blue cycle represents export production (EP), which involves the 'new' nutrient supply from the ocean interior and atmospheric deposition, uptake by autotrophic phytoplankton during growth, shift into large particles through heterotrophic grazing, and the sinking of organic matter out of the surface ocean. The red cycle illustrates the predominant fate of organic matter produced in the surface ocean which is used for respiration by heterotrophic organisms to meet energy demands and releases nutrients back into surface waters for phytoplankton uptake. The green cycle depicts the internal respiration of phytoplankton, where the products of photosynthesis are used for purposes other than growth. Together, these nested cycles contribute to gross primary production (GPP) representing the gross photosynthesis, and net primary production (NPP) that represents phytoplankton biomass production. *Modified from Sigman and Hain (2012).*

nutrients supplied by aerosols can significantly influence the structure of phytoplankton communities, often driving shifts towards species with varying sinking rates, which in turn affects carbon export efficiency (Kramer et al., 2020; Li et al., 2024). Fe availability is a key driver of these community dynamics. In Fe-rich conditions, diatoms—large, Si-based phytoplankton with high sinking rates—tend to dominate, facilitating carbon export to the deep ocean. Conversely, Fe-poor

1.5. Ocean response to aerosol iron deposition

environments favor smaller phytoplankton, such as cyanobacteria, which are more buoyant and contribute less to vertical carbon transport. These shifts in phytoplankton composition propagate through the marine food web, influencing the abundance and distribution of zooplankton, fish, and higher trophic levels, thereby altering ecosystem functionality and carbon cycling dynamics. Additionally, Fe inputs can support N-fixing cyanobacteria, such as *Trichodesmium*, which convert atmospheric N into a form usable by other organisms. This process adds bioavailable N to the marine system, further enhancing productivity. Thus, Fe indirectly supports nutrient cycling and the broader functionality of marine ecosystems.

Moreover, lithogenic aerosol components, such as aerosol dust, can act as ballasts for otherwise buoyant marine organic particles, a mechanism sometimes called the Lithogenic Carbon Pump or the ballast effect (Korte et al., 2017; Bressac et al., 2014). This effect could be of higher importance close to dust source regions where deposited particles tend to be coarser.

Fe supply-induced surface productivity increases may also lead to feedbacks affecting the climate not traditionally accounted for. For instance, experimental results (Turner et al., 1996, 2004; Belviso et al., 2008) as well as simulations over longer time scales (Bopp et al., 2008) support the occurrence of a transient increase in dimethyl sulfide (DMS) emissions following Fe fertilization. Enhanced DMS emissions may lead to an increase in sulfate aerosol impacting the radiative balance (Charlson et al., 1987; Simó, 2011). To which extent these transient increases would impact the global climate however is thought to be limited (Bopp et al., 2008).

The response of phytoplankton to atmospheric Fe deposition occurs over varying timescales. Factors such as deposition rates, regional oceanographic conditions, and the physiological readiness of phytoplankton influence these responses. In HNLC regions, Fe deposition have been shown stimulate phytoplankton growth within days to weeks, leading to detectable blooms (Bishop et al., 2002; Gabric et al., 2010; Han et al., 2011; Yoon et al., 2019; Li et al., 2024; Nguyen et al., 2024). However, long-term ecological responses unfold over months to years, as nutrient cycling adjusts and populations potentially deplete other nutrients, such as N or Si. Recurring Fe deposition events, such as Saharan dust storms or volcanic eruptions, can create periodic pulses of biological activity, reinforcing productivity in downwind regions and influencing global carbon cycles on seasonal to interannual scales (Moore et al., 2013).

Despite the critical role of aerosols in marine biogeochemistry, their influence remains poorly represented in current Coupled Model Intercomparison Project Phase 6 (CMIP6) models. Simplifications in aerosol emission processes, chemical transformations (e.g., solubility), and deposition timing (Drenkard et al., 2023) hinder accurate predictions. Processes that could be key in the ocean carbon cycle like the lithogenic carbon pump is currently not represented in any ocean biogeochemical model.

1.6. The iron cycle in the anthropocene

The atmospheric Fe cycle and its implications for the broader Fe and carbon cycles have evolved significantly due to anthropogenic activities.

1.6. The iron cycle in the anthropocene

Since the onset of the Industrial Revolution, human influence on the climate system has reshaped the dynamics of the Fe cycle, altering its role in climate regulation and its interactions with other biogeochemical cycles. This Section focuses on these human-driven changes in the Fe cycle and their implications for climate and climate change as those will be explored along the Thesis.

Human activities modify the magnitude of the atmospheric aerosol Fe flux to the oceans (Mahowald et al., 2018), primarily through the following mechanisms: increased combustion of fossil fuels for industrial, transportation, and domestic purposes; changes in land cover driven by deforestation, urbanization, and agricultural or pastoral land use; and alterations in atmospheric concentrations of acidic and organic species, which enhance Fe solubility during transport.

When constraining the Fe cycle in models, it is crucial to account not only for the natural components and their feedbacks within the Earth system but also for the multiple forcings introduced by human activities such as new emission sources, or land-use change affecting dust and fire emissions. This forms a highly interconnected system, making its full understanding a challenging yet vital scientific goal (Fig. 1.11). This Section summarizes the main mechanisms through which human activities may directly or indirectly impact the Fe cycle.

1.6.1 Human-induced changes to aerosol iron sources

Since the Industrial Revolution, many economic sectors, including industry, transportation, mining, and agriculture, have grown at

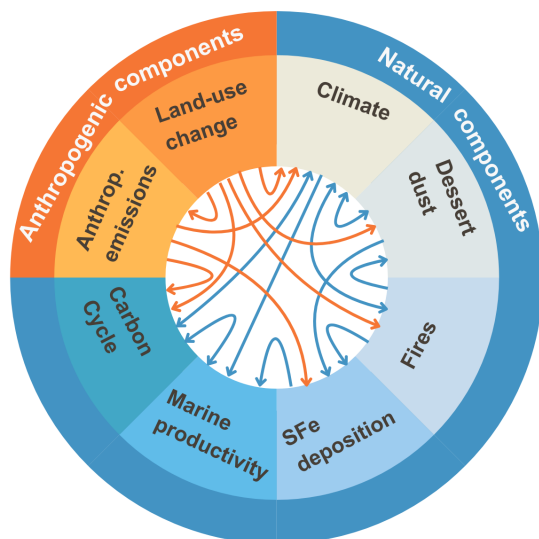


Figure 1.11: **Schematic of natural and anthropogenic feedbacks of the Fe cycle in the climate system.** Schematic illustrating the interconnected feedbacks among global climate, the carbon cycle, and iron (Fe) inputs to the ocean, highlighting how human activities may disrupt these natural feedbacks.

an unprecedented rate, introducing new and growing sources of pollutants and nutrient emissions to the atmosphere. Additionally, natural emissions have been influenced by human activity through anthropogenic land use and climate changes. For instance, dust emissions may have doubled (Mahowald et al., 2010; Kok et al., 2023), while fire emissions may have halved (Hamilton et al., 2018). Overall, the hemispheric balance of aerosol nutrient concentrations in the atmosphere has likely shifted positively toward the NH since the Industrial Revolution (Hamilton et al., 2020a; Jickells et al., 2017; Myriokefalitakis et al., 2020).

How each of these sources has changed due to anthropogenic activities

1.6. The iron cycle in the anthropocene

and human-mediated climate change, as well as how they are projected to evolve in the future, are explored in the following subsections.

1.6.1.1 Shifts in desert dust emission

Dust emissions are influenced by anthropogenic activities both directly, through soil disturbance, vegetation cover changes, or lake or river changes, and indirectly, through alterations in the hydrological cycle and climate. Anthropogenic activities currently account for 5–25% of the world’s dust emissions (Mahowald and Luo, 2003; Tegen et al., 2004; Ginoux et al., 2012; Chen et al., 2018). Their role in the Fe cycle, however, has little been investigated. Human-induced dust sources may exhibit significant temporal fluctuation. The composition of the natural sources may differ from that of the agricultural land’s underlying soil mineralogy.

Global dust loading has been shown to have increased by $55 \pm 30\%$ since pre-industrial times (Kok et al., 2023; Leung et al., 2024) (Fig. 1.12), consequently leading to an increase in the atmospheric Fe burden. This rise is linked to a combination of natural and anthropogenic climate changes as well as human land-use changes. However, modeling efforts have been unable to determine whether this historical increase in dust is primarily driven by climate changes or land-use changes. Moreover, current climate models fail to reproduce this historical increase in dust loading (Fig. 1.12) and, as a result, inadequately account for long-term trends in aerosol Fe dust emissions.

In addition, current models differ in their projections of future dust sources depending on their formulation (Mahowald and Luo, 2003;

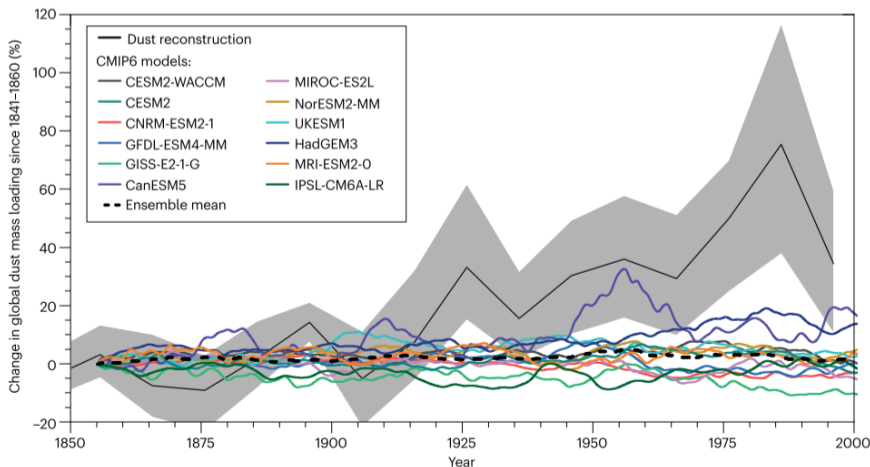


Figure 1.12: **Climate model representations of historical changes in dust loading.** Changes in global dust loading relative to 1841–1860 from the dust reconstruction (solid black line) and 12 CMIP6 models with prognostic dust aerosol cycles (coloured lines, and dashed black line for the ensemble mean). *Extracted from Kok et al. (2023).*

Tegen et al., 2004; Kok et al., 2023). Drier conditions can lead to increased dust emissions by reducing soil moisture, while extreme rainfall events mobilize sediments and increase the material available for wind erosion. Changes in wind speed, influenced by anthropogenic climate change, could also significantly impact dust emissions. On the other hand, CO_2 fertilization can promote vegetation growth in arid regions, reducing active dust sources. Human activities, such as land management and agricultural irrigation, will also affect the location of future dust sources. Finally, future climate and land-use changes could drive a decline in biological soil crusts increasing dust emissions, a mechanism unaccounted for in current models (Rodríguez-Caballero et al., 2022). Due to the multiple factors involved, current model

1.6. The iron cycle in the anthropocene

estimates range from increased dust emissions, primarily driven by greater aridity, to decreases resulting from the CO₂ fertilization effect (Kok et al., 2023).

1.6.1.2 Trends in fossil fuel iron emissions

Increased industrial, transport, mining, and agricultural activities provide new nutrient emission sources to the atmosphere, leading to a significant increasing trend in nutrient deposition to marine ecosystems (Hamilton et al., 2020b; Ito, 2015; Jickells et al., 2017; Luo et al., 2008; Matsui et al., 2018; Myriokefalitakis et al., 2020; Liu et al., 2022b). Increased anthropogenic activities directly impact the emission burden of Fe aerosols, each sector i) has its own Fe emission factors, ii) distinct PSD at emission, iii) different Fe solubility at emission (see Section 1.2.2).

However, the evolution of these factors under future anthropogenic activity changes and the unique trajectories of each sector remain highly uncertain. Scenario development and analysis offer a means to connect socioeconomic and technological progress with potential future climate outcomes. By providing projections for various emission species, including greenhouse gases, aerosols, and their precursors, these scenarios enable a wide array of climate analyses, such as evaluating future warming pathways, localized pollution impacts, and other critical studies (see Section 4.4).

For example, in the Shared Socioeconomic Pathways (SSPs) of the CMIP6 scenarios (see Section 4.4), black carbon (BC) (Fig. 1.13) and OC emissions, which can be linked to Fe-fossil fuel emissions

Chapter 1. The relevance of iron in the Earth system

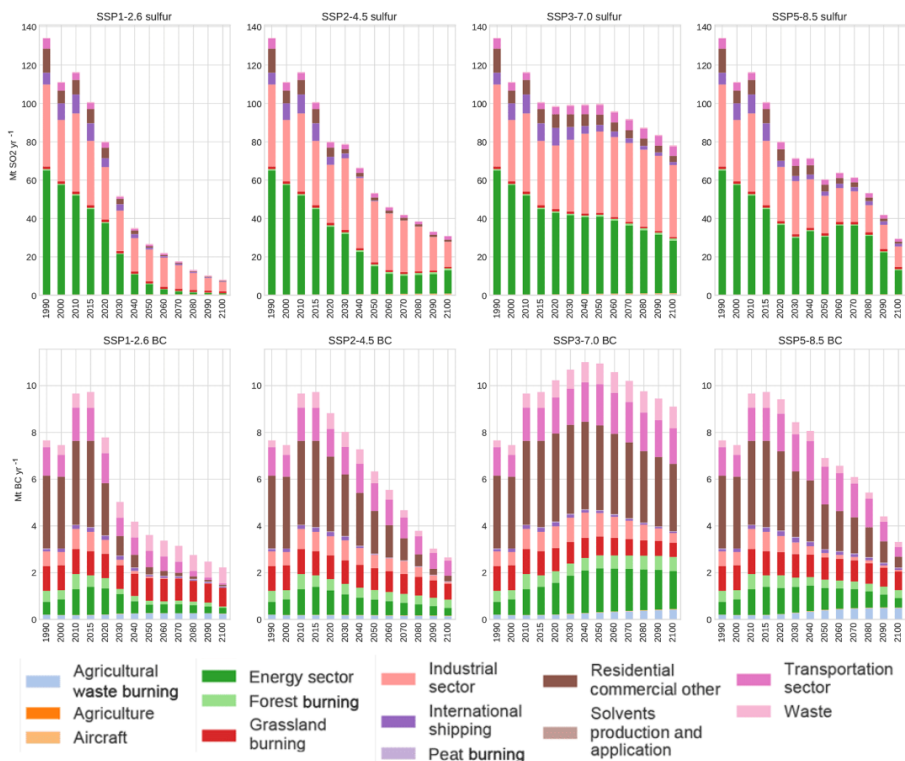


Figure 1.13: **Emissions trajectories for sulfur and BC.** Decadal annual mean emission trajectories for sulfur and black carbon (BC), showing historical trends and Tier-1 scenarios analyzed in this study (see Section 4.4), with sectoral contributions to sulfur and black carbon emissions. *Extracted from Gidden et al. (2019).*

(see Section 1.2.2), are projected to decline by the end of the century compared to present-day levels, except in certain high-emission scenarios (Gidden et al., 2019). Key sectors for Fe emissions, such as shipping transportation, are anticipated to see emission reductions across all scenarios.

1.6.1.3 Alterations in fire-related iron emissions

The present-day patterns of fires are relatively well understood, as they are constrained by satellite data (van Marle et al., 2017), but their evolution since the pre-industrial era and in the future remains uncertain. Recent studies suggest that, contrary to previous assumptions, the increased population over the last decades has reduced the burned area compared to the pre-industrial era (Hamilton et al., 2018). This reduction is attributed to human-induced changes in land use, fragmentation of ecosystems, implementation of fire management practices, and air quality mitigation policies in some regions (Andela et al., 2017). However, while these factors will continue to influence fires in the future, their impact is likely to be offset by increased fire activity expected under warmer and drier climates driven by human-induced climate change (Pechony and Shindell, 2010).

Recent shifts in fire regimes reflect the complex interplay of climate change, human land use, and ecosystem dynamics (Pechony and Shindell, 2010; Bowman et al., 2011). Global forest ecoregions can be categorized into different pyromes where forest fire characteristics depend on a similar set of controls (e.g., extratropical, subtropical, tropical, and suppression-zone pyromes dominated by fire management efforts) (Jones et al., 2024). Over the past two decades, global burned area has declined by $\approx 25\%$, mainly due to the conversion of natural grasslands to agriculture, particularly in African savannas (Andela et al., 2017; Jones et al., 2022). However, wildfire frequency and severity have increased, especially in extratropical pyromes (Westerling et al., 2006; Dennison et al., 2014; Jolly et al., 2015; United Nations Department of Economic and Social Affairs et al., 2021; Zheng et al.,

2021; McCarty et al., 2021; Jones et al., 2024), due to changes in climate (See Fig. 1.14). Consequently, global fire emissions have remained relatively constant (Zheng et al., 2021).

CMIP6 emission estimates (Gidden et al., 2019) include the effect of direct anthropogenic-induced fires but neglect the impact of climate change on fire regimes, potentially leading to an underestimation of these sources in the future. Vegetation models embedded within global ESMs represent the processes connecting changes in the fuel complex (the amount and arrangement of fuels in a landscape) to future estimates of climate and land cover distribution. Inclusion of an interactive fire model within such a vegetation modelling framework enables predictions of how fire evolves as a function of fuel flammability changes due to temperature, humidity, precipitation, vegetation distribution, and fuel load. This fire modelling framework can address questions related to the changing role of fire in the Earth System.

These shifts in fire regimes will likely significantly influence the burden and geographical distribution of fire-related Fe emissions. Increased fire activity in extratropical pyromes, coupled with the drying of midlatitude forests, may elevate Fe emissions in these regions, altering deposition patterns in adjacent oceanic areas. Conversely, the reduction of burned areas in tropical and subtropical pyromes, especially savanna-dominated regions, may decrease Fe emissions from these zones. The interplay of these dynamics could shift the global Fe aerosol burden towards higher latitudes, with implications for the nutrient supply to high-latitude oceans and associated impacts on marine productivity. Therefore, understanding these evolving patterns is essential for quantifying Fe emissions' role in modulating atmospheric chemistry and ecosystem

1.6. The iron cycle in the anthropocene

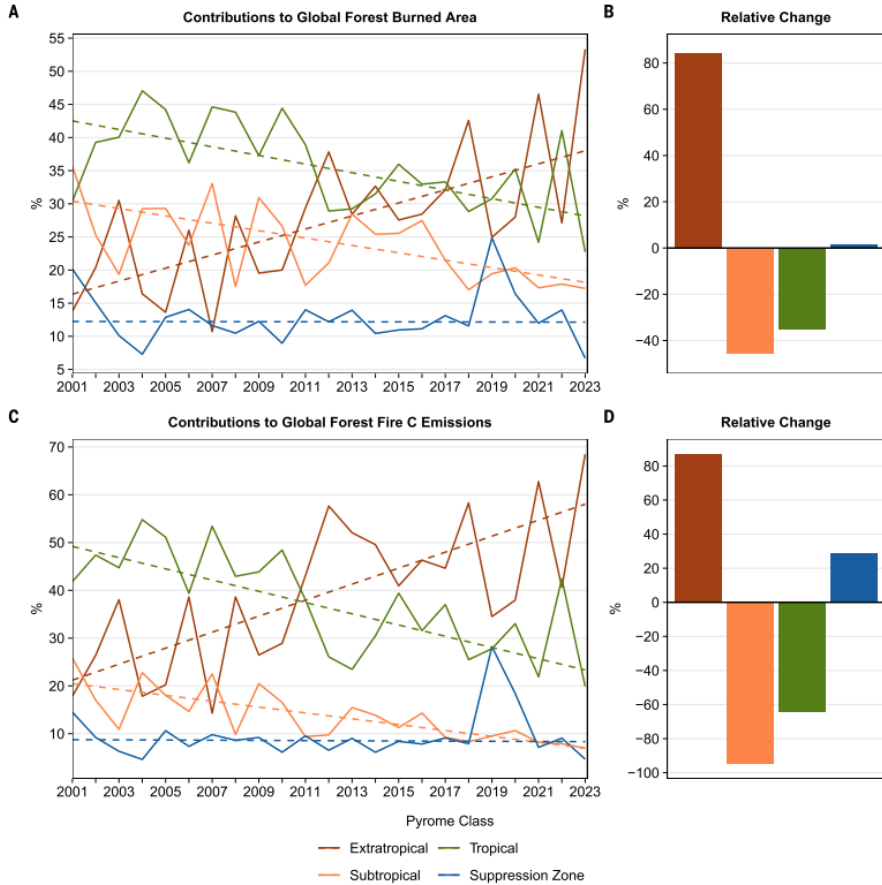


Figure 1.14: **Geographical shifts in forest burned area and fire carbon emissions from 2001 to 2023.** The plot shows contributions of groups of forest pyromes in the tropics, subtropics, extratropics and zones of suppression to (A) and (B) forest BA in all forest ecoregions globally and (C) and (D) the fire carbon emissions in all forest ecoregions globally. The left column (A and C) shows annual data (solid lines) and trendlines (dashed lines) for each pyrome, right column (B and C) shows the total relative changes from 2023 with respect to 2001. *Extracted from Jones et al. (2024).*

feedbacks in a changing climate.

1.6.2 Changes in global atmospheric chemistry

Shifts in aerosol emissions due to human activities impacting them directly or indirectly, as detailed in Sections 1.6.1.1, 1.6.1.2, and 1.6.1.3, will directly influence the atmospheric processing of Fe.

For instance, if dominant dust sources change over time, the mineralogy of the dust aerosol burden would also shift accordingly. This alteration affects the abundance of alkaline elements such as calcite, which can directly influence aerosol pH in the atmosphere (Karydis et al., 2021), impacting the acidic dissolution of Fe.

Changes in fossil fuel anthropogenic emissions, particularly sulfur dioxide (SO_2) emissions, also significantly influence aerosol pH and the acidic dissolution of Fe-containing particles. As seen in Fig. 1.13, SO_2 emissions have already declined due to mitigation policies (Yoshioka et al., 2024) in the last decades and are projected to decrease further in future scenarios (Gidden et al., 2019). This decline may reduce the acidity of the atmosphere, potentially altering the pathways of Fe solubilization from both combustion and dust aerosols.

Last but not least, shifts in fire emissions are expected to alter the chemistry of Fe aerosols. Fires emit Fe-containing particles along with organic compounds such as OXL and its precursors (Kundu et al., 2010; Cao et al., 2017). These Fe aerosols, enriched with OXL, form a chemically reactive cocktail that facilitates ligand-promoted solubilization of Fe during atmospheric processing (Perron et al., 2022). As fire regimes evolve under climate change, particularly with increasing wildfire activity in extratropical regions, the production of this "perfect cocktail" for Fe solubilization may intensify.

1.6.3 Changes in global ocean biogeochemistry

The potential response of marine ecosystems to aerosol deposition cannot be disentangled from the broader context of human-mediated climate change.

ESM projections and global observations (Li et al., 2020; Kwiatkowski et al., 2020) agree that ocean temperatures are expected to rise globally, leading to increasingly stratified oceans and the poleward expansion of oligotrophic gyres. A more stratified ocean results in shallower turbulent mixing layers, decreasing the number of months when phytoplankton growth is light-limited. While this reduction in light limitation could potentially increase productivity, enhanced stratification also reduces the vertical supply of nutrients (Llort et al., 2019). Consequently, the nutrient limitation landscape depicted in Fig. 1.9 may shift significantly. CMIP6 models, despite low inter-model agreement, suggest that the balance between these opposing effects generally favors a reduction in productivity across most ocean basins (Kwiatkowski et al., 2020; Tagliabue et al., 2021).

Furthermore, significant acidification and deoxygenation of seawater have been observed over the last decade and are projected to intensify in the future. These changes constitute a planetary-scale anthropogenic perturbation that could alter oceanic biogeochemical fluxes and severely impact marine biota (Hofmann and Schellnhuber, 2009). However, the effects of ocean acidification on Fe uptake by marine organisms remain poorly understood. Some studies suggest that increased acidification may slow the Fe-uptake rate under Fe-limited conditions (Shi et al., 2012a), while others indicate that acidification weakens

Fe(II) oxidation and decreases organic complexation, potentially increasing Fe bioavailability (Wang et al., 2022a).

In addition, the extent of sea ice in polar regions is expected to decline as climate change progresses. This reduction is likely to enhance Fe inputs from glacial sediments, potentially altering Fe availability in high-latitude ocean ecosystems.

Human activities directly intersect with the natural Fe cycle in the ocean through the practice of ocean iron fertilization (OIF), a carbon dioxide removal technique aimed at enhancing phytoplankton productivity and carbon sequestration (GESAMP, 2010; Moore and Doney, 2007). OIF experiments have shown that, despite some short-term success in triggering phytoplankton blooms following Fe addition, there is limited evidence that these blooms result in significant long-term carbon sequestration (Boyd et al., 2007). Additionally, OIF raises concerns about unintended ecological consequences, such as nutrient robbing, where the carbon drawdown induced by OIF may deplete essential nutrients in surrounding waters, ultimately limiting the effectiveness of such interventions and altering ecosystems (Gnanadesikan et al., 2003; Aumont and Bopp, 2006; Oschlies et al., 2010; Tagliabue et al., 2023). Recent studies suggest that OIF's contribution to global carbon removal is likely to be modest, especially in the context of climate change (Tagliabue et al., 2023).

1.7. Constraining the atmospheric iron cycle

The complexity of the atmospheric Fe cycle arises from the multifaceted nature of Fe emissions and chemistry, its interactions with atmospheric processes, and its varying solubility, which collectively dictate its bioavailability to marine ecosystems as seen in Section 1.2, 1.3 and 1.4.

In order to unravel all these research gaps, at the beginning of this century, a number of researchers initiated a new expanding aerosol nutrient research field, driven by Martin (1990) assertions (section 1.1.4) as well as improvements in instrumentation and analytical methodologies. International research initiatives such as GEOTRACES have provided guidance (Cutter et al., 2017) and have boosted the collection of observational data on aerosol nutrients in research cruises in the last decades.

Despite the advances, ocean observations of Fe and its soluble fraction are still limited both spatially and temporally owing to the significant costs and logistical constraints associated with accumulating data from scientific cruises. Some oceanic regions, especially in the SH, remain even less studied due to difficulties in accessibility reducing the number of research campaigns sailing southern and polar oceans and the difficulty of collecting suitable atmospheric samples in rough sea conditions. The limitations associated with ship-based data across multiple remote ocean regions and the lack of continuous long-term records (Schulz et al., 2012) hinder the required understanding of basic statistical properties in the Fe cycle (Smith et al., 2017).

Modeling is, therefore, key to analyzing geographical regions not covered by observations and making assessments on global scales to understand the different sources and processes affecting SFe deposition, as well as to assess their impacts on the ocean and the climate. However, modeling the atmospheric supply of SFe to the global ocean remains challenging, due to the diversity of Fe forms in aerosols and the complex processes influencing their solubility.

Over the last decade, models have seen advances in the representation of Fe emission sources and subsequent atmospheric processing. Early works neglected Fe sources such as combustion aerosols (Hand et al., 2004; Johnson and Meskhidze, 2013; Moxim et al., 2011), which have been later identified as relevant contributors to the atmospheric SFe (Guieu et al., 2005; Ito et al., 2021; Luo et al., 2008). Atmospheric dissolution has been represented with different levels of complexity in models. Simple approaches exist following first-order rate processing constants and considering a globally uniform 3.5% of Fe content in dust (Duce and Tindale, 1991; Hand et al., 2004; Luo et al., 2008). Mid-complexity representations allow for different types of acidic species to interact with dust, and consider mineral-specific dissolution rates (Ito and Xu, 2014; Meskhidze et al., 2005). Some models further account for OXL processing, even when the full complexity of the OXL formation in cloud water is not explicitly considered, but parameterized (Hamilton et al., 2020a; Johnson and Meskhidze, 2013; Scanza et al., 2018). More recently, complex schemes have been developed where both FeD and FeC are dissolved during atmospheric transport, multiphase chemistry is resolved explicitly including the OXL and sulfur cycles, and aerosol acidity is considered in both accumulation and coarse aerosol modes that

1.7. Constraining the atmospheric iron cycle

account for aerosol microphysics. This is the case of **EC-Earth3-Iron**, the model that will be used within this Thesis, which is described in Section 4.2 and Myriokefalitakis et al. (2015, 2022).

The future landscape of SFe deposition is highly uncertain. Such models are also a powerful tool in projecting future trends in the atmospheric Fe cycle. The impacts of climate mitigation strategies; how population, consumerism, and economics will drive manufacturing and agriculture practices; how aridification will impact dust production; and how wildfire activity will change in a warmer world among other things could significantly impact the fluxes of atmospheric SFe to the open ocean surface (see Section 1.6). Models that embody the representation of the different earth components and their interaction, together with the definition of plausible climate scenarios, can serve as powerful tools to unravel such questions.

Chapter 1. The relevance of iron in the Earth system

CHAPTER 2

Objectives

The overarching aim of this Thesis is to enhance our understanding and quantification of the atmospheric supply of bioavailable iron (SFe) to the ocean under a changing climate. Achieving this understanding is critical for improving estimates of marine productivity and its influence on the carbon and nitrogen cycles. To address this overarching objective, this Thesis focuses on refining existing estimates of SFe deposition. It does so by improving the representation of the atmospheric Fe cycle and aerosol-driven biogeochemical processes in climate models. Additionally, it aims to deepen our understanding of their global implications within the context of human-induced climate change. Specifically, the following objectives have been defined and pursued:

- Evaluate the relative contributions of different sources and processes to the deposition of soluble Fe in the ocean under the present climate.
- Characterize the extent and magnitude of bioavailable Fe's effects on surface ocean ecosystems.
- Quantify changes in soluble Fe deposition to the ocean across past, present-day, and future climates (end of the century), with

Chapter 2. Objectives

a focus on how human activities have shaped these changes.

- Improve the representation of commonly used future Fe emissions, particularly from wildfires, which may be key to determining both the total Fe burden, its solubilization through atmospheric processing and its impact on HNLC oceanic regions.

CHAPTER 3

Framework

3.1. Thesis structure

Besides the current **Part I: Introduction**, this Thesis is structured into three additional parts that aim at explaining how the goals described in Chapter 2 have been achieved.

Part II: Methods comprises Chapter 4 and provides a description of the EC-Earth3-Iron ESM used throughout this Thesis, along with detailed information on the observational data used to evaluate the model and the statistical methods applied. Chapter 4 also describes the general simulation protocols used throughout the Thesis, the standardized future scenarios considered, and a description of the High Performance Computing (HPC) systems utilized.

Part III: Results and Discussion is subdivided into four chapters, each addressing one of the four specific objectives of this Thesis (see Chapter 2). Chapter 5 presents the results of an SFe deposition reconstruction spanning from 1991 to 2020, highlighting the relative contributions of different sources and processes under the present

climate, along with the main long-term trends observed over recent decades. Chapter 6 builds on the reconstruction presented in Chapter 5 and provides an analysis of the responses of high-frequency SFe deposition data on ocean surface ecosystems, analyzing it in conjunction with satellite-derived surface chlorophyll observations. Chapter 7 investigates changes in SFe deposition from pre-industrial times to end-of-century projections based on the CMIP6 scenario protocol, spanning a wide range of possible future pathways. Chapter 8 extends the results shown in Chapter 7 by examining how improved future fire emission estimates, accounting for climate-driven changes in fires, affect SFe deposition over HNLC regions, and explores the resulting impacts on NPP in those regions. In Chapter 8, EC-Earth3-Iron is used alongside an additional atmospheric Fe model (CAM6-MIMI (Hamilton et al., 2019)), allowing for a multimodel approach. Each chapter in this part consists of a brief specific introduction, a description of the distinct methodologies used, followed by the presentation and discussion of the results, and ends with a conclusions section.

The content in Chapter 7 has been published in a Q1 open-access journal as listed in Appendix B:

Bergas-Massó et al. (2023), *Earth's Future*, doi: 10.1029/2022EF003353.

The content in Chapter 8 is under review in a high-impact open-access journal as listed in Appendix B:

Bergas-Massó et al. (2024), *Nature Climate Change*.

Part IV: Discussion and conclusion is composed by Chapter 9, which presents a summary of the main outcomes of this Thesis and perspectives for future work.

Finally, **Part V: Appendices** contains additional information to support the obtained results.

3.2. Framework within the Earth Sciences Department at the BSC-CNS

This Ph.D. Thesis was developed within the Atmospheric Composition (AC) group of the Earth Sciences (ES) department at the Barcelona Supercomputing Center - Centro Nacional de Supercomputación (BSC-CNS).

The AC group, co-led by Carlos Pérez García-Pando and Oriol Jorba, focuses on advancing the understanding of the atmosphere's chemical composition and its impacts on air quality, weather, and climate spanning scales from urban to global. The AC group comprises four research teams: (i) Emissions, (ii) Atmospheric Chemistry and Air Quality, (iii) Data Assimilation, Forecasting, and Applications, and (iv) Dust, Aerosols, and Climate (AC-CLIM). This Thesis has been conducted within the AC-CLIM team, led by María Gonçalves-Ageitos.

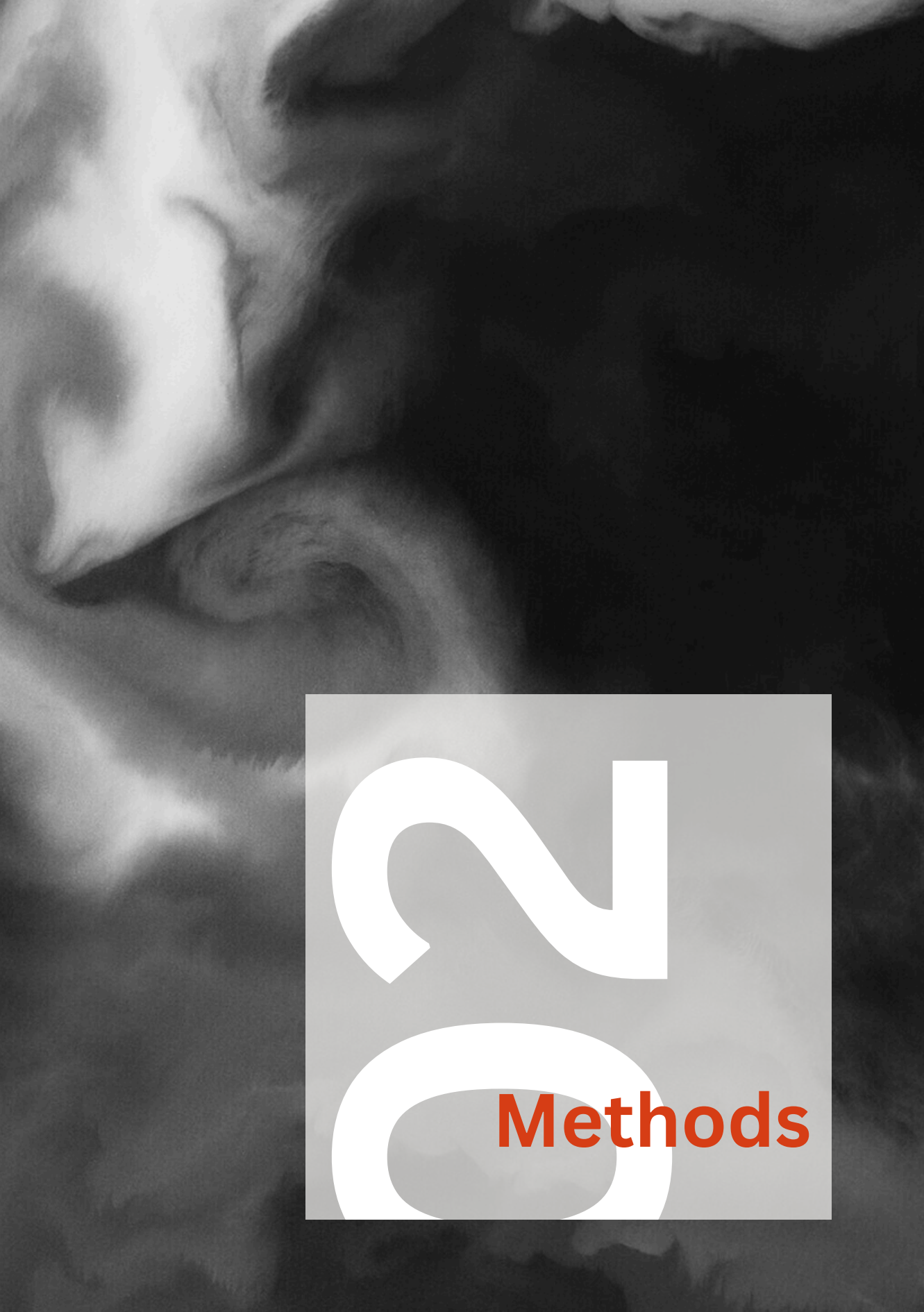
Collaboration within other department groups is central to the AC team's work. The AC group partners with the Computational Earth Sciences group to optimize model codes, develop pre- and post-processing tools, and refine operational settings, using tools such as autosubmit (Manubens-Gil et al., 2016), an open-source Python-based experiment and workflow manager for Cloud and HPC platforms. They also work with the Climate Variability and Change group on the connections between atmospheric aerosols

and climate, primarily through the EC-Earth framework, to which BSC is a contributing member of the EC-Earth Consortium (<https://eearth.org/consortium/>). Furthermore, collaborations with the Earth System Services group ensure the application of forecast products in key socio-economic sectors.

This Thesis has significantly benefited from the department's interdisciplinary environment, expertise, and resources. The Computational Earth Sciences group has supported the development of EC-Earth capabilities for modeling the atmospheric Fe cycle and managing complex workflows on HPC systems. On the other hand, interactions with ocean biogeochemistry experts from the Climate Variability and Change group, enriched discussions on the results and implications of SFe deposition for ocean biogeochemistry, enhancing the quality of the research presented here.

The department's reputation within the ES community has fostered a wide network of external collaborators. Interactions with researchers at BSC-CNS and international institutions, such as Stelios Myriokefalitakis (National Observatory of Athens), Ron L. Miller (NASA Goddard Institute for Space Sciences), Twan van Noije (Koninklijk Nederlands Meteorologisch Instituut), and Douglas S. Hamilton (North Carolina State University) among others have been instrumental in the development of this Thesis. These collaborations have also facilitated the co-authorship of research articles, as detailed in Appendix B.





2

0

Methods

CHAPTER 4

Methodology

In this Chapter, the core methodologies employed in this Thesis are detailed. These include a description of EC-Earth3-Iron, the climate model utilized in all results Chapters, the observational datasets used for validating the model outputs, and the statistical analysis methods applied in this evaluation. Additionally, the Chapter provides an overview of the climate scenarios used to project SFe deposition fluxes and the various model configurations employed. Specific methodologies relevant to individual Chapters are presented within each Chapter.

4.1. The EC-Earth Earth System Model

A model organizes our understanding of a subject, allowing us to analyze its behavior across different time periods and predict its response to external influences. Models are especially valuable when conducting direct, controlled experiments is impractical or impossible, as is the case of the global Fe cycle.

Global climate models (GCMs), also referred to as general circulation models, are fundamental tools for advancing our understanding of

Earth's evolving climate. These models solve mathematical equations that describe the physical processes governing the atmosphere, ocean, and land surface. However, physical processes alone, such as radiation and fluid dynamics, are insufficient to fully describe the climate system. Chemical and biological processes play equally critical roles. For instance, the growth of plants and respiration of microbes influence atmospheric CO₂ concentrations and Earth's surface albedo. In turn, climate conditions affect biological processes: temperature and precipitation dictate terrestrial metabolism, while ocean circulation shapes nutrient availability for phytoplankton, which modulate atmospheric CO₂ uptake.

To capture the interactions among all components of the Earth system, a new generation of climate models, called ESMs, has emerged in the last decades. At their core ESMs have the atmospheric and ocean components of a GCM. Additionally, they include the representation of the global carbon cycle, dynamic vegetation, atmospheric chemistry, ocean biogeochemistry, and continental ice sheets. This makes ESMs an excellent tool to study atmospheric aerosol-ocean interactions.

EC-Earth3 is a state-of-the-art ESM co-developed by a consortium of European research centers including the BSC-CNS. It is composed of modular components, each representing a specific aspect of the Earth's system, that is, the atmosphere, ocean, sea ice, land surface, dynamic vegetation, atmospheric composition, and ocean biogeochemistry, which can be coupled in various model configurations according to different scientific needs (Döscher et al., 2022). EC-Earth3 took part in the CMIP6 initiative (Eyring et al., 2016).

4.1. The EC-Earth Earth System Model

The GCM of EC-Earth3 is based on cycle 36r4 of the Integrated Forecast System (IFS) from the European Centre for Medium-Range Weather Forecasts (ECMWF), which includes the land surface model H-TESSSEL (Balsamo et al., 2009). The ocean model is the Nucleus for European Modeling of the Ocean (NEMO) release 3.6 (Gurvan et al., 2019), with sea ice processes represented by the Louvain-la-Neuve sea ice model (LIM) (Rousset et al., 2015; Vancoppenolle et al., 2009). The ESM presents the following two configurations: (1) the carbon cycle configuration that represents the marine biogeochemistry processes through PISCES (Aumont et al., 2015), the dynamic terrestrial vegetation through LPJ-Guess (Smith et al., 2001, 2014), the atmospheric cycle of CO₂ through the Tracer Model version 5 release 3.0 (TM5-MP 3.0) (Huijnen et al., 2010) and (2) the EC-Earth3-AerChem configuration (van Noije et al., 2021) that represents the atmospheric chemistry and transport of aerosols and reactive species (also through the TM5-MP 3.0). The exchange of information and interpolation between these modules is managed by the Ocean Atmosphere Sea Ice Soil version 3 (OASIS3) coupler (Craig et al., 2017).

The IFS horizontal resolution is T255 (i.e., a spacing of roughly 80 km), 91 layers are used in the vertical direction up to 0.01 hPa, and a time step of 45 min is applied. On the other hand, TM5-MP has an horizontal resolution of 3° in longitude by 2° in latitude and uses 34 layers to represent the vertical direction up to 0.1 hPa (≈ 60 km).

This Thesis had contributed to the development and application of the recently introduced EC-Earth3-Iron model configuration (Myriokefalitakis et al., 2022). This version of the model builds upon the CMIP6 EC-Earth3-AerChem configuration (van Noije et al.,

2021), extending its capabilities to include advanced representations of atmospheric Fe processes. The tropospheric multiphase chemistry developments needed to include the atmospheric Fe cycle, are included in the TM5-MP atmospheric chemistry module of EC-Earth3.

4.1.1 Tropospheric chemistry in EC-Earth

TM5-MP simulates tropospheric aerosols and the reactive greenhouse gases CH_4 and ozone (O_3) and allows the coupling of those species to relevant processes in the atmospheric module IFS (e.g., radiation and clouds). The model can be executed in an atmospheric mode only, i.e., using prescribed sea surface temperature (SST) and sea ice concentration (SIC), or coupled to the NEMO-LIM ocean and sea ice model. In addition, TM5-MP can run as a standalone (offline) atmospheric chemistry and transport model (CTM) driven by meteorological and surface fields (Krol et al., 2005).

In TM5-MP, SO_4^{2-} , BC, organic aerosols (OA), sea salt, and mineral dust microphysics are described by the modal aerosol scheme M7 (Vignati et al., 2004). M7 defines seven log-normal modes to represent the aerosols' size distribution and mixing state; four water-soluble modes (nucleation, Aitken, accumulation, and coarse) and three insoluble modes (Aitken, accumulation, and coarse). Natural emissions of mineral dust, sea salt, DMS, and N oxides from lightning are calculated online, while other natural emissions are prescribed (e.g., biogenic emissions of non-methane volatile organic compounds). Mineral dust emission is parameterized according to Tegen et al. (2002) with particle diameter ranges of 0.1–0.3, 0.3–8 μm for the accumulation and coarse mode.

In the EC-Earth3-Iron version, the gas-phase chemistry scheme is resolved by the MOGUNTIA chemical mechanism (Myriokefalitakis et al., 2020) replacing the original carbon bond chemical mechanism (CB05) (Yarwood et al., 2005). MOGUNTIA explicitly simulates the organic polar species that partition in the atmospheric aqueous phase like nitrates and allows for a sophisticated parameterization of the multiphase processes needed for the representation of Fe in the atmosphere.

4.2. EC-Earth3-Iron

EC-Earth3-Iron includes a representation of the atmospheric Fe cycle, and explicitly calculates the dissolution of Fe in aerosol water and in cloud droplets, aqueous-phase OXL formation, and cloud and aerosol acidity, the latter in both accumulation and coarse modes. Its ability to represent tropospheric aerosols has been shown in Myriokefalitakis et al. (2022), and remains similar to the standard EC-Earth3-AerChem version (Gliß et al., 2021), regardless of the substantial differences in the gas-phase and aqueous chemistry.

The new features required to determine the global aqueous-phase OXL formation, atmospheric acidity, and the Fe cycle in the atmosphere can be summarized as follows:

1. Treatment of mineral dust emissions that incorporates variations in soil mineralogical composition to account for the emission of Fe-containing minerals and calcite, along with detailed speciation of anthropogenic combustion and biomass burning emissions to explicitly represent Fe in both soluble and insoluble forms.

2. Acidity calculations for water present in fine and coarse aerosols, as well as in cloud droplets.
3. A comprehensive aqueous-phase chemistry scheme applicable to both cloud droplets and aerosol water.
4. An explicit description of Fe-containing aerosol dissolution processes for mineral dust, anthropogenic combustion, and biomass burning aerosols.

EC-Earth3-Iron represents a state-of-the-art atmospheric Fe model within the framework of Earth system modeling. Below, a more detailed summary of the main features related to the calculation of SFe in the model are provided.

4.2.1 Fe-dust representation

Three different dust-Fe (FeD) pools are considered according to their susceptibility to dissolve (Shi et al., 2011a) (see Section 1.2.1.1): (a) A fast dissolution pool that relates to ferrihydrite (i.e., hydrated ferric Fe oxide) on the surface of minerals (FeH); (b) an intermediate dissolution pool that considers nano-sized Fe oxides from the surface of dust minerals (FeO); and (c) a slow dissolution pool that takes into account the Fe release from aluminosilicates, hematite, and goethite (FeA).

This version of the model explicitly traces the three Fe pools and calcium (Ca) originating from mineral dust sources. The emitted FeD in the accumulation and coarse insoluble modes of each pool is based on the soil mineralogy of Claquin et al. (1999), including the updates proposed in Nickovic et al. (2012). The atlas provides the soil mineralogical

composition in arid and semi-arid regions of the world, distinguishing between two soil size classes (i.e., the clay size fraction up to 2 μm and the silt size fraction from 2 to 50 μm diameter). Eight different minerals are considered: illite, kaolinite, and smectite for the clay fraction, feldspars, hematite and gypsum for the silt fraction, and quartz and calcite in both mineral size fractions. The Fe content of each mineral is based on Nickovic et al. (2013) (Table 4.1). Following Ito and Shi (2016), EC-Earth3-Iron assumes an initial solubility (i.e., the fraction of soluble FeD, SFeD, over total FeD) of 0.1% for all Fe mineral soil emissions.

Table 4.1: **Modeled Fe content in minerals.** Minerals in the Claquin et al. (1999) in the clay or silt fraction with prescribed iron (Fe) content as in Nickovic et al. (2012) and model partitioning among the three Fe-dust pools (FeH, FeO and FeA) as used in EC-Earth3-Iron.

	Illite	Kaolinite	Smectite	Iron <i>oxides</i> ^a	Feldspar
Clay	✓	✓	✓	-	-
Silt	-	-	-	✓	✓
Fe content (%)	4.8	0.7	16.4	66	2.5
FeH/FeO/FeA partitioning at emission (%)	0.65/1.3/98.5	0.65/1.3/98.5	0.65/1.3/98.5	0/0/100	0.65/1.3/98.5

^a Iron oxides include Hematite and Goethite.

BFT (Kok, 2011) is used to have a better estimation of the PSD of each mineral at emission (Pérez García-Pando et al., 2016; Perlwitz et al., 2015a,b). The resulting mineral mass fractions are then applied to the dust emission fluxes, as calculated online in the model, yielding the corresponding accumulation- and coarse-mode emission of each mineral (Fig. 1.4).

Direct estimates of FeH and FeO are not available from the mineralogical

soil maps, instead Fe dust pools are computed proportionally to the available Fe minerals. According to Ito and Shi (2016) the content of FeH (0.65%) and FeO (1.3%) on the surface of minerals is prescribed. Fe sourcing from illite, kaolinite, smectite, and feldspar is distributed among the three pools, as shown in Table 4.1, while Fe oxides are entirely allocated to the slow Fe dissolution pool. The resulting FeD emissions by pool (p), gridcell (g), aerosol mode (d), and model time step (t) follow equation 4.1:

$$FeD(p, g, d, t)_{emi} = Dust(g, d, t)_{emi} \cdot \sum_m F(g, d)_m \cdot F_{fe}(g, d)_m \cdot F_{pool}(p, g, d)_m \quad (4.1)$$

where $Dust_{emi}$ is the modeled dust emission flux, F_m is the fraction of each mineral (m) in dust emission as calculated through BFT, F_{fe} is the Fe fraction content in each mineral m , and F_{pool} is the fractionation of Fe sourcing from each mineral m in the three different Fe pools considered.

4.2.2 Fe-combustion representation

EC-Earth3-Iron combustion Fe emissions (FeC), encompassing both fossil fuel combustion (FeF) and biomass burning (FeB), are prescribed as described in Ito et al. (2018) and Hajima et al. (2019). The methodology for estimating these emissions relies on commonly used standard emission inventories. However, these inventories don't typically report Fe emissions directly. Instead, carbonaceous emissions (Carb) (e.g., particulate organic matter (POM) and BC) are used as a proxy for Fe emissions, based on empirical data. These proxies are applied

by using specific emission factors for each aerosol mode and activity sector (e.g., energy, industry, iron and steel production, residential and commercial activities, shipping, waste management, and biomass burning), as follows:

$$FeC(g, d, t)_{emi} = \sum_s (Carb(s, g, d, t)_{emi} \cdot F_{fe}(s, g, d, y)) \quad (4.2)$$

$$Carb(s, g, d, t)_{emi} = BC(s, g, d, t)_{emi} + \frac{OC(s, g, d, t)_{emi}}{F_{oc2pom}} \quad (4.3)$$

where g is the model gridcell, d is the aerosol mode, t is the model time step, s is the considered economic activity sector, y is the year corresponding to time step t , $F_{oc2pom} = 1.6$ is the factor for conversion of OC mass to POM, and F_{fe} is the Fe emission factor. The FeF emission factors change year-to-year during the historical period (Ito et al., 2018), but are assumed to be constant in the future (set to the latest available value of the historical period). For FeB, the emission factors are kept constant through time following Ito et al. (2018).

Separate tracers are defined in the model for FeF and FeB to enable the differentiation of Fe contributions from biomass burning and other combustion sources.

FeC emissions are assumed to be insoluble, except for ship oil combustion ($\approx 80\%$ solubility) (Ito, 2013). Prior studies have indicated uncertainty regarding the solubility of Fe combustion aerosols at emission with Fe emissions from other sectors also being considered soluble (Ito, 2012; Rathod et al., 2020); nonetheless, within the framework of EC-Earth3-Iron, non solubility at emission

except for shipping has been adopted, as the model incorporates a rapid-dissolution pool for FeC that allows swift dissolution within the same emission gridcell.

4.2.3 The iron solubilization scheme

The solubilization of Fe-containing dust mineral pools is described using a three-stage kinetic approach (Shi et al., 2011a; Ito and Shi, 2016). The dissolution process involves three distinct stages: (1) a rapid dissolution of ferrihydrite on the surface of minerals, known as the fast pool, (2) an intermediate stage dissolution of nano-sized Fe oxides from the mineral surfaces, referred to as the intermediate pool, and (3) the slow release of Fe from Fe-containing minerals, such as aluminosilicates, hematite, and goethite, termed the slow pool. Additionally, a separate Fe pool for combustion aerosols (Ito, 2015) is included in the model.

The dissolved Fe in the model is produced via dissolution processes in aerosol water and cloud droplets depending on the acidity levels of the solution (i.e., proton-promoted dissolution scheme), the OXL concentration (i.e., ligand-promoted dissolution scheme), and irradiation (photo-reductive dissolution scheme), following Ito (2015) and Ito and Shi (2016). The Fe release from different types of minerals thus depends on the solution acidity (pH) and the temperature (T), as well as on the degree of solution saturation. In more detail, the dissolution rates for each of the three dissolution processes considered can be empirically described (Ito, 2015; Ito and Shi, 2016; Lasaga et al., 1994) as follows:

$$RFe_i = K_i(pH, T) \cdot \alpha(H^+)^{m_i} \cdot f_i \cdot g_i \quad (4.4)$$

where K_i ($\text{mol Fe } g_i^{-1} \text{ s}^{-1}$) is the Fe release rate due to the dissolution process i , $\alpha(H^+)$ is the H^+ activity of the solution, and m_i is the empirical reaction order for protons derived from experimental data. The functions f_i and g_i represent the suppression of the different dissolution rates due to the solution saturation state as follows:

$$f_i = 1 - \frac{\alpha_{Fe^{3+}} \cdot \alpha_{H^+}^{-n_i}}{K_{eq_i}} \quad (4.5)$$

$$g_i = 0.17 \cdot \ln\left(\frac{\alpha_{OXL}}{\alpha_{Fe^{3+}}}\right) + 0.63 \quad (4.6)$$

where α_{H^+} , $\alpha_{Fe^{3+}}$, and α_{OXL} stand for the solution's activities of protons, ferric cations, and OXL, respectively, as calculated each time step in the model, and K_{eq_i} ($\text{mol}^2 \text{ kg}^{-2}$) is the equilibrium constant.

The dissolution rate constants K_i depend on the ambient temperature (T) and acidity (pH) as follows:

$$K_i(pH, T) = K_{298} \cdot \exp[E_{pH} \cdot (1/298 - 1/T)] \quad (4.7)$$

Where the activation energy (E_{pH}) is derived as a function of acidity based on soil measurements (Bibi et al., 2014; Ito and Shi, 2016), i.e.

$$E_{pH} = -1.56 \times 10^3 \cdot pH + 1.08 \times 10^4 \quad (4.8)$$

and pH is defined as

$$pH = -\log_{10}(H^+) \quad (4.9)$$

Overall, the net Fe dissolution rate results from the sum of the three rates. All parameters used for the calculation of dissolution rates in EC-Earth3-Iron are shown in Table 4.2.

Table 4.2: **Dissolution scheme for Fe-containing combustion and mineral dust aerosols. *Extracted from Myriokefalitakis et al. (2022).***

Iron pool	Scheme	K_{298}^a	m^b	K_{eq}^c	n^d	Reference
FeC	H^+	5.24×10^{-8}	0.36			(Ito, 2015)
	OXL	3.85×10^{-6}	1			(Ito, 2015)
	$h\nu^f$	4.10×10^{-6}	1			(Ito, 2015)
FeH	H^+	7.13×10^{-5}	1.1	1550	3	(Ito and Shi, 2016)
	OXL	4.61×10^{-8}	0.069	1550	3	(Ito and Shi, 2016)
	$h\nu^f$	4.61×10^{-8}	0.069			(Ito and Shi, 2016) ^a
FeO	H^+	1.43×10^{-4}	1.6	42	2.75	(Ito and Shi, 2016)
	OXL	1.28×10^{-8}	0.069	1550	3	(Ito and Shi, 2016)
	$h\nu^f$	1.28×10^{-8}	0.069			(Ito and Shi, 2016)
FeA	H^+	5.85×10^{-8}	0.76	3.3	2.85	(Ito and Shi, 2016)
	OXL	1.68×10^{-9}	0.056	1500	3	(Ito and Shi, 2016)
	$h\nu^f$	1.68×10^{-9}	0.056			(Ito and Shi, 2016)

in mol Fe $g^{-1} s^{-1}$,

^b m is the reaction order (Ito, 2015; Ito and Shi, 2016),

^c K_{eq} is the equilibrium constant ($mol^2 kg^{-2}$) (Bonneville et al., 2004; Ito and Shi, 2016)

^d n is the stoichiometric ratio (Bonneville et al., 2004; Ito and Shi, 2016)

^e The unit for combustion aerosol is converted from moles $m^{-2} s^{-1}$ to mol Fe $g^{-1} s^{-1}$ (Ito, 2015)

^f Photoinduced dissolution rate constants are scaled on the model's H_2O_2 gas-phase photolysis frequencies

Estimates of the degree of acidity of particles affecting proton-promoted Fe solubilization rely on the use of the thermodynamic model ISORROPIA II (Fountoukis and Nenes, 2007). ISORROPIA II is used to predict not only aerosol acidity (taking into account both basic and acidic species in both the fine and coarse modes) but also equilibrium gas-particle partitioning for inorganic species, liquid-phase activity

coefficients, solid-liquid and liquid-liquid equilibria, dynamic mass transfer of semivolatile species and aerosol liquid water content. The modeling approach in ISORROPIA II does not consider single-ion activity coefficients that allow the calculation of pH as a proxy of acidity, but instead, the pH values presented in this Thesis are based on the free-H⁺ molality. In-cloud proton concentration and, hence, cloud acidity are solved via aqueous-phase chemistry (Myriokefalitakis et al., 2022).

The formation of OXL, which influences ligand-promoted Fe solubilization, is computed online in the model, considering aqueous-phase chemistry (Myriokefalitakis et al., 2022). OXL has a strong correlation with levoglucosan and elemental carbon, both of which are found in considerable amounts during biomass fire episodes in the Amazon (Kundu et al., 2010). This suggests that oxalic acid is not only formed rapidly during biomass combustion but may also be directly emitted in some cases. Although the direct emission of OXL is low compared to secondary formation, EC-Earth3-Iron includes primary OXL emissions, derived as a fraction of biomass burning and anthropogenic wood burning BC emissions (0.763% (Yamasoe et al., 2000) and 0.863% (Schmidl et al., 2008), respectively).

4.3. Model evaluation

Evaluating the EC-Earth3-Iron model against observations is crucial to ensure its accuracy in representing real-world processes, particularly for complex systems. Observational data serve as the foundation for validating model assumptions, refining parameterizations, and

identifying gaps or biases in simulations. Without the support of experimental and observational work, models risk losing their connection to reality. The interplay between modeling and observations is indispensable, as neither can independently capture the full complexity of the Fe cycle.

4.3.1 Observations

A substantial collection of ship-borne surface concentration observations of Fe and SFe has been compiled over the past two decades. This compendium of measurements has been curated by atmospheric Fe modelers and updated iteratively, with the latest version provided in Hamilton et al. (2022) (Fig. 4.1). However, those ship-borne observations are still scarce and sparse in time, with less density of observations in key areas such as HNLC regions. The highly episodic nature of aeolian dust and wildfire plumes (e.g., the range in daily Fe deposition may be ≥ 10 orders of magnitude for some ocean regions (Hamilton et al., 2019), and an increasing appreciation of the role of atmospheric processing in enhancing aerosol nutrient solubility during transport (Longo et al., 2016; Stockdale et al., 2016) make data acquisition of representative field observations a challenge that needs to be addressed.

Other observational databases can be used to evaluate and infer other aerosols that directly impact the Fe burden such as dust. Pure dust measurements of surface concentration and deposition complement the evaluation of the model and simulations shown in this Thesis. The modeled annual mean surface dust concentration for the years 2000–2014 is compared to climatological observations from the Rosenstiel School

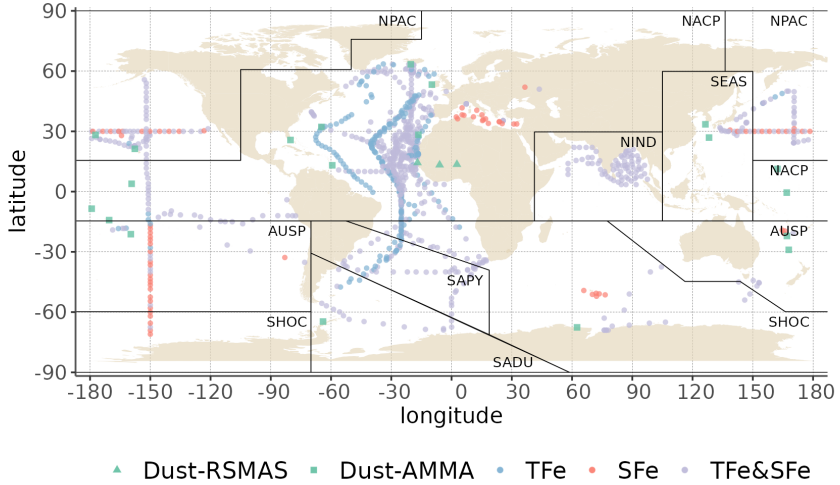


Figure 4.1: **Observation sites used for evaluation.** Observation sites collected in Hamilton et al. (2022). Red dots indicate total iron surface concentration observations, blue dots indicate observations of soluble iron surface concentration, and purple points indicate observations with both total and soluble iron surface concentrations. Locations of dust surface concentration in green (Rosenstiel School of Marine and Atmospheric Science (RSMAS) and the African Monsoon Multidisciplinary Analysis (AMMA) international program Marticorena et al. (2010)). Eight soluble iron ocean deposition regions defined by dominant source region apportionment as in Hamilton et al. (2019). Region 1: North Indian Ocean (NIND). Region 2: South East Asian Ocean (SEAS). Region 3: North Pacific (NPAC). Region 4: North Atlantic and Central Pacific (NACP). Region 5: Southern Hemisphere Oceans (SHOC). Region 6: Australian and Southern Pacific (AUSP). Region 7: South American Dust (SADU). Region 8: South American Pyrogenic (SAPY).

of Marine and Atmospheric Science (RSMAS) of the University of Miami (Arimoto et al., 1995; Prospero, 1996, 1999) and the African Aerosol Multidisciplinary Analysis (AMMA) international program (Marticorena et al., 2010) observations. The 23 available sites cover locations close to sources (e.g., the AMMA stations over the Sahelian

dust transect), transport regions (e.g., stations from RSMAS in the Atlantic), and remote regions (e.g., RSMAS sites close to Antarctica). The modeled dust deposition fluxes are compared to the compilation of observations for the modern climate in Albani et al. (2014), including measurements at 110 locations, and the mass fraction for particles with a diameter lower than $10\ \mu\text{m}$ is used to keep the observed mass fluxes within the range of the modeled sizes.

Other datasets like the Aerosol Robotic Network (AERONET) version 3 (Giles et al., 2019) level 2.0 direct sun retrievals have been used in additional studies not included in this Thesis for a more general evaluation of EC-Earth3-Iron modeled aerosols in terms of the aerosol optical depth (AOD) (Myriokefalitakis et al., 2022).

4.3.2 Statistical analysis for evaluation

Given the scarcity of ship-borne observations, all available data are taken as a representation of the climatological average over the modeled period. Modeled and observed values are temporally and spatially collocated to ensure consistency. Temporal collocation is performed on a monthly basis. Specifically, if an observation corresponds to a particular month (e.g., January), the model's value is calculated as the mean of all January data within the modeled period. Spatially, for fixed-site measurements, the model grid cell nearest to the observation site is selected. For ship-based measurements, the model values of the grid cells nearest to the ship's trajectory are averaged, ensuring spatial alignment with the cruise track.

The evaluation of the modeled Fe and SFe surface concentration against

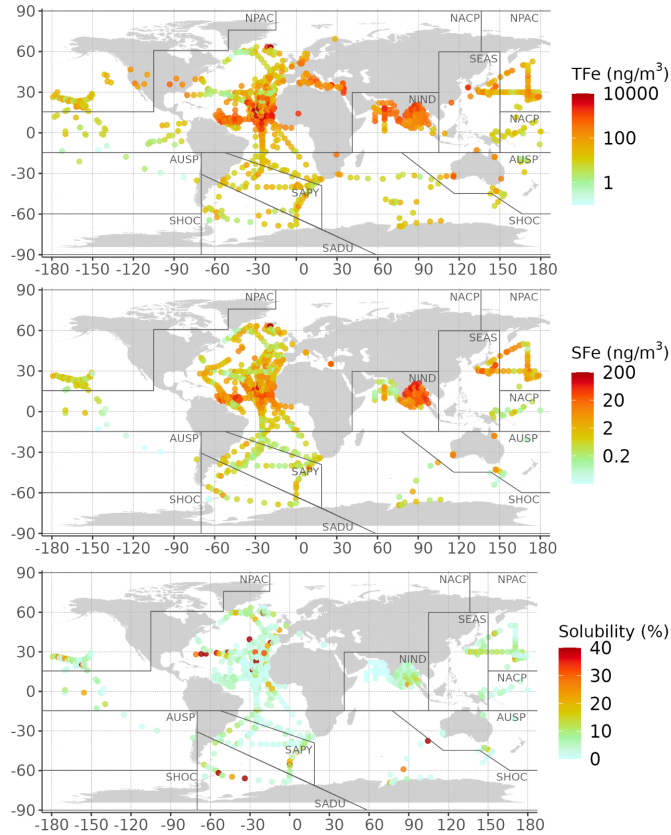


Figure 4.2: **Surface concentrations of Fe and SFe as reported by observations.** Surface concentrations of iron (Fe) (top panel) and soluble Fe (SFe) (middle panel) in ng/m^{-3} . Fe solubility of surface concentrations (bottom panel) in %.

observations uses three different evaluation metrics: the normalized mean bias (nMB), eq. 4.10, the normalized root-mean-square error (nRMSE), eq. 4.11, and the Pearson's correlation (r), eq. 4.12, where M_i represents the modeled value at the observation location and time, O_i the corresponding observed value, N the number of

observations considered, and \overline{M} and \overline{O} the mean values for the model and observations, respectively

$$nMB = \frac{\sum_i (M_i - O_i)}{\sum_i O_i} \cdot 100 \quad (4.10)$$

$$nRMSE = \frac{\sqrt{\frac{1}{N} \sum_i (M_i - O_i)^2}}{\overline{O}} \cdot 100 \quad (4.11)$$

$$r = \frac{\sum_i (M_i - \overline{M}) \cdot (O_i - \overline{O})}{\sqrt{\sum_i (M_i - \overline{M})^2 \cdot \sum_i (O_i - \overline{O})^2}} \quad (4.12)$$

The three evaluation metrics described above are used with the aim of providing a quantitative assessment of the model skills when compared to observations not only on a global scale but also for each of the regions considered, shown in Fig. 4.1. Relying exclusively on the mean values of the nMB, nRMSE and r to compare with the two model experiments could be misleading, especially for those cases with a low number of observations. Therefore, the information of the number of data points that are available to produce these metrics (n) and their uncertainty ranges at a 95% confidence level are incorporated into the model evaluation assessments.

4.4. Socio-economic Development, Scenarios, and Pathways

In this Thesis, the scenario framework is applied to model atmospheric Fe concentrations at the end of the century, contributing to a

4.4. Socio-economic Development, Scenarios, and Pathways

better understanding of future atmospheric dynamics under varying socio-economic and mitigation pathways. Scenarios are essential tools in climate research, as they link socioeconomic and technological advancements to potential future climate outcomes. They model emission trajectories for greenhouse gases, aerosols, their precursors, and other human-induced changes, such as land-use changes, enabling the exploration of emissions trends, climate impacts, and strategies for mitigation and adaptation.

The SSPs provide a structured framework for designing scenarios that combine socioeconomic development with future radiative forcing (RF) outcomes. RF, measured in watts per square meter (W m^{-2}), represents the net change in the Earth's energy balance due to greenhouse gases and other factors. Representative Concentration Pathways (RCPs) define these RF outcomes, ranging from low (e.g., 2.6 W m^{-2} in RCP2.6) to high levels of warming (e.g., 8.5 W m^{-2} in RCP8.5) by 2100. The SSP-RCP framework forms a scenario matrix architecture (Moss et al., 2010) (Fig. 4.3), allowing the investigation of how socioeconomic development interacts with climate forcing.

The five existing SSPs (SSP1 to SSP5) represent distinct socio-economic futures, ranging from sustainable development (SSP1; van Vuuren et al. (2017)) to fossil-fueled growth (SSP5; Kriegler et al. (2017)), high inequality (SSP3; Fujimori et al. (2017) and SSP4; Calvin et al. (2017)), and a “middle-of-the-road” trajectory (SSP2; Fricko et al. (2017)). Each SSP explores near-, medium-, and long-term outcomes across a wide range of socio-economic and environmental conditions. For each SSP, various RF targets can be met depending on global and local policies (Riahi et al., 2017).

The SSPs are widely used in climate research and policy, underpinning IPCC Assessment Reports and supporting decision-making frameworks. As part of CMIP6, the ScenarioMIP project has selected nine key combinations of SSPs and RCPs to investigate how the Earth system responds to climate forcing and to assess future climate changes under scenario uncertainties (O'Neill et al., 2017). These combinations are grouped by Tier-1 scenarios, which span a wide range of uncertainty in future forcing, and Tier-2 scenarios, which enable detailed studies of mitigation and adaptation policies (Eyring et al., 2016).

For this Thesis, four Tier-1 scenarios were selected for analysis (Fig. 4.3):

- **SSP1-2.6** (hereafter SSP126) represents a sustainable and optimistic pathway with expanded pollution controls, low emissions of Near-Term Climate Forcers (NTCF), and a reduced demand for energy- and resource-intensive agricultural commodities.
- **SSP2-4.5** (hereafter SSP245) is a business-as-usual scenario with moderate population growth and continued growth of greenhouse gas (GHG) emissions, combined with some efforts to reduce pollutant emissions.
- **SSP3-7.0** (hereafter SSP370) is a scenario with high NTCF emissions, particularly for SO₂, and decreased global forest cover, along with increased population in low- and middle-income countries and ineffective policies to control air pollution and GHGs emissions.

4.4. Socio-economic Development, Scenarios, and Pathways

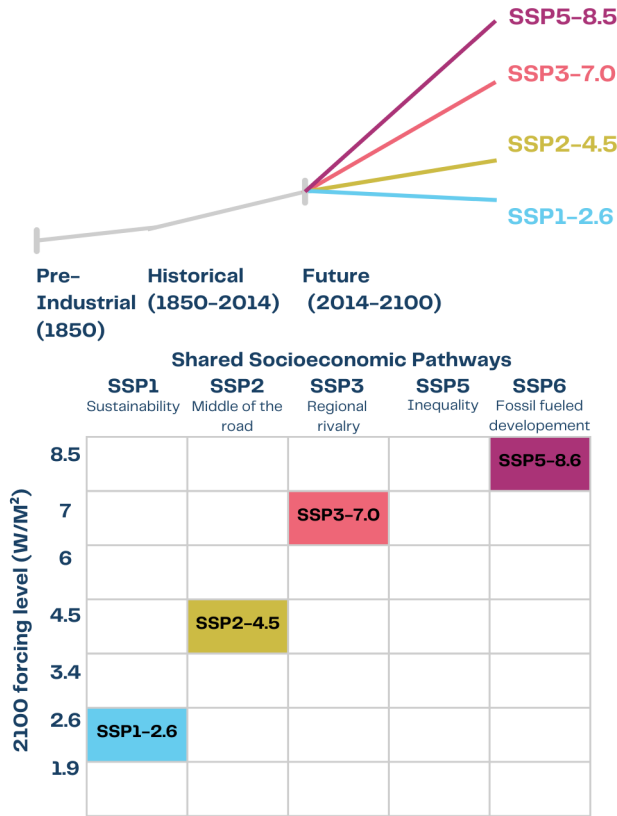


Figure 4.3: **Summary schematic of the CMIP6 scenarios used in this Thesis.**

The upper panel shows a schematic of the periods and projections tendencies across time. The Shared Socioeconomic Pathways (SSPs) radiative forcing matrix is shown on the bottom panel, with the SSP socio-economic narratives shown as columns and the indicative radiative forcing categorization by 2100 shown as rows.

- **SSP5-8.5** (hereafter SSP585) is a scenario representing the high end of the range of future pathways. SSP5 was chosen for this forcing pathway because it is the only SSP scenario with emissions high enough to produce a RF of 8.5 W m^{-2} in 2100.

4.5. Simulations Protocol

EC-Earth3-Iron, as an ESM, supports simulations with various configurations depending on the study objectives. This Section summarizes the protocols used throughout the Thesis.

4.5.1 Nudged experiments

To make the best possible use of a model for research as well as for scenarios, it is important to first understand to what degree and within which limitations an ESM truthfully represents the complexity that governs the real system. Comparing model output to real-world observations is crucial to obtaining such understanding (Eyring et al., 2019). By nudging the large-scale atmospheric circulation in coupled climate models, the model output can be compared to local observations for individual days. Nudging, or Newtonian relaxation, is a form of data assimilation that adjusts dynamical variables of free-running GCMs using meteorological re-analysis data to give a realistic representation of the atmosphere at each time step time (Coindreau et al., 2007). Nudging can be restricted to certain regions, altitudes, and variables.

For Chapter 5 and 6, with the aim of generating a reconstruction of the atmospheric deposition of SFe in the present climate (1991-2020), a simulation in "nudged" mode is performed. The modeled atmospheric circulation was constrained in this setup, using a slight nudging of wind vorticity and divergence towards ECMWF ERA5 reanalysis data (Hersbach et al., 2020). To that end, EC-Earth3-Iron is configured to run in atmosphere-chemistry mode using observed ocean conditions

(SST and SIC) as in the Atmospheric Model Intercomparison Project (AMIP) protocol (Gates et al., 1999).

The vertical extent and the strength of the nudging induced can be defined by the user. In this work, a light nudging is favored to prevent sharp model corrections that risk causing inconsistent model states. At the same time, nudging alters surface winds and turbulent fluxes that are responsible for soil dust emission. Applying nudging to above-surface vertical levels helps minimize its impact on emission.

In addition, dust emission involves complex processes that are poorly understood and often occur at smaller scales than those resolved by global ESMs. Consequently, these processes are typically calibrated against observational data. For the Fe reanalysis run, the nudged parameters and dust calibration values that showed the best performance against dust observations are used. This was achieved through a series of experiments that varied the vertical extent of the nudging, the strength of the correction, and the calibration factor for the dust emission flux. The model outputs were then compared with a range of observational datasets. The reference datasets included climatological observations of dust surface concentration and AOD, as described in Section 4.3.1 (RSMAS, AMMA, and AERONET).

4.5.2 Time-slice experiments

Climate projections using ESMs are simulations of future climate conditions based on a range of possible scenarios for greenhouse gas emissions, land use, and other human and natural influences on the climate system (see Section 4.4). These simulations provide essential

insights for climate adaptation and mitigation planning.

A common standard for running climate projections is established within the framework of the CMIP6 project. In this project, simulations are conducted in an atmosphere-ocean coupled mode, where the ocean requires a long spin-up period to reach stable conditions. Multiple simulations are performed for specific scenarios and models (referred to as ensemble members) to account for climate internal variability and uncertainties in the initial conditions.

Within this Thesis, climate projections have been performed for Chapter 7 and 8. However, although the CMIP6 scenarios are followed (see Section 4.4) the simulation setup methodology is slightly different as in the standard CMIP6 runs.

For Chapter 7, ensembles of atmosphere-only time-slice experiments that represent pre-industrial (PI; 1850) and present-day (PD; 1985-2014) conditions along with three different future scenarios based on Tier-1 CMIP6 SSPs (SSP1-2.6, SSP2-4.5, and SSP3-7.0; 2070-2099) are performed. The initial conditions for the atmospheric tracers, gas phase, and aerosols use 2 years of spin-up to ensure realistic concentrations at the global scale, and the third year of simulation is used to construct the ensembles presented in the Chapter. Each ensemble is composed of 30 different members where the atmospheric initial conditions were created by applying infinitesimal random perturbations, with the aim of sampling the internal climate variability.

Those simulations were run with IFS and TM5-MP coupled (as in the nudging case), where potential feedbacks between the atmosphere and the ocean are neglected. Also, to maintain consistent conditions

between the atmosphere and the ocean state, the aerosols and gas-phase species were not allowed to interact with the atmospheric state. This model configuration is used because it is less computationally costly and it is useful to focus on the atmospheric model without the added complexity of ocean-atmosphere feedback in the climate system.

The experiments use prescribed SSTs and SICs climatologies created from a selection of historical and scenario simulations performed with the coupled atmosphere-ocean version of EC-Earth3, all contributing to the CMIP6 exercise. For each of the selected periods (1850–1879 for the pre-industrial, 1985–2014 for the present, and 2070–2099 for the future scenarios), seven realizations available in the Earth System Grid Federation (ESGF) repository were used to account for potential differences due to the sampling of internal climate variability. The corresponding climatological ocean and sea ice boundary conditions for each experiment were produced by first averaging across the seven realizations and then, averaging in time each 30-year period, ending up with a climatological average for each calendar month.

Climatological monthly emission fields for both anthropogenic and natural species (not computed online) are generated for each experiment, with data for the historical period sourced from the Community Emissions Data System (Hoesly et al., 2018) and future period data obtained from the ESGF archives (<https://esgf-node.llnl.gov/search/cmip6>). For the pre-industrial period, fixed 1850 emissions are used. Historical fire emissions are derived from the Biomass Burning Emissions Dataset for CMIP6 (BB4CMIP6) data set (van Marle et al., 2017), and future emission scenarios are outlined in Gidden et al. (2019).

4.5.3 Sensitivity experiments

While nudging enables simulations to closely resemble historical observations, model time-slice simulations provide insights into potential climate changes under different socioeconomic scenarios by accounting for climate feedbacks. Sensitivity simulations, on the other hand, help us understand how a specific process affects the Earth system by isolating the impacts of that process while keeping all other factors constant.

This broad methodology has been used across this work at different points. For instance, in Chapter 7, the sensitivity of future SFe deposition to potential increases in dust emission is explored through sensitivity simulations. Five simulations based on a specific future scenario for the period 2070–2099 as explained in Section 4.5.2 are defined. In each simulation the dust emission flux from a different source region is doubled: North Africa (NAfr), Middle East (MEast), East Asia (EAsia), SH and North America (NAm). All simulations have exactly the same prescribed input but only the perturbed region for dust emission changes.

Chapter 8 results also are built upon sensitivity simulations where 5-year simulations (with an extra first spinup year) were run nudged towards meteorology (2007-2011) in atmosphere-only mode as in the nudged simulations described in Section 4.5.1. The only thing that changes between simulations are prescribed aerosol and gas-phase emissions and in specific emissions from fire sources.

4.6. Use of HPC systems

ESMs such as EC-Earth3-Iron demand significant computational resources. These models are designed to exploit intensive parallelism, enabling them to solve complex problems within a limited timeframe. At BSC-CNS this system was deployed on the MareNostrum 4 supercomputer. MareNostrum 4 has a performance capacity of 13.7 Petaflop/s. The machine consists of two distinct parts. The general-purpose element, provided by Lenovo, included 48 racks with more than 3,400 nodes equipped with next-generation Intel Xeon processors and a central memory of 390 Terabytes. Its peak power exceeded 11 Petaflop/s, which is ten times more than its predecessor, MareNostrum 3. Despite this substantial increase in capacity, it consumed only 30% more power, reaching 1.3 Megawatt/year. Like its predecessors, MareNostrum 4 was connected to the network of European research centers and universities through the RedIris and Geant networks.

MareNostrum 4 was decommissioned in April 2024 and replaced by its successor, MareNostrum 5. With the assistance of the Computational Earth Science team at BSC-CNS, the EC-Earth3-Iron model was successfully ported to MareNostrum 5. This next-generation pre-exascale EuroHPC supercomputer also hosted at BSC, achieves a total peak computational power of 314 Petaflop/s. Supplied by Bull SAS, it combines Bull Sequana XH3000 and Lenovo ThinkSystem architectures. MareNostrum 5 consists of four partitions, tailored to meet a wide range of HPC requirements. The two primary partitions are: i) a general-purpose partition based on Intel Sapphire Rapids

processors, with 6,408 nodes and 72 high-bandwidth memory nodes, providing a total peak of 45 Petaflop/s, ii) an accelerated partition featuring Intel Sapphire Rapids processors and Nvidia Hopper GPUs, with 1,120 nodes (each equipped with four Hopper GPUs), delivering a peak of 230 Petaflop/s.

To manage and execute EC-Earth3-Iron runs, the workflow manager Autosubmit (Manubens-Gil et al., 2016), its GUI interface (Uruchi et al., 2021), and the EC-Earth-specific extension Auto-EC-Earth, developed within the ES department at BSC-CNS have been employed. This combination of tools facilitates the easy management of model runs as well as pre-and post-processing on HPC platforms. The specific model configuration and workflow setup have been finely tuned to leverage MareNostrum 4 and Marenostrum 5 resources.

In Marenostrum 4, an EC-Earth3-Iron atmosphere-chemistry simulation, with prescribed ocean variables at standard resolution (T255L91 for IFS, $3^{\circ}\times 2^{\circ}$ for TM5) had an average performance of 1.4 simulated years per day (using 326 CPU). The model performance has been slightly improved in the new Marenostrum 5 supercomputer with an average performance of 1.9 simulated years per day.

Other machines hosted at BSC-CNS such as Nord III and CTE-AMD have been used for the analysis shown in this Thesis. Nord III is a supercomputer based on Intel SandyBridge processors, iDataPlex Compute Racks, a Linux Operating System and an Infiniband interconnection. The current Peak Performance is 251,6 Teraflops. The total number of processors is 12,096 Intel SandyBridge-EP E5-2670 cores at 2.6 GHz (756 compute nodes) with at least 24.2 TB of main

memory. CTE-AMD is a cluster based on AMD EPYC processors, with a Linux Operating System and an Infiniband interconnection network.

Additionally, during my doctoral research at North Carolina State University, the CAM6-MIMI experiments presented in Chapter 8 were conducted on the Cheyenne supercomputer at the NCAR-Wyoming Supercomputing Center. Cheyenne, built by Silicon Graphics International with DataDirect Networks for data storage, was a 5.34-petaflop system capable of performing 5.34 quadrillion calculations per second. Its data storage was integrated with NCAR's GLobally Accessible Data Environment (GLADE) file system. Cheyenne was decommissioned at the end of 2023.

The combination of these advanced HPC systems enabled the simulations and analyses presented in this Thesis, significantly reducing computational time and enhancing the overall performance of the experiments.





**Results &
Discussion**

CHAPTER 5

A reconstruction of soluble iron deposition [1991-2020]

5.1. Introduction

The present-day spatial and temporal patterns in the atmospheric loading and deposition of Fe-bearing aerosol is highly uncertain (Myriokefalitakis et al., 2018), partially due to high episodicity in natural emissions originating from multiple sources and regions (Carslaw et al., 2010). Over the Anthropocene, increasing aridity and land use/cover change alters dust and fire emissions (Mahowald et al., 2010; Pechony and Shindell, 2010; Prospero et al., 2002; Tegen et al., 2004) (see Section 1.6.1). In addition, increasing anthropogenic activity has provided a new SFe source via the combustion of fossil fuels (Ito, 2013; Luo et al., 2008) and industrial processes (Rathod et al., 2020). Furthermore, human activity is also a source of those acidic and organic compounds found to increase Fe solubility during transport (Ito and Shi, 2016; Johnson and Meskhidze, 2013; Myriokefalitakis et al., 2015; Solmon et al., 2009). Consequently, SFe deposition sources have

changed temporally and spatially in recent decades, with anthropogenic activity being the prime determinant of recent changes (Conway et al., 2019; Hamilton et al., 2020a,b; Ito et al., 2019; Krishnamurthy et al., 2009; Luo et al., 2008; Mahowald et al., 2009, 2018; Matsui et al., 2018; Myriokefalitakis et al., 2015, 2020).

In this Chapter, the state-of-the-art EC-Earth3-Iron model is used, constrained by the most up-to-date observational data, to analyze the sources, seasonality, long-term trends, and spatial distribution of SFe deposition over the last three decades (1991–2020) under present climate conditions. The reconstruction, performed at daily temporal resolution, provides a robust framework for this analysis. This work seeks to deepen our understanding of atmospheric Fe deposition in the ocean, offering valuable insights to the ocean biogeochemistry community.

5.2. Methods

The atmospheric deposition of SFe for the present climate (1991–2020) is reconstructed using the EC-Earth3-Iron (Myriokefalitakis et al., 2022) experiment. This reconstruction is performed at daily temporal resolution and includes fields for total Fe, SFe, dust, and N deposition. The EC-Earth3-Iron model, described in Section 4.2, simulates key processes such as multiphase chemistry and aerosol microphysics that influence the solubility and transport of Fe in the atmosphere.

The simulation period spans from the year 1991 to 2020. For the 1991–2014 period, anthropogenic and biomass burning emissions are taken from the CMIP6 historical datasets (Hoesly et al., 2018), while for the 2015–2020, an intermediate scenario from those defined in the

CMIP6 protocol, the SSP2-4.5 (Gidden et al., 2019), has been selected. Dust emissions are computed online (see Section 4.2)

With the aim to represent the present-day climate conditions in a realistic way, EC-Earth3-Iron is configured to run in atmosphere-chemistry mode using observed ocean conditions (SST and SIC) as in the AMIP protocol (Gates et al., 1999). The atmosphere is nudged towards reanalysis, favoring a light nudging to prevent sharp model corrections that risk causing inconsistent model states (see Section 4.5.1).

An evaluation of modeled SFe and Fe deposition against available observations, as produced in Hamilton et al. (2022), has been conducted as described in Section 4.3. While the observational dataset includes over 1000 observations globally, their distribution across regions and months is uneven, resulting in low numbers of observations for specific regions or time periods. To address this, the observations are aggregated by month to compare them with climatological monthly values from the model. Both monthly means and monthly medians were evaluated to capture potential differences in central tendency and reduce the influence of outliers. Regional statistics were computed based on the regional definitions provided in Hamilton et al. (2019), enabling a more spatially focused analysis of the model's performance.

Furthermore, an analysis of long-term trends was performed by computing linear regressions on modeled daily data for the 1991–2020 period. Regressions were carried out for each model grid cell to determine the spatial distribution of trends. The statistical significance of the trends was assessed using a two-tailed t-test, with p-values less

than 0.05 considered significant (Student, 1908). Global trends were also evaluated based on this significance threshold.

5.3. Results & discussion

5.3.1 Evaluation of the iron deposition reconstruction

The comparison of surface Fe concentrations from the reconstruction with observations (1234 observation samples) reveals that globally modeled monthly means overestimate surface Fe concentrations, with high nRMSE values indicating significant variability in Fe deposition (Fig. 5.1, Table A.2). However, when comparing with monthly medians, the modeled median values show a lower nMB but are slightly underestimated relative to observations. As previously noted in Mahowald et al. (2009) and Hamilton et al. (2019), the discrepancy between the median and mean deposition amounts arises because isolated, large deposition events significantly skew the total mean deposition toward higher values. In contrast, the median values are less affected by these extreme events and therefore provide a closer representation of the sparse observational data.

Since most observations are concentrated in the Atlantic Ocean, the global statistics are skewed towards conditions in this region. Regionally, overestimations are more pronounced in areas with high deposition rates (NACP, NIND, SEAS, see Fig. 4.1 for region definition), while remote regions (SADU, SHOC, SAPY, A USP) show underestimations of surface Fe concentrations (Table A.2).

Given that total Fe is predominantly influenced by primary sources,

discrepancies in observed concentrations downwind of continental sources likely result from inaccuracies in emission parameterizations or misrepresentations of the mineralogical composition of larger Fe-containing soil particles. Conversely, underestimations in remote areas may reflect a combination of factors, including an underrepresentation of atmospheric transport to these regions, mischaracterizations of sources contributing to these areas (e.g., high-latitude dust), or an inadequate representation of sinks such as wet or dry deposition processes.

When analyzing how well the modeled SFe surface concentrations correspond to observations (1359 observation samples), less overestimation is observed compared to total Fe surface concentrations, along with lower nRMSE values. High deposition regions still show overestimations, while remote regions exhibit underestimations, similar to total Fe concentrations, although the extent of underestimation is smaller.

Fe solubilities at the surface are generally well captured but are notably overestimated in the NIND, SHOC, and SAPY regions, where combustion Fe sources dominate, as discussed in Section 5.3.2. This overestimation could suggest that Fe emissions from these regions are underestimated and/or that the solubilization parameterization for combustion Fe sources is overly efficient in the model.

An evaluation of additional EC-Earth3-Iron species aside from Fe, such as dust, OXL, and SO₄, is presented in Myriokefalitakis et al. (2022). Dust optical depth (DOD) is shown to be slightly underestimated by the model based on data from AERONET sites (see Section

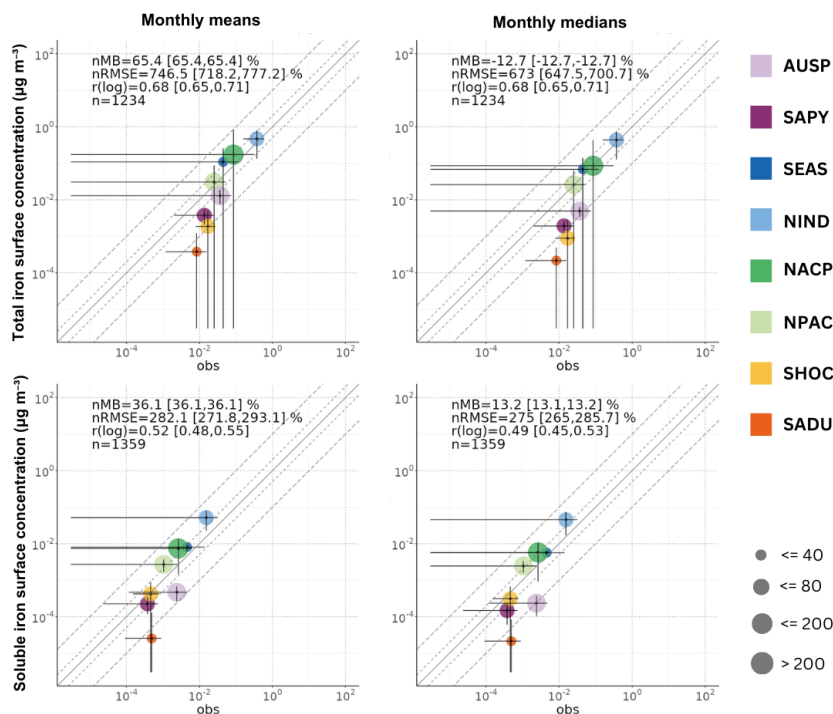


Figure 5.1: **Evaluation of Fe surface concentrations.** Modeled versus observed surface concentrations of total iron (Fe) (upper row), soluble iron (SFe) (bottom row) for monthly mean modelled values (right column) and monthly median values (left column). Regions are depicted in Supplementary Fig. 4.1. The size of each colored point shows a number of observations corresponding to that region. Error bars indicate the interquartile range for each region. Global statistics are shown, where n is the number of total measurements, nRMSE is the normalized root mean square error, nMB is the normalized mean bias, and r is the correlation over all the points. The ranges for the nMB, nRMSE and r correspond to the 95% confidence level. Dashed lines represent differences of 2 times and 1 order of magnitude.

4.3.1). This is consistent with results from the parent version of the model, EC-Earth3-AerChem, which tends to produce lower dust emissions compared to multimodel estimates (Gliß et al., 2021). The underestimation may reflect inaccuracies in processes like dust size distribution, transport, or deposition. OXL and SO_4 concentrations show good agreement with observations, accurately reproducing features such as the seasonal dependence of OXL, which peaks during the warm season due to intense photochemical activity combined with higher precursor abundance.

5.3.2 Climatological atmospheric iron cycle

The EC-Earth3-Iron reconstruction estimates global mean annual Fe emissions of 47.96 ± 3.42 Tg which falls within the range of previous studies estimates (Table A.4). Dust sources represent 95% of Fe emissions (with 45.53 ± 3.48 Tg/yr global mean emissions), followed by fossil fuel combustion representing 4% (with 1.89 ± 0.50 Tg/yr global mean emissions) and fires representing the remaining 1% (with 0.53 ± 0.09 Tg/yr global mean emissions (Fig. A.2). The relative contributions of these sources to total Fe emissions align with findings in previous literature (Luo et al., 2008; Mahowald et al., 2009; Hamilton et al., 2020a). Notably, only 0.13% of the total emitted Fe burden is prescribed as soluble at emission (Fig. A.1b).

As illustrated in Fig. 5.2, the primary Fe emission hotspots are major dust source regions within the dust belt, spanning from North Africa to East Asia. Consequently, the highest Fe deposition fluxes occur in areas predominantly affected by NH dust sources, such as those influenced by North African and East Asian dust. The mean annual

Chapter 5. A reconstruction of soluble iron deposition

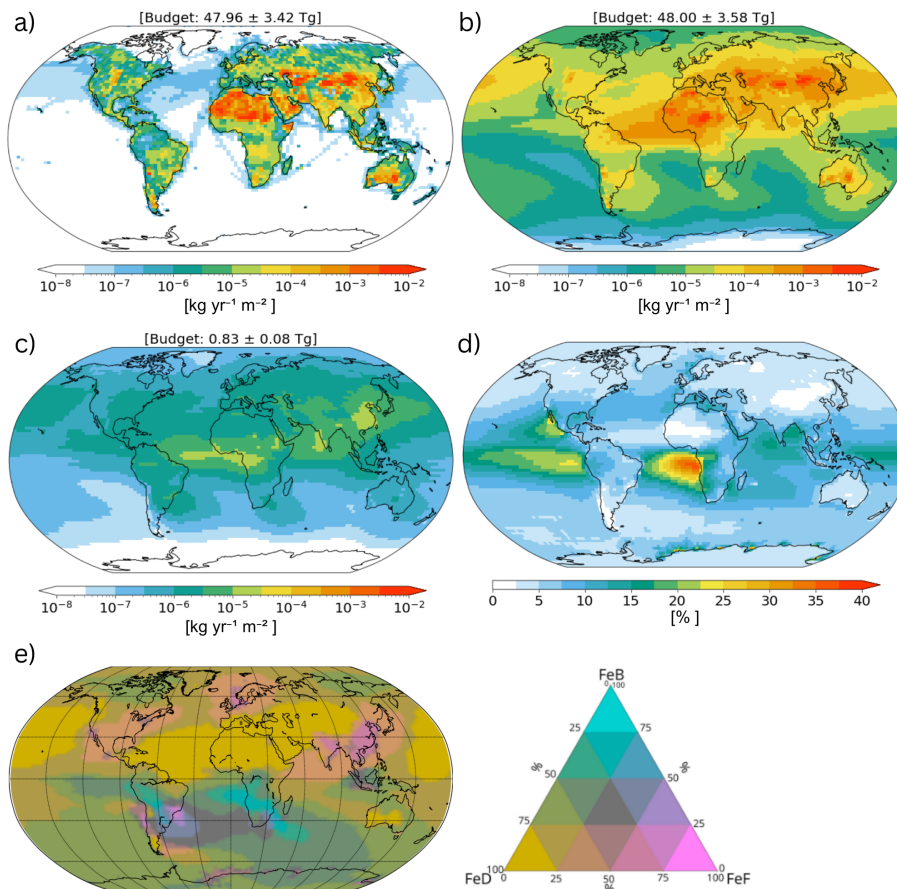


Figure 5.2: **Mean annual Fe emission and deposition fluxes.** Mean annual fluxes in $\text{kg yr}^{-1} \text{m}^{-2}$ of iron (Fe) emission (a), Fe deposition (b), soluble Fe (SFe) deposition (c), mean Fe solubility at deposition in % (d) and source contribution to SFe deposition in % (e) (yellow represents FeD deposition dominates, in blue FeB deposition dominates and in pink FeF deposition dominates). Mean annual global budgets in Tg are given for (a, b, and c).

Fe deposition flux is estimated at $48.00 \pm 3.58 \text{ Tg}$, consistent with the emission budget.

SFe deposition patterns mirror Fe deposition trends but emphasize

regions where multiple sources converge. For instance, the equatorial Atlantic experiences high fluxes from both dust and fire aerosols, while coastal regions of the Indian and western North Pacific oceans show a mix of dust and fossil fuel aerosol contributions. In contrast, the SH basins receive less atmospheric deposition overall, with notable contributions from biomass-burning aerosols combined with dust and anthropogenic sources over the South Atlantic and South Indian oceans.

Fe solubilities at deposition (Fig. 5.2d) are generally lower (between 0 and 10 %) downwind main dust source regions (e.g, the North Atlantic and North Pacific). In the SH mean solubilities range between 2.5% and 7.5%. However, in the equatorial Atlantic and Pacific solubilities peak and show mean values above 20% reaching 40% mean solubilities in some areas of the South Atlantic. This falls in line with previous studies (Mahowald et al., 2009; Scanza et al., 2018; Hamilton et al., 2019). EC-Earth3-Iron, however, highlights elevated solubilities in the equatorial Atlantic, potentially attributed to enhanced OXL-promoted dissolution in this region. Unlike other models, EC-Earth3-Iron explicitly includes interactive OXL dissolution, which is supported by observed high OXL concentrations in this area (Myriokefalitakis et al., 2022).

The fraction of particles in the accumulation mode ($\approx D < 1\mu\text{m}$) compared to those in the coarse mode is significantly higher ($>50\%$) in regions far from sources, such as the SO, the equatorial Pacific, and the high-latitude North Atlantic. In contrast, in the North Atlantic, downwind of North African dust sources, nearly all the deposited flux is in the coarse mode (Fig. 5.3a). As discussed in Section 1.4, coarser particles have shorter atmospheric lifetimes due to more efficient

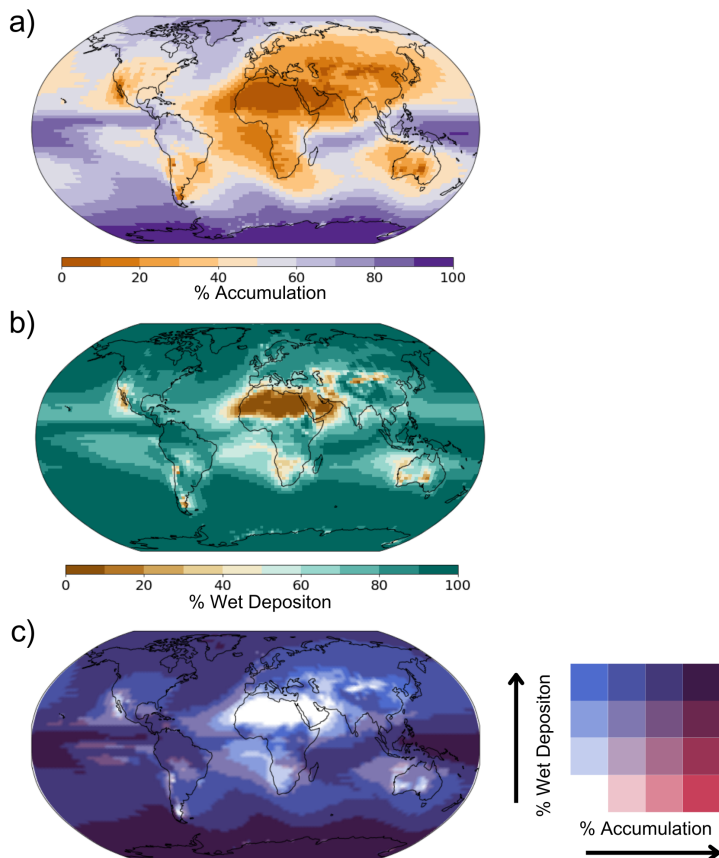


Figure 5.3: **Fractions of accumulation vs. coarse mode and wet vs. dry SFe deposition.** Mean relative fraction of accumulation aerosol mode over total soluble iron (SFe) deposition (a) and of wet deposition over total SFe deposition (b) for the 1991-2020 period. Concurrent fractions of accumulation and wet deposition (c).

removal processes, such as gravitational settling.

A similar pattern is observed in the relative contribution of wet versus dry deposition. Directly over dust source regions, dry deposition dominates; however, moving even slightly away from these sources,

wet deposition rapidly becomes the primary mode of deposition. Wet deposition accounts for more than 90% of total deposition in most open ocean regions, including the SO, the North Pacific, and the high-latitude North Atlantic (Fig. 5.3b).

Together, these findings illustrate a deposition regime where, far from sources (e.g., high-latitude oceans), SFe deposition is primarily driven by wet deposition and occurs predominantly in the aerosol accumulation mode (Fig. 5.3c).

5.3.3 Seasonality of soluble iron deposition

The total SFe deposited fluxes and geographical patterns over the ocean show significant seasonal variations (Fig. 5.4). Higher mean global deposition fluxes occur in the NH summer (JJA) (83 ± 8 Gg month⁻¹, on average for that season), while the season with lower SFe deposition flux is during the NH autumn and winter months (SON and DJF) (61 ± 7 Gg month⁻¹ and 64 ± 26 Gg month⁻¹ respectively).

Geographically, a latitudinal displacement of the highest deposition area in the Atlantic is seen. Particularly, in boreal summer (JJA) and autumn (SON) SFe deposition follows the pattern of dust transport towards the Caribbean area and the Guiana basin. In boreal winter (DJF) and spring (MAM), the largest deposition fluxes occur over the equatorial region. This can be in part attributed to the shift of the inter-tropical convergence zone (ITCZ) that moves north in the NH summer and south in the NH winter (Nicholson, 2018). In the North Pacific, the highest deposition fluxes occur during MAM, coinciding with the peak activity of East Asian dust sources (Fig. A.5), while

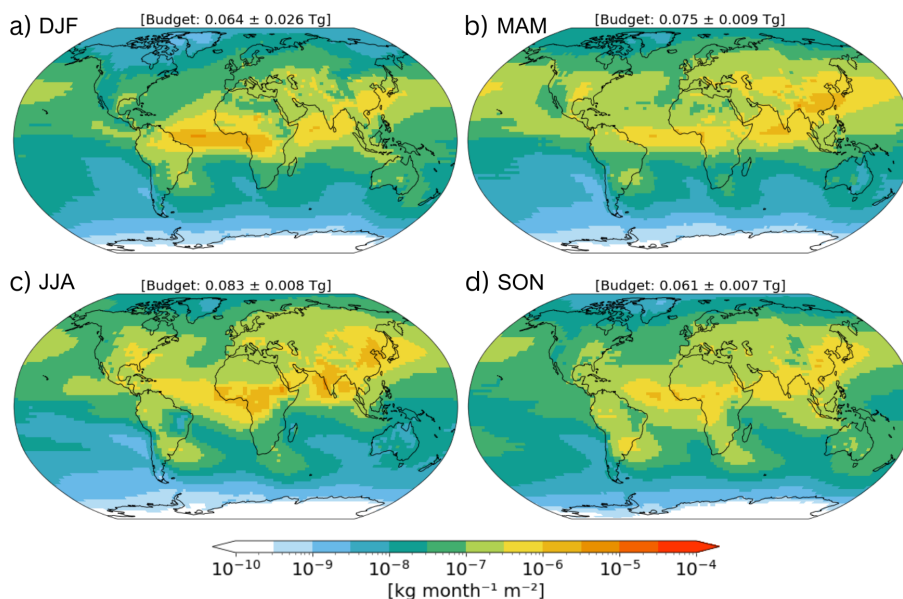


Figure 5.4: **Seasonal SFe deposition.** Mean seasonal (1991-2020) soluble iron (SFe) deposition in $\text{kg month}^{-1} \text{m}^{-2}$ for (a) DJF, (b) MAM, (c) JJA, and (d) SON as derived from the reconstruction with EC-Earth3-Iron. Mean monthly budgets \pm the standard deviation along the 30 simulated years are given for each season in Tg of SFe.

both polar and subtropical jet streams contribute to the long-range transport of East Asian dust (Yu et al., 2019). In the SO, for JJA and SON an increase in SFe deposition is seen compared to DJF and MAM. This increase is due to the seasonality of biomass burning sources where emissions and total contribution to SFe deposition is the highest during these seasons (Fig. 5.5 A.5

When examining total Fe deposition fluxes, a different seasonality is observed compared to SFe deposition fluxes. The highest Fe deposition fluxes are happening in MAM and DJF ($6.39 \pm 1.06 \text{ Tg month}^{-1}$ and

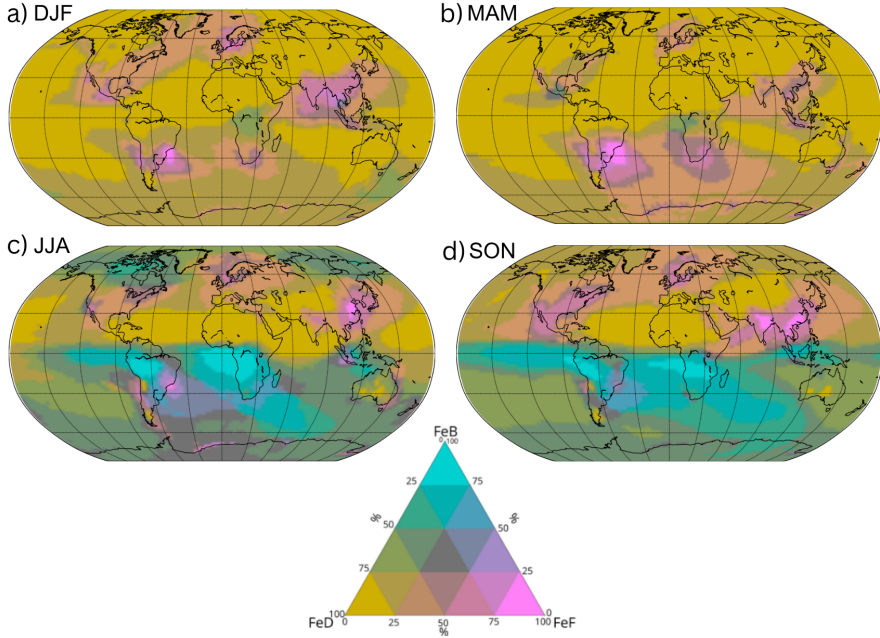


Figure 5.5: **Seasonal SFe deposition source contribution.** Relative contribution of the different sources to the seasonal mean (1991-2020) soluble iron (SFe) deposition for (a) DJF, (b) MAM, (c) JJA, and (d) SON, with FeD: dust, FeF: fossil fuel combustion, FeB: biomass burning aerosols.

$4.98 \pm 0.71 \text{ Tg month}^{-1}$, respectively) (Fig. A.3). The seasonality of deposited Fe closely follows the seasonality of dust emissions and deposition, as the total Fe burden is dominated by Fe from dust sources that peaks in North Africa in the DJF and MAM seasons and in East Asia during MAM season (Figs. A.4, A.5).

This shift in seasonality between SFe deposition and Fe deposition fluxes results in high seasonality of solubility values at deposition (Fig. 5.6). For JJA and SON, when there are less dust emissions sourcing from the dust belt, high solubilities ($>25\%$) are reported over the equatorial Atlantic and Pacific oceans. This matches in time with

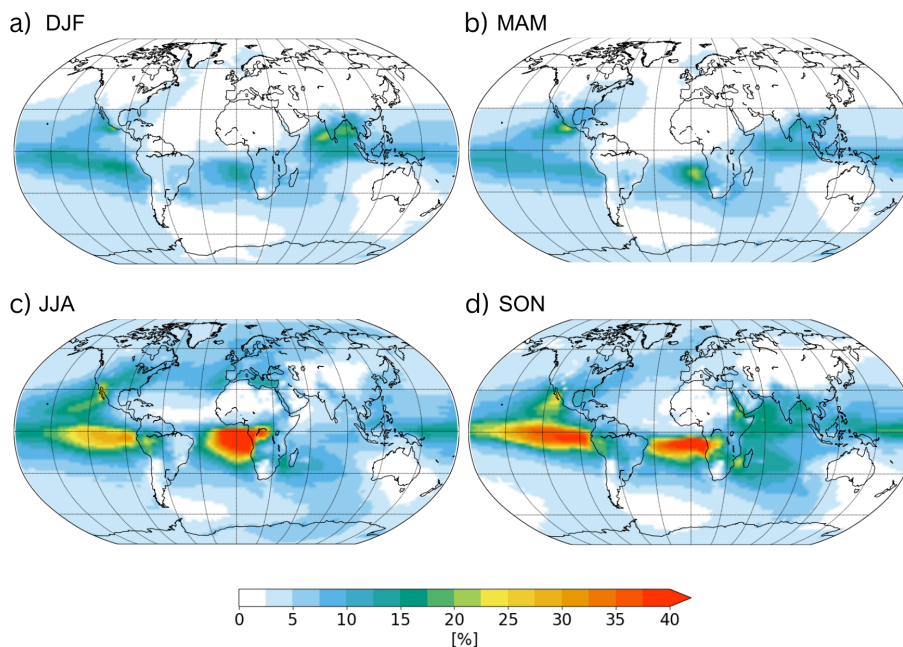


Figure 5.6: **Seasonal Fe solubility at deposition.** Mean seasonal solubility of iron (Fe) at deposition for the 1991-2020 period for (a) DJF, (b) MAM, (c) JJA, and (d) SON, as derived from the reconstruction with EC-Earth3-Iron.

higher concentrations of Fe sourcing from fires during those seasons in this area where solubility peaks (5.5). As explained in Section 1.2.3, fires are a perfect "cocktail" for Fe solubilization as Fe is co-emitted with other species such as OXL that foster Fe solubilization. This can be specially seen in the South Atlantic downwind African fire source regions in the boreal summer where high concentrations of OXL and SO_4 are seen (Fig. A.6 A.7).

The fraction of wet deposition to total SFe deposition does not show a distinct seasonal variation in the NH (Fig. A.9). However, in equatorial regions, particularly the equatorial Atlantic, a higher proportion of

dry deposition relative to wet deposition is observed during the boreal summer and fall. This pattern may seem counterintuitive, as these seasons coincide with higher precipitation rates in these areas (Adler et al., 2017). During periods of high precipitation, both wet and dry deposition increase, but the proportion of wet to dry deposition in terms of mass can decrease because dry deposition often involves larger particles that contribute more mass per unit of deposition. Additionally, during these seasons, the particles transported to these areas tend to include a higher fraction of coarse particles compared to other seasons (Fig. A.10), likely due to intensified activity in nearby Fe-fire source regions. However, this relationship is not universal and depends on the specific characteristics of the source regions and transport mechanisms.

5.3.4 Long-term trends in soluble iron deposition

For the first time, trends in SFe deposition during the past three decades are presented using a model that incorporates high-complexity solubilization processes of Fe in the atmosphere. SFe deposition increased significantly over the 1991–2020 period (Fig. 5.7a), with a mean global relative change of 32%. A significant positive trend in SFe deposition is observed for most regions during the study period, except for parts of the North Atlantic and equatorial Atlantic oceans. Geographic variations in this positive trend are evident, with the largest increases (more than double) occurring over India, East Asia, South America, and nearby regions, including the Bay of Bengal, the Arabian Sea, and the South Atlantic. In these regions, fossil fuel combustion sources dominate SFe deposition (Fig. 5.2e and 5.5), suggesting that the substantial increases in SFe deposition can primarily be attributed

to heightened emissions from combustion sources.

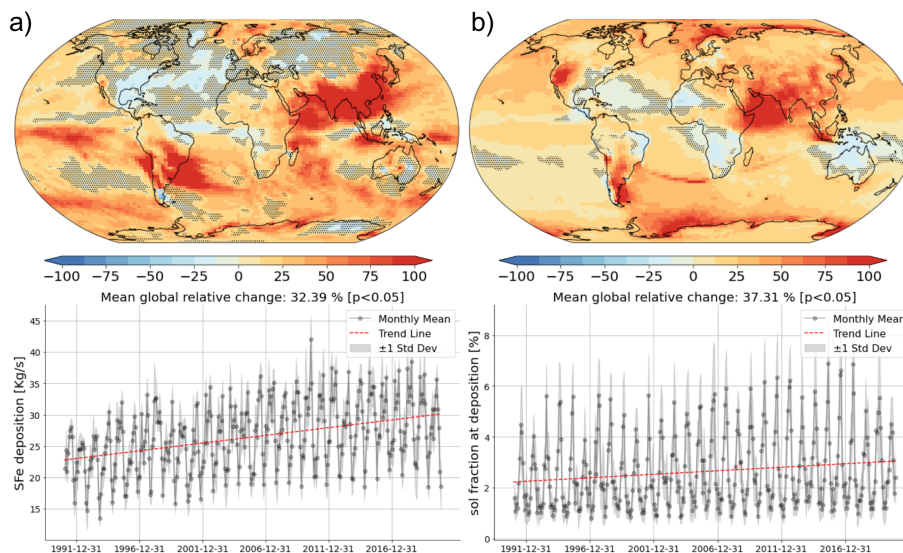


Figure 5.7: **Long term changes in SFe and Fe solubility deposition.** Relative changes in soluble iron (SFe) deposition (a) and Fe solubility at deposition (b). The maps display trends for each grid cell, with areas marked by dots indicating regions where the computed trends are not statistically significant (t-test, $p > 0.05$). At the bottom of each map, the time evolution of each variable is shown, with monthly mean values represented by dots and the variability within each month depicted by shaded gray areas. The global mean computed trend is shown in red.

A closer look at the contributions from individual sources reveals that fossil fuel combustion is responsible for the most prominent increase in SFe deposition (Fig. 5.8c). The mean global relative change in SFe deposition from this source is a striking 228%, with particularly strong positive trends in the regions previously mentioned. However, the trajectory of this increase is not uniform throughout the study period. While a sharp rise is observed between 2001 and 2011, this is followed by a plateau, with SFe deposition remaining relatively stable from 2011

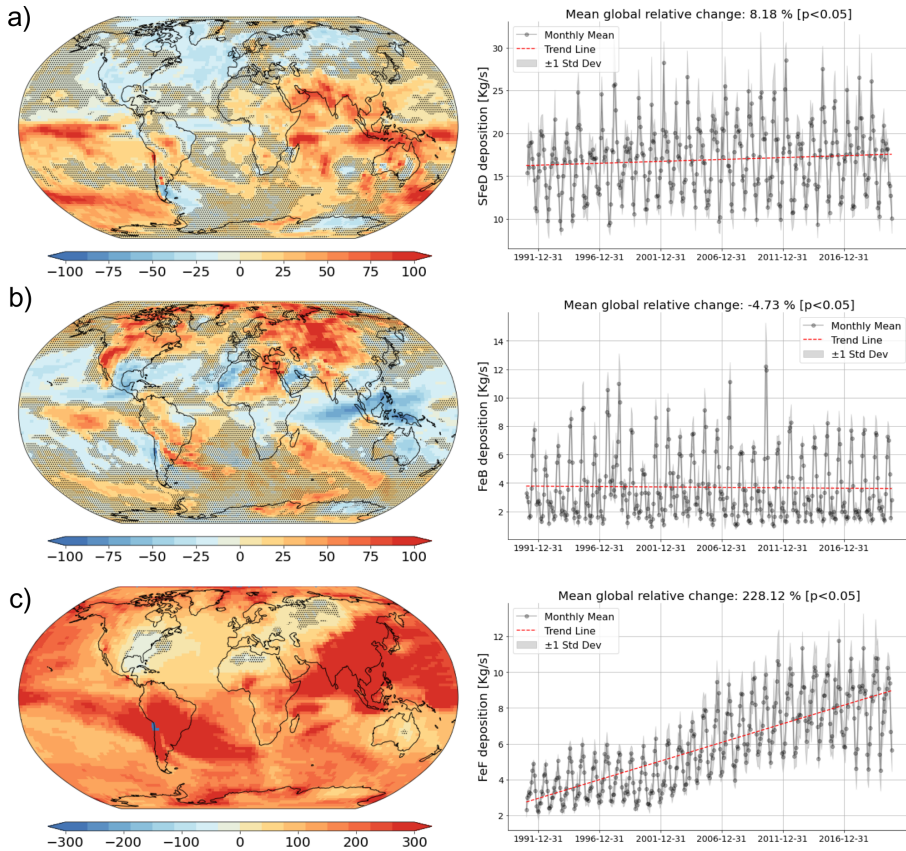


Figure 5.8: **Long term changes in SFe deposition by source.** Relative changes in soluble iron (SFe) deposition from dust (SFeD) (a), SFe from fires (SFeB) (b), and SFe from fossil fuel combustion (SFeF) (c). The maps display trends for each grid cell, with areas marked by dots indicating regions where the computed trends are not statistically significant (t -test, $p > 0.05$). At the bottom of each map, the time evolution of each variable is shown, with monthly mean values represented by dots and the variability within each month depicted by shaded gray areas. The global mean computed trend is shown in red.

to 2020. This pattern aligns with trends observed in FeF emissions (Fig. A.2c), suggesting that emissions from fossil fuel combustion and

more effective mitigation strategies in the last decade have played a major role in the recent fluctuations in SFe deposition.

SFe deposition from dust sources also shows a statistically significant positive global mean relative trend (8%), with notable regional differences. Decreases are observed in the North Atlantic, while more pronounced increases occur in the equatorial Pacific, Indian Ocean, and South Pacific. However, FeD emissions do not exhibit a significant trend over the 30-year study period (Fig. A.2a). This indicates that the observed trends in SFeD deposition are likely driven by enhanced solubilization processes in the atmosphere rather than an increase in the FeD emission burden. It has to be drawn to attention, however, that EC-Earth3-Iron, as well as all the other ESMs, do not capture well the long-term trends of dust as observed by observations (see Section 1.6.1.1) (Kok et al., 2023).

SFe deposition from fire sources shows a mean global decrease of 5%, with significant latitudinal variations (Fig. A.2b). SFeB deposition increases in high-latitude regions while generally decreases in equatorial regions. This aligns with observed satellite trends in fire emissions (a decrease of 17% in Fe fire emissions is here estimated) (see Section 1.6.1.3) (Jones et al., 2024).

Across all sources of Fe, the trends in SFe deposition show a greater increase than those of Fe emissions. This suggests that solubility at deposition has globally increased across nearly the entire globe (Fig. A.1b), indicating a shift in atmospheric chemistry towards a more acidic environment together with higher concentrations of organic ligands sourcing from anthropogenic activities, likely contribute to enhanced

Fe solubilization.

Moreover, as previously noted by Hamilton et al. (2020b), a shift in deposited SFe particles toward smaller diameters is observed. This shift suggests that Fe particles have longer lifetimes and a higher potential for solubilization (Fig. A.11).

5.4. Conclusions

This Chapter presents an analysis of a 30-year reconstruction of SFe deposition using the state-of-the-art model EC-Earth3-Iron driven by ERA5 reanalysis data. Unlike similar models, EC-Earth3-Iron explicitly resolves multiphase chemistry, including the OXL and sulfur cycles. Additionally, aerosol acidity is considered in both accumulation and coarse aerosol modes.

The model demonstrates acceptable performance when compared with observational data. However, the evaluation would greatly benefit from a more extensive observational dataset. The lack of long-term monitoring sites for Fe and SFe deposition limits opportunities to refine model accuracy and better understand potential biases.

Climatological fields of SFe deposition are described in detail, including solubility, source contributions, wet and dry deposition patterns, and size characterizations. Quantifying the magnitude and sources of SFe fluxes, alongside their physicochemical forms, is essential for understanding their impacts on ocean biogeochemistry and the carbon cycle.

Characterizing deposition in HNLC regions, such as the SO, is

particularly important. The SO plays a critical role in carbon export, a key pathway for atmospheric CO₂ removal (Kohfeld and Ridgwell, 2009; Martin, 1990). This work highlights that dust, fires, and fossil fuels contribute significantly to SFe deposition in this region, making it highly susceptible to anthropogenic activities.

Additionally, it is shown here how the EC-Earth3-Iron model responds to recent climate changes and evolving socioeconomic activities. Anthropogenic fossil fuel Fe shows a significant increasing trend, accompanied by enhanced Fe solubility in the atmosphere. These changes underscore the importance of accounting for anthropogenic and climate-driven shifts in long-term studies and projections, a topic further explored in Chapter 8.

Notably, Fe solubility at deposition exhibits strong seasonality in regions such as the equatorial Pacific and Atlantic. This seasonality is driven by fire sources that provide a unique combination of conditions favorable for Fe solubilization.

Ocean biogeochemistry is highly sensitive to both physical variables (e.g., temperature and light) and nutrient deposition. PP and community structure can respond to changes in Fe availability within days to weeks (e.g., in oligotrophic ocean gyres; (Guieu et al., 2014)), while carbon export responds on interannual timescales (Aumont et al., 2008; Doney et al., 2009). However, most current biogeochemistry models rely on fixed ratios of Fe to dust (e.g., 3.5%; (Aumont et al., 2015)) and use monthly climatologies, neglecting trends in SFe deposition. Such limitations may underestimate the impacts of Fe flux variability on ocean biogeochemistry.

The reconstruction presented here is a high-resolution, source-specific product that provides valuable input for ocean biogeochemistry models. It includes daily deposition rates and traces Fe from different sources (e.g., FeD, FeF, and FeB), enabling a more detailed understanding of their impacts. Additionally, N deposition, which is accounted for through both thermodynamic equilibrium and gas-phase chemistry in this reconstruction, serves as a useful byproduct for biogeochemical modeling (Fig. A.12).

This work marks significant progress in capturing the temporal and spatial variability of SFe deposition over recent decades (1991–2020), providing valuable insights into its role in ocean systems and its broader implications for the global carbon cycle.

CHAPTER 6

Impact of Soluble Iron Deposition Events on Subseasonal Chlorophyll Dynamics

6.1. Introduction

Aerosol atmospheric SFe deposition exhibits a highly episodic nature (Hamilton et al., 2020b), with daily dust deposition rates in the North Atlantic reaching up to four times the monthly mean flux (Moxim et al., 2011). This pulsed character, evident in long-term records such as the Barbados dust aerosol sampling series initiated in 1965 (Prospero and Lamb, 2003), contrasts sharply with the climatological-state assumptions often employed in ocean biogeochemistry models (Hamilton et al., 2020b). These models traditionally treat aerosol deposition as a continuous constant input, overlooking the episodic dynamics that influence nutrient delivery and ecosystem responses

(Drenkard et al., 2023). Moreover, remote marine observations, constrained by their sparse and intermittent nature, require precise atmospheric data to model episodicity accurately (Guieu et al., 2014). Addressing these limitations is crucial to advancing our understanding of the variability in SFe deposition and its far-reaching impacts on marine ecosystems.

The ocean's response to deposition pulses, whether transient or long-term, remains an active area of research. Oceanic regions exhibit diverse biogeochemical conditions, such as nutrient upwelling, light availability, SST, mixed layer depth (MLD), and community composition, that shape varying responses to nutrient inputs. Nutrient manipulation experiments, including in situ enrichments and bottle incubations, have provided valuable insights into these responses. Some studies report regional patterns of increased autotroph biomass following aerosol deposition (Moore et al., 2013; Browning and Moore, 2023; Hamilton et al., 2022). However, these responses are not universal. In certain regions, aerosol deposition fails to alleviate nutrient limitation (Guieu et al., 2010), reinforces heterotrophic dominance (Marañón et al., 2010), or induces toxicity (Paytan et al., 2009).

Despite these findings, many regions remain under-sampled, and the limited temporal scope of experiments restricts our understanding of responses across different timescales. Research has largely focused on HNLC regions, which currently receive relatively low atmospheric inputs (Fig. 5.2c). In contrast, low-nutrient low-chlorophyll (LNLC) regions (characterized by low chlorophyll-a concentrations and domination of small phytoplankton and heterotrophic bacteria) have received less

attention. LNLC regions, exhibit nuanced responses to deposition (Uitz et al., 2010; Cho and Azam, 1990). The impact of atmospheric deposition there has been suggested to be more complex than a simple "fertilization effect" as traditionally seen in HNLC regions (Guieu et al., 2014).

The episodic nature of aerosol deposition poses additional challenges. Observing anomalous deposition events in situ is inherently unpredictable, and experimental studies are limited (Hamilton et al., 2022). However, satellite data offers promising opportunities, providing near-continuous monitoring of atmospheric and surface ocean conditions on a global scale.

In HNLC regions, dust deposition events, for instance, have been shown to induce increases in satellite-derived chlorophyll-a with time lags of approximately 5–14 days (Bishop et al., 2002; Gabric et al., 2010; Han et al., 2011; Yoon et al., 2019; Li et al., 2024; Nguyen et al., 2024). Similarly, episodic volcanic ash deposition has been linked to biological responses in these regions (Achterberg et al., 2013; Henson et al., 2013; Hamme et al., 2010; Westberry et al., 2019). Beyond dust and volcanic ash, extreme events such as the 2019–2020 Australian megafires resulted in observed anomalies in phytoplankton blooms in the SO (Tang et al., 2021; Wang et al., 2022b), and Ardyna et al. (2022) demonstrated that fire aerosols can amplify blooms in the Arctic Ocean.

In LNLC regions, although less studied, deposition events yield valuable insights. For instance, Neuer et al. (2004) found no significant impact on annual phytoplankton production at the ESTOC station near the Canary Islands over two years, although high-deposition events

Chapter 6. Impact of Soluble Iron Deposition Events on Subseasonal Chlorophyll Dynamics

produced detectable signals. In the Mediterranean, dust storms reduced *Prochlorococcus* abundance while slightly increasing Chl-*a* and bacterial activity (Herut et al., 2005). In North Atlantic oligotrophic waters, wet deposition events were linked to rapid phytoplankton accumulation and a shift in community structure favoring *Prochlorococcus* over *Synechococcus* (Yuan et al., 2023).

Nevertheless, challenges persist in leveraging satellite data for studying ocean biogeochemical responses. One significant challenge is accounting for atmospheric corrections, particularly for regions affected by high dust fluxes (Volpe et al., 2009). Dust particles in the atmosphere scatter and absorb sunlight, altering the spectral properties of light that satellites detect. This interference introduces significant biases in chlorophyll retrievals, as the satellite sensors struggle to distinguish between signals from the ocean surface and those altered by atmospheric dust.

Recent advancements, however, are promising. Westberry et al. (2023) combined global satellite ocean color products with modeled dust deposition to show that strong deposition events contribute approximately 4.5% of global carbon EP, with regional impacts ranging from biomass enhancement in high-latitude seas to improved physiological conditions in LNLC regions.

In conclusion, available data reveal diverse and regionally variable responses to strong atmospheric deposition in ocean systems, underscoring the complexity of these processes. Despite advancements in reconstructing SFe deposition and linking it to ocean biogeochemistry, significant uncertainties persist, particularly regarding episodic events

and their impacts in LNLC regions. This study aims to build upon existing methodologies, such as those outlined in Westberry et al. (2023), by utilizing the daily SFe deposition fields presented in Chapter 5 and combining it to global satellite data from the European Space Agency Ocean Color Climate Change Initiative (ESA OC-CCI) product over a 17-year time-frame (1998 to 2014). This approach seeks to better constrain the episodic nature of SFe inputs and assess their impacts on ocean biogeochemical processes across diverse regions.

6.2. Methods

Westberry et al. (2023) proposed that the characteristics of short-term high dust deposition events, together with the deviations from the annual cycle in surface chlorophyll (SChl) concentration records, could provide a means to isolate the effects of strong atmospheric deposition events on surface ocean biogeochemistry from other sources of ecosystem variability.

In their study, 5°-by-10° gridded 8-day-resolution dust deposition data (obtained using the NASA Goddard Earth Observing System model) were combined with satellite-observed ocean color products (MODIS Aqua Level 3 data) to evaluate ecosystem responses to the largest 10% of dust deposition events at each grid point between 2003 and 2016. SChl was assessed before and after the largest deposition events in each grid cell using the following equation:

$$\Delta X_{rel} = 100 \cdot \frac{(X_{t+1} - X_{t-1})}{X_{t-1}} \quad (6.1)$$

Chapter 6. Impact of Soluble Iron Deposition Events on Subseasonal Chlorophyll Dynamics

where X represents any ocean color property, and t denotes the timing of a dust deposition event.

However, the methodology of Westberry et al. (2023) can lead to misleading conclusions. When the seasonality of Chl- a and aerosol deposition is correlated, ΔX_{rel} will tend to report positive values because higher deposition events may coincide with seasonal blooming periods, during which SChl naturally increases following its seasonal cycle.

To address this issue, an extension to this methodology is here proposed and explored with another set of model and satellite data. Specifically, this study focuses on SFe deposition data rather than dust, recognizing SFe's critical role as a bioavailable nutrient influencing ocean productivity. Ocean color data at a 5-day frequency (described in Section 6.2.2) and SFe deposition data at a 5-day frequency (derived from the same simulation as in Chapter 5) are re-gridded to 6°-by-9° resolution, closely mimicking the spatial approach of Westberry et al. (2023).

Specifically, ocean color data at a 5-day frequency (described in Section 6.2.2) and SFe deposition data at a 5-day frequency (from the same simulation presented in Chapter 5) are re-gridded to 6°-by-9° resolution to mimic the approach of Westberry et al. (2023). The data is then decomposed into distinct components representing the interannual trend (T), the seasonal signal (S), and the intraseasonal signal (I). For details on this decomposition, see Section 6.2.1. Following the decomposition, the top 10% of SFe intraseasonal deposition events are identified, and changes in the intraseasonal signal of Chl- a are computed as follows:

$$\Delta X_{rel} = 100 \cdot \left(\bar{I}_{rel,t,t+1} - I_{rel,t-1} \right) \quad (6.2)$$

where

$$I_{rel,t} = \frac{I_t}{S_t + T_t} \quad (6.3)$$

and $\bar{I}_{rel,t,t+1}$ is the mean of I_{rel} for time t (when the high deposition event happens) and $t+1$. This approach captures the responses within the 0–10 day time-frame, serving as a reasonable compromise for the observed time responses in previous studies.

6.2.1 Temporal decomposition

At each grid point, SFe and ocean color time series $X(t)$ are decomposed into three components:

$$X_t = T_t + S_t + I_t \quad (6.4)$$

using a mathematical approach based on a simplified version of the X-11 method (Zellner, 1978). The method was first used in a climate variability context by Pezzulli et al. (2005) and adapted by Keerthi et al. (2020).

This method ensures that equation 6.4 is satisfied at every location. The seasonal component (S) reflects variability over a period of three months to one year, while the multi-annual component (T) comprises variability over a timescale longer than eight months. Finally, the sub-seasonal component (I) captures variability in the 5–90-day frequency range, plus all irregular variability outside of that range.

In summary, this bandpass-filtering method uses a series of filters, such as Henderson, seasonal, and simple moving average filters. An iterative process that alternately computes the trend component from the seasonally adjusted series and the seasonal component from the series corrected for the trend is used to estimate each component. A key characteristic of the X-11 decomposition is that the seasonal term has a variable amplitude (i.e., a quasi-periodical signal) because it is specified locally in time. Continuous time series are necessary for the X-11 approach. Thus, before the decomposition is applied, linear interpolation is used to fill in the gaps in the data, which are then masked.

This adapted algorithm consists of eight successive steps to decompose the signal X_t , which are described below.

1. Estimation of the first interannual component (T_t) by an annually centered moving average (73 terms moving average as each year contains 73 5-day long time steps) on the initial time series X_t . Z_t , comprises the seasonal and intraseasonal components and is defined as:

$$Z_t = X_t - T_t \quad (6.5)$$

2. Estimation of the first seasonal component ($S(t)$), by applying a seasonal running mean on $Z(t)$.
 - First, $Z(t)$ is averaged over three successive years at every time step of the considered years:

$$S_t^0 = (Z_t(i-1, m) + 2(Z_t(i, m)) + Z_t(i+1, m))/4 \quad (6.6)$$

where $Z_t(i, m)$ is the series subsample for each time step m

= 1, 2,.. 73 of each year $i = 1, 2 \dots n$.

- The resulting time series (S_t^0) is then normalized by subtracting its annually centered running mean (MS_t^0).

$$S_t^1 = S_t^0 - MS_t^0 \quad (6.7)$$

The seasonally adjusted series is then computed as:

$$Z_t^1 = X_t - S_t^1 \quad (6.8)$$

3. The improved estimate of the interannual component (T_t^2) is obtained by applying a Henderson filter (Henderson, 1916) of weight 81 on the seasonally adjusted series (Z_t^1). Then the interannual adjusted series is estimated:

$$Z_t^2 = X_t - T_t^2 \quad (6.9)$$

4. Step (2) is applied on the interannual adjusted series (Z_t^2) to obtain the secondary estimate of the seasonal component (S_t^2). Then the seasonally adjusted series is estimated:

$$Z_t^3 = X_t - S_t^2 \quad (6.10)$$

5. The intraseasonal signal (I_t^1) is estimated by applying a bandpass filter of 8–88 days on the secondary estimate of the seasonal component (S_t^2).
6. The interannual component (T_t) is estimated by repeating step (3) to the seasonally adjusted series (Z_t^3).
7. The seasonal component (S_t) is obtained by subtracting (I_t^1) from (S_t^2)

8. The intraseasonal component (I_t) is the result of:

$$I_t = X_t - S_t - T_t \quad (6.11)$$

This methodology introduces errors at the beginning and end of the time series (Zellner, 1978). To address these, the time series is extended for decomposition to include data up to 2016, while the year 1997, also included in the decomposition, is then excluded from the analysis.

6.2.2 Ocean Color Data

Within this study, Level 3 Mapped 25 × 25 km resolution five-day averaged product (version 6.0) from January 1998 to December 2014 distributed by the ESA OC-CCI (available at <http://www.oceancolour.org/>) is used. The dataset consists of merged records measured by six different satellite sensors; OrbView-2-SeaWiFS, MODIS-A, and SNPP-VIIRS by NASA/NOAA, and MERIS, OLCI-A, and OLCI-B by ESA/EUMETSAT. The use of various ocean color sensors, each offering distinct spectral, spatial, and temporal characteristics, presents challenges for achieving consistency in the time series. While the OC-CCI group implemented a comprehensive bias correction to the dataset, some inter-mission variations in the time series persist due to differences in the surface water coverage across the input sensor datasets (van Oostende et al., 2022).

This product has good data coverage, exceeding 50%, over most low and mid-latitudes (Fig. 6.1a). However, coverage is lower in areas characterized by high annual or seasonal cloud cover, such as the Intertropical Convergence Zone. Poleward of about 50° in

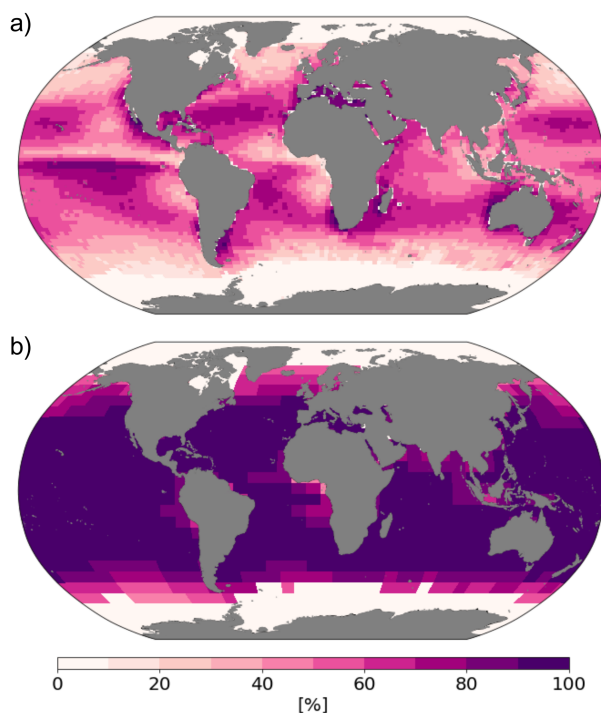


Figure 6.1: **Percentage of SChl data in time series.** Percentage of available surface chlorophyll (SChl) data from the ESA OC-CCI version 6 between 1st of January 1998 to 31 December 2014 for a) $2 \times 3^\circ$ and b) $6 \times 9^\circ$ gridcell resolution. Polar oceans are masked based on ocean biome regions (see Appendix A)

both hemispheres, data coverage rapidly falls below 30%, and data availability becomes restricted mostly to the summer period due to the high solar angle, elevated cloudiness during winter, and sea ice cover.

Still, the merged ocean color product used here has better coverage and extends over a longer time period than any individual satellite product. A further dilemma is whether the sub-seasonal SChl variability captured by the merged satellite product is reliable or is strongly affected by noise. Previous comparison with high-frequency in situ mooring observations

in the Mediterranean Sea revealed that the merged satellite product was accurate at sub-seasonal timescales, although it is unclear whether this can be extrapolated to other locations (Keerthi et al., 2020). It is also important to recognize that variations in SChl do not always reflect changes in depth-integrated biomass. High-frequency, continuous, depth-resolved in situ observations from a range of locations are needed to further characterize temporal variability in SChl and its relationship to NPP.

In light of these limitations and in order to compare our results with the findings in Westberry et al. (2023), the ocean color product and SFe deposition data are regrided to a coarser resolution ($6 \times 9^\circ$) to: (i) reduce satellite retrieval noise and (ii) increase data coverage within each grid cell (Fig. 6.1). Polar oceanic regions are masked from this analysis due to low data cover.

6.2.3 Statistical analysis

6.2.3.1 Quantifying variability

There are different ways to quantify temporal variability. In this analysis the temporal variability of SChl and SFe deposition is explored. The coefficient of variation (CV) is used as a key measure of variability. It is defined as the ratio of the standard deviation to the mean, expressed as a percentage as follows:

$$CV = 100 \cdot \frac{\sigma}{\mu} \quad (6.12)$$

where σ is the standard deviation and μ is the mean of the dataset. The CV provides a dimensionless measure of variability that allows

comparisons between datasets with different units or scales.

The total variance $var(X_t)$ of the original time series can be written as $var(X_t) = var(S_t) + var(I_t) + var(T_t) + 2cov(S_t, I_t, T_t)$, where $var(S_t)$, $var(I_t)$ and $var(T_t)$ represent the variances associated with the seasonal, intraseasonal, and interannual components, respectively. $Cov(S_t, I_t, T_t)$ is the covariance of the three components. This term makes up only a few percent of the total variance (typically $<5\%$ in absolute value) and can, therefore, be neglected. The relative contribution of each component to the total signal is expressed as a percentage. This decomposition highlights the dominant temporal scale of variability in the dataset, helping to identify whether seasonal, intraseasonal, or interannual fluctuations play a greater role.

6.2.3.2 Median responses and statistical significance

The median response in SChl data to top deposition events is computed for each grid cell. The median is chosen over the mean because the response distribution includes positive outliers that could skew the mean. This approach helps in understanding the typical behavior across all top deposition events, as the median is a non-parametric measure and does not assume any specific distribution shape.

To determine whether the median responses shown in each grid cell are statistically significant compared to the median responses outside the top 10% of deposition events, a non-parametric statistical test is performed. Specifically, a bootstrap random selection (with replacement) of a random 10% subset from the deposition distribution below the top 10% events is conducted 1000 times. Then, the

Kruskal–Wallis test is used to analyze whether the medians of the responses to top deposition events differ statistically from those of the random subsets. The Kruskal–Wallis test is a non-parametric statistical method (Kruskal and Wallis, 1952) that assesses whether samples originate from the same distribution and is suitable for comparing two or more independent samples of equal or varying sizes.

6.3. Results & discussion

6.3.1 The episodic nature of soluble iron deposition

SFe deposition exhibits significant variability across all timescales (Fig. 6.2). Regions with higher SFe deposition fluxes, such as the Equatorial and North Atlantic and the North Pacific, tend to have lower coefficients of variation (CVs), typically between 0.5 and 1.5. In contrast, higher latitudes display greater variability (CVs > 2), driven by interactions between long-range transport and precipitation dynamics (Werner et al., 2002).

The spatial structure of the intraseasonal, seasonal and interannual variabilities in SFe deposition is in general agreement with results from previous studies focused on dust and SFe deposition (Werner et al., 2002; Mahowald et al., 2003; Aumont et al., 2008; Hamilton et al., 2020b). As already shown by Mahowald et al. (2003) for dust, intraseasonal variability is by far the largest with more than 70% of the variance in all latitudes explained by the intraseasonal signal (Fig. 6.2).

In comparison, SChl fields generally exhibit lower CVs than SFe deposition, with values typically below 1.5. Consistent with earlier

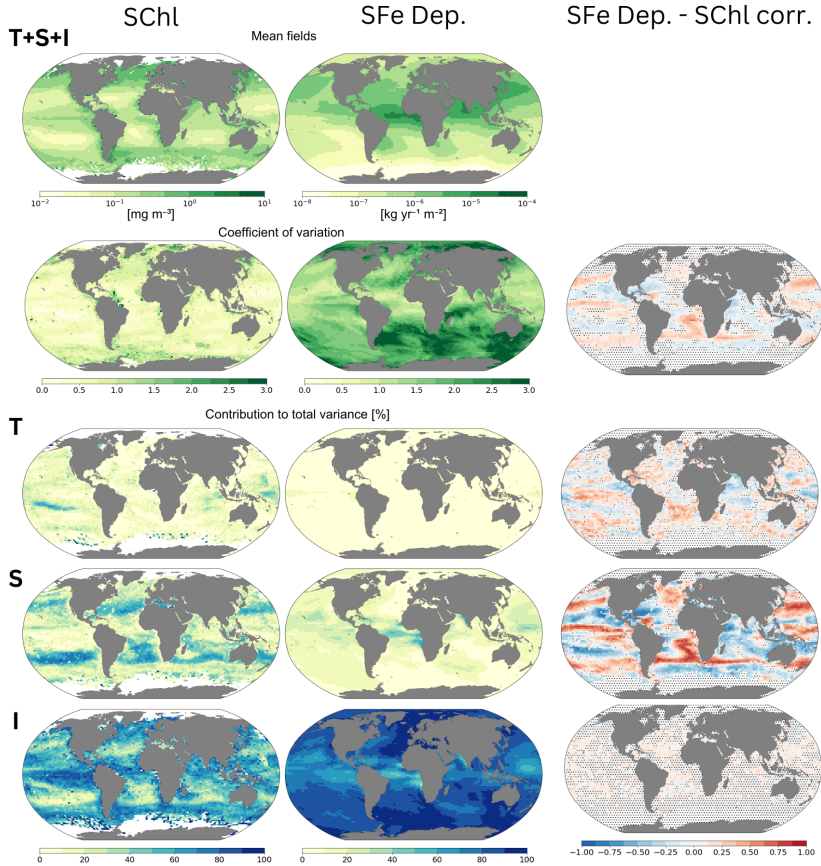


Figure 6.2: **Variance of SFe deposition and SChl levels.** Mean annual (1998–2014) surface chlorophyll (SChl; left column) and soluble iron (SFe; middle column) data are shown in the top row. The second row illustrates the coefficient of variation for SChl (left column) and SFe deposition (middle column), with the right column displaying the correlation between the SChl and SFe deposition time series. The bottom three rows decompose the total variance into interannual (T), seasonal (S), and intraseasonal (I) components for SChl (left column) and SFe deposition (middle column), while the right column shows the correlation of each component between SChl and SFe deposition. Grid cells with statistically insignificant correlations ($p > 0.05$) are masked in the right column.

Chapter 6. Impact of Soluble Iron Deposition Events on Subseasonal Chlorophyll Dynamics

analyses of global SChl variability (Keerthi et al., 2022), intraseasonal variance often exceeds seasonal and interannual contributions, particularly in tropical and subpolar regions, where it accounts for over 70% of total variance. However, in mid-latitudes, the seasonal signal is dominant.

Multi-annual variability in both SFe deposition and SChl is relatively modest, contributing less than 20% of the total variance in most regions. An exception is the tropical Pacific for SChl, where multi-annual fluctuations dominate, reflecting the well-known horseshoe pattern associated with El Niño–Southern Oscillation (ENSO) (Chen et al., 2024).

When analyzing the correlation between SFe deposition and SChl temporal series, statistically significant but generally modest correlations are observed. Positive correlations are noted in regions such as the Equatorial Pacific, South Atlantic, and mid-to-high latitude oceans. Conversely, slight negative correlations are found in tropical regions.

When these correlations are analyzed separately for the interannual, seasonal, and intraseasonal components of both variables, the pattern for the full signal strongly aligns with the correlation between their seasonal components. However, correlation does not imply causation, and it is challenging with this analysis to pinpoint regions where nutrient deposition directly contributes to the seasonality of SChl, as many other factors influence this relationship (e.g., light conditions, SST, MLD, surface winds, etc.), some of which may co-vary with aerosol deposition.

The interannual signals also show slight positive correlations in many

open ocean regions, such as the South Atlantic, where SFe deposition has significantly increased over the 1991–2020 period (see Section 5.3.4) and SChl has also been shown to increase (Hammond et al., 2020). Conversely, in the Arabian Sea and Bay of Bengal, the interannual signals are negatively correlated. These regions have experienced a substantial increase in SFe deposition in recent decades, while SChl levels have decreased (Hammond et al., 2020). Such decreases in SChl have previously been linked to rising SSTs (Krishnapriya et al., 2023). Finally, the intraseasonal components exhibit minimal correlation. Only isolated ocean patches show statistically significant correlations, and even in these areas, correlation coefficients are close to zero.

6.3.2 SChl responses to high soluble iron deposition events

Applying the methodology of Westberry et al. (2023) to the dataset used in this study reveals notable differences from their findings. While Westberry et al. (2023) reported predominantly positive ΔX_{rel} values (equation 6.1) across their study regions, the analysis reported here shows significant regional variability, with ΔX_{rel} exhibiting both positive and negative values depending on the location (Fig. 6.3a). This regional variation in the sign of ΔX_{rel} aligns with the correlation patterns between the seasonal components of SFe deposition and SChl (Fig. 6.2). For instance, regions such as the Pacific SO and the high-latitude North Atlantic demonstrate a correspondence between the sign of ΔX_{rel} and the sign of this seasonal correlation.

Using Eq. 6.2 to estimate the response of SChl to the top 10% of SFe

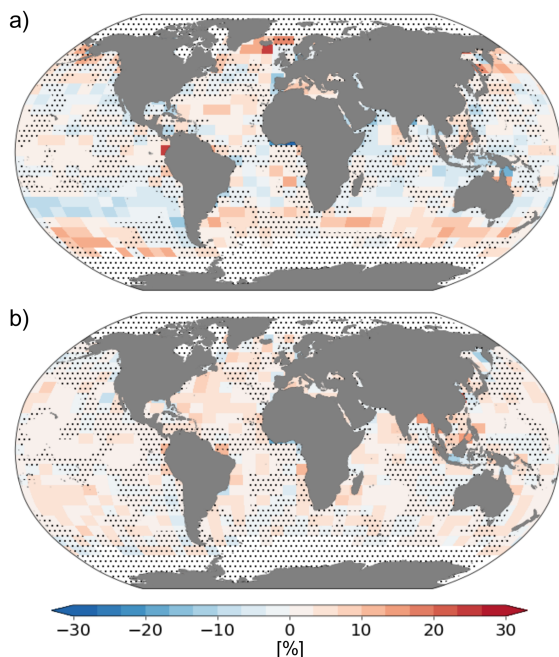


Figure 6.3: **SChl response to high SFe deposition events.** The median surface chlorophyll (SChl) response to the top 10% of soluble iron (SFe) deposition events is computed following Westberry et al. (2023) (Eq. 6.1) (a) and the approach proposed in this study (Eq. 6.2) (b). Pointed areas indicate regions where the median responses are not statistically significant ($p > 0.05$) compared to a random 10% sample of SFe deposition events outside the top 10% window, based on a Kruskal-Wallis test.

deposition events reveals a widespread positive response across most regions. These responses are generally modest in magnitude, typically less than 10%, and are comparable in relative magnitude between oligotrophic regions and higher-latitude seas. However, statistical significance varies across regions. Broad areas with significant responses include the oligotrophic Pacific and Atlantic, the equatorial Pacific, and portions of the Indian Ocean, while other regions exhibit poor

statistical significance at gridcell level when comparing the median response of top events to randomly sampled events (Fig. 6.3b).

When dust deposition fields are used instead of the top SFe deposition events, significant positive ΔX_{rel} values persist across broad regions of the oligotrophic North Atlantic and North Pacific oceans (Fig. A.18a). These regions are known to be N- and P-limited, with dust serving as an important source of nutrients like P. However, Fe-limited regions, such as the high-latitude North Atlantic and specific patches in the SO, which showed positive responses to the top SFe deposition events, do not exhibit corresponding signals under the dust deposition analysis. This suggests that the SFe reanalysis deposition product is more informative in these regions, as it accounts for Fe contributions from diverse sources and atmospheric dissolution processes.

By separating the analysis by Fe source (Fig. A.18b,c,d), it becomes evident that in certain regions, positive signals in ΔX_{rel} are associated with specific Fe sources. For example, downstream of the Patagonian region, no significant signal is observed for dust-derived SFe from top deposition events, which has been already highlighted in some regional studies (Cosentino et al., 2020). However, a positive signal is apparent for SFe sourced from fire and fossil fuel emissions. Similarly, in the high-latitude North Atlantic, a stronger and more extensive signal emerges when considering only fossil fuel-derived SFe. These findings suggest that the underlying ocean biogeochemistry in these regions may be more sensitive to specific sources of Fe, reflecting differences in bioavailability, deposition timing, or the associated nutrient profiles delivered by these sources.

These findings are consistent with previous studies (Herut et al., 2005; Guieu et al., 2014; Yuan et al., 2023; Westberry et al., 2023), which indicate that responses to aerosol deposition are not confined to HNLC regions but are also observed in oligotrophic seas. However, an increase in SChl does not necessarily correspond to a proportional rise in PP or carbon export. Changes in chlorophyll concentrations in the surface ocean may result not only from variations in phytoplankton biomass but also from alterations in physiological status.

To better interpret observed changes in chlorophyll, additional satellite-derived ocean color products are available. These have been used before to highlight the significant influence of physiological factors on satellite-observed chlorophyll records (Siegel et al., 2013; Behrenfeld et al., 2016). One such property is the particulate backscattering coefficient (bbp), which has been quantitatively linked to phytoplankton carbon biomass (C_{phyto}) (Graff et al., 2015; Martinez-Vicente et al., 2013). Unlike chlorophyll concentration, C_{phyto} is not influenced by physiological adjustments driven by light or nutrient availability (Geider et al., 1998).

Analysis of the top SFe deposition events reveals that few grid cells exhibit statistically significant responses in C_{phyto} (Fig. A.20a), likely due to the limited temporal coverage of the bbp product (Fig. A.21). When examined on a regional basis, however, several regions across various biome types demonstrate significant negative responses within the same 5-window time-frame as the strong deposition events. This pattern suggests that in these areas, SFe deposition events may enhance phytoplankton's physiological status without substantially affecting standing stocks.

6.3.3 Timing and duration of SChl responses across regions

By computing I_{rel} (i.e., the fraction of the SChl intraseasonal signal over the non-intraseasonal component; Eq. 6.3) at the 5-day window time step of the top deposition events, as well as at preceding and subsequent time steps, and comparing these median values with the time step before the high deposition event ($t-1$) as a reference, insights into the timing and duration of the effects of pulsed deposition events on ocean biogeochemistry can be inferred (Fig. 6.4).

A generalized positive signal is observed across all regions at the same time step as the deposition event, with median I_{rel} tending to be higher than the time step prior to the high deposition event (Fig. 6.4). This pattern suggests that median SChl responses to aerosol deposition are rapid, initiating within a time frame of less than five days.

In some upwelling and equatorial regions (like the upwelling and equatorial Atlantic), a positive difference in median I_{rel} is shown at t and $t + 1$ but with no statistical significance, likely due to the limited spatial extent of these regions, the reduced data availability, and the fact that these regions are typically not Fe-limited. By contrast, regions like the equatorial and upwelling Pacific, which are known to be Fe-limited (Browning and Moore, 2023), display statistically significant positive signals in SChl following strong SFe deposition events.

For oligotrophic regions, a clear positive signal emerges at t and $t + 1$, but the signal diminishes beyond $t + 1$. This indicates that for these regions, a quick, pulsed SChl response (lasting from days to about one

Chapter 6. Impact of Soluble Iron Deposition Events on Subseasonal Chlorophyll Dynamics

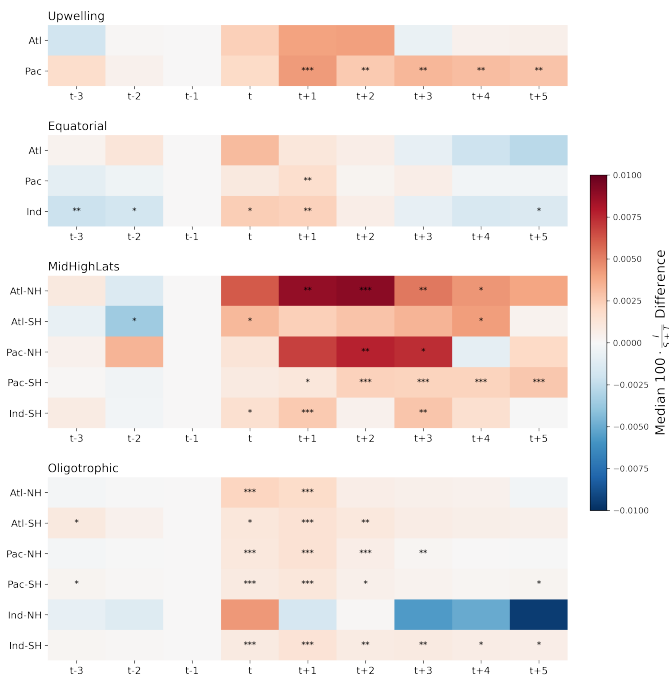


Figure 6.4: **Timeline of SChl response to top SFe deposition events.** Difference between the median surface chlorophyll (SChl) I_{rel} values for the time step t of the high soluble iron (SFe) deposition event and previous ($t-2$, $t-3$) and subsequent ($t+1$, $t+2$, $t+3$, $t+4$, $t+5$) time steps and the median I_{rel} for $t-1$. Significance levels (from Kruskal-Wallis testing) expressed by asterisks (***) for p -value ≤ 0.001 , ** for p -value ≤ 0.01 , * for p -value ≤ 0.05).

week) follows the top SFe deposition events.

In contrast, mid- to high-latitude regions exhibit a stronger and more prolonged response to strong deposition pulses. Here, the increase in I_{rel} typically begins at t or $t + 1$ and persists beyond a two-week time frame (Fig. 6.4). This extended response could be attributed to longer phytoplankton growth cycles in colder, nutrient-rich waters, which tend to be Fe-limited.

Across all regions, I_{rel} values prior to deposition events are generally similar to the values reported to $t - 1$ with non- or low statistical significance showing these differences. This highlights the significance of the increases seen from t onwards.

When conducting the same analysis for dust deposition, signals in oligotrophic regions are comparable to those seen with SFe deposition (Fig. A.19). On the other hand, in mid- to high-latitude regions, the signals associated with dust deposition are less prominent, highlighting the comparatively greater influence of SFe fluxes in these areas. Interestingly, in some areas, such as the oligotrophic Indian NH Ocean (encompassing the Arabian Sea and Bay of Bengal), a pronounced negative signal is observed at $t + 2$ and $t + 3$ after strong dust deposition events. This could suggest a potentially toxic response, such as an abrupt increase in ocean pH (Sarma et al., 2021), the grazing effects of higher trophic groups, or the impacts of lithogenic ballast. These mechanisms warrant further exploration to disentangle their contributions to the observed dynamics.

6.3.4 SChl responses to lower soluble iron deposition events

So far, the response to the top 10% deposition events has been analyzed. However, can responses to deposition events falling outside this top 10% also be detected? By maintaining the regional divisions used in the previous Section and computing ΔX_{rel} for deposition events categorized by percentiles, some clear regional patterns emerge (Fig. 6.5).

As expected, the strongest signal, with the highest ΔX_{rel} values and

Chapter 6. Impact of Soluble Iron Deposition Events on Subseasonal Chlorophyll Dynamics

statistical significance, is observed for the top 10% percentile. However, significant positive responses are also evident below this threshold in most regions. In mid- to high-latitude regions, significant positive ΔX_{rel} can be detected even for deposition events in the 40–50th percentile range. For instance, in the SH Atlantic, ΔX_{rel} increases progressively with higher percentiles, reflecting a robust response across a wide range of deposition intensities.

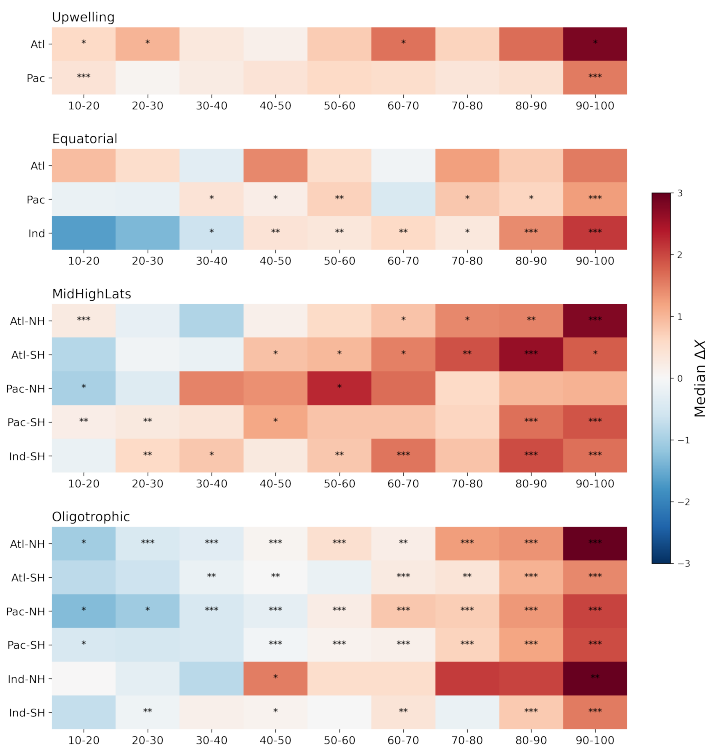


Figure 6.5: **SChl response to SFe deposition events by percentile.** Regional median surface chlorophyll (SChl) ΔX_{rel} values after soluble iron (SFe) deposition events divided by deposition percentiles. Significance levels (from Kruskal-Wallis testing) expressed by asterisks (***) for p-value ≤ 0.001 , ** for p-value ≤ 0.01 , * for p-value ≤ 0.05).

In contrast, in oligotrophic regions, significant positive ΔX_{rel} responses are only evident above the 50-60th percentile, and the magnitude of the response is generally lower compared to mid- to high-latitude regions. Furthermore, the difference between the signal from top 10% events and lower percentiles is more pronounced. A similar pattern is observed in equatorial regions, such as the Indian and Pacific Equatorial Oceans, where detectable responses at lower percentiles are weaker and less statistically significant.

The reason mid- to high-latitude regions exhibit significant effects at lower deposition rates can be attributed to their distinct oceanographic and biological characteristics. In these regions, even relatively small increases in SFe deposition can alleviate the existing Fe-limitation, triggering phytoplankton growth and biogeochemical changes. By contrast, in oligotrophic and equatorial regions, where the water column is often nutrient-depleted and stratified, stronger deposition events are required to overcome the severe nutrient limitation and produce detectable biological responses.

6.3.5 Strong deposition events characterization

This study has demonstrated the effects of strong SFe deposition events on SChl levels. The EC-Earth3-Iron dataset enables further characterization of these strong deposition events in terms of Fe sources (Fig. 6.6), deposition type (Fig. 6.7a), and the aerosol size range being deposited (Fig. 6.7b).

Dust sources dominate SFe deposition across all percentiles in most ocean regions, except in the Indian NH oligotrophic region, where fossil

Chapter 6. Impact of Soluble Iron Deposition Events on Subseasonal Chlorophyll Dynamics

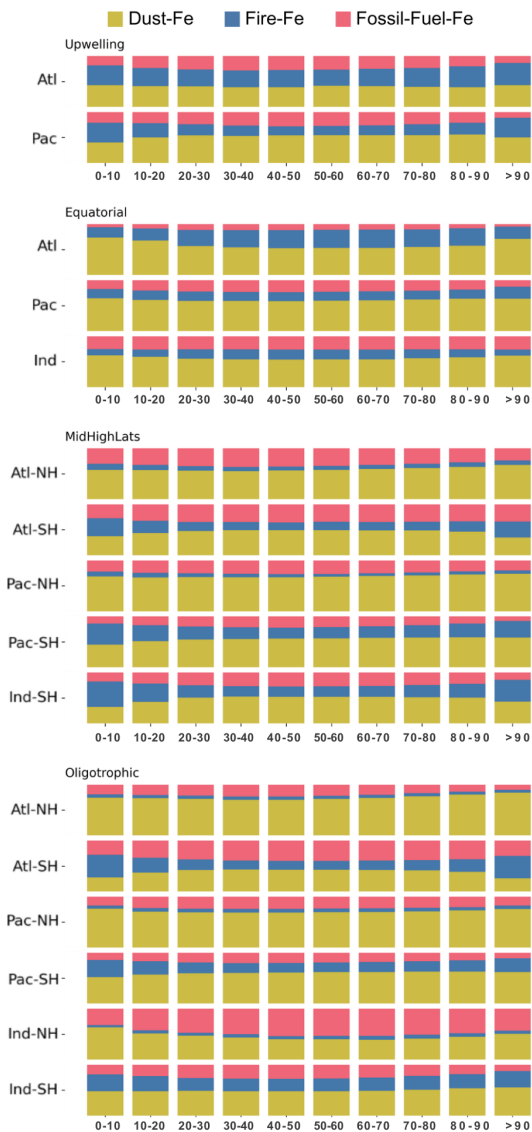


Figure 6.6: **Regional SFe source contribution by deposition percentiles.** Contribution of dust-iron (dust-Fe) (yellow), fire-Fe (blue) and fossil-fuel-Fe (pink) to soluble iron (SFe) deposition by ocean biome region and SFe deposition percentile.

fuels are the primary contributors. In regions with high deposition fluxes located downwind of major dust source areas, such as the North Atlantic, the top 10% deposition events exhibit a slight increase in the contribution of dust compared to other percentiles. Conversely, in regions where fires significantly contribute to the SFe deposition burden, the strongest deposition events show an increased contribution from these sources compared to lower-intensity deposition events.

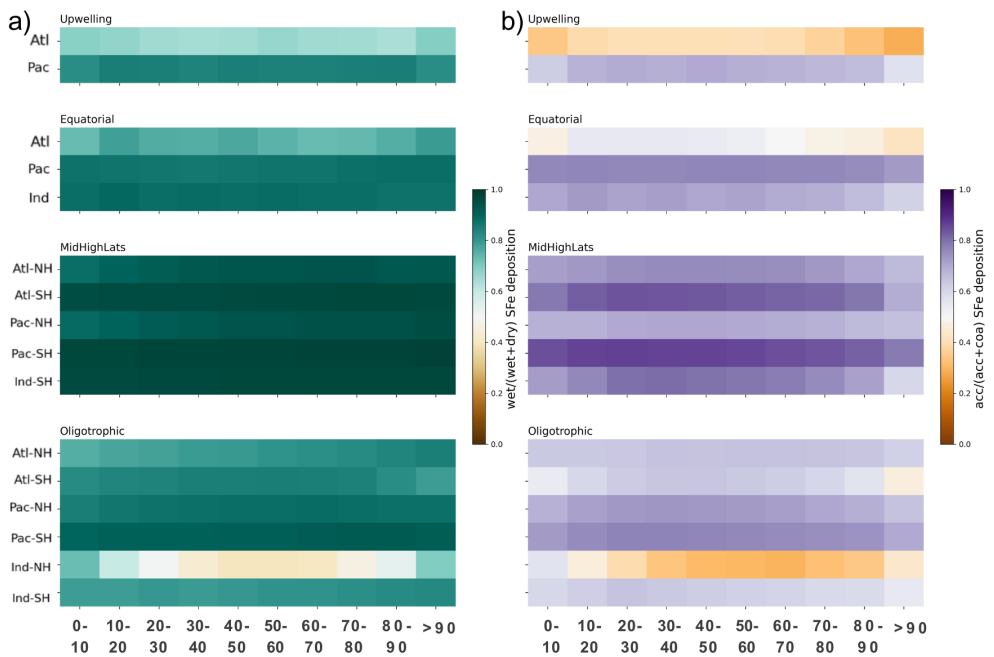


Figure 6.7: **Regional SFe wet vs dry and accumulation vs coarse mode deposition by deposition percentiles.** Fraction of wet to total soluble iron (SFe) deposition (a) and fraction of accumulated mode deposition over total SFe deposition (b) for each biome region and SFe deposition range.

In terms of wet or dry deposition types, wet deposition dominates across all deposition ranges in almost all regions, except the Indian NH oligotrophic ocean. A similar pattern is observed for the aerosol size

deposition mode, where the accumulation mode consistently dominates over the coarse mode across most regions and deposition ranges. However, mid- to high-latitude biomes show a stronger contribution of wet deposition in the accumulation mode. This dominance can be attributed to the fact that these regions are often located far from primary Fe sources. As a result, SFe deposition is characterized by long-range transport of smaller particles with longer lifetimes, which are more effectively deposited through wet deposition processes than by dry deposition.

Understanding how these differences in composition and deposition type differentially impact ocean biogeochemistry remains challenging, as it is difficult to disentangle these effects from the distinct underlying biome characteristics of each region. Nevertheless, the contrasts between the Indian NH oligotrophic ocean (Bay of Bengal and Arabian Sea) and other regions in terms of Fe source, deposition type, and aerosol size are striking. These differences may help explain the strong negative signals observed between 10 and 20 days after strong deposition events.

6.4. Conclusions

This study has demonstrated that pulsed strong SFe deposition events have widespread effects on surface ocean chlorophyll-a concentrations across a varying spectrum of ocean biomes.

The effects of aerosol deposition on ocean biogeochemistry exhibit a pulsed character in oligotrophic waters, where nutrient availability is typically low, and PP is often limited by nutrients like N or P. In these regions, aerosol deposition provides a sporadic influx of nutrients,

triggering brief phytoplankton blooms that quickly dissipate as the newly supplied nutrients are consumed. This leads to transient changes in biogeochemical processes. In contrast, in HNLC regions, where macronutrients like N are abundant but Fe is the limiting nutrient, aerosol deposition can have more enduring effects. The Fe supplied by strong deposition events stimulates phytoplankton growth over longer timescales, as the ecosystem responds more gradually to the alleviation of Fe limitation. These sustained responses can enhance carbon sequestration and alter biogeochemical cycles in a way that persists over weeks to months, reflecting the differing nutrient dynamics and biological responses between these two types of marine environments.

Satellite-derived chlorophyll data provide only a limited understanding of changes in ocean biogeochemistry. However, additional satellite ocean color products can help disentangle observed variations in chlorophyll. One such property, *bbp*, which is linked to phytoplankton C_{phyto} , is further explored here, showcasing negative regional signals coinciding with strong deposition events. However, the data coverage of *bbp* is limited, making it challenging to draw definitive conclusions about C_{phyto} changes following aerosol deposition. Further analysis using improved coverage data could enhance our understanding of the observed signals. Moreover, satellite-derived sub-products provide information on chlorophyll-a levels associated with different phytoplankton functional types (Xi et al., 2021, 2023). These datasets, if available at the required time frequency, could be further explored to determine whether aerosol deposition induces shifts in phytoplankton functional types.

This analysis is restricted to the surface. Yet, SFe deposition may

also induce temporal variations in Fe in the subsurface by several pathways. First, aerosol particles probably also dissolve as they sink in the water column. Second, some of the Fe that is supplied at the surface is scavenged, especially in high aerosol deposition regions, and is potentially released in the subsurface. Third, variations in the phytoplanktonic Fe/C ratios produced by varying surface Fe concentrations change the amount of Fe that is exported below the surface by the biological activity. This subsurface variability can then be transmitted to the surface by the ocean dynamics with a spatial and temporal lag. This highlights that for a comprehensive understanding of the fate of aerosol nutrient particles in ocean waters, in situ observations in combination with satellite data are needed.

Intraseasonal SChl variations may arise from processes operating across a wide range of spatial scales. These variations can be driven by intraseasonal basin-scale climate modes, such as the Madden-Julian Oscillation (Resplandy et al., 2009), synoptic atmospheric forcing from storms (Carranza & Gille, 2015; Fauchereau et al., 2011) and tropical cyclones (Menkès et al., 2016), or oceanic mesoscale and submesoscale processes (Lévy et al., 2018; Mahadevan et al., 2012; Pascual et al., 2017; Ruiz et al., 2019) operating on even smaller scales. Intraseasonal events, such as storms, often coincide with significant aerosol deposition events. However, this methodology does not fully disentangle the effects of aerosol nutrient supply from other storm-driven mechanisms, such as increased turbulence in the surface ocean caused by stronger winds. A complementary analysis of SST and MLD would be necessary to better understand these concurrent changes.

The characterization of strong SFe deposition events has revealed

significant regional differences in Fe sources, deposition types, and aerosol size ranges, with implications for their biogeochemical impacts. Dust-Fe dominates most ocean regions across all deposition percentiles, except for the Indian NH oligotrophic ocean, where fossil-fuel-Fe emerges as the primary contributor. Wet deposition and accumulation mode aerosols are consistently dominant across regions, especially in mid- to high-latitude biomes where long-range transport favors smaller particles deposited primarily through precipitation. These regional contrasts, particularly the distinct Fe source and deposition patterns in the Indian NH oligotrophic ocean compared to other biomes, suggest that the composition and transport pathways of aerosol Fe play a critical role in modulating the biogeochemical responses to strong aerosol deposition events. Future studies integrating in situ observations with detailed aerosol characterization will be essential to disentangle the complex interplay between aerosol deposition from different sources and ocean biogeochemistry responses.

The current analysis demonstrates measurable ocean biological responses to a wide dynamic range in atmospheric inputs. Although these responses are thought to represent only a modest contribution to total plankton stocks or annual NPP, they nevertheless are an important component of ocean production that is likely to change in the face of a warming planet.

CHAPTER 7

Pre-Industrial, Present and Future Atmospheric Soluble Iron Deposition Under CMIP6 Emissions

7.1. Introduction

While the present-day Fe cycle has been estimated and described in Chapter 5 and in numerous studies, changes in the atmospheric Fe cycle that have occurred over the industrial period or that are expected to occur over the 21st century have been less explored, and only with simple or intermediate-complexity schemes. Modelling studies focusing on the present day estimate a global atmospheric dissolved Fe deposition flux into the ocean in the range 0.1–0.8 Tg-Fe yr⁻¹ (Hamilton et al., 2020a, 2019; Ito et al., 2019; Myriokefalitakis et al., 2018; Scanza et al., 2018; Ito and Shi, 2016; Luo et al., 2008) (Table A.3). Some studies estimate that pre-industrial Fe would have been

at least 2 times lower, mainly due to lower emission of SO_4^{2-} and nitrate precursors leading to a decline in proton-promoted solubilization (Myriokefalitakis et al., 2015); other studies, however, point towards higher values (Hamilton et al., 2020a) due to a possible underestimation of wildfires in the pre-industrial era in commonly used emission datasets such as the CMIP6 inventory (Hamilton et al., 2018). Despite the large uncertainties, it has been accepted that the rise in anthropogenic combustion emissions since pre-industrial times has increased the Fe atmospheric burden along with atmospheric acidity due to a drastic increase in SO_2 emissions (Smith et al., 2004; Hand et al., 2012). Future projections are even more uncertain as anthropogenic and fire emissions depend on hypothetical future human activities and the impact of land-use change and climate change on dust emission sources and fires is complex to estimate (Mahowald et al., 2009; Harris et al., 2016).

This work aims to estimate the pre-industrial, present, and future atmospheric delivery of SFe to the ocean using the state-of-the-art ESM EC-Earth3-Iron (Myriokefalitakis et al., 2022). The atmospheric Fe cycle component in EC-Earth3-Iron incorporates numerous advances, including a detailed atmospheric Fe solubilization mechanism that accounts for complex multiphase chemistry driving aerosol acidity and an explicit representation of OXL. With these novel model capabilities, SFe deposition into the ocean is estimated, and aerosol acidity, OXL, and their effects on Fe solubilization are assessed, while quantifying the contribution of natural and anthropogenic sources under pre-industrial and present-day conditions and across a range of future scenarios based on the SSPs of the CMIP6 (Eyring et al., 2016) (see Section 4.4). Although the primary focus is on SFe and its drivers, the assessment of

aerosol acidity and OXL in future scenarios addresses aspects that have been understudied in previous literature, with implications extending beyond the Fe cycle.

7.2. Methods

7.2.1 Experimental setup

In order to consistently quantify OXL concentrations, aerosol acidity and SFe deposition for pre-industrial, present and future climates, five ensembles of atmosphere-only time-slice experiments are performed as explained in Section 4.5.2.

Time-slices were simulated to represent pre-industrial (PI) and present-day (PD) conditions, along with three different future scenarios based on Tier-1 CMIP6 SSPs (O'Neill et al., 2017) (SSP126, SSP245, and SSP370), which respectively represent forcing levels of 2.6, 4.5, and 7.0 W/m^2 by the end of this century. The future scenarios depict different pathways for socio-economic development and their potential impact on climate change (sec. 4.4). The PD simulation considers climatological conditions based on CMIP6 historical for the 1985-2014 period and serves as a baseline for the assessment of past and future changes. To reproduce the PI climatological conditions, CMIP6 historical information for the 1850-1879 period is used. For the future scenarios, the climatological period considered is 2070-2099 (Table 7.1).

Additionally, the sensitivity of future SFe deposition to potential increases in dust emission is explored. The dust emission scheme in EC-Earth is mostly sensitive to surface roughness and cultivated

Chapter 7. Pre-Industrial, Present and Future Atmospheric Soluble Iron Deposition Under CMIP6 Emissions

Table 7.1: **List of simulations for this chapter.** List of simulations executed in this Chapter with its time period, prescribed emissions, and regions where dust has been perturbed.

Experiment	Time period	Prescribed emissions	Dust-region pert.*
PI	1850	CMIP6 historical	-
PD	1985-2014	CMIP6 historical	-
SSP126	2070-2099	CMIP6 SSP1-2.6	-
SSP245	2070-2099	CMIP6 SSP2-4.5	-
SSP370	2070-2099	CMIP6 SSP3-7.0	-
SSP370-NAfr	2070-2099	CMIP6 SSP3-7.0	North Africa
SSP370-MEeast	2070-2099	CMIP6 SSP3-7.0	Middle East
SSP370-EAsia	2070-2099	CMIP6 SSP3-7.0	East Asia
SSP370-SH	2070-2099	CMIP6 SSP3-7.0	Southern Hemisphere
SSP370-NAm	2070-2099	CMIP6 SSP3-7.0	North America

* The regions perturbed in each experiment are defined according to the Hemispheric Transport of Air Pollution (HTAP) project (Koffi et al., 2016) and can be seen in Fig. A.23

fraction fields that consider exclusively intra-annual changes (Tegen et al., 2002). Therefore, dust projections with EC-Earth3-Iron depend primarily upon changes in simulated wind and soil humidity. To account for these uncertainties and eventual changes in source area extent in the future, an additional set of sensitivity experiments where dust emissions from different regions are perturbed are performed (see Section 4.5.3). Five simulations based on the SSP370 scenario for the period 2070-2099 are defined. In each simulation the dust emission flux from a different source region is doubled: North Africa (NAfr), Middle East (MEast), East Asia (EAsia), SH and North America (NAm). The regions selected are based on Koffi et al. (2016) and are shown in Fig. A.23a. Selecting the SSP370 scenario allows us to assess the impact of the increased dust emissions in an environment rich in iron dissolution precursors. SSP370 is characterized by large emissions of reactive gases and aerosols, and the aerosols' acidity and OX_L concentrations are expected to be the

highest within the scenarios here used. Under these conditions, the impact of doubling FeD emissions on the soluble iron deposition will be maximized and less limited by the availability of dissolution precursors than in the other scenarios. As such, the responses to the perturbations in dust sources will lie on the upper end of the potential variability and their signal will be easier to identify and characterize.

Regarding data analysis, multiple analytical approaches have been employed in this study. Yearly budget calculations are performed for variables such as Fe emission, solubilization, and deposition or OXL surface concentrations. The spread of the ensemble of those budgets (e.g., the difference between members of a simulation) is shown through the standard deviation (σ) with respect to the ensemble mean. Differences in fields of extensive variables (e.g., SFe deposition) are shown as relative differences in %, taking the PD simulation as reference. The statistical t-test with a 95% confidence interval is carried out over those relative difference fields, and only significant relative changes are presented. On the other hand, aerosol pH values presented in this work are a diagnostic product and are not the same as the ones used by the model itself (see Appendix A).

7.3. Results & discussion

7.3.1 Iron emissions

The present-day simulation (PD) estimates a mean annual Fe emission for the 1985-2014 period of 42 ± 5 Tg Fe/*yr* (Fig. 7.1). In agreement with previous studies (Luo et al., 2008; Mahowald et al., 2009), emissions

Chapter 7. Pre-Industrial, Present and Future Atmospheric Soluble Iron Deposition Under CMIP6 Emissions

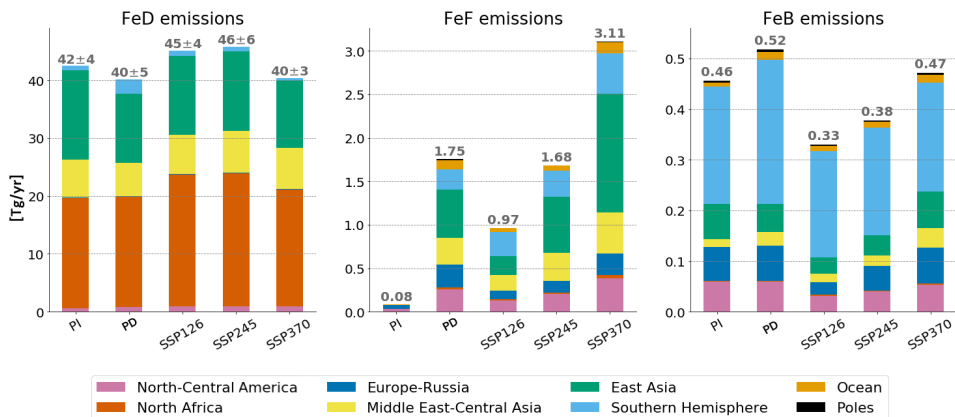


Figure 7.1: **Mean annual Fe emissions by source, region and scenario.** Mean annual emissions in Tg/yr of iron (Fe) from dust (FeD) (left panel), Fe from fossil fuels (FeF) (middle panel), Fe from biomass burning (FeB) (right figure) for each of the simulations considered. The different colors represent the contribution of the different HTAP regions considered to the total emission budget.

from dust sources represent a 94.6% of total Fe emissions, while anthropogenic combustion and biomass burning represent the remaining 4.2 and 1.2 %, respectively. The mean emission for each Fe source is 40 ± 5 Tg Fe/yr for FeD, 1.75 Tg Fe/yr for FeF, and 0.52 Tg Fe/yr for FeB (no uncertainty is shown for FeF and FeB emissions as the same emission climatology is used for the 30 simulated single years). These estimates are in good agreement with prior studies, where FeD emissions estimates range between 35 and 72 Tg Fe/yr, FeF between 0.7 and 7.2 Tg Fe/yr and FeB between 0.16 and 2.2 Tg Fe/yr (Rathod et al., 2020; Hamilton et al., 2020a, 2019; Scanza et al., 2018; Myriokefalitakis et al., 2018; Ito and Shi, 2016; Myriokefalitakis et al., 2015; Wang et al., 2015; Luo et al., 2008) (Table A.4).

FeD emissions contribute the most to the total Fe emission burden in all

simulations. Changes in FeD emissions between simulations follow the changes in dust emissions. Mean annual dust emission budgets range between 860 and 970 Tg dust/*yr* for the pre-industrial, present, and future estimates with some variability among runs of the same ensemble ($\approx \pm 100$ Tg Fe *yr*⁻¹) (Fig. A.24). These estimates fall in the lower limit of the simulated emission budget by other ESMs. This is partly due to current assumptions in the dust size distribution at emission and the lack of a super-coarse mode (Adebiyi and Kok, 2020; Wu et al., 2020; Gliß et al., 2021). In the simulations here shown, wind strength plays a dominant role in controlling the variability of dust emissions. Specifically, EC-Earth3-Iron estimates stronger winds over the SH in the PD simulation than in any future scenario, and consequently higher FeD emissions (Fig. A.25). This decrease is not noticeable at the global scale, where NH sources dominate. Particularly, the North African dust emissions increase under low to moderate RF levels by the end of the century (SSPs 126 and 245), while they remain similar to present-day estimates under the highest forcing level (SSP370), consistent with the changes in surface winds (Fig. A.25). Deposition records reveal a 55 ± 30 % increase in dust load for PD compared to PI, according to Kok et al. (2023), with Asian dust sources contributing significantly to this rise. Despite this, the simulation here shown and other climate models with prognostic dust cycles in the CMIP6 ensemble do not show this increase, indicating that dust emissions in models may not be sensitive enough to climate changes.

The PI simulation is characterized by an insignificant anthropogenic influence, as a result FeF emissions are negligible (in line with the limited anthropogenic emissions in the CMIP6 inventory for year 1850).

In the future, different directions depending on the scenario considered are found. SSP126 projects a decrease in FeF emissions compared to present day as a result of strong mitigation strategies (the emission budget is almost halved; 0.97 vs 1.75 Tg Fe/*yr*). The FeF global emission for scenario SSP245 is similar to the PD one (1.68 Tg Fe/*yr*), while for SSP370 a sharp increase in FeF emissions is projected (3.11 Tg Fe/*yr*). In particular, FeF emissions are projected to drastically increase along with population and anthropogenic activities in East Asia for the SSP370 scenario. The estimated range of future FeF emissions (0.97-3.11 Tg Fe/*yr*) lies in good agreement with what other studies have used (Hamilton et al., 2020a) (Table A.4).

FeB emissions for the PI simulation do not contribute much to the total Fe emission (0.46 Tg Fe/*yr*). This estimate is tightly linked to the prescribed fire emissions from the CMIP6 dataset (van Marle et al., 2017), which are likely underestimated (e.g., Hamilton et al., 2018). Recent works have shown that, in contrast to what was previously assumed, increased population during the historical period lead to a reduction in burned area (Andela et al., 2017). This stems from models not accounting for the effect of human-induced land use changes, fragmentation of ecosystems, as well as the implementation of fire management practices in some regions (Knorr et al., 2014; Andela et al., 2017), and hence not being able to capture the variations in fire activity from the observationally constrained present-day information towards the pre-industrial period. Model estimates that account for the human-driven decline in fire emissions during the historical period, place PI FeB emissions from 3 to 5 times higher than this work estimate, i.e, between 1.5 and 2.7 Tg Fe/*yr* (Hamilton et al., 2020a). Projected FeB

emissions decrease in the three future scenarios considered with 0.33, 0.38 and 0.47 Tg Fe/*yr* for SSP126, SSP245 and SSP370, respectively. This decrease is observed for all regions and scenarios, except for East Asia for the SSP370 scenario, which is consistent with the trends defined in the CMIP6 emission inventory. Another weakness of the CMIP6 future fire emission estimates is that they do not incorporate the potential impact of vegetation and climate changes in fire regimes. Neglecting these factors may result in underestimated projections of FeB emissions. For instance, this work estimates using CMIP6 data are approximately six times lower than those in Hamilton et al. (2020a), who used the CMIP5-RCP4.5 intermediate scenario and fire emissions that accounted for the impacts of climate and vegetation changes (Ward et al., 2012). All in all, CMIP6 and other estimates are highly uncertain, as the human-vegetation-fire-climate feedbacks are still not well understood. Multiple recent studies have tried to better constrain future fire emissions, but with diverging results (Yu and Ginoux, 2022; Hamilton et al., 2024a).

7.3.2 OXL concentrations and aerosol acidity

PD OXL primary emissions are estimated to be 0.36 Tg OXL/*yr*. The trend in OXL emissions for past and future projections with respect to the PD follows FeB emissions (Fig. A.24). PD OXL net chemical production is 9.2 Tg OXL/*yr*, which is in the lower range of what has been reported in previous studies, i.e., 9.0-27.3 Tg/*yr* (Lin et al., 2014; Liu et al., 2012; Myriokefalitakis et al., 2022). The PI simulation shows a drop in the annual global mean OXL net chemical production compared to PD estimates. However, an increase is seen for SSP245 and SSP370

where OXL net chemical production is especially boosted over areas where anthropogenic activities are expected to increase (e.g., East Asia, South America and South Africa) (Fig. 7.2). The primary mechanism of global OXL production is glyoxal oxidation ($\approx 74\%$), followed by glycolaldehyde ($\approx 11\%$), methylglyoxal ($\approx 8\%$), and acetic acid ($\approx 7\%$) (Myriokefalitakis et al., 2022). The primary sources of glyoxal is the secondary production through the oxidation of different volatile organic compounds of biogenic origin (mainly isoprene), followed by direct emissions from biofuel consumption and biomass burning. The observed differences in OXL net chemical production between the PI, PD, and future scenarios are consistent with changes in anthropogenic emissions between scenarios and regions.

Focusing in particular on SO_4^{2-} , which plays a key role in determining atmospheric acidity, it primarily forms in the atmosphere from gas-phase precursors, specifically SO_2 , despite direct emission from certain sources. SO_2 emissions are $128 \text{ Tg SO}_2/\text{yr}$ in the PD simulation, which represents a 9-fold increase over the PI period. SO_2 emissions dominated by the energy and industrial sector are expected to decrease overall as the energy sector gets decarbonized, with a more abrupt general decrease for SSP126 (i.e., the optimistic scenario, see Fig. A.24) (Gidden et al., 2019). This is true with the exception of some regions under the more pessimistic scenarios (e.g., the Middle East and Central Asia, North Africa and the SH for SSP370) where an increase in the industrial demand is hypothesized (Fig. A.24). SO_4^{2-} net chemical production for PD is $149.9 \text{ Tg SO}_4^{2-}/\text{yr}$ and follows the trends seen in SO_2 emissions; a 2.8-fold increase in PD estimates is seen compared with the PI while a decrease is projected for all three future scenarios, especially in the

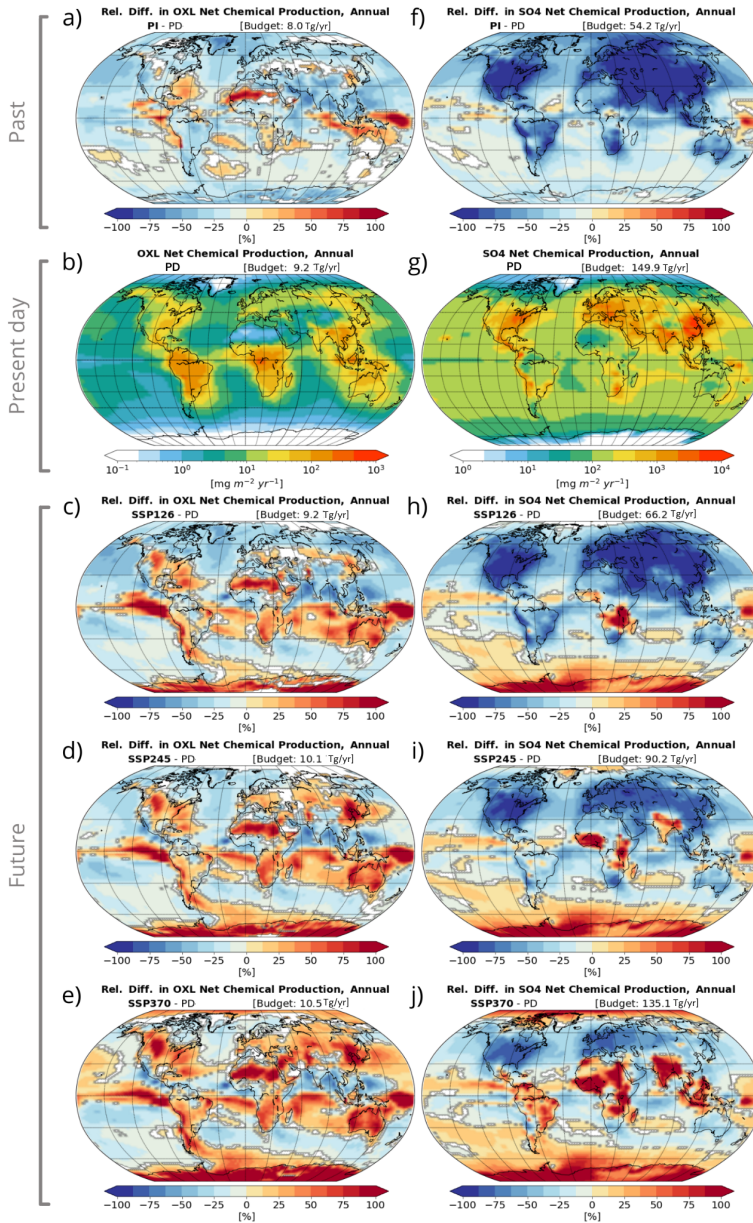


Figure 7.2: Net primary production of OXL and SO_4^{2-} across scenarios. Mean annual PD net primary production of oxalate (OXL) (b) and sulfate (SO_4^{2-}) (g) (in Tg/yr) and relative differences between other simulation fields and the PD (a,c,d,e for OXL and f,h,i,j for SO_4^{2-}). The mean annual global chemical production budget is shown in brackets.

NH, where projected air quality mitigation strategies are expected to effectively reduce SO_2 emissions in most NH countries (Fig. 7.2).

Aerosol pH and OXL concentrations, present notable differences among simulations (Fig. 7.3). Mean aerosol pH values are the lowest (i.e., more acidic) during the PD period, both in the accumulation and coarse modes, 1.69 and 3.61, respectively. The PI simulation, with a more pristine atmosphere, is the one presenting higher pH values (i.e., less acidic), 2.16 and 4.34 as global means for accumulation and coarse modes. Projections follow the SO_2 emission and SO_4^{2-} net chemical production trends discussed above, with the scenario representing a more sustainable pathway (SSP126) showing acidity values closer to PI estimates, 2.18 and 4.19, and the scenario with higher prescribed anthropogenic emissions (SSP370) showing values closer to the ones in the PD, 1.84 and 3.74 global pH means for accumulation and coarse modes, respectively.

Results indicate that the accumulation mode exhibits greater acidity across all simulations, especially over the tropical ocean, where values close to 1 are reached. While the majority of the sulfuric acid and SO_4^{2-} neutralize ammonia in the fine mode, cations present in the coarse dust, such as Ca^{++} , neutralize nitric acid in the coarse mode. Species found in sea salt and dust are then buffering the acidity of coarse aerosols, which are, for this reason, less acidic than fine ones (Fig. A.26). In the coarse mode, slightly acidic pH values are simulated over ocean due to sea salt species, whereas over continental regions the pH is lower (i.e., close to 1), particularly where anthropogenic activity is intense. Regionally, the SSP370 scenario projects an increase in acidity over developing regions (e.g., Africa, South America and the Middle East

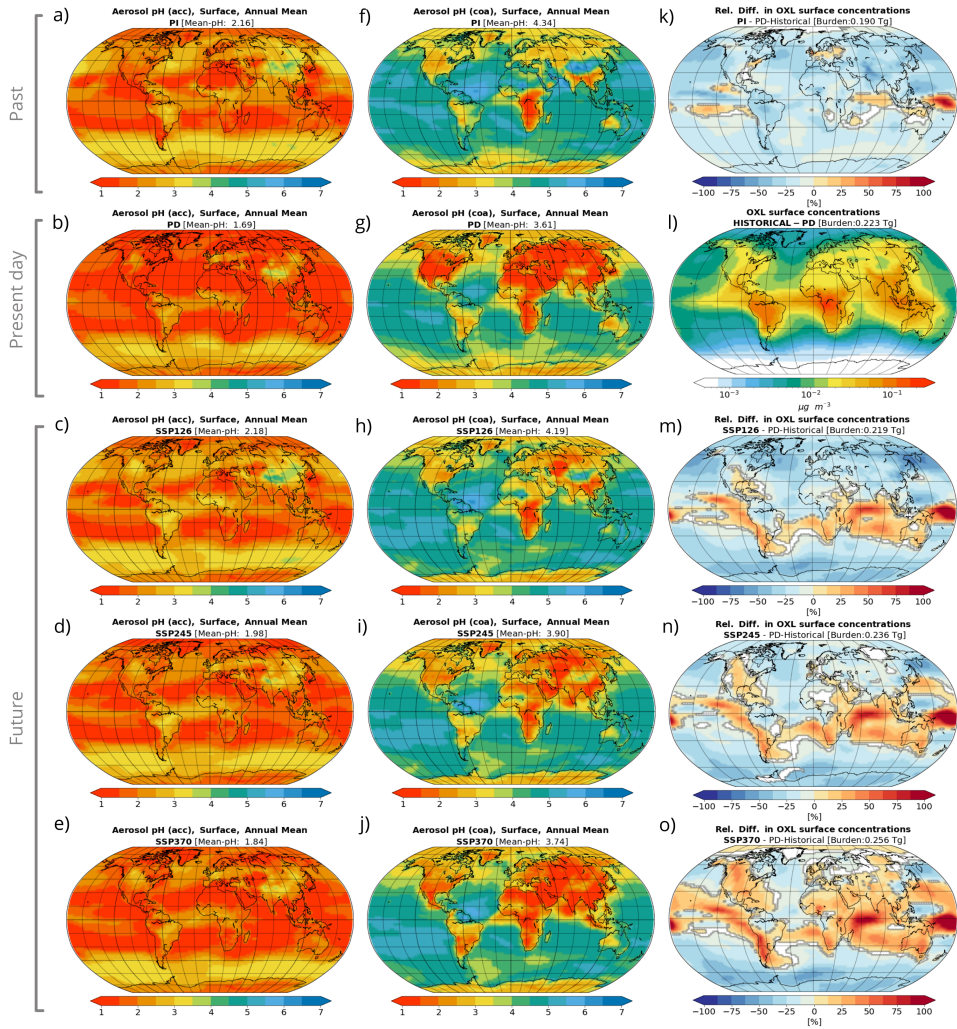


Figure 7.3: Aerosol pH and OXL surface concentrations across scenarios. Surface aerosol pH for the accumulation (left column, a-e) and coarse modes (middle column, f-j) of the model for all considered simulations (PI, PD, SSP126, SSP245 and SSP370, from top to bottom). Mean (area-weighted) pH values are shown for each simulation and mode. Oxalate (OXL) surface concentration for the PD simulation (l) and relative differences [in %] of other simulations compared to the PD one (right column; k,m,n,o). Mean annual OXL budget values are shown for each simulation and mode in Tg.

and Asia), where population and energy and industry requirements are expected to grow in the near future.

Present-day estimates of OXL (Fig. 7.3l) show maximum surface concentrations over major biomass burning sources such as Central Africa, South America and Indonesia, as well as OXL net chemical production (Fig. 7.2b), but also downwind of those sources (up to $0.2 \mu\text{g}/\text{m}^3$ on annual average) with a steeply decrease towards the poles. Overall, lower concentrations are found in the PI, with relative decreases between 10 and 30%, with except in certain equatorial regions of the Indian and Pacific Ocean, and Europe (Fig. 7.3k), where up to 100% higher concentrations are found. In the future projections, OXL sharply increases in the Indian Ocean and equatorial Pacific. Also, OXL is expected to increase over and downwind of South Africa, southern South America and Australia. Under SSP370, the increases extend over other areas such as the North American continent, North Africa and the Asian and European continent. As OXL has mostly a secondary origin, changes in OXL surface concentrations between simulations are fundamentally driven by changes in OXL net chemical production (Fig. 7.2a-e), which ultimately depends on the abundance of organic precursors.

7.3.3 Atmospheric Fe solubilization

Fe at emission is considered to be mostly insoluble; in EC-Earth3-Iron only 0.1% of the emitted FeD and 80% of the emitted Fe from shipping emissions are assumed to be soluble. In this Section, FeF and FeB are discussed together as Fe from those sources are considered to have the same dissolution rates and treated in the EC-Earth3-Iron solubilization

scheme as one pool (FeC) (see Section 4.2). For the PD, SFe emissions are 0.0425 and 0.00011 Tg/yr for FeD and FeC emissions, respectively. Additionally, 0.473 ± 0.013 Tg FeD/yr and 0.284 ± 0.016 Tg FeC/yr are dissolved in the atmosphere.

All in all, around 95% of atmospheric SFe results from atmospheric dissolution processes. FeD is primarily dissolved by acid dissolution, with a rate of 0.296 ± 0.007 Tg FeD/yr. Ligand-promoted dissolution additionally produces 0.138 ± 0.010 Tg FeD/yr and photo-induced processes have a small impact on the global dissolved Fe release from dust, with 0.039 ± 0.003 Tg FeD/yr (Fig. 7.4). On the other hand, the main dissolution path for FeC is ligand-promoted dissolution with a rate of 0.189 ± 0.004 Tg Fe/yr. Acidic and photo-induced dissolution each represent 17% of the FeC dissolution, with rates of 0.0478 ± 0.0011 Tg Fe/yr and 0.0476 ± 0.0011 Tg Fe/yr, respectively (Fig. 7.4). The primary mechanism for solubilizing FeC in the EC-Earth3-Iron model is ligand-promoted dissolution, which is consistent with the solubilization scheme proposed by the work by Chen and Grassian (2013) on which the model here used is based. This pathway is further fostered by the combustion activities emitting both FeC and OXL precursors, which results in the maximum values of OXL production (Fig. 7.2b) being spatially correlated with high solubilization values of FeC (Fig. A.27a-f). Nevertheless, these estimations of FeC solubilization represent an upper bound as recent experimental studies indicate a lower enhancement in Fe solubility than that reported by Chen and Grassian (2013) (Baldo et al., 2022).

Dissolution rates of FeC are 65% smaller in the PI scenario than in the PD. FeD dissolution is also smaller in the PI simulation, by 65% the

Chapter 7. Pre-Industrial, Present and Future Atmospheric Soluble Iron Deposition Under CMIP6 Emissions

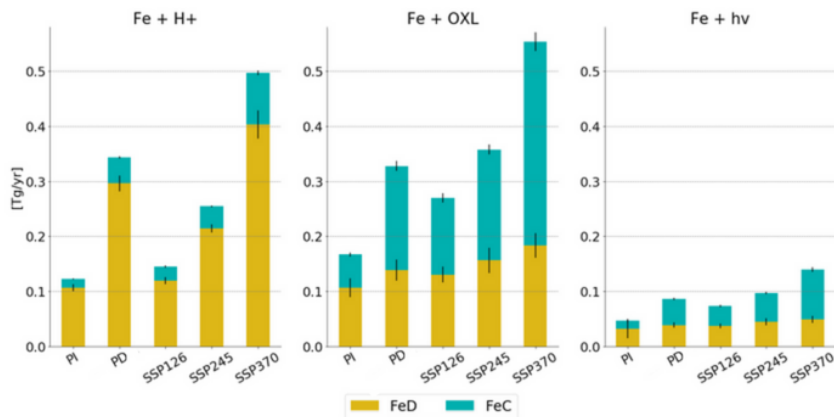


Figure 7.4: **Fe solubilization budgets across scenarios.** Iron (Fe) solubilization budgets for the different simulations and atmospheric processing mechanisms: acidic dissolution (left), oxl-promoted dissolution (middle), and photoreductive dissolution budgets (right). Solubilization of Fe from dust sources (FeD) is represented with the yellow-orange colour and solubilization of Fe from combustion sources (FeC) (i.e., both from biomass burning, FeB, and anthropogenic sources, FeF) is represented in blue-green colour. Black bars indicate the budget spread for the 30 ensemble members.

acidic dissolution and by 20% the OXL-promoted and photo-induced dissolution. The drop in Fe dissolution is mainly driven by a reduction in direct FeC emissions (75%) (Fig. 7.1) and a drop in OXL and SO_4^{2-} net chemical production ($\approx 13\%$ and $\approx 64\%$ respectively) (Fig. 7.2).

Different trends can be seen on the future scenarios of Fe dissolution compared to the PD. On the one hand, SSP126 shows a decrease in atmospheric Fe processing for both FeD and FeC, especially due to reduced acidic dissolution. Although FeD emissions in this scenario are 12.5% higher than in the PD, there is a relative reduction of nearly 60% in FeD acidic dissolution. The decrease is mainly driven by the drop in SO_2 emissions (Fig. A.24), leading to a less acidic atmosphere (Fig.

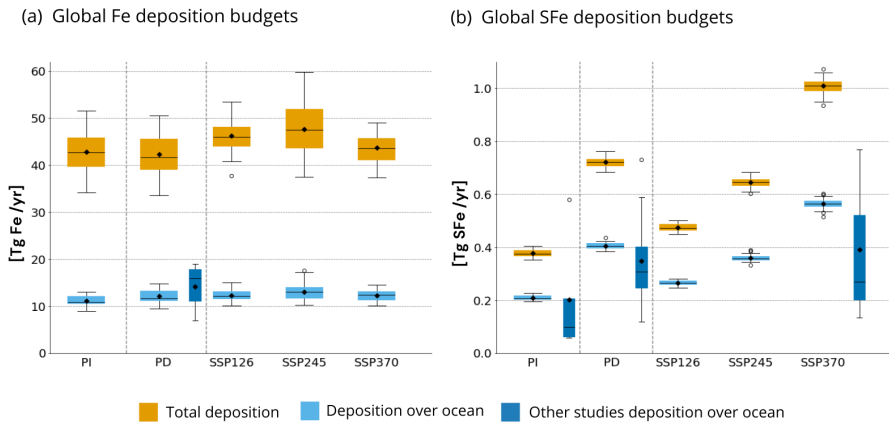


Figure 7.5: **Global Fe and SFe deposition across scenarios.** (a) Global total iron (Fe) deposition budgets (in orange, global deposition, in light-blue, deposition over ocean) for all simulations and (b) global soluble Fe (SFe) deposition budgets (in blue only deposition over ocean) for all simulations. Dark-blue boxes are built up from literature data of SFe deposition over the ocean (Table A.3).

7.3c and 7.3h). On the other hand, SSP245 estimates a 12% increase in OXL-promoted and photoinduced Fe dissolution, and a relative decrease of 26% in Fe acidic dissolution. The drop in proton-promoted dissolution is driven by a decrease in aerosol acidity (Fig. 7.3). The increase in OXL over some equatorial regions, where FeF emissions are projected to increase, leads to an enhanced ligand-promoted dissolution (Fig. A.27d). In SSP370, the scenario with higher NTCF levels projected, Fe dissolution increases for both FeD and FeC as a result of all processing mechanisms. The increase in FeC solubilization is especially abrupt compared to the PD, with values ranging between 91 and 98 % more for the different mechanisms. This results from a 78 % increase in FeF primary emissions relative to PD (Fig. 7.1), together with an OXL production and aerosol acidity increase around anthropogenic sources.

No substantial differences are evident when comparing the global solubilization budgets of the SSP370 scenarios with regionally perturbed dust emission with the base SSP370 simulation (Fig. A.28). Despite the large increase in global FeD emissions in some experiments, i.e., SSP370-NAfr ($\approx \times 2$), SSP370-EAsia ($\approx \times 1.3$) and SSP370-MEast ($\approx \times 1.2$), minor changes are seen in Fe solubilization budgets. This is explained by the increase in calcium carbonate, which buffers acidity and therefore limits FeD solubilization (Myriokefalitakis et al., 2022).

7.3.4 Soluble iron deposition and solubility

The Fe deposition in the PD simulation is 42 ± 5 Tg Fe/*yr*, with 12.1 ± 1.4 Tg Fe/*yr* deposited to the ocean. The SFe deposition is 0.721 ± 0.018 Tg SFe/*yr*, with 0.406 ± 0.011 Tg SFe/*yr* deposited to the ocean (Fig. 7.5). 70% of SFe deposited in the ocean comes from dust mineral sources, while the remaining 14 and 16 % come from anthropogenic combustion and biomass burning sources, respectively. Since FeD emissions represent $\approx 95\%$ of total Fe emissions (99.7% of directly SFe emissions), these results reflect the stronger atmospheric processing of FeC compared to FeD in present day conditions. As discussed in Section 7.3.3, this is due mainly to enhanced OXL-promoted dissolution in combustion aerosols. The Fe and SFe deposition budgets in the ocean along with contribution of each source to the total deposition are within the range of previous studies (Fig. 7.5 and Table A.3) (Hamilton et al., 2020a, 2019; Ito et al., 2019; Ito and Shi, 2016; Johnson and Meskhidze, 2013; Luo and Gao, 2010; Luo et al., 2008; Myriokefalitakis et al., 2020, 2018, 2015; Scanza et al., 2018).

Total Fe deposition budgets do not present significant differences among

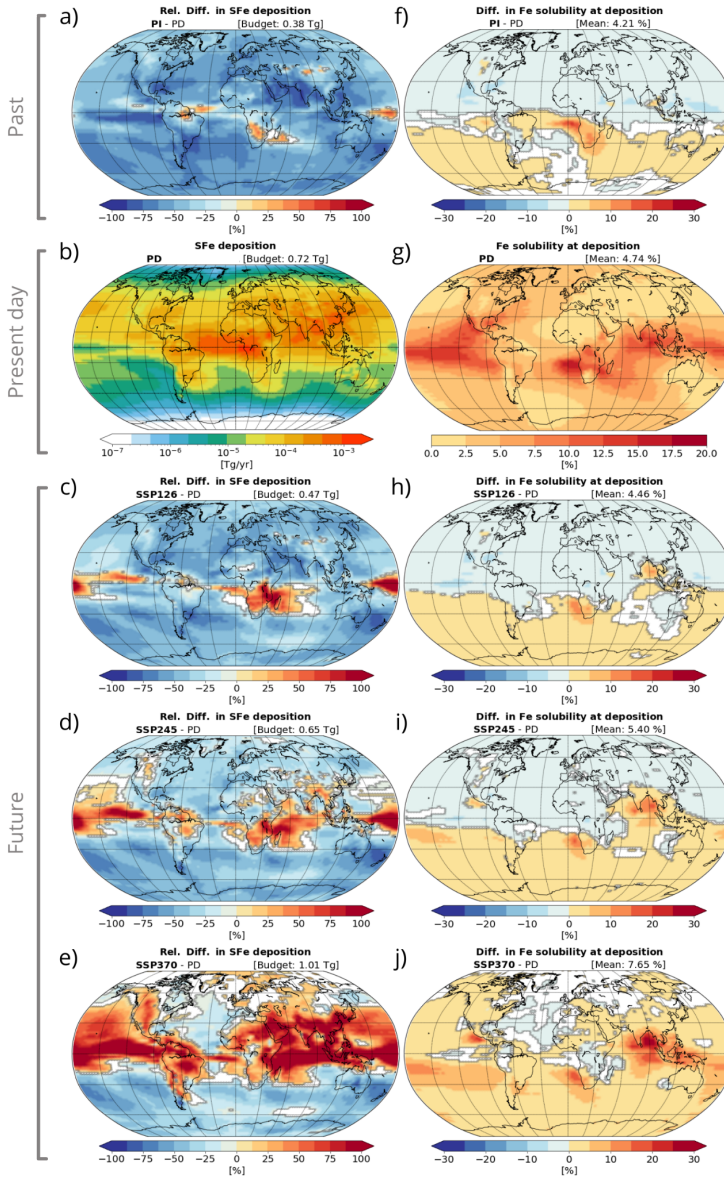


Figure 7.6: **SFe deposition and Fe solubility at deposition across scenarios.** Mean soluble iron (SFe) deposition (in Tg SFe/yr) for the PD simulation (b) and relative differences between other simulations and the PD (left column; a,c,d,e), iron (Fe) solubility at deposition (in %) for the PD simulation (g) and absolute differences compared to other simulations (right column; f,h,i,j). Mean annual SFe deposition budgets and mean solubility values are shown in the respective maps.

simulations (Fig. 7.5a), ranging between 42 and 47 Tg Fe/*yr*, and 11 and 13 Tg Fe/*yr* over the oceans. This follows from Fe emission shown in Fig. 7.1 being dominated by dust, whose global emission shows small variations between simulations. In contrast, SFe deposition budgets do show substantial variations among simulations with the lowest values reached in the PI, with 0.377 ± 0.015 Tg SFe/*yr* globally and 0.209 ± 0.009 Tg SFe/*yr* over ocean. The PI SFe deposition compares well with prior studies (Fig. 7.5b), except for Hamilton et al. (2020a) in which SFe deposition over the ocean more than doubles the estimates here shown, most likely due to the use of a different fire emission dataset (Hamilton et al., 2018).

A decline in SFe deposition is observed for the SSP126 and SSP245 scenarios compared to PD, with 0.474 ± 0.013 Tg SFe/*yr* (0.265 ± 0.009 Tg SFe/*yr*) globally (over ocean) for SSP126, and 0.646 ± 0.019 Tg SFe/*yr* (0.360 ± 0.013 Tg SFe/*yr*) for SSP245. The projected reductions under these two scenarios are consistent with the drop in atmospheric Fe solubilization due to a decrease in SO₂ emissions and hence a decrease in aerosol acidity (see Section 7.3.3). SSP370 scenario shows a clear increase in SFe deposition in comparison to all other scenarios, with 1.01 ± 0.03 Tg SFe/*yr* (0.56 ± 0.02 Tg SFe/*yr*) globally (over ocean). SFe deposition increases with increasing NTCF, and is almost doubled for SSP370 with respect to SSP126, while the SSP245 deposition falls in the middle. Although studies addressing Fe deposition in the future are limited, the estimates from the different scenarios presented here also fall within the range of values reported in previous literature (Table A.3).

PD estimates show maximum values of SFe deposition near the

equatorial Atlantic downwind of dust mineral and biomass burning sources, and the north coast of the Indian Ocean where Fe comes from dust mineral sources and anthropogenic combustion (Fig. 7.6b). In HNLC regions, such as the SO, the SFe deposition is lower than over the rest of the globe. The maximum solubility of Fe (i.e., the fraction of SFe over total Fe) at deposition ($\approx 20\%$) occurs downwind of South African biomass burning sources, East Asian anthropogenic combustion sources, and remote equatorial regions of the Pacific, dominated by long-range transport of dust (Fig. 7.6g). The higher solubility of Fe deposited over ocean compared to land is attributed to the longer lifetime of Fe-aerosols reaching the ocean, being thus more exposed to atmospheric processing. The PI simulation shows globally lower SFe deposition than the PD, except for some areas like South Africa (Fig. 7.6a) where higher biomass burning emissions affect the solubility levels. Future scenarios show a decrease in SFe deposition in mid- and high-latitudes, but an increase in equatorial regions such as the equatorial Pacific, Atlantic and Indian Ocean. Those increases are sharper and have a broader extension for SSP370, which is the future scenario with higher FeF emissions, aerosol acidity and OXL concentrations (Fig. 7.6e).

Solubility increases only in the SO and some regions of the Indian Ocean (e.g., the Bay of Bengal) for SSP126 and SSP245, while for SSP370 solubility increases in all regions but the North Atlantic. The increase in solubility for future scenarios could be driven by a change in Fe source contribution, likely related to a higher contribution of more labile Fe sources such as biomass burning and anthropogenic combustion. Those differences are reflected in the source contribution

Chapter 7. Pre-Industrial, Present and Future Atmospheric Soluble Iron Deposition Under CMIP6 Emissions

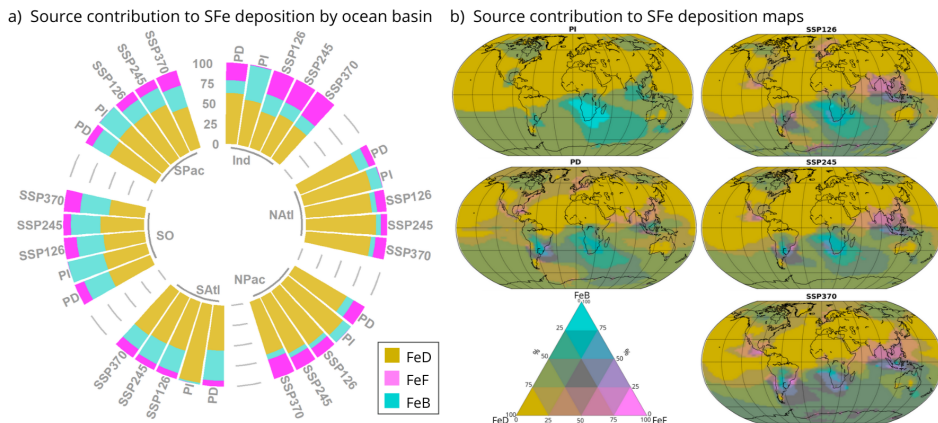


Figure 7.7: Source contribution of SFe deposition across scenarios and ocean basins. a) Source contribution (%) to soluble iron (SFe) deposition by ocean basin. Yellow indicates SFe from dust sources (SFeD), pink, Fe from fossil fuels (SFeF) and blue, Fe from biomass burning sources (SFeB). b) Source contribution to the SFe deposition flux at each grid cell where pure yellow indicates that $\approx 100\%$ of deposited SFe is SFeD, pure pink indicates $\approx 100\%$ of deposited SFe is SFeF and pure blue shows that $\approx 100\%$ of deposited SFe is SFeB; other colours represent the different mixtures of sources.

to SFe deposition for the different scenarios (Fig. 7.7). In line with the emissions, the contribution of anthropogenic sources to SFe deposition is negligible, but the contribution from biomass burning sources is particularly high, especially in the SH. Overall, the NH SFe deposition is dominated by dust in all scenarios, although in some areas, such as the North Pacific or the North Indian Ocean, there is an increase in anthropogenic contribution for future scenarios, especially for SSP370. Moreover, for SSP370 the dust contribution is below 50% for the Indian and SO, which does not happen in any other scenario and basin.

Doubling dust emissions per region under SSP3-7.0 conditions causes a slight increase in global SFe deposition independently of the perturbed

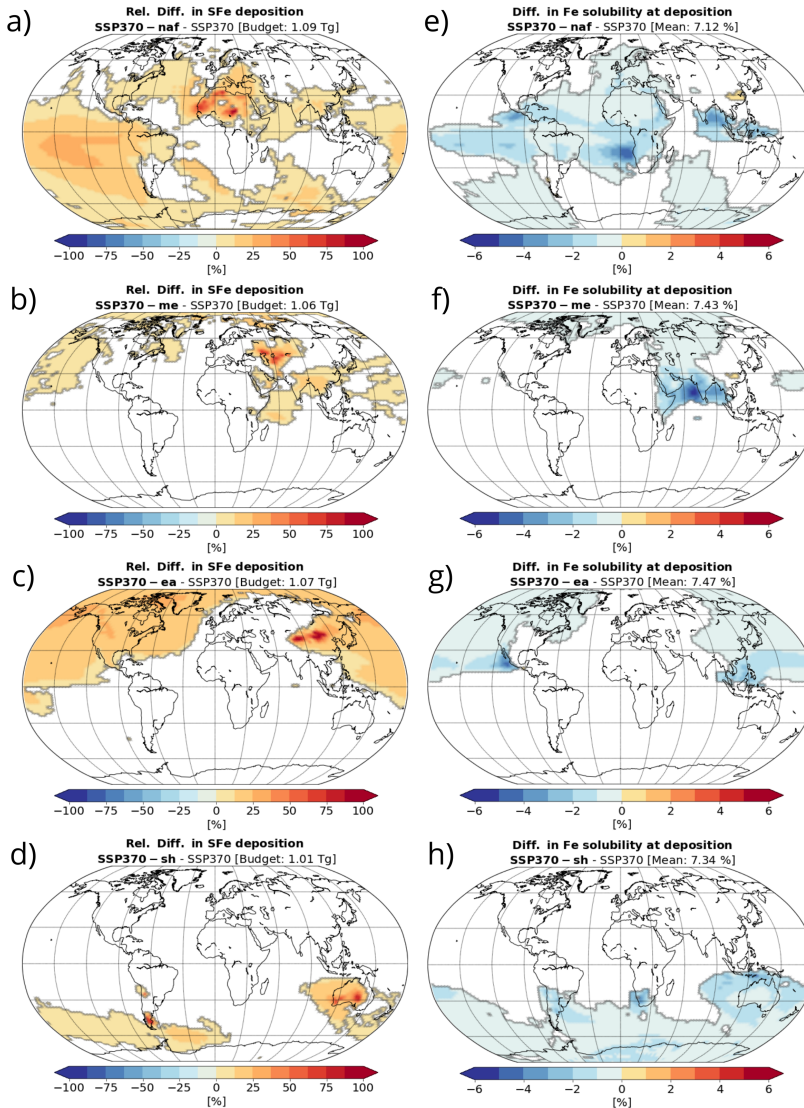


Figure 7.8: **Changes in SFe deposition due to shifts in dust emission.** Relative differences between soluble iron (SFe) deposition of SSP370 perturbed dust scenarios and SSP370 base scenario (left column). Absolute differences in Fe solubility at deposition (%) between SSP370 perturbed dust scenarios and SSP370 base scenario (right column). From first to last row the regions perturbed are: North Africa (NAfr), Middle East (MEast), East Asia (EAsia) and Southern Hemisphere (SH). Mean SFe deposition budgets and solubilities are shown within each scenario.

region, except for the North American sources, which does not induce any significant changes (Fig. 7.8a-d). However, those increases are more relevant in some regions especially downwind the perturbed sources. Perturbing North African dust sources causes a broader impact than changes in any other source, and leads to relative increases of up to 25% in SFe deposition with respect to the baseline SSP370 scenario in remote regions of the SH. In particular, EC-Earth3-Iron shows that SFe deposition in HNLC regions, such as the SO and the equatorial Pacific, is sensitive not only to changes in Australian or South American dust sources, but also to changes in North African sources. In all examined perturbation scenarios, a reduction in solubility was observed in proximity to the disturbed sources. Such an outcome is expected when dust emissions rise due to two primary factors. Firstly, Fe from dust sources is known to have relatively slower solubilization rates than other sources, implying that when its contribution to Fe deposition increases, Fe solubility at deposition decreases. Secondly, dust particles include calcium carbonate, which buffers acidity, thereby limiting the solubilization process.

7.4. Conclusions

Changes in climate and emissions can substantially modify atmospheric aerosol acidity, OXL production, and the strength and distribution of SFe deposition. Estimating these changes is crucial to assess future marine NPP and carbon and N cycles. Here, the past, present and potential future SFe deposition with an ESM (EC-Earth3-Iron) that is equipped with a detailed representation of atmospheric Fe dissolution

(Myriokefalitakis et al., 2022) has been characterized. In this way, the SFe deposition in EC-Earth3-Iron is expected to respond more realistically to changes in climate and emissions. The experimental setup covers the PI period, the PD, and a range of possible future climates following different CMIP6 emission scenarios. These scenarios cover from substantially reduced anthropogenic emissions, associated with very ambitious mitigation strategies, to large increases in emissions related to a growing population, especially in low- and middle-income countries, and a resurgence of coal dependence. The new model capabilities allow us to predict not only iron from different sources (FeD, FeF, and FeB) but also the precursors and processes controlling iron dissolution explicitly and interactively under changing climate conditions and emission levels.

Based on the calculations here presented, the SFe deposition to the ocean has doubled since the early pre-industrial (PI) era, with values of 0.406 ± 0.011 Tg SFe/*yr* and 0.209 ± 0.009 Tg SFe/*yr* for the present day and PI period, respectively. This trend is consistent with earlier studies (Hamilton et al., 2020a; Ito and Shi, 2016; Myriokefalitakis et al., 2015). The increase in SFe deposition since the PI can be attributed to a six-fold rise in fossil fuel emissions, which has led to an increase in FeF emissions and a rise in acidic solubilization in the atmosphere due to elevated SO₂ emissions. An increase in global SFe deposition of 40% by the late 21st century relative to PD is projected under the low mitigation scenario SSP370, while decreases of 35% and 11% are projected under the optimistic SSP126 and business-as-usual SSP245 scenarios, respectively. In all simulations, total Fe emissions are dominated by dust sources with a contribution above 90%. Dust

sources dominate as well SFe global deposition, but the contribution of FeC aerosols to SFe ($\approx 30\%$ during the PD) is enhanced relative to emissions as atmospheric processing is especially efficient for FeC aerosols. In all simulations, ligand-promoted dissolution is identified as the main FeC solubilization pathway, while proton-promoted dissolution is the primary pathway for FeD.

As ligand-promoted and proton-promoted dissolution are driven by aerosol acidity and OXL levels respectively, changes of those variables are in this work explored. Specifically, during the PI, low acidity levels (high pH) and OXL concentrations were observed, with a 15% reduction in OXL surface concentrations relative to the PD. While for the future, under the SSP370 scenario, OXL concentrations are projected to increase, with a 15% rise in OXL surface concentrations compared to PD and acidity levels are comparable to PD ones.

Dust sources dominate SFe deposition in the NH and globally. However, biomass burning and anthropogenic combustion emissions have a more crucial role in the SH. Anthropogenic combustion emissions do not contribute during the PI, but show significant contributions in the PD and future scenarios over the East Asian coast, Central American coast, and part of the South American region. SSP370 is the future scenario with the highest contribution of anthropogenic combustion sources to SFe deposition (especially in the Indian ocean). Biomass burning emissions dominate along the Southern African coast for all scenarios, especially in the PI. This shows that although dust sources are dominant, combustion sources are not at all negligible in regions such as the SO, known to be HNLC regions.

Results suggest potentially large differences in the ocean response among future scenarios. However, there are patterns shared among all future scenarios that could have important implications for the ability of the ocean to capture carbon in the future. All future scenarios show a decrease in SFe deposition over the Fe-limited SO and an increase over the equatorial Pacific, also known as a HNLC region. The net effect of these changes on global carbon capture remains uncertain. Further analyses are planned, using the SFe deposition fields in a biogeochemistry model to investigate regional and global ocean NPP changes associated with future scenarios.

Past and future projected emissions are very uncertain and need further investigation. Recent studies suggest that CMIP6 probably underestimates PI fire emissions (Hamilton et al., 2019), and others also suggest large uncertainties in future fire emission estimates as the impact of climate change on natural fire activity is neglected in current CMIP6 emission trajectories (Yu and Ginoux, 2022; Hamilton et al., 2024a). Such uncertainties in fire emissions may directly impact the Fe emission burden and its distribution together with the burden of precursors of OXL and, therefore, impact Fe dissolution. This might leave the pre-industrial and future SFe deposition estimates shown in this work at the lower end of estimates. In Chapter 8, this uncertainty will be further explored.

On the other hand, potential changes in the spatial extent of dust sources due to changes in vegetation (Mahowald, 2007), land use (Ginoux et al., 2012), and biocrusts (Rodriguez-Caballero et al., 2022) (see Section 1.6.1.1) are either poorly considered or not considered at all in ESMs. As seen in the perturbed dust experiments, HNLC regions such as the

Chapter 7. Pre-Industrial, Present and Future Atmospheric Soluble Iron Deposition Under CMIP6 Emissions

SO and equatorial Pacific could be very sensitive to those changes in dust emissions. Dust emissions associated with wildfires, where strong, turbulent fire-related winds most likely raise dust (Hamilton et al., 2022; Wagner et al., 2018) (see Section 1.2.3), are largely disregarded in current models. Additionally, by destroying vegetation, wildfires leave a bare source that often becomes a source of dust emission (Yu and Ginoux, 2022). Variations in these climate-sensitive yet unaccounted emissions could alter SFe deposition. Future observational and modeling studies should focus on better characterizing the evolution of fire and dust emissions and their interaction with other Earth System components to ultimately better represent the Fe cycle.

CHAPTER 8

Impact of future climate-driven fires on soluble iron deposition and oceanic productivity

8.1. Introduction

Wildfires are a crucial component of the Earth System, connecting the biosphere, hydrosphere, lithosphere, cryosphere, and atmosphere. They affect vegetation structure, alter the energy, water, carbon, and biogeochemical cycles, and change the composition of the atmosphere, which impacts the quality of the air and water (Bond et al., 2005; Bowman et al., 2009; Voulgarakis and Field, 2015; Senf et al., 2023; Ball et al., 2021). Although often viewed as carbon sources (Byrne et al., 2024), fires play essential ecological roles and can even enhance carbon capture through regrowth and nutrient cycling (Pausas and Keeley, 2019; Bowman et al., 2009). Downwind, fires supply nutrients, including

SFe, N, and P, which can stimulate marine productivity (Ardyna et al., 2022; Barkley et al., 2019; Guieu et al., 2005), potentially impacting carbon export.

Recent shifts in fire regimes reflect the complex interplay of climate change, human land use and ecosystem dynamics (Pechony and Shindell, 2010; Bowman et al., 2011). Over the past two decades, global burned area has declined by $\approx 25\%$, mainly due to the conversion of natural grasslands to agriculture, particularly in African savannas (Andela et al., 2017; Jones et al., 2022). However, wildfire frequency and severity have increased, especially at mid-to-high latitudes (Westerling et al., 2006; Dennison et al., 2014; Jolly et al., 2015; United Nations Department of Economic and Social Affairs et al., 2021; Zheng et al., 2021; McCarty et al., 2021), due to changes in climate. Consequently, global fire emissions have remained relatively constant (Zheng et al., 2021). In this context, understanding future fires' potential influence on marine biogeochemistry—particularly through SFe deposition, which can stimulate phytoplankton growth in Fe-limited areas—is of growing interest (Hamilton et al., 2020a; Riera and Pausas, 2023). Projections of future fire impacts, however, remain uncertain due to limited understanding of the interactions between human influence, climate, and fire dynamics (Hamilton et al., 2018; Li et al., 2019).

Recent studies of extreme fires highlight their potential impact on ocean productivity. The 2019–20 Australian fires led to phytoplankton blooms far exceeding the climatological mean in downwind regions (Tang et al., 2021; Perron et al., 2022; Wang et al., 2022b; Nguyen et al., 2024). Similarly, intense Siberian fires have been shown to increase SFe

deposition significantly in the Pacific Ocean (Ito, 2011). Fires are an important source of SFe compared to dust (Barkley et al., 2019; Ito et al., 2019), as fire Fe dissolves more readily in the atmosphere due to acidic and organic compounds in smoke plumes (Ito et al., 2019; Paris et al., 2010; Myriokefalitakis et al., 2022). As it reaches Fe-limited areas distant from the primary dust sources, Fe from fires may contribute to higher carbon export efficiency than Fe from lithogenic sources (Hamilton et al., 2020a; Ito et al., 2020).

Fe-limited ocean regions, spanning the subpolar North Pacific, SO, eastern Equatorial Pacific, and summer high-latitude North Atlantic, make up one-third of the global ocean (Hamilton et al., 2023; Browning and Moore, 2023; Ryan-Keogh et al., 2013). Even small increases in SFe deposition in these HNLC regions can boost productivity, alter community composition, and enhance carbon sequestration (Browning and Moore, 2023; Ryan-Keogh et al., 2013). Notably, the high-latitude North Atlantic and SO are particularly efficient at carbon uptake and long-term OC storage (Baker et al., 2022; Ricour et al., 2023; Achterberg et al., 2018; Siegel et al., 2023), making any shifts in SFe flux to these areas especially impactful.

Assessing the impact of future fire regimes on ocean health requires a global climate modeling framework. The SSP scenarios from the CMIP6 (as used in Chapter 7) offer fire emission projections linked to human activities, but they disregard climate-driven changes in natural fire activity (Guivarch et al., 2023). Fire-enabled vegetation models within ESMs can address this gap, simulating fire dynamics based on factors like temperature and precipitation. By combining SSP data with these ESM projections, fire scenarios shaped by both socioeconomic and

climate change influences can be better understood (Hamilton et al., 2024a).

This study builds on the findings of Chapter 7, which analyzed the future SFe deposition using CMIP6 emission inventories under SSP scenarios. Here, this analysis is extended by incorporating novel projections of fire emissions that explicitly include climate-driven changes in fire dynamics (Hamilton et al., 2024a) (see Section 8.2.1) to assess, for the first time, how combined anthropogenic and climate-driven factors affect future Fe emissions from fires and atmospheric SFe deposition to the global ocean. Additionally, the inclusion of a second ESM in this analysis, CAM6-MIMI (Hamilton et al., 2019), alongside EC-Earth3-Iron (Myriokefalitakis et al., 2022), allows for a multimodel approach, providing a more robust and comprehensive assessment of future Fe emissions and atmospheric SFe deposition. Three CMIP6 SSP scenarios, SSP126, SSP370, and SSP585, which span a range of mitigation and emission trajectories are explored. This analysis first isolates the future effects of these previously unaccounted Fe emissions from climate-driven fire changes relative to changes in other Fe sources across scenarios using atmosphere-only simulations. It also examines how future climate conditions may additionally alter SFe deposition by impacting atmospheric Fe dissolution and deposition dynamics. Potential significant increases in future Fe emissions from climate-driven fires in the northern high latitudes are here demonstrated. Key oceanic regions highly susceptible to these changes are identified by estimating changes in the SFe impact on marine productivity, with the high-latitude North Atlantic emerging as an area significantly affected. The study's framework also

assesses which factors, either current Fe cycle uncertainties or policy efficacy, most affect SFe deposition over HNLC regions. This allows us to highlight the importance of comprehensive, interdisciplinary approaches in climate impact assessments with the final aim of better informing CMIP efforts and future policy.

8.2. Methods

8.2.1 A new future fires dataset

The SSP emission projections from the sixth phase of the CMIP6 (as used in Chapter 7) provide a key dataset for studying fire regime changes over the 21st century. These SSP scenarios, developed through Integrated Assessment Models (IAMs), translate socioeconomic narratives into spatiotemporally resolved future fire emissions under various climate mitigation levels (Guivarch et al., 2023) (see Section 4.4). However, two limitations arise: SSP scenarios exclude the influence of climate change on natural fire activity (i.e. climate-driven fire changes), and each SSP relies on a different IAM, introducing diverse assumptions about the relationship between socioeconomic factors and fire emissions over time and space.

In contrast, fire-enabled vegetation models within ESMs can simulate how fire regimes respond dynamically to climate factors like temperature, humidity, precipitation, vegetation distribution, and fuel load. Including an interactive fire model in this framework enables more accurate predictions of fire behavior as influenced by climate.

A new methodology integrates data from the SSP dataset (only

accounting for anthropogenic fire changes) with CMIP6 ESMs projections (accounting for climate-driven fire changes) to produce monthly emission estimates for each decade throughout the 21st century (Hamilton et al., 2024a). This approach combines the strengths of both datasets, capturing anthropogenic and climate-driven changes in fire regimes while aligning with present-day satellite-derived estimates.

In this sense, anthropogenic fire changes are here defined as those caused by the direct impact of human activities on the land surface, such as land-use changes, land management, and accidents (Archibald et al., 2012). These are largely influenced by economic and demographic factors (Andela et al., 2017). In contrast, climate-driven fire changes are those occurring due to increasingly favorable fire weather conditions, such as low humidity and high temperatures. It is here acknowledge that changes in these climatic variables, and consequently climate-driven fire changes, are primarily influenced by anthropogenic climate change.

The generation of this emission dataset involves three main steps. Firstly, information from several CMIP6 climate models with interactive fires is collected as an alternative to the SSP emission inventories. In those models, unlike in the SSPs emission inventories, climate change impacts on fire activity are considered. A multi-model mean of fire emissions in each model grid cell is computed using a set of CMIP6 model outputs that incorporate interactive fires; the Community Earth System Model v2 (CESM2) (Danabasoglu et al., 2020), the CESM2 Whole Atmosphere Community Climate Model (CESM2-WACCM) (Danabasoglu et al., 2020), the Norwegian Earth System Model Medium atmosphere-Medium ocean resolution (NorESM-MM) (Seland et al., 2020), the CNRM-ESM2-1 (S  ferian et al., 2019), the Max Planck Earth

System Model v1.2 Lower Resolution (MPI-ESM1.2-LR) (Mauritsen et al., 2019), and the EC-Earth3-Veg (Döscher et al., 2022). Among these, three ESMs (CESM2, CESM2-WACCM, and NorESM-MM) use the same Community Land Model version 5 (CLM5) (Lawrence et al., 2019). To prevent any bias towards a CLM5 representation of vegetation and fires, the mean of these three ESMs is initially computed.

Agriculture, deforestation, and peat fires are added to the aforementioned ESM output datasets from the SSP datasets (van Marle et al., 2017), as these factors are not considered in the CMIP6 ESMs. However, the SSP dataset does not isolate deforestation fires, which could lead to double counting if added directly. To mitigate this, in tropical regions, peat and agricultural fires are assumed predominant, making the SSP estimates for these regions more reliable than those from the CMIP6 ensemble. By combining these two sources of information, a future fire emission dataset that accounts for both climate-driven and anthropogenic factors is created.

Finally, to produce a harmonized dataset with present-day estimates based on observations, each model dataset is bias-corrected towards the present-day (2001-2011 decade) satellite-derived Global Fire Emissions Database, Version 4 (GFED4s) dataset (Randerson et al., 2017). Although the existence of other satellite fire retrievals is here acknowledged, GFED4s is chosen here as the observational reference, as is the one used in CMIP6 to estimate present-day fire emissions (van Marle et al., 2017), and hence used there as a departure point for the SSP projections. Following the approach described in Hamilton et al. (2022), the ratio in monthly mean emissions within 20 regions, based on GFED region definitions with additional subdivisions mainly

reflecting similarities in fire behavior (Werf et al., 2006), is calculated between each of the four fire model emission datasets and that of a GFED4s-derived present-day emission climatology. The regional fire model emission biases are assumed to persist and remain constant through time. Therefore, the regional corrections to the ensemble of modeled future fire emissions for each decade in the 21st century are propagated.

The resulting dataset provides monthly mean carbon (as CO₂) emissions for each decade (units: kg C m⁻² s⁻¹ or kg C m⁻² month⁻¹). To convert to aerosol emissions, the CO₂ emissions are first backward converted to the mass (kg) of biomass burned, assuming 450 g CO₂ emitted per kg biomass burned (Akagi et al., 2011). Then, the aerosol emission factors per biomass burned (g kg⁻¹) in Andreae (2019) are used to calculate the emissions rates of BC, OC, SO₂ and other aerosol species needed for the EC-Earth3-Iron and CAM6-MIMI models.

Emissions for the present day and the last decade of the century are geographically interpolated to the needed input for CAM6-MIMI and EC-Earth3-Iron (TableA.7) to ultimately assess the future SFe deposition compared to present-day conditions.

8.2.2 Models

To assess how model differences affect estimates of SFe deposition, this study relies on simulations from two distinct ESMs: EC-Earth3-Iron and CAM6-MIMI. Both models incorporate an atmospheric Fe module encompassing Fe emissions, transport, atmospheric chemistry, and both wet and dry deposition. However, they diverge on certain aspects,

such as the treatment of OXL formation, which may be parameterized (Hamilton et al., 2020a; Johnson and Meskhidze, 2013; Scanza et al., 2018) as in CAM6-MIMI, or explicitly included (Myriokefalitakis et al., 2022; Lin et al., 2014) as in EC-Earth3-Iron. Further distinctions between the models are summarized in Table A.7, and brief descriptions of both models are provided hereinafter.

The EC-Earth3-Iron is described in Section 4.2 while the NCAR Community Earth System Model version 2 (CESM2) (Danabasoglu et al., 2020) in its CAM6-MIMI configuration is here briefly described.

CAM6-MIMI uses the Community Atmosphere Model v6 (CAM6) as the atmospheric GCM where Fe aerosols are traced using the Modal Aerosol Module-4 (MAM4) (Liu et al., 2016). Mineral dust aerosol is modeled via an updated version of the Dust Entrainment and Deposition model (Zender et al., 2003) (Hamilton et al., 2019). The Mechanism of Intermediate complexity for Modeling Iron (MIMI) (Hamilton et al., 2019) is used to model global atmospheric surface concentration and deposition fluxes of total and soluble Fe. The model resolution is $1.25^\circ \times 0.9375^\circ$ (latitude \times longitude) and has 56 hybrid-sigma pressure levels from 1,000 hPa (ground) to up to 2 hPa (top of atmosphere).

Fe emissions coming from dust, combustion anthropogenic activities and biomass burning are considered in CAM6-MIMI. The emitted FeD in the accumulation and coarse insoluble modes are based on the soil mineralogy of Claquin et al. (1999). The Fe content of each mineral is based on Journet et al. (2008) as adopted by Ito and Xu (2014) (Ito and Xu, 2014). FeF and fire Fe emissions, are derived by applying specific emission factors to the total BC emissions for

each aerosol mode considered and activity sector. Land combustion emissions and shipping combustion emissions Fe:BC ratios are based on Rathod et al. (2020); Klimont et al. (2017). Size distribution and initial solubilities are based on Rathod et al. (2020). A two-stage kinetic approach is applied to describe the solubilization of FeD as the fast soluble Fe pool is considered soluble at emission. A separate Fe pool for combustion aerosols is also considered in the model. The dissolved Fe in the model is produced via proton- and organic-ligand-promoted Fe dissolution. The proton-promoted dissolution scheme is dependent upon an estimated $[H^+]$, calculated from the ratio of SO_4^{2-} to calcite, and the simulated temperature. Organic ligand dissolution is dependent upon the simulated secondary OC concentration, as OXL (the main reactant) itself is not modeled.

An evaluation following Section 4.3 of the present-day simulations used in this study reveals a promising level of agreement with surface concentration observations of Fe and SFe. Notably, the EC-Earth3-Iron and CAM6-MIMI models exhibit strong correlation coefficients (0.69 and 0.70 for total Fe, and 0.51 and 0.57 for SFe, respectively). Regions heavily influenced by dust sources, such as the North Atlantic and Central Pacific, tend to overestimate Fe concentrations. Conversely, in remote areas far from major Fe sources, like the SO downwind of the Patagonian region, there is a noticeable underestimation of Fe concentrations. For a more detailed analysis of this evaluation, please refer to Appendix A (Figures A.29-A.30 and Tables A.6-A.5).

8.2.3 Simulations

First, multiple sets of simulations are conducted, each spanning five years, with an additional year for spin-up, using two models: EC-Earth3-Iron and CAM6-MIMI. These simulations operate in atmosphere-only mode, nudged to reanalysis data representing present-day meteorological conditions (2007–2011). EC-Earth3-Iron is nudged using ERA5 reanalysis data from ECMWF (Hersbach et al., 2020), while CAM6-MIMI uses MERRA reanalysis (Rienecker et al., 2011). This setup isolates the effects of different emission scenarios while minimizing the influence of meteorological variability.

The simulations represent two distinct emission periods. The first is the present-day (2001–2010), used as a baseline for estimating future changes. The second covers the end of the century (2091–2100) under three CMIP6 SSP scenarios, while meteorological conditions remain constant at 2007–2011 levels. The three SSP scenarios, SSP1-2.6, SSP3-7.0, and SSP5-8.5, correspond to RF levels of 2.6, 7.0, and 8.5 W/m^2 by 2100, reflecting diverse socioeconomic pathways (O’Neill et al., 2017) (see Section 4.4).

To isolate the impact of fire emission changes and more specifically of changes in climate-driven fire emissions by the century’s end, three types of simulations are conducted per future scenario and model. One type of simulation uses the standard CMIP6 SSPs fire emissions (SSP), a second one employs the fire emission dataset that also incorporates climate-driven fire changes (SSP_wNATFIRES), and the third deactivates fire emissions entirely (SSP_noFIRES). For the present-day, two distinct setups are implemented: one using GFED4s

estimates and an additional one with fires deactivated. In total, 11 atmospheric-nudged simulations for each of the models is performed (Fig. A.32). Given the strong uncertainty in modeled past and future dust trends, for the purpose of this study, dust emissions in all simulations represent present-day levels consistent with meteorological conditions in each model. Note that all emissions except fire emissions are held constant across each the three types of simulations following CMIP6 SSPs data for the corresponding decade and SSP (Hoesly et al., 2018).

Additional sensitivity simulations are conducted using EC-Earth3-Iron, where, instead of applying present-day atmospheric nudging, the atmosphere is constrained by monthly SIC and SST, following the AMIP protocol (Gates et al., 1999). The monthly SIC and SST fields are generated by creating climatologies (2001–2010 for the present day and 2091–2100 for future projections) based on fully coupled EC-Earth3 simulations for each scenario. These outputs are part of the CMIP6 activity and are publicly available. For future projections, all fire emissions (accounting for both anthropogenic and climate-driven changes) are included in this set of sensitivity simulations. Combined with the present-day simulations, this results in four simulations (Fig. A.32). These simulations aim to estimate how changes in climate conditions impact Fe solubilization, transport pathways, and deposition, in addition to the climate-driven changes in fire emissions.

8.2.4 Source contributions to relative changes

Based on the simulation setup described above, the following methodology is employed to quantify the contributions of changes

in climate-driven fires (*NATFIRES*), anthropogenic-driven fires (*ANTFIRES*), and fossil fuel emissions and forcing at the end of the century (*OTHER*) to the future-to-present-day changes in SFe deposition and NPP_{iron} . Here, RC denotes relative change:

$$RC_{\text{NATFIRES}} = 100 \cdot \frac{SSP_{w\text{NATFIRES}} - SSP}{PD} \quad (8.1)$$

$$RC_{\text{ANTFIRES}} = 100 \cdot \frac{SSP - PD}{PD} - 100 \cdot \frac{SSP_{\text{noFIRES}} - PD_{\text{noFIRES}}}{PD} \quad (8.2)$$

$$RC_{\text{OTHER}} = 100 \cdot \frac{SSP_{\text{noFIRES}} - PD_{\text{noFIRES}}}{PD} \quad (8.3)$$

Summing up the three contributions yields the total change in SFe or NPP_{iron} at the end of the century compared to the present:

$$RC = 100 \cdot \frac{SSP_{w\text{NATFIRES}} - PD}{PD} \quad (8.4)$$

8.2.5 Fe-limited regions

Surface nitrate concentrations are used here as a proxy for identifying regions sensitive to atmospheric SFe deposition. Fe-limited regions are defined as areas where surface nitrate concentrations exceed $4 \mu\text{M}$, a threshold supported by both observational and modeling studies (Krishnamurthy et al., 2007, 2010; Moore et al., 2013). Additionally, threshold values of $2 \mu\text{M}$ and $8 \mu\text{M}$ are explored to test the sensitivity

of the results to this threshold selection, following previous studies (Rathod et al., 2022).

For present-day Fe-limited regions, surface nitrate concentrations are used from the World Ocean Atlas (WOA) 2023 (Garcia et al., 2024).

To assess future changes in Fe-limited areas, nitrate concentrations from seven CMIP6 models that include biogeochemistry and provide publicly available surface nitrate outputs are analyzed. These models are CESM2 (CESM2 and CESM2-WACCM versions), GFDL-ESM4, NorESM2 (NorESM2-LM and NorESM2-MM versions), ACCESS-ESM1-5, MIROC-ES2L, MPI-ESM1-2-LR, and UKESM1-0-LL. 10-year multimodel climatologies for both future (2091-2100) and present-day (2001-2010) scenarios are calculated.

To account for model biases, the difference between the WOA 2023 present-day surface nitrate fields and the modeled present-day climatologies are computed, applying this bias correction to the future model outputs.

Figure A.37 (left column) shows the resulting Fe-limited regions based on this method. To estimate how model divergence could affect the definition of Fe-limited regions, the same method is applied using the model climatologies adjusted by subtracting and adding the standard deviation of the models (middle and right columns, respectively).

8.2.6 Net primary productivity estimates

To estimate NPP_{iron} , the methodology outlined in Rathod et al. (2022) is adopted. Carbon to SFe (C/SFe) ratios are used in Fe-limited

regions. The C/SFe ratios, representing carbon relative to SFe content in phytoplankton biomass or uptake, can vary by several orders of magnitude across different phytoplankton groups and their physiological states. A set of different C/SFe ratios [6×10^3 , 3×10^4 , and 1.5×10^5 g C/g SFe] is tested, reflecting the broad range of values reported in the literature (Okin et al., 2011; Boyd et al., 2012; Moore et al., 2001; Twining and Baines, 2013).

Seasonal light changes in high latitudes are further accounted for by excluding the effects of SFe deposition in November, December, January, and February for the North Pacific and North Atlantic, and excluding June, July, August, and September for the SO from the NPP_{iron} calculations, based on phenology studies (Yamaguchi et al., 2022; Thomalla et al., 2023; Ardyna et al., 2017; Hieronymus et al., 2024; Sasaoka et al., 2011).

8.2.7 Sensitivity assessment

In order to understand to what extent projected changes in SFe deposition are sensitive to model uncertainty or socioeconomic scenario differences, the uncertainty is partitioned (Hawkins and Sutton, 2009). Assuming that both uncertainties are independent, the total uncertainty (T) can be decomposed as follows:

$$T = M + S \quad (8.5)$$

where M is the model uncertainty and S is the scenario uncertainty.

First, the model uncertainty for each scenario is estimated as the variance of the projected changes between both models. Then, the

average across scenarios is used as the estimate of the model uncertainty (M):

$$M = \frac{1}{N_s} \sum_s \text{var}_m(x_{m,s}) \quad (8.6)$$

where $x_{m,s}$ is the projected change relative to the present day for model m and scenario s , and N_s is the number of scenarios considered (3 in this case).

The scenario uncertainty (S) is calculated as the variance of the multi-model means of projected changes for all scenarios:

$$S = \text{var}_s\left(\frac{1}{N_m} \sum_m (x_{m,s})\right) \quad (8.7)$$

where N_m is the number of models considered (2 in this case).

The mean change for all the simulations (G) is the multi-scenario and multi-model mean of the changes:

$$G = \frac{1}{N_m N_s} \sum_{m,s} x_{m,s} \quad (8.8)$$

Then, the fractional uncertainty (F) at 90% confidence level is calculated as the total uncertainty (T) divided by mean change (G), as follows:

$$F = \frac{1.64\sqrt{T}}{G} \quad (8.9)$$

A two-tailed t-test was further conducted over the SFe deposition changes to assess statistical significance. P values lower than 0.1 are considered significant, with a 90% confidence level.

8.3. Results & discussion

8.3.1 The importance of climate-driven fires on future atmospheric fire iron

Fire Fe emissions are subject to the episodic and unpredictable nature of fires, which complicates obtaining globally representative aerosol samples for analyzing smoke plume composition and atmospheric transport pathways (Perron et al., 2022). Modeling can help to fill this gap by using estimates from available observational studies that link Fe emissions to co-emitted species like BC and OC aerosols (Hamilton et al., 2022).

Using two different ESMs and present-day emissions from the CMIP6 historical inventory, which uses GFED4s (Randerson et al., 2017), a mean present-day (ca 2010 CE) global fire Fe emission of 0.76 [0.57-0.94] Tg Fe/yr is obtained. These estimates align with recent modeling studies, which report values from 0.52 to 2.2 Tg Fe/yr (Bergas-Massó et al., 2023). Fire Fe emissions are mainly concentrated in vegetated regions from 45°S to 75°N, with tropical peaks near 10°N and 10°S (Fig. A.31). The northern peak is related to grassland fires, while the southern peak is driven by grassland fires and deforestation in South America and Indonesia. A secondary peak, around 55°N, corresponds to Boreal fires.

For future estimates, an emission dataset that accounts for fire scenarios influenced by both socioeconomic and climate factors is used (Hamilton et al., 2024a). This dataset integrates information from an ensemble of six ESMs within the CMIP6 framework, which simulate interactive

fires in response to changes in climate and vegetation, combined with SSP emission data (Hamilton et al., 2024a). The projections are then bias-corrected using present-day GFED4s (Hamilton et al., 2024a) (see Section 8.2.1). Additionally, simulations using the standard SSP fire emission projections (Fig.A.32) are conducted, enabling us to isolate climate-driven changes in fires from those driven by anthropogenic factors (see Section 8.2.3). Anthropogenic fire changes in the methodology employed here are attributed to human activities such as land-use changes, management, and accidents, which are driven by economic and demographic factors (Archibald et al., 2012; Andela et al., 2017). In contrast, climate-driven fire changes arise from fire-favorable conditions like low humidity and high temperatures, primarily influenced by anthropogenic climate change.

Climate drivers enhance global future fire Fe emissions, leading to increases of 1.7 to 1.8 times above CMIP6-SSP standard projections across all scenarios. Without these drivers, even the most extreme scenarios (SSP370 and SSP585) would yield fire Fe emissions below present-day levels.

Projections indicate a substantial increase in fire Fe emissions across the extra-tropics by the century's end, consistent across all socioeconomic scenarios. The highest increases appear in scenarios with limited climate mitigation and high RF (SSP370 and SSP585). Under SSP585, for example, emissions may reach levels three times present-day levels in some latitudinal bands. This rise is more pronounced in the NH than the SH due to the limited extra-tropical land area in the SH (Fig. 8.1). The steep rise in high-latitude emissions is largely climate-driven, with peak increases occurring during NH summers (Fig. A.33). In

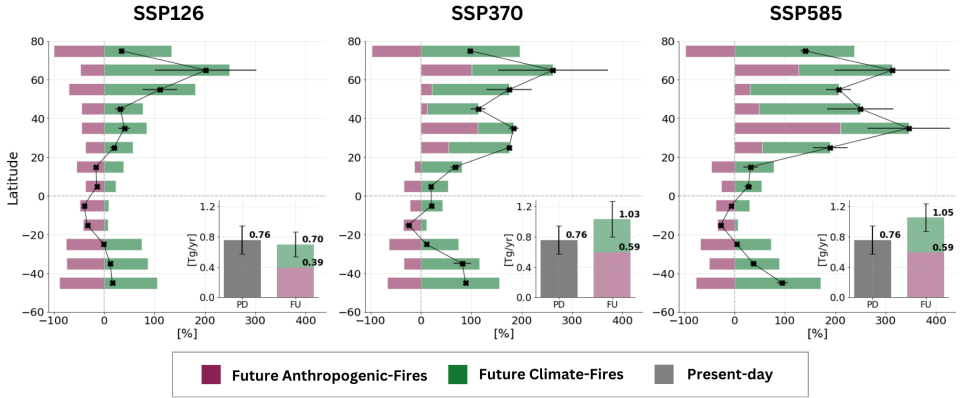


Figure 8.1: **Future changes in fire Fe emissions.** Model-derived changes in fire iron (Fe) emissions relative to present-day estimates by 10° latitude bands for each scenario [SSP126 (left), SSP370 (middle), SSP585 (right)] in black. Black dots show the two model mean and bars indicate the corresponding range between the two models. Purple-coloured bars denote the contribution of anthropogenic fires to future changes, while green bars illustrate the influence of climate-driven fires. Bar plots in the lower right corner display global emission budgets in Tg/yr of fire Fe emissions for present-day (depicted in gray) and end-of-the-century scenarios for each SSP. Bars indicate the corresponding difference between the two models.

these latitudes, lightning-induced (climate-driven) fires are expected to remain dominant (Janssen et al., 2023; Hessilt et al., 2022; Chen et al., 2021). The extraordinary fire season in Canada in 2023 exemplifies the large and severe fires that lightning can trigger in these regions (Jain et al., 2024; Byrne et al., 2024).

In tropical regions, especially in Africa, recent declines in fire emissions are primarily due to human activities like converting grasslands to agricultural and pastoral land (Andela et al., 2017). Future shifts in fire emissions will vary widely across socioeconomic scenarios: SSP126, a sustainable, low-intervention pathway, shows decreases

in anthropogenic-driven fires across all latitudes, while SSP370 and SSP585 show regional increases in the NH extra-tropical regions. SSP126's minimal climate impact contrasts with SSP370 and SSP585, which project moderate to high climate forcing combined with varying levels of human intervention (see Section 4.4). As a result, global fire Fe emission trends diverge, with SSP126 indicating a slight decline, and SSP370 and SSP585 showing increases up to 1.4 times above present-day levels.

Changes in fire Fe emissions lead to corresponding shifts in fire SFe deposition downwind. During atmospheric transport Fe aerosols undergo chemical transformations, transitioning from insoluble to soluble forms that marine biota can utilize as micronutrients. The primary solubilization pathways are acidic and organic ligand-promoted dissolution, which are represented in the employed ESMs (see Sections 4.2 and 8.2.2). Fire plumes, rich in acids (Rickly et al., 2022) and organics (Zhou et al., 2015), thereby facilitate the dissolution of Fe in the atmosphere.

The global fire SFe deposition and its attribution to climate versus anthropogenic factors mirror the patterns seen in fire Fe emissions (Fig. A.34 and A.35). Maximum global fire SFe deposition occurs near the equator, primarily in the Atlantic basin downwind of African anthropogenic fire sources. Climate-driven fires significantly affect NH fire SFe deposition (over 60%), particularly from North American Boreal regions impacting the Arctic Ocean and North Atlantic (Fig. 8.2). Only in a limited number of regions (shown in pink in Fig. 8.2), fire emissions are suppressed due to climatic factors, such as increased soil moisture, higher precipitation, or decreased wind speed.

8.3.2 Interplay of fires and fossil fuel emissions on future iron deposition changes

The importance of incorporating climate-driven fire changes in future fire Fe emission estimates has been here emphasized, particularly in the high latitudes. However, to fully assess how future fires will impact SFe deposition in the ocean, it is crucial to consider concurrent changes in other sources of Fe influenced by socioeconomic pathways. The simulation here shown distinguishes between changes in SFe deposition from fires and the SSP projected changes in fossil fuel emission sources (see Section 8.2.4).

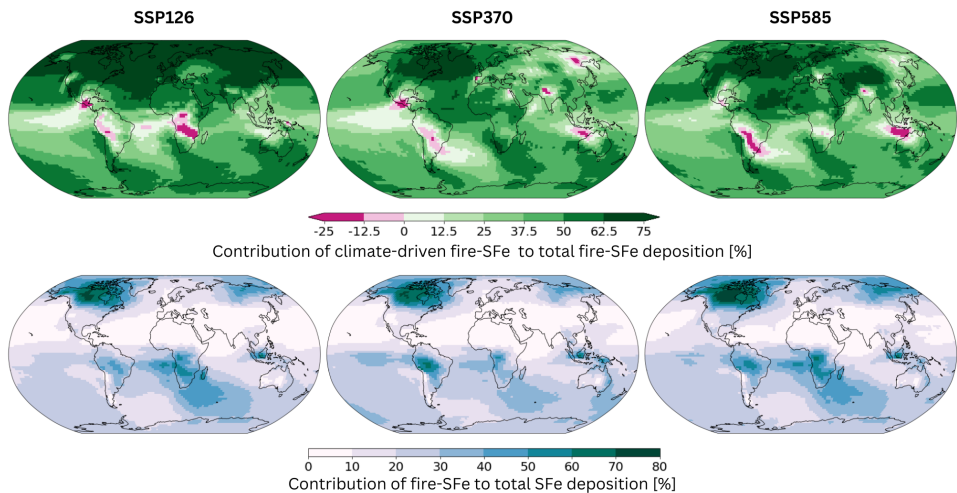


Figure 8.2: **Contribution of climate and anthropogenic-driven fires to SFe deposition.** The upper row represents the percentage of soluble iron (SFe) deposition from fires attributed to climate-driven fires. The second row shows the percentage of SFe deposition originating from fires considering all other sources. Fields are shown for future scenarios (SSP126, SSP370, and SSP585, from left to right). All fields shown represent the mean of two models (CAM6-MIMI and EC-Earth3-Iron).

Fires contribute over 30% of SFe deposition across various regions, regardless of the SSP scenario. Key areas affected include the Arctic, North Atlantic, equatorial Atlantic and Pacific, and southern Indian Ocean (Fig. 8.2). Notably, fires in the Arctic and high-latitude North Atlantic contribute up to 70% of total deposition, with regions like the Beaufort Sea and Hudson Bay reaching the upper end of this range. This dominance results from minimal dust and fossil fuel contributions. In the SH, fire SFe contributes between 20 and 50% to total SFe deposition in the Atlantic, influenced by southern African biomass burning. The impact of SFe from fires is also significant in the Equatorial Pacific, where biomass burning in Central and South America contributes 20-30%. While climate-driven fires dominate the fire contribution in the NH, anthropogenic fires primarily affect the SH regions.

Changes in SFe deposition between future and present-day levels exhibit significant variability depending on the scenario (Fig. 8.3). Under SSP126, a reduction in SFe deposition is observed below 60°N, due to decreased anthropogenic activities affecting both fire and other anthropogenic aerosol emissions. Above 60°N, no discernible change occurs as increased climate-driven fires offset reductions in fossil fuel emissions. SSP370 shows a global rise in SFe deposition, especially in equatorial regions and NH high latitudes, with mean latitudinal increases of up to 40%. The increment in equatorial SFe deposition is driven by both fossil fuel and fire aerosol Fe increases. In the NH high latitudes, the escalation stems from heightened anthropogenic ($\approx+10\%$) and climate-driven fires ($\approx+30\%$), reflecting the high population growth in this scenario. SSP585 shows a reduction in SFe deposition below 60°N, though smaller than under SSP126, due

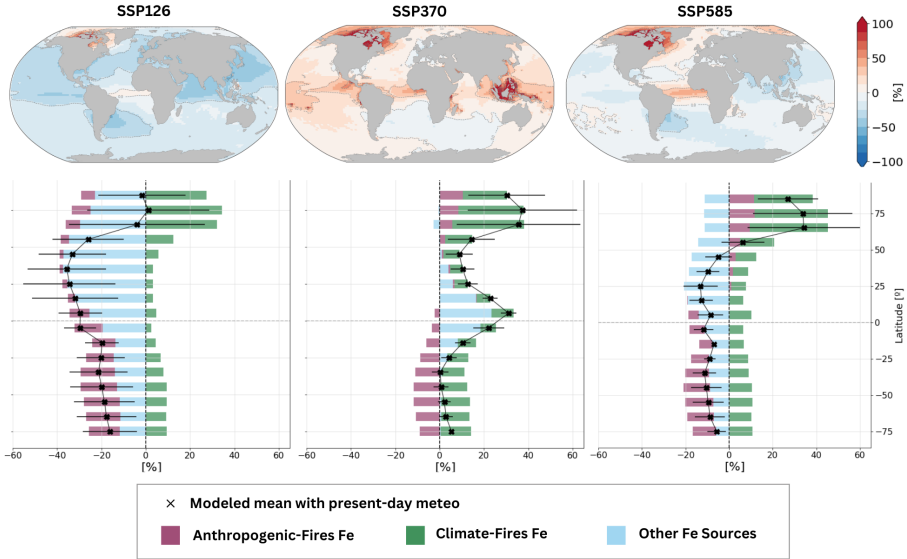


Figure 8.3: **Future changes in SFe deposition compared to present-day.** Annual mean relative changes in soluble iron (SFe) deposition for future scenarios relative to the present-day scenario (SSP126, SSP370, and SSP585, from left to right). Bottom panels: Corresponding latitudinal relative changes are represented by black crosses, accompanied by the contributions to the total change of changes in anthropogenic fires (depicted in purple), climate-driven fires (depicted in green), and other emissions (depicted in blue). Black crosses show the model mean and bars indicate model differences.

to decreases of non-fire anthropogenic emissions. Above 60°N , both anthropogenic and climate-driven fire increases outweigh the effects of non-fire aerosol reductions, leading to a 40% rise in SFe deposition under certain latitudinal bands. Notably, there are regional variations, with more pronounced increases downwind of North American Boreal fires for the three scenarios. However, Eurasian Boreal fires do not show such a strong signal. This disparity is due to differences in fire regimes (Jones et al., 2024) and the lower baseline SFe deposition rates

downwind of North American Boreal regions (Myriokefalitakis et al., 2022; Hamilton et al., 2020b), making them more sensitive to changes in aerosol deposition.

In addition to emissions changes, climate-driven shifts in meteorological conditions may further influence SFe deposition from all Fe sources. This sensitivity has been assessed using EC-Earth3-Iron (see Section 8.2.3), and results (Fig. A.36) show that under high mitigation scenarios (SSP126), projected changes remain similar to those under present-day meteorology. However, for SSP370 and SSP585, SFe deposition increases up to 100% higher than present-day levels in equatorial and tropical regions, with smaller increases in high latitudes. This rise is associated with increases in water content and warmer temperatures (Collins et al., 2024; Tebaldi et al., 2021), which, together with high atmospheric acidity, enhance solubilization and result in greater SFe deposition (Bergas-Massó et al., 2023).

8.3.3 Impacts on Fe-limited oceanic regions: the North Atlantic stands out

Projected changes in SFe deposition are likely to impact Fe-limited HNLC ocean regions, where N and other nutrients are abundant, and light conditions during certain seasons support marine productivity, but Fe remains scarce (Hamilton et al., 2023; Moore et al., 2013; Browning and Moore, 2023). Studies from Fe fertilization experiments, ocean surveys, and modeling confirm that Fe supports phytoplankton growth, impacting NPP—the rate of photosynthetic carbon fixation minus the carbon used for respiration by autotrophic microbes—and, consequently,

carbon export to the deep ocean.

The impact of the here used new future fire projections on NPP is estimated by calculating the portion specifically attributable to SFe deposition, denoted as NPP_{iron} . To quantify NPP_{iron} , a range of carbon-to-SFe (C/SFe) ratios derived from experimental data are applied in Fe-limited ocean regions (Boyd et al., 2012; Okin et al., 2011). Additionally, following previous studies (Rathod et al., 2020), Fe-limited regions are defined based on varying surface nitrate concentration thresholds (Garcia et al., 2024) (Fig. A.37) (see Section 8.2.5).

Fig. 8.4 shows present-day NPP_{iron} estimates in four Fe-limited regions (i.e., the SO, the Equatorial Pacific, the North Pacific and the high-latitude North Atlantic) and projected end-of-century changes across scenarios, assuming present-day surface nitrate levels. The SO and North Pacific display higher NPP_{iron} estimates than the Equatorial Pacific and North Atlantic, due to the larger area of the former and the higher SFe deposition rates in the latter.

Under SSP126, a 17–46% reduction in NPP_{iron} is projected across all Fe-limited regions, mainly due to decreased fossil fuel emissions and reduced anthropogenic SFe from fires reaching the Equatorial Pacific. Conversely, SSP370 shows increased global SFe deposition, boosting NPP_{iron} in Fe-limited regions. The SO’s increase is modest ($\approx 5\%$), as rising SH climate-driven fires are balanced by suppressed anthropogenic African fires. The Equatorial Pacific sees a $\approx 25\%$ increase, mainly from non-fire SFe sources. Under SSP585, NPP_{iron} decreases in most Fe-limited areas but the North Atlantic, where a mean 17% rise is expected owed to climate-driven North American Boreal fires.

The Southern and high-latitude North Atlantic Oceans are most impacted by climate-driven future fire activity changes, though with differing effects. In the SO, reductions in anthropogenic fires and fossil fuel emissions offset climate-driven fire increases, leading to minimal NPP_{iron} change. In contrast, climate-driven fires have a stronger effect on the Fe-limited North Atlantic.

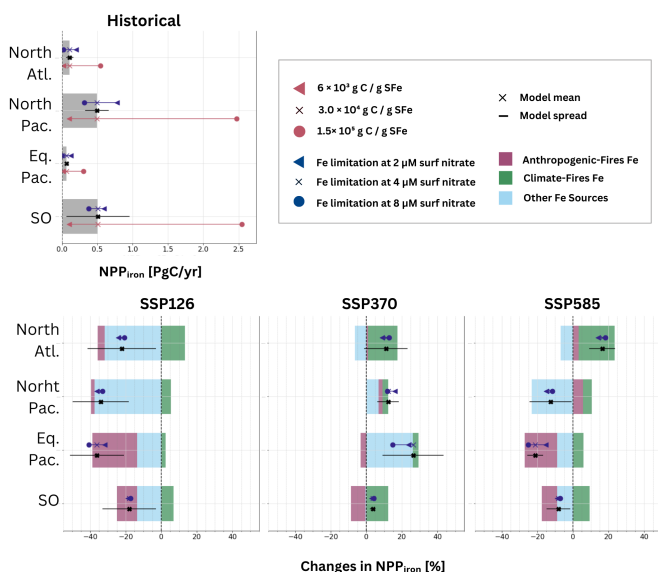


Figure 8.4: **Future atmospheric Fe-induced changes in NPP.** Upper panel illustrates the historical net primary productivity (NPP) induced by atmospheric soluble iron (SFe) deposition (NPP_{iron}) in Fe-limited regions (North Atlantic, North Pacific, Equatorial Pacific, and SO). Black crosses indicate model means, black bars show model differences. Blue symbols denote different nitrate thresholds used to define Fe-limited regions (triangle: $2 \mu\text{M}$, cross: $4 \mu\text{M}$, and circle: $8 \mu\text{M}$). Red symbols show a range of C ratios observed in previous studies (triangle: $6 \times 10^3 \text{ g C/g SFe}$, cross: $3 \times 10^4 \text{ g C/g SFe}$, and circle: $1.4 \times 10^5 \text{ g C/g SFe}$). The bottom panel displays annual mean relative changes in NPP_{iron} for future scenarios (SSP126, SSP370, SSP585) and contributions from anthropogenic fires (purple), climate-driven fires (green), and other emissions (blue).

The response of NPP_{iron} in the North Atlantic exhibits pronounced seasonality, with higher relative changes in NH summer (32 [10-53]% under SSP370 and 44 [30-58]% under SSP585), reflecting the seasonality of Boreal fires (Fig. A.38). This seasonal effect is critical, as Fe-limitation in the North Atlantic peaks in NH summer (Ryan-Keogh et al., 2013). The high-latitude North Atlantic exhibits a strong NH spring diatom bloom, producing a substantial seasonal surge of rapidly sinking carbon. Following the spring diatom bloom, extensive coccolithophore blooms persist into late NH summer under Fe-limited conditions (Sanders et al., 2014), contributing to carbon export via sticky exopolymer particles and biominerals (Shutler et al., 2013; Nissimov et al., 2018). Increased NH summer SFe deposition in some scenarios may extend coccolithophore blooms and boost carbon export, aligning with prior studies showing wildfire aerosol can amplify N-limited Arctic blooms (Ardyna et al., 2022).

Projections here shown thus far have assumed stable surface nitrate levels, but total NPP changes by century's end will also reflect broader climate impacts. Under low mitigation scenarios, global warming is expected to increase upper ocean stratification, reducing nutrient mixing from the deep ocean and altering surface macronutrient distribution (Li et al., 2020). This could shrink Fe-limited regions, as shown in CMIP6 projections (Fig. A.37). When factoring in these macronutrient changes (see Section 8.2.5), NPP_{iron} is projected to decline across all regions (Fig. A.37). However, climate-driven fires could mitigate this decline, by up to 7-8% in the high-latitude North Atlantic. Additionally, although not considered here nor in CMIP6 projections, shifts in fire and other Fe sources will also affect micronutrient-to-macronutrient ratios, by

influencing not only SFe but also N deposition (Fig. A.39). This is particularly significant as stratification may increase the sensitivity of ocean primary production to atmospheric macronutrient inputs, such as those from fire aerosols (Ardyna et al., 2022).

These findings are crucial as changes in NPP_{iron} , particularly in the high-latitude North Atlantic, can significantly influence global carbon export and marine ecosystems. Wildfire aerosols may also impact climate by altering albedo and ice sheet melt rates, affecting nutrient availability in high-latitude oceans (Wadham et al., 2019). Additionally, increased wildfires in Boreal regions may enhance nutrient runoff to the ocean, further amplifying these effects (Riera and Pausas, 2023).

8.3.4 Assessing regional sensitivity: model uncertainty vs. socioeconomic emission scenarios

Understanding future SFe deposition is crucial for predicting shifts in marine ecosystems and biogeochemical cycles. To understand the drivers of projections' spread, the fractional uncertainty across models and scenarios is calculated (Fig. 8.5; see Section 8.2.7), assessing whether model disparities or different socioeconomic scenarios have a greater impact on projected SFe deposition. Regions with low uncertainty show consistent projections regardless of scenario or model differences, while in areas with higher uncertainty it is here shown whether changes are driven mostly by mitigation policies or model variations. This analysis aims to pinpoint key factors influencing SFe deposition, providing insights for both policy and future research.

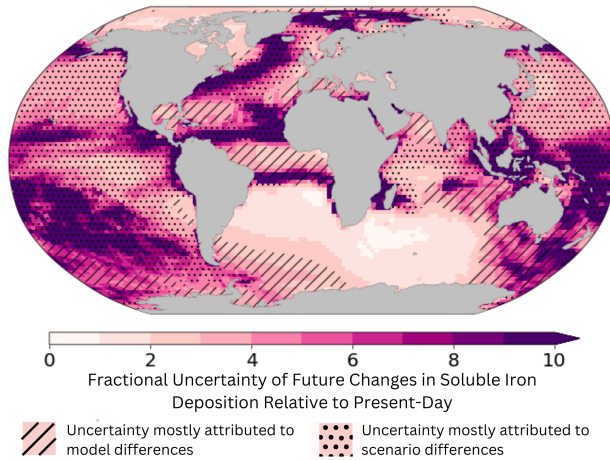


Figure 8.5: **Model uncertainty versus socioeconomic scenarios.** Total estimated fractional uncertainty in soluble iron (SFe) deposition changes from the present day to the end of the century, taking into account all scenarios and models. The attribution of uncertainty to model differences and scenario differences is shown with hashed and dotted masks, respectively. Areas without hashed or dotted masks correspond to regions where across models and scenarios projected changes remain statistically similar with a 90% confidence interval after performing a two-tailed t-test.

This analysis reveals that projected SFe deposition in the NH Fe-limited regions, such as the Equatorial and North Pacific and North Atlantic, are mainly driven by socioeconomic and climate forcing emission scenarios, including changes in fire emissions. In the North Atlantic, areas near fire sources, such as the Labrador Sea, where SFe deposition strongly increases (Fig. A.40), exhibit a low fractional uncertainty despite model differences. Fractional uncertainty is significantly higher over other areas of the Fe-limited North Atlantic, but decreases markedly in the NH summer when the projected increase in SFe deposition is at its peak, indicating consistency across models and scenarios (Fig. A.41).

Variations in emission policies mainly affect the eastern high-latitude North Atlantic.

In the Fe-limited SO, regional differences are evident. In the South American Pyrogenic region (Fig. 4.1) and the SH oceans near Africa, the fractional uncertainty is low, as models and scenarios consistently indicate a slight decrease in SFe deposition. In contrast, in other regions, higher fractional uncertainty arises mainly from model disparities, such as in the South American Dust region (Fig. 4.1), where differences in Fe from dust drive variability. (Fig. A.42). Model differences also dominate uncertainty in parts of the North Atlantic, South Atlantic, Indian Oceans, and Mediterranean.

While projected changes in the Fe-limited North Atlantic are consistent, model differences exist in the magnitude of SFe deposition, with CAM6-MIMI predicting higher deposition than EC-Earth3-Iron (Fig. A.43 and A.36). These discrepancies may partly arise from differences in fire SFe aerosol representation, particularly in fire Fe emission estimates and their global distribution. EC-Earth3-Iron uses both BC and OC emissions to estimate Fe Fe (Ito, 2011), while CAM6-MIMI relies only on BC (Hamilton et al., 2019) (Table A.7). As a result, the fire Fe emission distribution in EC-Earth3-Iron is mainly driven by the pattern of OC, since OC emissions are higher by mass compared to BC. In CAM6-MIMI, however, the Fe emission distribution is primarily driven by the BC pattern (Fig. A.44).

Model differences also arise from how emitted mass is allocated between fine and coarse aerosols. EC-Earth3-Iron assigns approximately 22% of the mass to fine particles, while CAM6-MIMI assigns 14%.

Coarser particles, with shorter atmospheric lifetimes, lead to more localized SFe deposition in CAM6-MIMI (Fig. A.45). Additionally, differences in aerosol vertical distribution at emission (Table A.7) affect spatial deposition patterns, as higher injection heights result in longer transport and particle lifetimes. Disparities in fire Fe dissolution also contribute: CAM6-MIMI assumes 33% and 4% solubility for fine and coarse particles, respectively, while EC-Earth3-Iron emits all fire Fe as insoluble, but with enhanced dissolution during transport (Table A.7). These differences explain the higher fire Fe solubilities at deposition closer to the Boreal fire sources in CAM6-MIMI (Fig. A.46).

8.4. Conclusions

This study examines the impact of 21st-century fire emissions on oceanic SFe supply, considering both climate and anthropogenic drivers across various socioeconomic scenarios. Climate change is here shown to have the potential to increase fire-driven Fe emissions by at least 1.7-1.8 times compared to direct anthropogenic drivers of fires alone, with regional variations.

In the NH, particularly under higher warming scenarios, increased fire emissions lead to a 30-40% rise in SFe deposition. This effect is especially pronounced in the Fe-limited North Atlantic during summer. This increase could boost the effects of SFe deposition on NPP during summer phytoplankton blooms by up to 40%, potentially extending their duration (Ardyna et al., 2022) and enhancing carbon export, when assuming present-day macronutrient levels. When accounting for projected declines in macronutrients, climate-driven fires could offset the

impact of these declines by 7-8%. In the SO, changes in Fe deposition are smaller due to opposing effects from reduced anthropogenic fires, but the region remains sensitive to these shifts, with potential implications for productivity and carbon cycling.

Uncertainties persist despite the detailed sensitivity analyses, partly due to discrepancies in fire emissions estimates (Liu et al., 2020; Hua et al., 2024; Carter et al., 2020). GFED4s present-day estimates are here retained to align with the CMIP6 SSP inventory. As GFED4 is on the lower bound of other satellite-based fire emission estimate ranges (Pan et al., 2020; Liu et al., 2020), the present-day and future fire Fe emission estimates and associated impacts here shown are likely conservative. Extreme fire events, such as the 2019-2020 Australian megafires, are expected to increase with climate change but are not accounted for in current models, making these projections even more conservative (United Nations Environment Programme, 2022).

Model uncertainties also stem from how fire aerosol solubility and vertical distribution are handled, with varying solubility assumptions between models affecting the deposition of fire Fe in different regions (Hamilton et al., 2022). These discrepancies highlight the need for more accurate observational data to refine nutrient emission estimates and improve the representation of fire aerosols in models. This includes the relationship between nutrient content and fire severity, vegetation biome, and the type and properties of biomass burning, along with potential shifts between flaming and smoldering in response to a changing climate (Ito, 2011). Since model results of SFe deposition are shown to be dependent on these parameters, a multimodel approach, as used here, is essential in such studies.

Fire-driven nutrient supply does not end when a fire ceases, as the removal of vegetation by fire can expose the soil surface, enhancing dust emissions that are also potentially enriched with ash from the fire or modified by its heat (Hamilton et al., 2022; Yu and Ginoux, 2022). Such complex interactions between fire and dust emissions are challenges to tackle in future-generation ESMs.

Additionally, dust emission changes, not considered in this study, could alter SFe deposition in sensitive regions as seen in Chapter 7. The North Atlantic and SO could be impacted by shifts in dust emissions from regions like North Africa and East Asia (Bergas-Massó et al., 2023). Given current limitations in dust projections (Kok et al., 2023), future research should focus on the combined impact of climate- and human-induced changes in both fire and dust emissions.

The focus in this study is on assessing how future changes in Fe emissions could impact HNLC regions while keeping other factors constant. However, broader climate change factors, like shifts in meteorological conditions and macronutrient redistribution, also influence biogeochemical dynamics. It is here shown that a warming climate may amplify Fe solubilization and SFe deposition, especially in regions like the Equatorial Pacific, and alter marine productivity through changes in macronutrient distributions and phytoplankton dynamics, further altering the impact of future increases in fires.

This study motivates detailed ocean biogeochemistry modeling simulations to estimate the overall impact of the refined SFe and nutrient deposition fluxes on ocean biogeochemistry here produced. Climate-driven fires also influence N deposition, altering Fe:N

deposition ratios (Fig. A.39). This may have an increasingly important effect in HNLC regions under stratification-driven declines in surface nitrate levels, and could significantly impact N fixation in other oceanic areas that are depleted in surface nitrate (Duce et al., 2008). Moreover, while previous research focused primarily on the fertilization effect of Fe deposition, it is crucial to consider other effects on the ocean BCP, such as shifts from small phytoplankton to diatoms, potentially enhancing carbon fixation (Hamilton et al., 2020a). Expanded observational networks monitoring ocean responses to atmospheric supply, particularly in high-latitude oceans, over the long term should be further supported.

This work exemplifies the trans-disciplinary nature of fire science and the need for a better understanding of fire's role in the oceanic carbon cycle across both spatial and temporal scales. Collaboration among atmospheric science, oceanography, and climate policy is crucial to address the challenges posed by shifting fire regimes and their effects on ocean health (Hamilton et al., 2024b) and to tackle key objectives set by the UN Decade of Ocean Science for Sustainable Development (Muller-Karger et al., 2024; Calewaert et al., 2024).



**Conclusions
& Future
Perspectives**

CHAPTER 9

Conclusions and future perspectives

The main general outcomes of the Thesis and specific conclusions obtained in each Chapter are outlined in Section 9.1, while the subsequent Section 9.2 discusses potential future research based on these findings.

9.1. Conclusions

This PhD Thesis has made significant advances toward the main research goal stated in Chapter 2: *"To enhance our understanding and quantification of the atmospheric supply of SFe to the ocean under a changing climate"* by addressing key uncertainties and providing valuable insights into the mechanisms influencing this process under changing climate conditions.

By improving our ability to model and quantify SFe deposition, this research contributes essential data that can be integrated into the next generation of ESMs, offering a more comprehensive view of how

atmospheric Fe impact ocean biogeochemistry. The use of advanced models like EC-Earth3-Iron and new tracers for differentiating between SFe sources, coupled with an analysis of past, present, and future climate scenarios, has allowed for a deep exploration of the factors driving variations in SFe deposition and its implications for marine ecosystems.

Furthermore, this Thesis directly addresses critical gaps in emission inventories and model constraints, particularly in relation to fire emissions, to more accurately project future SFe dynamics. The sensitivity of SFe deposition to changes in anthropogenic emissions, along with projections for future climates, emphasizes the complex interplay between emission sources, regional variability, and global climate change. By enhancing our understanding of these processes, this Thesis paves the way for future research aimed at predicting the response of marine ecosystems to a changing climate, ultimately contributing to the broader field of global biogeochemical cycles.

These advancements were achieved by addressing specific objectives through the results presented in this Thesis. The key contributions are summarized below.

Validating an ESM with online atmospheric iron: EC-Earth-3-Iron

The EC-Earth3-Iron model, a cutting-edge tool for simulating atmospheric Fe dynamics, has been rigorously validated against observational data. This validation demonstrates the model's ability to accurately reproduce observed Fe distributions and magnitudes

for recent decades. Additionally, its sophisticated solubilization mechanisms for atmospheric Fe successfully generate soluble Fe fields that align with observational datasets. These strengths establish the model as a reliable resource for studying the atmospheric Fe cycle and its interactions with other components of the Earth system.

Nonetheless, the analysis emphasizes the challenge posed by the limited availability of Fe observations, which restricts the capacity to further refine estimates of current soluble Fe deposition fluxes. A comparative analysis with another state-of-the-art Fe aerosol model underscores this point. While the two models generally deliver comparable results, significant differences emerge in aspects such as Fe dissolution mechanisms, which affect the global distribution of soluble Fe deposition. These findings highlight the importance of multimodel approaches in enhancing our understanding of atmospheric Fe processes and improving the accuracy of model predictions.

Gaining insight into the characterization of SFe deposition

A novel feature of this work is the use of separate tracers within EC-Earth3-Iron to differentiate between Fe originating from dust, biomass burning, and fossil fuel combustion. This approach has enabled detailed quantification of SFe deposition fluxes by source, highlighting the critical contributions of fire and fossil fuel combustion sources in Fe-limited ocean regions. The inclusion of such sources and their corresponding solubilization efficiencies showcase that in certain key regions non-dust SFe sources are essential to the quantification of SFe

deposition fluxes.

Additionally, separate tracers were employed for emitted particle size modes, allowing for a refined analysis of deposition pathways. The model incorporates both dry and wet aerosol deposition mechanisms, leading to key insights: coarse SFe is predominantly deposited near source regions via dry deposition, while in remote Fe-limited regions, SFe deposition is dominated by wet removal processes, particularly for particles in smaller-size ranges.

The Fe deposition reconstruction presented in this Thesis is a valuable product for ocean biogeochemistry research. It provides a high-resolution, source-specific, and multi-nutrient product (including N deposition fields). This offers a foundation for future studies aimed at deepening our understanding of the impacts of aerosol deposition.

Quantifying changes in SFe deposition to the ocean across past, present-day, and future climates (end of the century).

This Thesis analyzes recent trends in SFe deposition between 1989 and 2020, demonstrating that the rise in anthropogenic fossil fuel emissions has significantly increased SFe deposition. These emissions not only elevate Fe fluxes but also enhance aerosol acidity and OX_L concentrations, making atmospheric Fe solubilization more efficient.

The analysis is extended over a longer timescale, from pre-industrial conditions to the end of the 21st century, to examine how changes in climate and emissions have influenced atmospheric aerosol acidity,

OXL production, and the magnitude and distribution of SFe deposition. Results indicate that since the pre-industrial era, SFe deposition has doubled, a trend consistent with prior studies (Hamilton et al., 2020a; Ito and Shi, 2016; Myriokefalitakis et al., 2015), and aligns with the recent decade trends observed in this work. This increase is largely attributed to a six-fold rise in fossil fuel combustion emissions, which has intensified atmospheric acidity and enhanced Fe solubilization due to elevated SO₂ emissions.

The sensitivity of SFe deposition trends to anthropogenic emissions is further highlighted through end-of-century projections that consider a range of socioeconomic pathways, representing low to high mitigation strategies. Under a low mitigation scenario, global SFe deposition is projected to increase by 40% relative to present-day levels by the late 21st century. Conversely, SFe deposition is expected to decrease by 35% and 11% under optimistic and business-as-usual scenarios, respectively. These findings underscore the critical role of scenario-based approaches in projecting future atmospheric Fe dynamics and their implications for ocean biogeochemistry.

Better constraining the impacts of changes in emission sources.

This Thesis highlights the current uncertainties in emission inventories used in climate models and explores the consequences of these uncertainties on SFe estimates.

The impact of uncertainties in future dust emissions on SFe deposition is examined through sensitivity simulations, where dust emissions are

regionally perturbed under prescribed future climate scenarios. The results reveal that changes in North African dust source regions could significantly alter the SFe deposition burden in distant regions, such as HNLC areas like the Southern Ocean and the equatorial Pacific. This underscores the critical need for better constraints on dust emission changes in Earth System Models (ESMs).

Another key uncertainty addressed is fire emissions. Current CMIP6 inventories are known to underestimate the effects of human-mediated climate change on fire activity. By using a new set of future fire emissions that comprehensively account for these changes, a substantial increase in SFe deposition in the Fe-limited North Atlantic high-latitude ocean is detected. In contrast, with the standard CMIP6 emission data, no significant changes in future SFe deposition were previously projected for this region.

These findings highlight the complex nature of accurately estimating future SFe deposition, representing a significant step forward in understanding the interplay between uncertainties in dust and fire emissions, regional variability, and climate feedbacks.

Characterize the extent and magnitude of bioavailable Fe's effects on surface ocean ecosystems

Pulsed SFe deposition events have been shown to drive notable increases in SChl concentrations, as observed through satellite data. These events highlight the role of Fe in stimulating phytoplankton growth, even across varying regions including HNLC and LNLC areas. While their direct impact on total NPP and carbon export appears limited, the

widespread SChl response underscores the importance of Fe deposition as a transient but significant factor in global surface ocean productivity.

Projections of future Fe-driven NPP in HNLC regions suggest substantial shifts by the end of the century, influenced by changing deposition rates and nutrient distributions. When analyzed alongside projected changes in other macronutrients, these findings reveal the complex interplay between Fe availability, broader nutrient dynamics, and other changing factors such as ocean warming and acidification. Understanding these interactions is essential for predicting the responses of ocean ecosystems to future climate scenarios, highlighting the need for integrated approaches that consider multiple drivers of marine productivity.

9.2. Future work

This work exemplifies the trans-disciplinary nature of nutrient Fe cycling science and the need for a better understanding of Fe's role in the Earth system across both spatial and temporal scales. The work presented in this PhD Thesis expands our knowledge of such interactions in a climate change perspective and serves as starting point for coming studies aimed to further understand it. In particular, the following ideas could be explored:

- Improve the coverage of observation data. More Fe data in the atmospheric-sea interface is needed. The episodic and localized nature of natural aerosol deposition events in marine areas sensitive to this input (Mahowald et al., 2009; Hamilton et al., 2019), along with the challenges of collecting data in remote

ocean regions (Anderson et al., 2016), make it difficult to obtain sufficient observations. This hinders our availability to validate and constrain current models and hinders our knowledge on the multiple biological, physical, and chemical processes and couplings at play.

- Recent and upcoming advancements in satellite remote sensing, marine autonomous platforms, and nutrient aerosol modeling offer promising opportunities to deepen our understanding of the aerosol-ocean biogeochemistry connection in the coming decades. Chapter 6 provides evidence of these developments, yet further efforts are needed to fully utilize the wealth of data already available to the scientific community (Hamilton et al., 2023). Newer data from recently deployed satellite platforms and argo-floats remain to be fully explored from the viewpoint of aerosol and ocean biology detection. Additionally, with both modeling and satellite systems producing vast amounts of data, there is significant potential for leveraging machine learning and other artificial intelligence techniques. These tools could accelerate scientific progress in this field, offering novel insights and enhancing the ability to predict and understand complex aerosol-ocean interactions.
- Better constraining Fe emissions requires an improved understanding of how much Fe is being emitted. This could be achieved by refining Fe emission factors by sector and examining how these factors change over time, particularly for emissions from wildfires and fossil fuel combustion, as demonstrated in previous studies such as Rathod et al. (2020); Ito et al. (2021).

Additionally, better constraints on the Fe content in soil minerals are crucial. Ongoing initiatives, such as NASA's Earth Surface Mineral Dust Source Investigation (EMIT) mission (Green et al., 2023), aim to address this need by characterizing the mineralogy of dust sources using advanced hyperspectral spectroscopy techniques. The EMIT sensor, measuring from the International Space Station (ISS) since July 2023, enables the quantification of 10 distinct soil minerals with unprecedented detail in terms of spatial resolution and geographic coverage. These advancements hold significant relevance for understanding the climate impacts of these minerals, including their role in the Fe cycle.

- To date, most research has focused on investigating the impact of single-nutrient deposition, primarily Fe, on marine ecosystems. However, to fully understand and quantify the oceanic response to aerosol nutrient deposition, multi-nutrient assessments are essential. The marine food web can respond to a variety of nutrients, and co-limitation is known to be a common phenomenon (Browning and Moore, 2023). Moreover, changes in the flux of one nutrient can shift the marine web limitation towards another nutrient, further complicating the understanding of the dynamics of marine ecosystems.
- Future observational and modeling studies should focus on better characterizing the evolution of dust emissions. Potential changes in the spatial extent of dust sources due to changes in vegetation (Mahowald, 2007), land use (Ginoux et al., 2012), and biocrusts (Rodriguez-Caballero et al., 2022) are either poorly considered or not considered at all in ESMs (Kok et al., 2023). As seen in the

perturbed dust experiments in Chapter 7, HNLC regions such as the SO and equatorial Pacific could be very sensitive to those changes.

- Dust emissions associated with wildfires, where strong, turbulent fire-related winds most likely raise dust (Hamilton et al., 2022; Wagner et al., 2018), are largely disregarded in current models. Additionally, by destroying vegetation, wildfires leave a bare source that often becomes a source of dust emission (Yu and Ginoux, 2022). Such complex interactions between fire and dust emissions are challenges to tackle in future-generation of ESMs and could have a big impact on SFe deposition estimates.

Finally, understanding the complexities of aerosol nutrient processes—spanning land emissions to remote ocean deposition and extending from the upper troposphere to the ocean depths (Fig. 9.1), requires multidisciplinary collaboration and the flexibility to adapt as new knowledge emerges (Hamilton et al., 2023). This demands open-mindedness, refined perspectives, and a willingness to rethink traditional approaches. By embracing these principles, the scientific community can gain not only a clearer understanding of nutrient cycling but also a deeper appreciation of the intricate interplay between science, society, and the natural world. The exploration of aerosol nutrient changes in the coming years promises to be exciting.

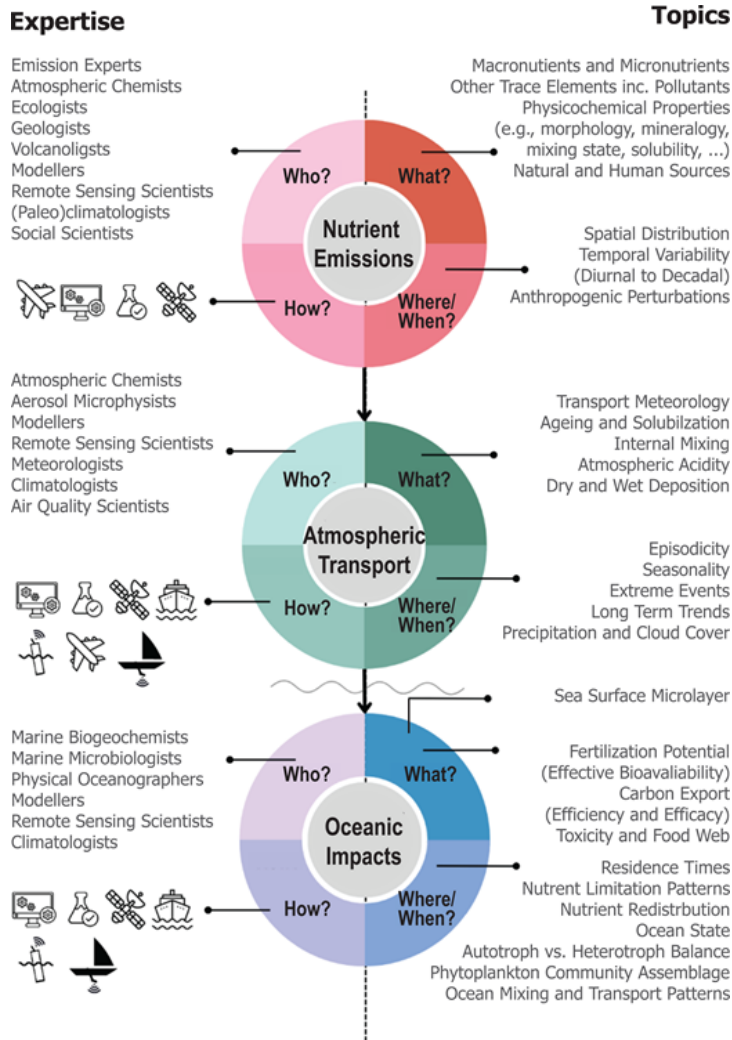


Figure 9.1: Summary schematic of the expertise and topics requiring investigation to further understand aerosol nutrient—ocean biogeochemistry links. All topics are likely to be influenced by climate change. “How?” icons pictorially represent the tools needed, as identified in the text, such as increased computing resources, laboratory measurements, and observational tools. *Extracted from Hamilton et al. (2023).*





LO

Appendices

APPENDIX A

Supplementary material

This appendix contains additional text, figures and tables mentioned along this Thesis. The goal of this appendix is to provide supportive information to the different results discussed within the Chapters. However, they are presented in an appendix to enhance the Thesis readability. The appendix A has been divided in four different Sections according to the results Chapters:

A.1 - Supplementary material for Chapter 4

A.2 - Supplementary material for Chapter 5

A.3 - Supplementary material for Chapter 6

A.4 - Supplementary material for Chapter 7

A.1. Supplementary material Chapter 4

Reg	n	nMB	nMB _{min}	nMB _{max}	nRMSE	nRMSE _{min}	nRMSE _{max}	r(log)	r(log) _{min}	r(log) _{max}
AUSP	156	-0.81	-0.81	-0.8	1.83	1.65	2.06	0.37	0.23	0.5
SAPY	69	-0.88	-0.88	-0.88	1.88	1.69	2.11	0.14	-0.02	0.29
SEAS	27	-0.44	-0.45	-0.44	1.7	1.46	2.04	-0.09	-0.32	0.15
		-0.65	-0.66	-0.65	1.69	1.45	2.02	-0.06	-0.3	0.18
		-0.37	-0.38	-0.35	1.18	0.93	1.61	0.66	0.38	0.83
		-0.55	-0.57	-0.53	1.26	1	1.72	0.67	0.4	0.84
NIND	75	1.61	1.61	1.62	2.47	2.13	2.94	-0.3	-0.5	-0.08
		1.42	1.42	1.42	2.36	2.03	2.81	-0.32	-0.51	-0.1
NACP	784	0.2	0.2	0.2	2.39	2.27	2.51	0.61	0.56	0.65
		0.59	0.59	0.59	2.66	2.54	2.8	0.64	0.59	0.68
NPAC	160	0.38	0.38	0.38	1.38	1.25	1.55	0.25	0.1	0.39
		-0.06	-0.06	-0.06	2.35	2.24	2.47	0.6	0.56	0.64
SHOC	52	0.25	0.24	0.26	2.16	1.81	2.67	-0.1	-0.36	0.18
		-0.1	-0.1	-0.09	1.79	1.5	2.21	-0.02	-0.29	0.25
SADU	36	-0.8	-0.81	-0.78	1.7	1.39	2.21	0.34	0.01	0.6
		-0.86	-0.88	-0.85	1.72	1.4	2.24	0.32	-0.01	0.59

Table A.1: **Model evaluation statistics across regions of SFe surface concentrations.** Normalized Mean Bias (nMB), normalized Root Mean Square Error (nRMSE), and correlation in logarithmic base (r(log)) between monthly observations and model outputs of soluble iron (SFe) surface concentrations. The table presents estimates for each region (Reg), including the corresponding number of data points (n) and lower and upper 95% confidence intervals for each statistic. The first row of each region depicts results for daily mean monthly values compared to observations, while the second row shows daily median monthly values.

Appendix A. Supplementary material

Reg	n	nMB	nMB _{min}	nMB _{max}	nRMSE	nRMSE _{min}	nRMSE _{max}	r(log)	r(log) _{min}	r(log) _{max}
AUSP	175	-0.37	-0.37	-0.37	1.79	1.62	2	0.62	0.53	0.71
SAPY	53	-0.76	-0.76	-0.76	1.58	1.43	1.77	0.56	0.45	0.66
SEAS	33	-0.72	-0.73	-0.71	1.45	1.21	1.78	-0.04	-0.3	0.24
		-0.84	-0.84	-0.83	1.47	1.24	1.82	0.03	-0.24	0.3
		0.45	0.44	0.46	1.5	1.21	1.97	0.67	0.42	0.82
		-0.18	-0.19	-0.17	1.31	1.05	1.72	0.66	0.41	0.82
NIND	75	0.35	0.35	0.35	1.36	1.17	1.61	0.41	0.21	0.59
		0.1	0.1	0.1	0.98	0.85	1.17	0.48	0.28	0.64
NACP	634	0.71	0.71	0.71	5.99	5.68	6.34	0.68	0.64	0.72
		-0.13	-0.13	-0.13	5.4	5.12	5.72	0.71	0.66	0.74
NPAC	178	0.67	0.67	0.67	1.94	1.75	2.16	0.48	0.36	0.59
		0.3	0.29	0.3	1.64	1.49	1.83	0.47	0.34	0.58
SHOC	55	-0.78	-0.78	-0.77	1.09	0.92	1.34	0.38	0.12	0.58
		-0.86	-0.86	-0.85	1.14	0.96	1.4	0.38	0.13	0.59
SADU	31	-0.09	-0.11	-0.08	1.83	1.46	2.43	0.5	0.17	0.72
		-0.68	-0.69	-0.66	1.34	1.08	1.79	0.48	0.15	0.71

Table A.2: **Model evaluation statistics across regions of Fe surface concentrations.** Normalized Mean Bias (nMB), normalized Root Mean Square Error (nRMSE), and correlation in logarithmic base (r(log)) between monthly observations and model outputs of iron (Fe) surface concentrations. The table presents estimates for each region (Reg), including the corresponding number of data points (n) and lower and upper 95% confidence intervals for each statistic. The first row of each region depicts results for daily mean monthly values compared to observations, while the second row shows daily median monthly values.

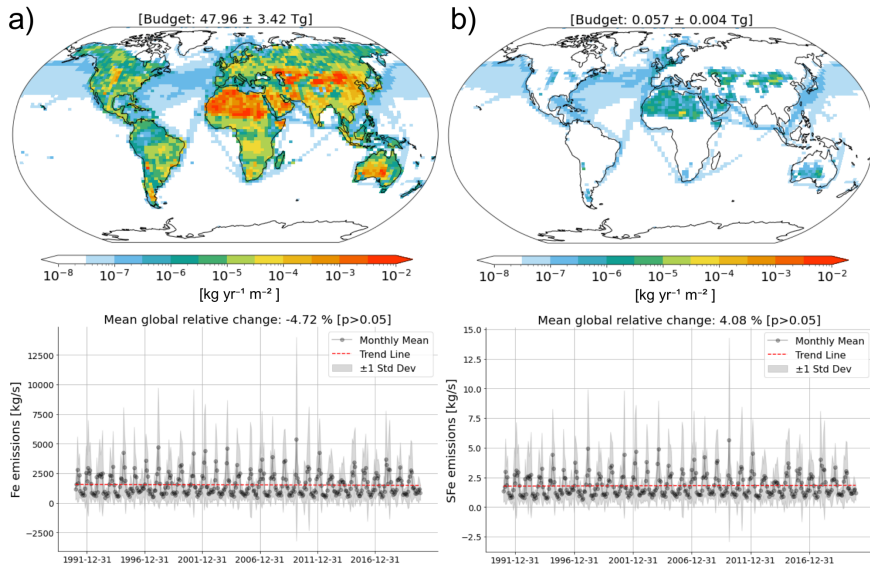


Figure A.1: **Fe and SFe emissions distribution and trends.** Mean annual emissions for the period 1991–2020 for total iron (Fe) (a), soluble Fe (SFe) (b). The global mean annual budget (in Tg) is shown in brackets above each map. The global mean monthly flux (in kg/s) over the period is depicted in black, with the grey-shaded area representing ± 1 standard deviation around the monthly median. The red line indicates the long-term trend, computed using linear regression. Global relative changes are shown and are calculated conservatively as the absolute change divided by the period mean. The p-values for the trend lines from the linear regression indicate whether the trends are statistically significant ($p < 0.05$) or not ($p \geq 0.05$).

Appendix A. Supplementary material

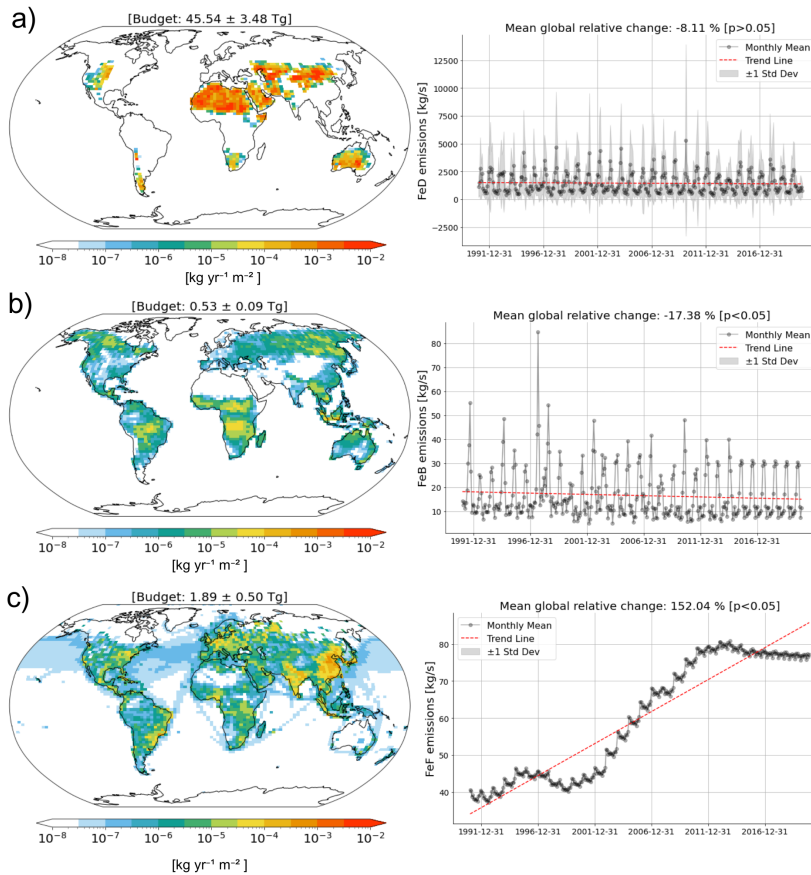


Figure A.2: **Fe emissions distribution and trends by source.** Mean annual emissions for the period 1991–2020 for iron (SFe) sourcing from dust (a), fire (b), and fossil-fuel-combustion (c). The global mean annual budget (in Tg) is shown in brackets above each map. The global mean monthly flux (in kg/s) over the period is depicted in black, with the grey-shaded area representing ± 1 standard deviation around the monthly median. The red line indicates the long-term trend, computed using linear regression. Global relative changes are shown and are calculated conservatively as the absolute change divided by the period mean. The p-values for the trend lines from the linear regression indicate whether the trends are statistically significant ($p < 0.05$) or not ($p \geq 0.05$).

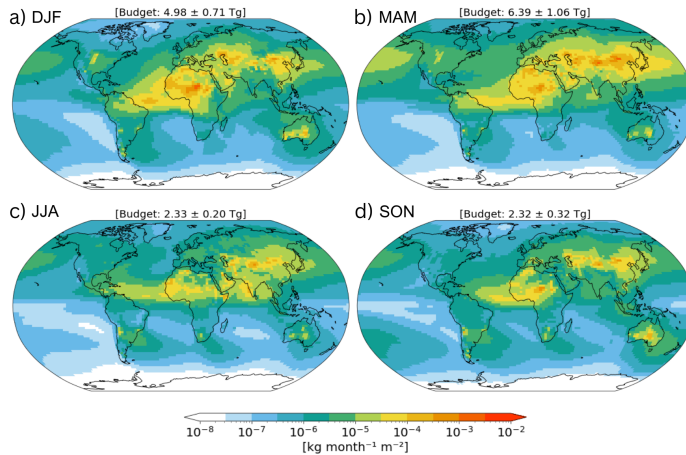


Figure A.3: **Seasonal SFe deposition.** Seasonal mean (1991–2020) soluble iron (SFe) deposition for (a) DJF, (b) MAM, (c) JJA, and (d) SON, derived from the EC-Earth3-Iron reconstruction. Global mean monthly budgets (in Tg) with standard deviation are shown above each map.

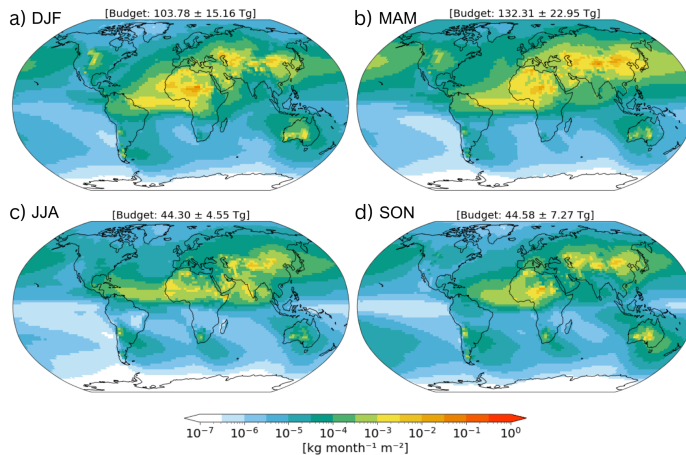


Figure A.4: **Seasonal Fe deposition.** Seasonal mean (1991–2020) iron (Fe) deposition for (a) DJF, (b) MAM, (c) JJA, and (d) SON, derived from the EC-Earth3-Iron reconstruction. Global mean monthly budgets (in Tg) with standard deviation are shown above each map.

Appendix A. Supplementary material

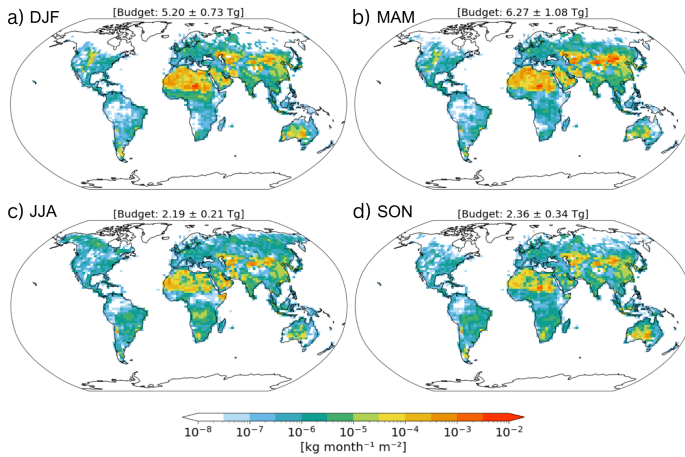


Figure A.5: **Seasonal Fe emission.** Seasonal mean (1991–2020) iron (Fe) emission for (a) DJF, (b) MAM, (c) JJA, and (d) SON, derived from the EC-Earth3-Iron reconstruction. Global mean monthly budgets (in Tg) with standard deviation are shown above each map.

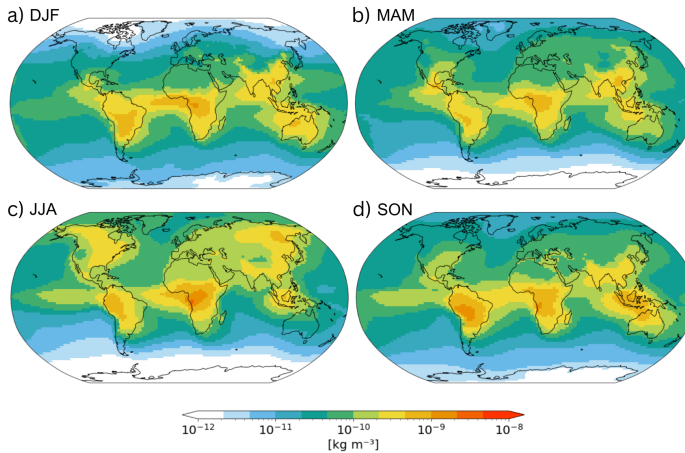


Figure A.6: **Seasonal OXL surface concentration.** Seasonal mean (1991–2020) oxalate (OXL) surface concentrations $[\text{kg}/\text{m}^{-3}]$ for (a) DJF, (b) MAM, (c) JJA, and (d) SON, derived from the EC-Earth3-Iron reconstruction.

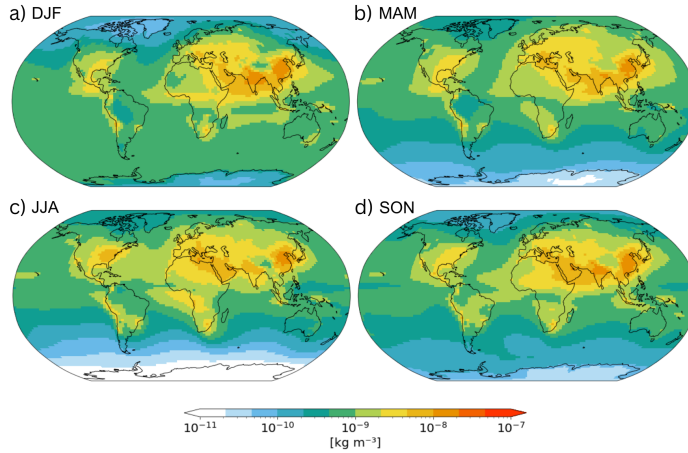


Figure A.7: **Seasonal SO_4 surface concentration.** Seasonal mean (1991–2020) sulfate (SO_4) surface concentrations [kg m^{-3}] for (a) DJF, (b) MAM, (c) JJA, and (d) SON, derived from the EC-Earth3-Iron reconstruction.

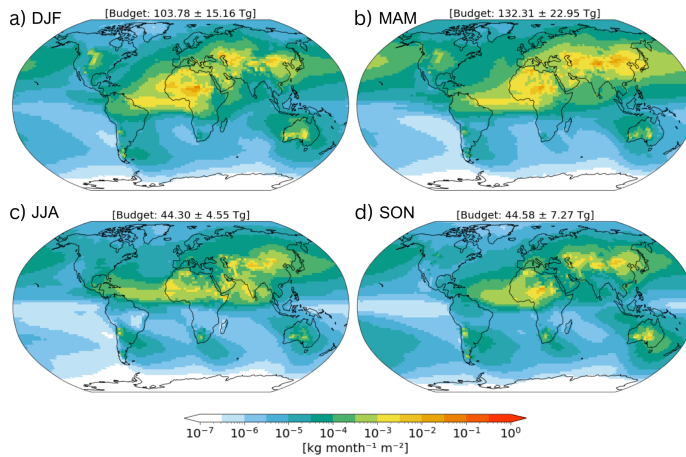


Figure A.8: **Seasonal dust deposition.** Seasonal mean (1991–2020) dust deposition for (a) DJF, (b) MAM, (c) JJA, and (d) SON, derived from the EC-Earth3-Iron reconstruction. Global mean monthly budgets (in Tg) with standard deviation are shown above each map.

Appendix A. Supplementary material

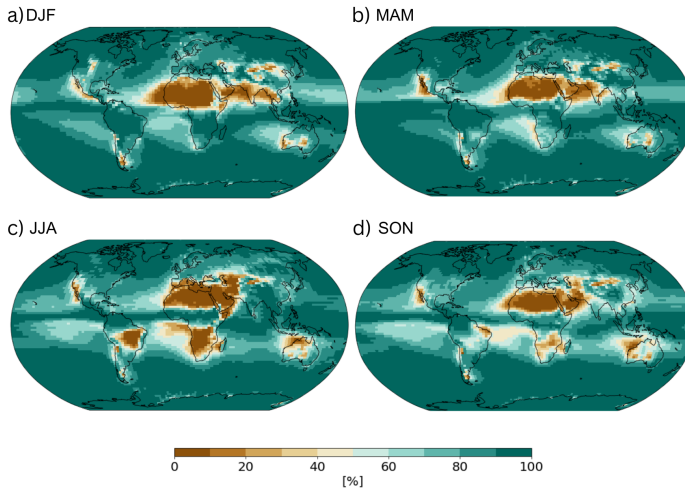


Figure A.9: **Seasonal percentage of wet SFe deposition.** Seasonal mean (1991–2020) percentage of soluble iron (SFe) wet deposition over total deposition (wet and dry) for (a) DJF, (b) MAM, (c) JJA, and (d) SON, derived from the EC-Earth3-Iron reconstruction.

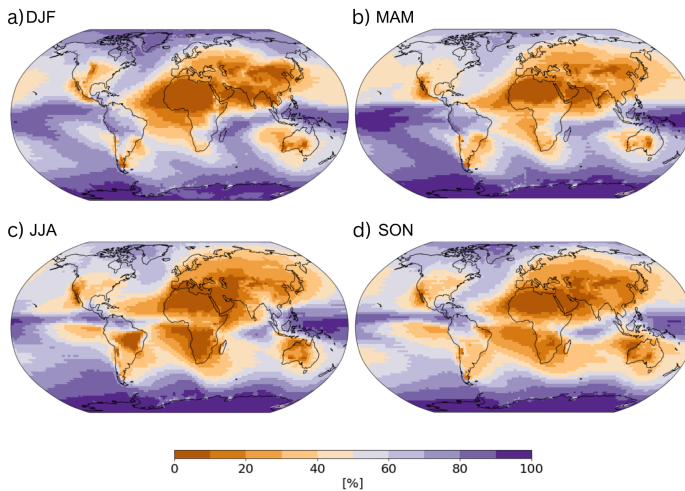


Figure A.10: **Seasonal percentage of SFe deposition in the accumulation mode** Seasonal mean (1991–2020) percentage of soluble iron (SFe) deposition in the accumulation mode over total deposition (accumulation and coarse) for (a) DJF, (b) MAM, (c) JJA, and (d) SON, derived from the EC-Earth3-Iron reconstruction.

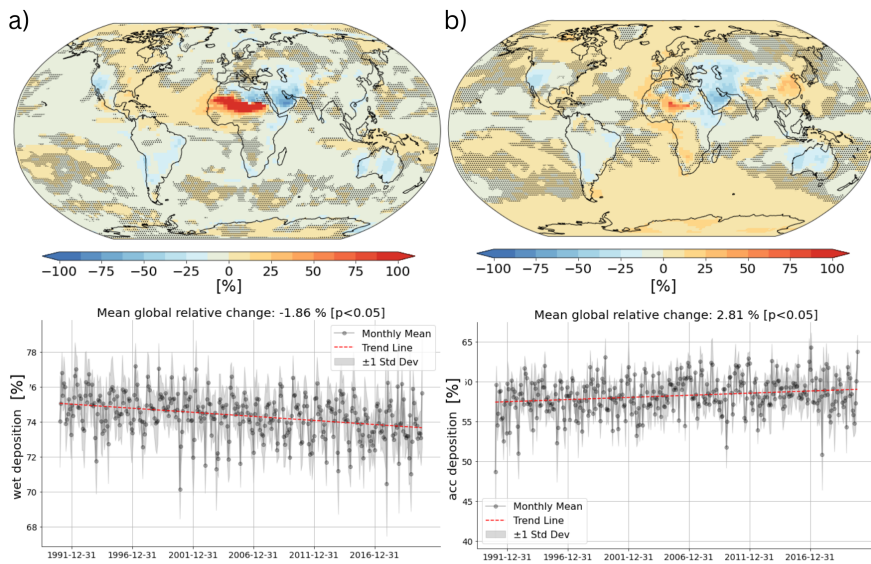


Figure A.11: **Trends in size mode deposition and deposition type.** Relative changes in the percentage of wet deposition over total deposition (a) and accumulation mode deposition over total deposition (b), as derived from the reconstruction using EC-Earth3-Iron. The maps display trends for each grid cell, with areas marked by dots indicating regions where the computed trends are not statistically significant (t-test, $p > 0.05$). At the bottom of each map, the time evolution of each variable is shown, with monthly mean values represented by dots and the variability within each month depicted by shaded gray areas. The global mean computed trend is shown in red.

Appendix A. Supplementary material

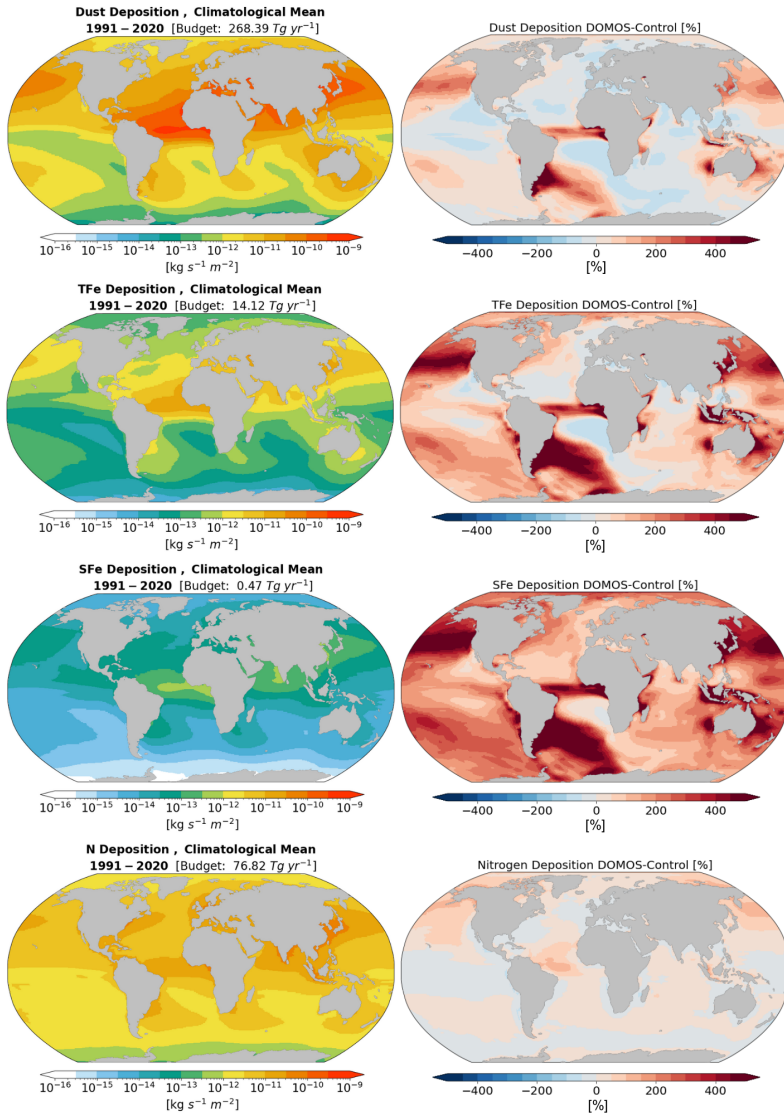


Figure A.12: **Comparison of ocean biogeochemistry inputs: control vs. EC-Earth3-Iron reconstruction.** The left column shows mean annual fields (1991–2020) from the EC-Earth3-Iron reconstruction used as input for the PISCES ocean biogeochemistry model: dust deposition, total iron (Fe) deposition, soluble iron (SFe) deposition, and nitrogen (N) deposition (from top to bottom). The right column depicts the relative changes between the EC-Earth3-Iron reconstruction fields and those typically prescribed in the PISCES model.

A.2. Supplementary material Chapter 5

Marine Biomes

In order to characterize the impact of atmospheric deposition inputs in regions with different sensitivity, the North Atlantic region is further divided into multiple sub-regions or ocean biomes (Fig. A.13): Polar, Mid-high latitudes, oligotrophic, equatorial, and upwelling. These five different biomes, defined following Henson et al. (2010) and using ESA's 21-year long surface chlorophyll dataset (OC-CCIv4), divide the global ocean by surface phytoplankton seasonality and magnitude.

Polar biomes are characterized by strong seasonal light limitation, which results in pronounced phytoplankton blooms during short periods of high light availability. Mid-high latitude biomes, while also susceptible to light limitation during winter months, exhibit strong seasonal phytoplankton blooms that are influenced by nutrient availability and mixed-layer dynamics.

Oligotrophic biomes, primarily located in subtropical gyres, are characterized by low nutrient availability and correspondingly low phytoplankton biomass throughout the year. These regions exhibit relatively stable, stratified conditions, leading to limited vertical nutrient exchange.

Equatorial biomes are defined by relatively consistent year-round light availability but are distinguished by varying nutrient dynamics due to equatorial divergence and trade wind patterns. These dynamics often result in moderate to high levels of primary production compared to

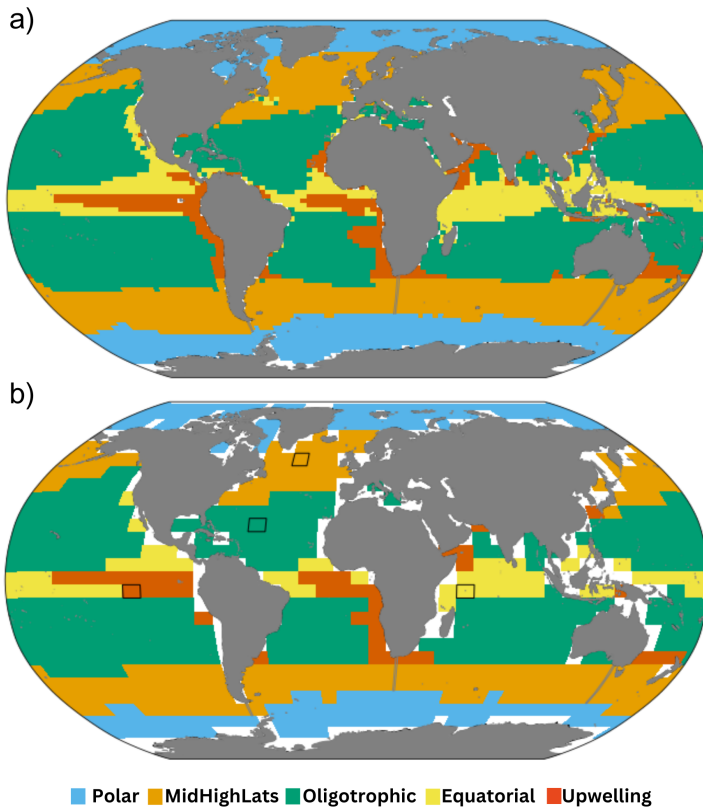


Figure A.13: **Ocean biomes.** Regional division of the ocean based on ocean biomes following Henson et al. (2010), displayed on a $2 \times 3^\circ$ grid (a) and $6 \times 9^\circ$ grid (b). Grid cells highlighted in Fig. A.14, A.15, A.16, A.17 are outlined in black in b.

oligotrophic regions.

Upwelling biomes are regions of intense nutrient enrichment caused by wind-driven coastal upwelling, which brings nutrient-rich deep waters to the surface. These areas are among the most productive in the ocean

The biomes can be further divided by hemisphere and ocean basin except for polar oceans biomes where no division by ocean basin is

done in this work. With resulting 18 sub-biomes: NH polar, SH polar, Mid-High latitudes North Atlantic, Mid-High latitudes North Pacific, Mid-High latitudes South Atlantic, Mid-High latitudes South Pacific, Mid-High latitudes Indian, Oligotrophic North Atlantic, Oligotrophic North Pacific, Oligotrophic South Atlantic, Oligotrophic South Pacific, Oligotrophic Indian, Oligotrophic Arabian Sea and Bay of Bengal, Upwelling Atlantic, Upwelling Pacific, Equatorial Atlantic, Equatorial Pacific, Equatorial Indian.

Appendix A. Supplementary material

Upwelling Pacific, [120°W-111°W, 8°S-2°S]

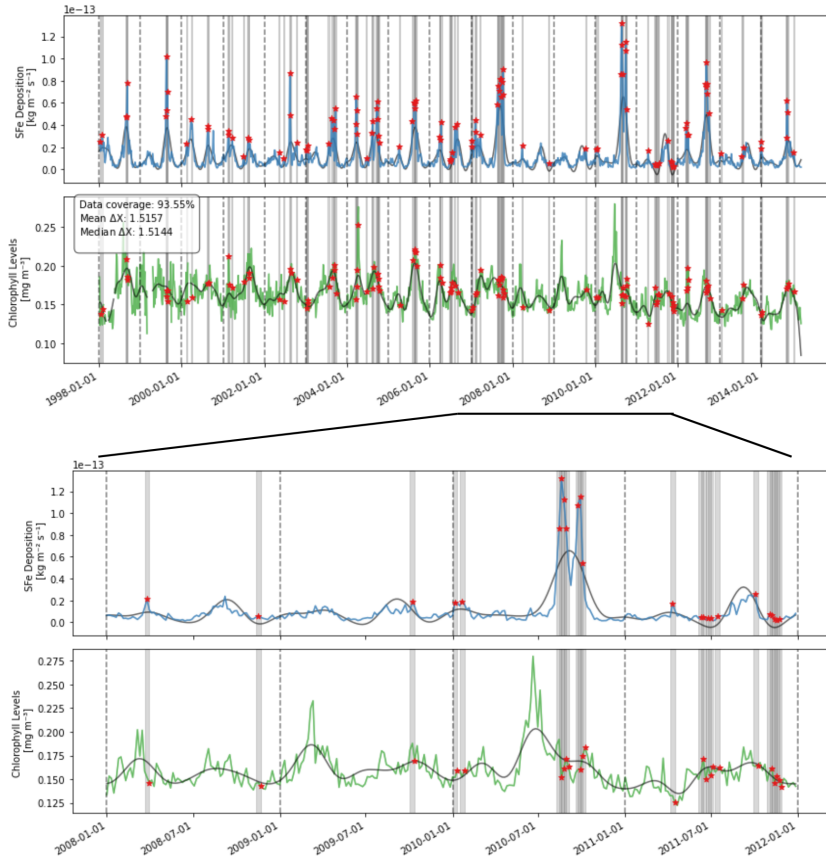


Figure A.14: **Modelled SFe deposition and satellite-derived SChl from 1998 to 2014 in a region of the upwelling Pacific.** Modeled soluble iron (SFe) deposition (blue) and satellite-derived surface chlorophyll-a (SChl) concentration (green) from 1998 to 2014 at a 5-day frequency for a grid cell in the upwelling Pacific. The combined interannual and seasonal components are shown in black, while the intraseasonal signal corresponds to the difference between the colored lines and the black line. Red points represent the top 10% of SFe deposition events, and gray shaded areas indicate the 0–10 day period following SFe deposition. A zoomed view of the 2008–2011 period is shown below.

Equatorial Indian, [51°E-60°E, 8°S-2°S]

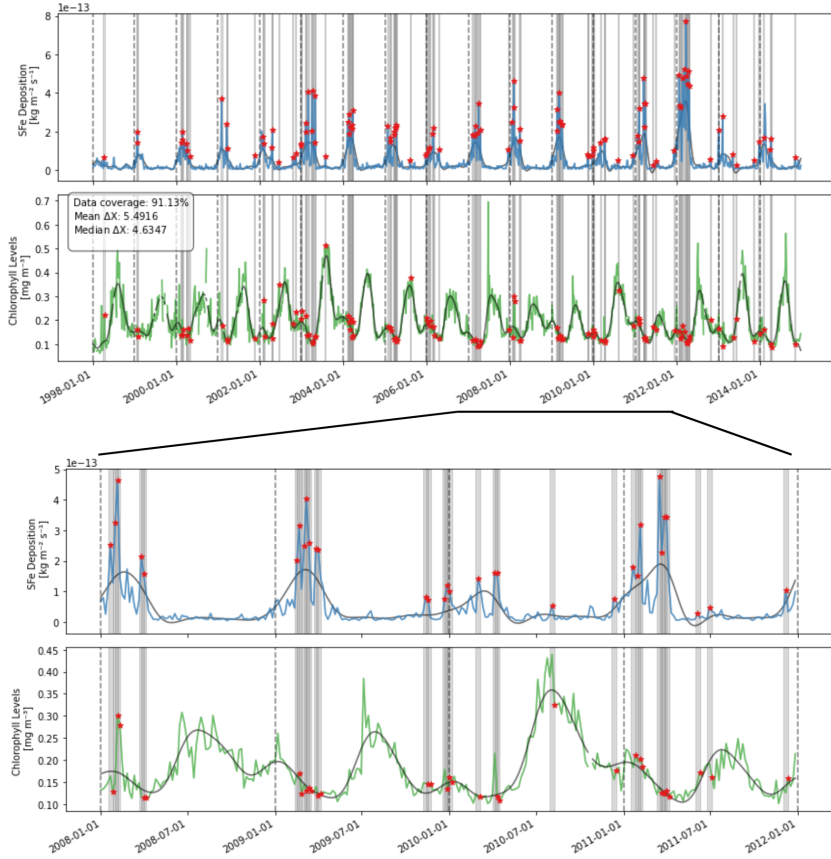


Figure A.15: **Modelled SFe deposition and satellite-derived SChl from 1998 to 2014 in a region of the equatorial Indian ocean.** Modeled soluble iron (SFe) deposition (blue) and satellite-derived surface chlorophyll-a (SChl) concentration (green) from 1998 to 2014 at a 5-day frequency for a grid cell in the equatorial Indian ocean. The combined interannual and seasonal components are shown in black, while the intraseasonal signal corresponds to the difference between the colored lines and the black line. Red points represent the top 10% of SFe deposition events, and gray shaded areas indicate the 0–10 day period following SFe deposition. A zoomed view of the 2008–2011 period is shown below.

Appendix A. Supplementary material

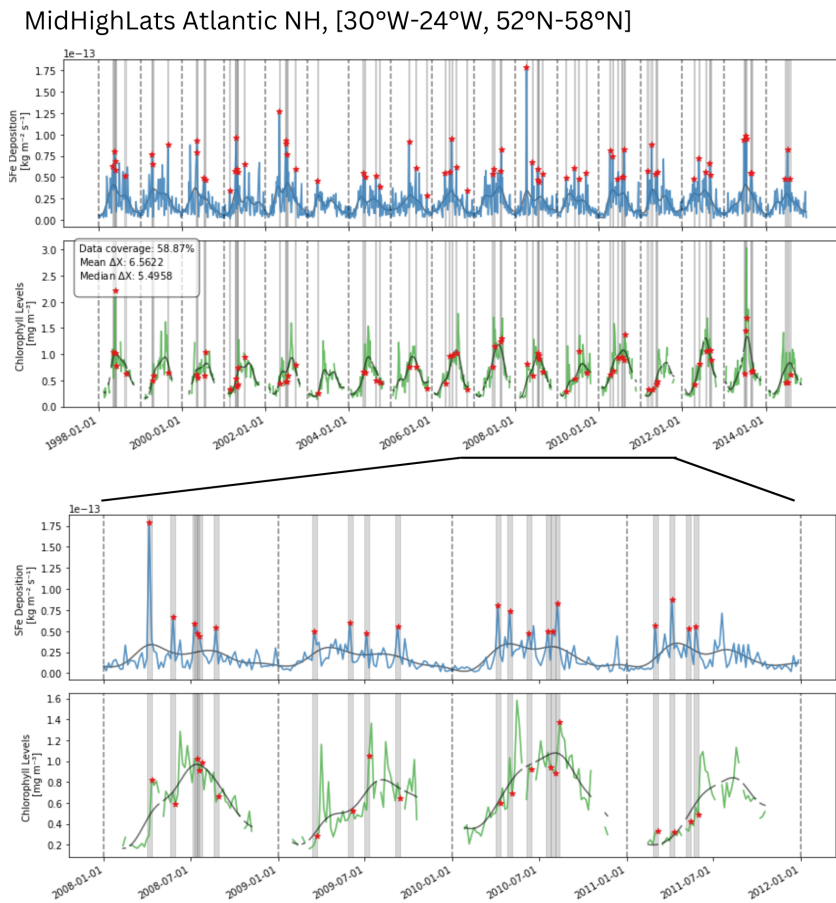


Figure A.16: **Modelled SFe deposition and satellite-derived SChl from 1998 to 2014 in a region of the mid-high-latitudes of the NH Atlantic.** Modeled soluble iron (SFe) deposition (blue) and satellite-derived surface chlorophyll-a (SChl) concentration (green) from 1998 to 2014 at a 5-day frequency for a grid cell in the mid-high-latitudes of the NH Atlantic. The combined interannual and seasonal components are shown in black, while the intraseasonal signal corresponds to the difference between the colored lines and the black line. Red points represent the top 10% of SFe deposition events, and gray shaded areas indicate the 0–10 day period following SFe deposition. A zoomed view of the 2008–2011 period is shown below.

Oligotrophic Atlantic NH, [48W-39°W, 22°N-28°N]

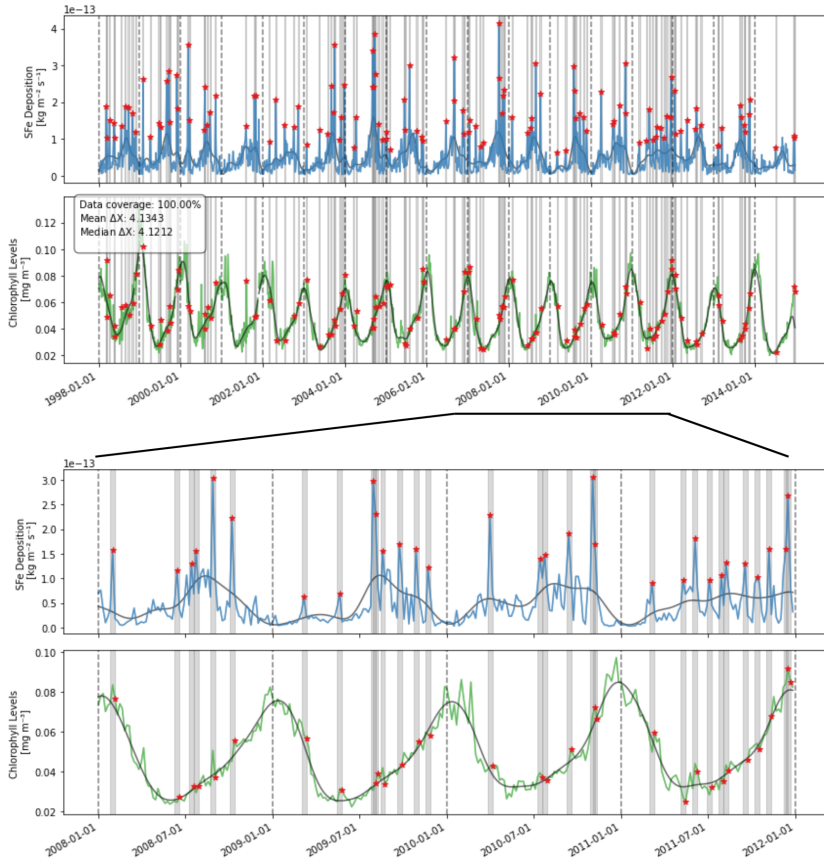


Figure A.17: **Modelled SFe deposition and satellite-derived SChl from 1998 to 2014 in a region of the oligotrophic NH Atlantic.** Modelled soluble iron (SFe) deposition (blue) and satellite-derived surface chlorophyll-a (SChl) concentration (green) from 1998 to 2014 at a 5-day frequency for a grid cell in the oligotrophic NH Atlantic. The combined interannual and seasonal components are shown in black, while the intraseasonal signal corresponds to the difference between the colored lines and the black line. Red points represent the top 10% of SFe deposition events, and gray shaded areas indicate the 0–10 day period following SFe deposition. A zoomed view of the 2008–2011 period is shown below.

Appendix A. Supplementary material

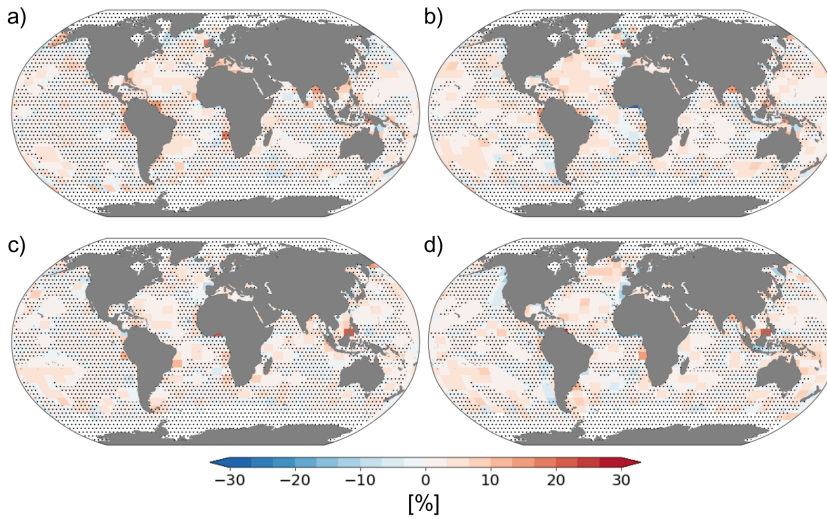


Figure A.18: **SChl response to high dust and SFe by source deposition events** The median surface chlorophyll (SChl) response is computed following the approach proposed in this study (Eq. 6.2) to top 10% dust deposition events (a), soluble iron (SFe) from dust deposition events (b), SFe from fires (c) deposition events and SFe from fossil fuel deposition events (d). Pointed areas indicate regions where the median responses are not statistically significant ($p > 0.05$) compared to a random 10% sample of SFe deposition events outside the top 10% window, based on a Kruskal-Wallis test.

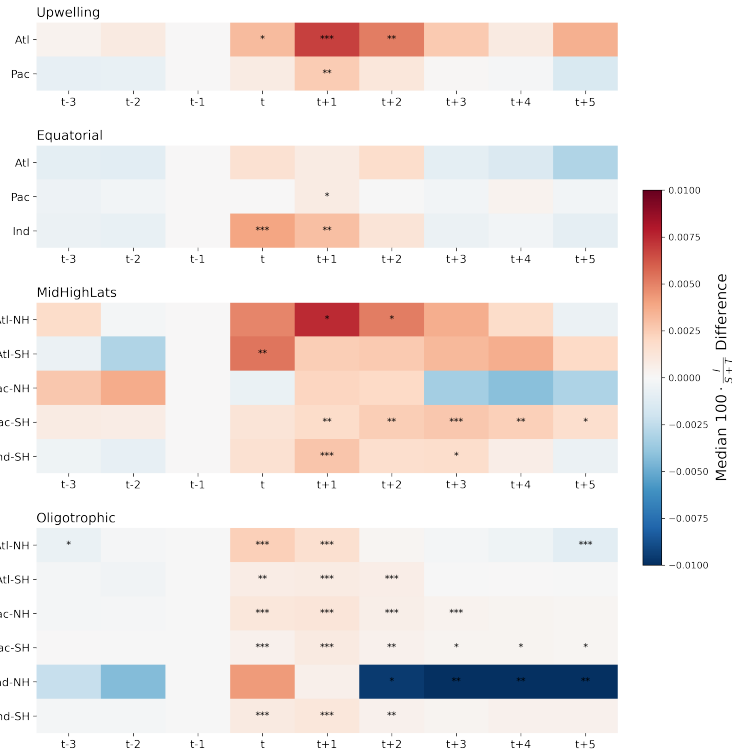


Figure A.19: **Timeline of SChl response to top dust deposition events.** Difference between the median surface chlorophyll (SChl) I_{rel} values for the time step t of the high dust deposition event and previous ($t-2$, $t-3$) and subsequent ($t+1$, $t+2$, $t+3$, $t+4$, $t+5$) time steps and the median I_{rel} for $t-1$. Significance levels (from Kruskal-Wallis testing) expressed by asterisks (***) for p-value ≤ 0.001 , ** for p-value ≤ 0.01 , * for p-value ≤ 0.05).

Appendix A. Supplementary material

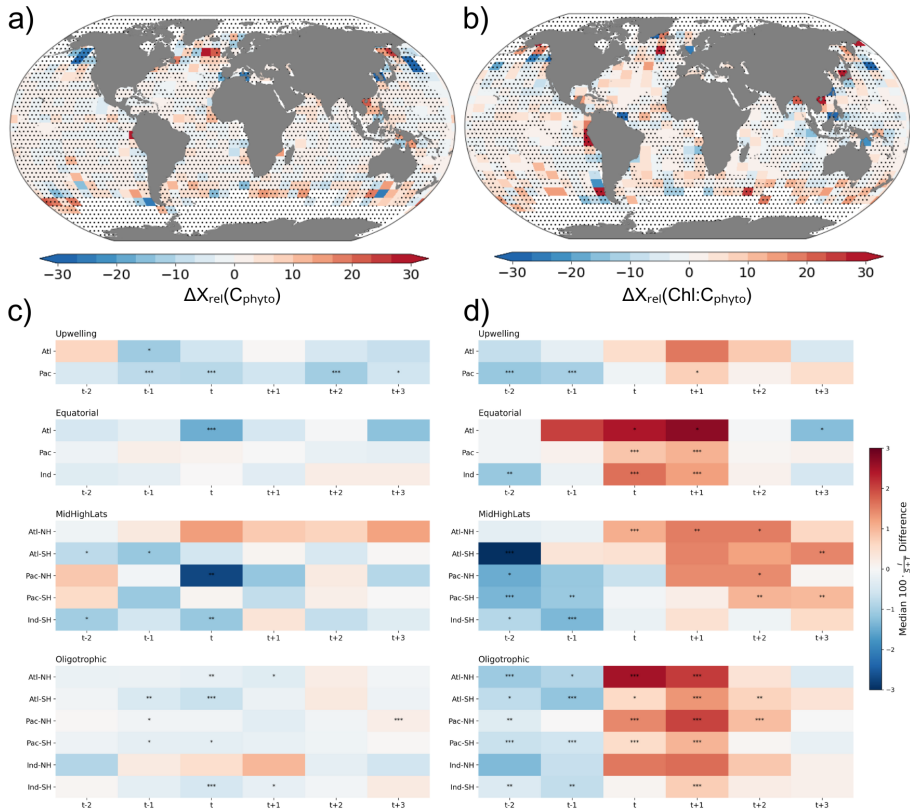


Figure A.20: C_{phyto} and $SChl : C_{phyto}$ response to top SFe deposition events. Median phytoplankton biomass (C_{phyto}) (a) and surface chlorophyll-phytoplankton biomass fraction ($SChl : C_{phyto}$) (b) response to the top 10% of soluble iron (SFe) deposition events computed as in Eq. 6.2. Pointed areas indicate regions where the median responses are not statistically significant ($p > 0.05$) compared to a random 10% sample of SFe deposition events outside the top 10% window, based on a Kruskal-Wallis test. Difference between the median I_{rel} values for the time step t of the high deposition event and previous ($t-1, t-2, t-3, t-4, t-5, t-6, t-7, t-8$) and subsequent ($t+1, t+2, t+3, t+4, t+5, t+6, t+7, t+8, t+9$) time steps and median I_{rel} for a random sample of events outside the top 10% for (c) C_{phyto} and (d) $SChl : C_{phyto}$. Significance levels (from Kruskal-Wallis testing) expressed by asterisks (***) for p-value ≤ 0.001 , ** for p-value ≤ 0.01 , * for p-value ≤ 0.05 .

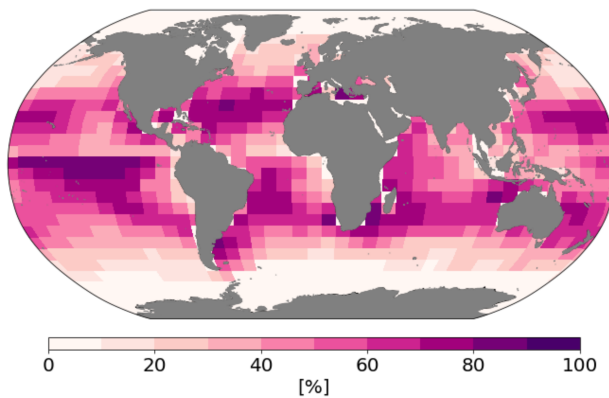


Figure A.21: **Percentage of bbp443 data in time serie.** Percentage of available particulate backscattering coefficient at 443nm (bbp443) data from the ESA OC-CCI version 6 between 1st of January 1998 to 31 December 2014 for 6x9 ° gridcell resolution. Polar oceans are masked based on ocean biome regions (see Section A)

Appendix A. Supplementary material

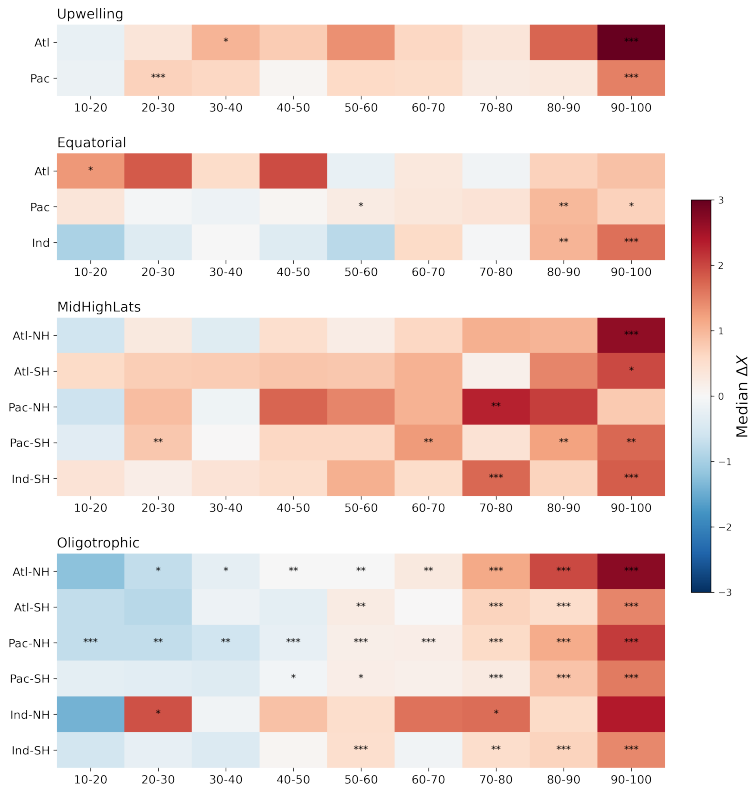


Figure A.22: **SChl response to dust deposition events by percentile.** Regional median surface chlorophyll (SChl) ΔX_{rel} values after dust deposition events divided by deposition percentiles. Significance levels (from Kruskal-Wallis testing) expressed by asterisks (***) for p-value ≤ 0.001 , ** for p-value ≤ 0.01 , * for p-value ≤ 0.05).

A.3. Supplementary material Chapter 6

Data Analysis

Relative Differences between Scenarios

When comparing fields from different scenarios, the PD simulation is always taken as reference. Differences in fields of extensive variables are shown as relative differences in % as in Equation 1.

$$RD(X)_{simulation_i} = \frac{X_{simulation_i} - X_{PD}}{X_{PD}} \cdot 100 \quad (\text{A.1})$$

where $RD(X)_{simulation_i}$ refers to the relative difference of variable X for the $simulation_i$. $X_{simulation_i}$ and X_{PD} is the mean value among ensemble members of the variable X for the $simulation_i$ and the PD simulation respectively.

Statistical Test

When representing relative changes between simulations with its spatial distribution, a statistical test is carried on to only show relative changes that are statistically significant. Here we use the t-test to compare the 30 ensemble values in each grid cell between simulations. The level of statistical significance is expressed as a p-value between 0 and 1. Following this procedure, we mask all grid-cells where p-values are lower than 0.05 (Student, 1908).

Ensemble spread

To have a measure of the ensemble spread (e.g., the difference between the 30 members of the same ensemble) we compute the standard deviation (σ) with respect to the ensemble mean (X) as shown in Equation 2.

$$\sigma = \sqrt{\frac{1}{N} \sum_{i=1}^N (x_i - X)^2} \quad (\text{A.2})$$

where N is the number of ensemble members, x_i is the value of a variable x in a grid cell for the member i , and X is the ensemble mean for that variable x in that grid cell.

Acidity in terms of the pH

The acidity level of a solution can be quantified based on the thermodynamic activity of dissolved hydrogen ions (H^+). This measure of acidity is reported as a dimensionless quantity known as the pH. Here we use pH as a diagnostic of acidity computed based on the H^+ molality (m_{H^+}):

$$\text{pH} = -\log_{10}(m_{\text{H}^+}) \quad (\text{A.3})$$

Annual mean pH values are computed by averaging monthly pH diagnosed from modelled monthly H^+ molality. As a result, all data points with monthly aerosol water equal to 0 are not considered in the calculation. An additional masking is applied to the monthly pH values to avoid unrealistically acidic pH estimates. These arise fundamentally from situations where the relative humidity and the aerosol water content are very low, which result in highly concentrated aqueous

phases, far from the ideal state, and in which the thermodynamic models hold the largest uncertainties. To partially correct for this issue, we impose a minimum monthly pH of 1 to produce the annual mean pH diagnostics (i.e., all monthly values below 1 are set to 1). This default value is selected following a conservative approach, because the Fe dissolution rates are independent of the pH for extremely acidic solutions Chen and Grassian (2013).

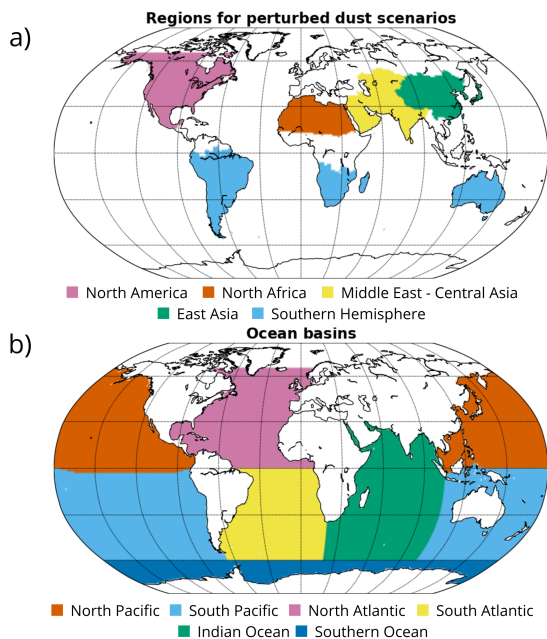


Figure A.23: **Region definition.** Regions defined for (a) perturbed dust scenarios and (b) analysis of deposition in different ocean basins. Regions are based on the defined ones by the HTAP project Koffi et al. (2016)

Appendix A. Supplementary material

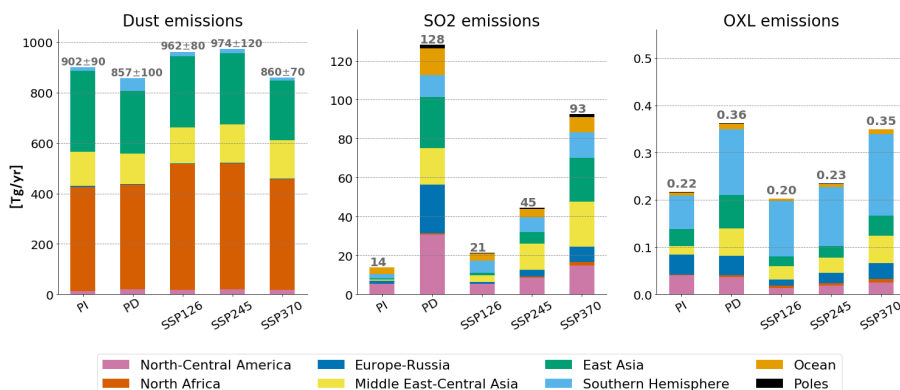


Figure A.24: **Dust, SO₂ and OXL emissions.** Mean annual emissions in Tg/yr of dust (right figure), sulfur dioxide (SO₂) (middle figure) and oxalate (OXL) (right figure) for each of the simulations considered. The different colors represent the contribution of the different HTAP regions considered to the total emission budget.

Table A.3: **Fe deposition budgets.** Annual deposition rates of total iron (Fe) and soluble Fe (Tg Fe/yr) over the open ocean for pre-industrial (PI), present day (PD) and future (FU) time in this study and in the literature.

	TFe	SFe		
	PD	PI	PD	FU
<i>This study</i>	12.1 (± 1.4)	0.21 (± 0.01)	0.41 (± 0.01)	0.27-0.56
<i>Myriokefalitakis et al. (2020)</i>		0.18-0.23	0.28-0.35	0.24-0.30
<i>Hamilton et al. (2020a)</i>		0.46-0.70	0.70-0.76	0.77
<i>Hamilton et al. (2019)</i>	12-26		0.50-0.53	
<i>Ito et al. (2019)</i>	16 (± 7)		0.26 (± 0.12)	
<i>Myriokefalitakis et al. (2018)</i>	17 (± 7)		0.30 (± 0.09)	
<i>Scanza et al. (2018)</i>	18.5		0.59	
<i>Ito and Shi (2016)</i>	10.2	0.051-0.067	0.11-0.12	
<i>Myriokefalitakis et al. (2015)</i>	6.964	0.063	0.19	0.136
<i>Johnson and Meskhidze (2013)</i>			0.26	
<i>Luo and Gao (2010)</i>			0.34	
<i>Luo et al. (2008)</i>		0.1	0.21	

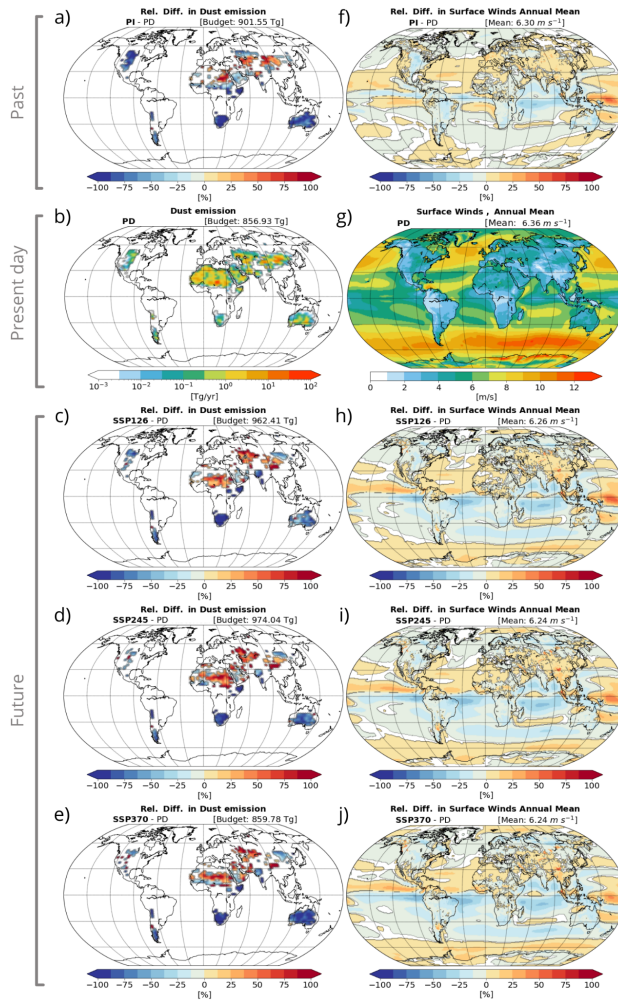


Figure A.25: **Dust emission and surface winds.** Mean annual dust emission (Tg/yr) for the PD simulation (b) and relative differences (%) in the estimates for the PI (a) and the future scenarios SSP1-2.6 (c), SSP2-4.5 (d), and SSP3-7.0 (e) with respect to the PD, mean annual surface winds (m s^{-1}) for the PD simulation (g) and relative differences (%) in the estimates for the PI (f) and the future scenarios SSP1-2.6 (h), SSP2-4.5 (i), and SSP3-7.0 (j) with respect to the PD (f,h,i,j).

Appendix A. Supplementary material

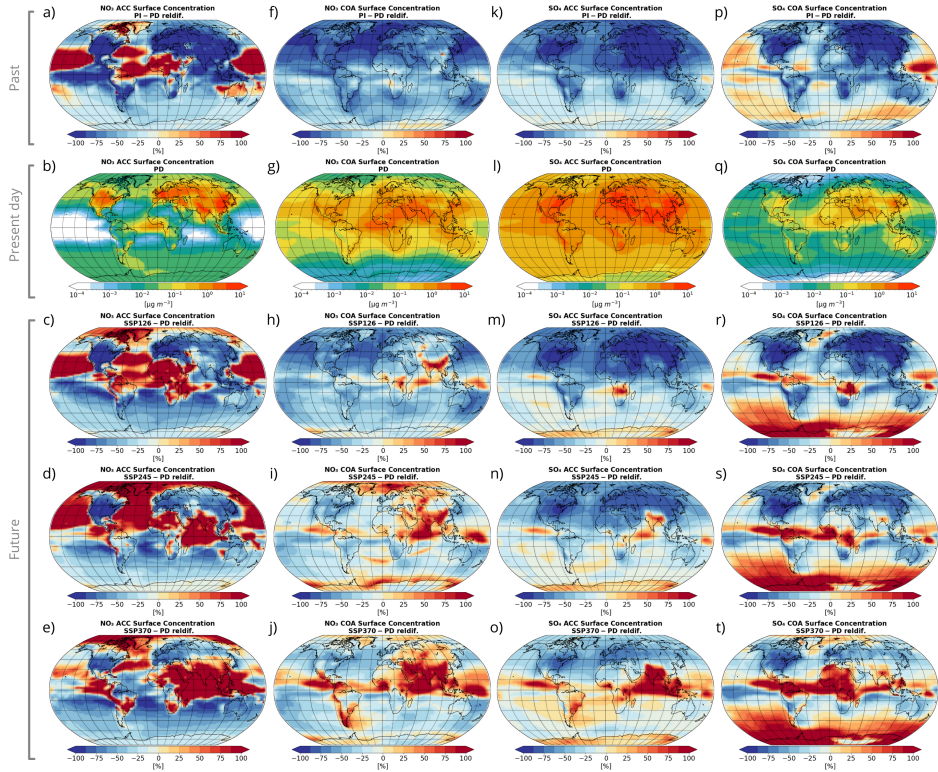


Figure A.26: **Surface concentrations of nitrate and SO_4 .** Left column shows nitrate for accumulation mode, second column shows nitrate for coarse mode, third column shows SO_4 for accumulation mode, and right column shows SO_4 for coarse mode. Units are in micrograms per cubic meter ($\mu\text{g}/\text{m}^3$) for present-day (PD) conditions and relative differences (%) for past and future scenarios (PI, SSP126, SSP245, and SSP370).

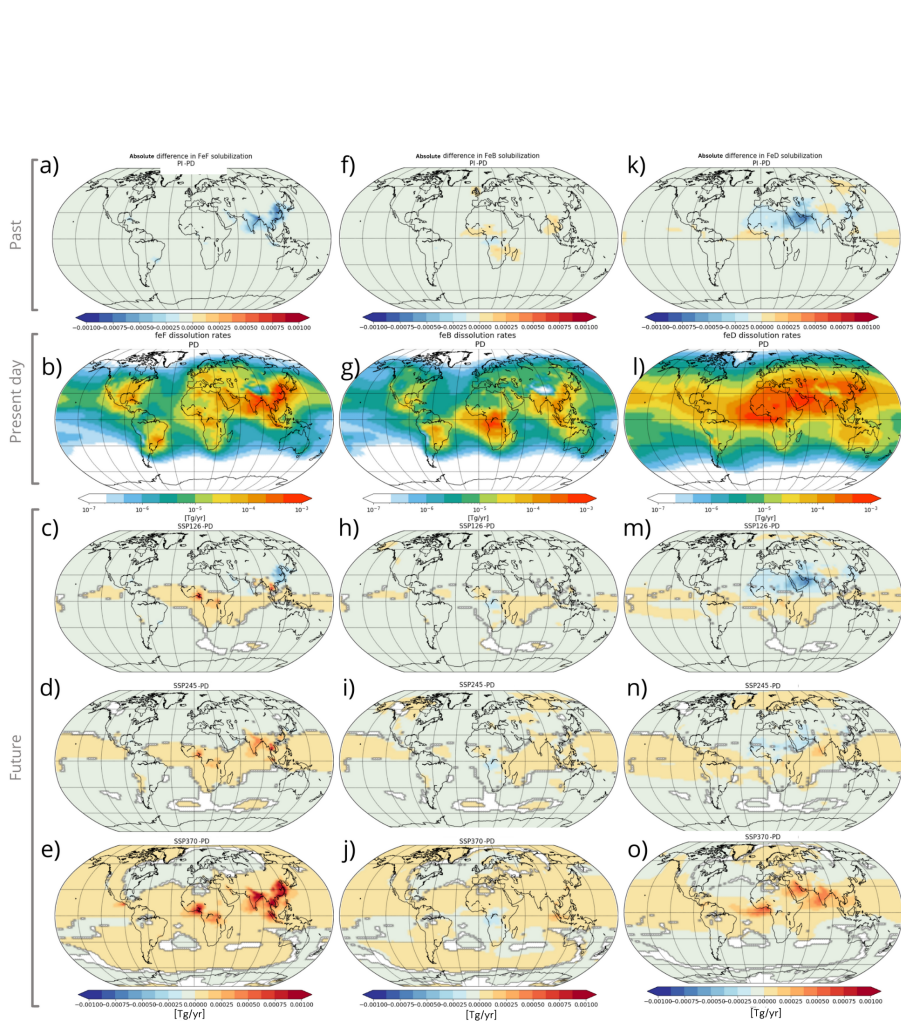


Figure A.27: **Fe dissolution rates by Fe source.** Mean annual dissolution rate for PD for iron (Fe) from fossil fuels (FeF) (b), fires (FeB) (g) and dust (FeD) (l) for the PD. Absolute differences of the mean annual dissolution rate for FeF, FeB and FeD in the PI (a,f,k), and the future scenarios SSP1-2.6 (c,h,m), SSP2-4.5 (d,i,n) and SSP3-7.0 (e,j,o) with respect to the PD.

Appendix A. Supplementary material

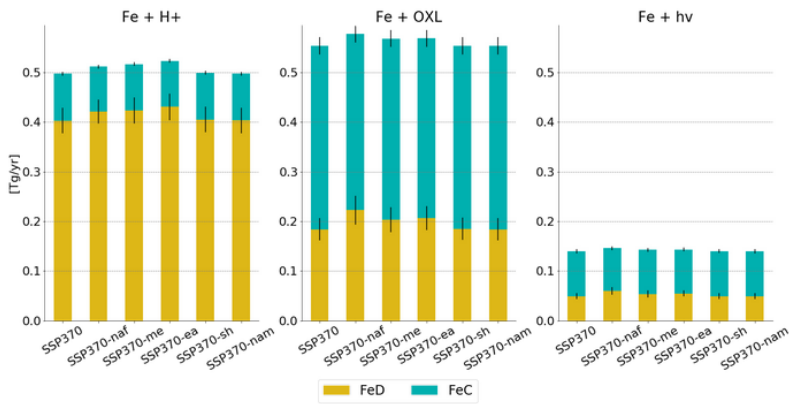


Figure A.28: **Fe solubilization budgets for the different perturbed-dust scenarios and atmospheric processing mechanisms:** acidic dissolution (left), oxalate (OXL)-promoted dissolution (middle), and photoreductive dissolution budgets (right). Solubilization of iron (Fe) from dust sources (FeD) is represented with the yellow-orange colour and solubilization of Fe from combustion sources (FeC) (i.e., both from biomass burning, FeB, and anthropogenic sources, FeF) is represented in blue-green colour. Black bars indicate the budget spread for the 30 ensemble members.

Table A.4: **Fe emission budgets.** Annual emission rates of total iron (Fe) (Tg Fe/yr) from dust, anthropogenic and fire sources for pre-industrial (PI), present day (PD) and future (FU) time in this study and in the literature. (*) Fossil fuels and fires are counted together.

	Dust iron			Anthropogenic iron			Fire iron		
	PI	PD	FU	PI	PD	FU	PI	PD	FU
<i>This study</i>	42 (± 4)	40 (± 5)	40-46	0.08	1.75	0.97-3.11	0.46	0.52	0.33-0.47
<i>Rathod et al. (2020)</i>					2.2				
<i>Hamilton et al. (2020a)</i>	36	57	57	$0.7 \cdot 10^{-3} - 0.13$	0.68 - 3.4	2.4	1.5 - 2.7	0.94	2.3
<i>Hamilton et al. (2019)</i>		57-130			0.66 - 3.3			1.2 - 2.2	
<i>Scanza et al. (2018)</i>		56.9 - 62.0			2.1 (± 0.51)*				
<i>Myriokefalitakis et al. (2018)</i>		71.5 (± 42.69)			2.1 (± 0.51)*				
<i>Ito and Shi (2016) (2016)</i>	69	69		0.28	0.712		0.66	0.66	
<i>Myriokefalitakis et al. (2015)</i>	35.048	35.048	35.048	0.147	0.768	0.158	0.120	1.200	1.456
<i>Wang et al. (2015)</i>		38.5 - 41			1.2 - 7.2			0.16 - 1.27	
<i>Luo et al. (2008)</i>		54.76						1.07	

A.4. Supplementary material Chapter 7

Model Evaluation

The model evaluation (for both models) against observations was conducted following the guidelines outlined in Section 4.3.

Global statistics are shown in Figure in A.29 and regional statistics in Table A.5 and A.6. Relying exclusively on the mean values of the nMB, nRMSE and r to compare with the two model experiments could be misleading, especially for those cases with a low number of observations. Therefore, we incorporate to our assessment the information of the number of data points that are available to produce these metrics (n) and their uncertainty ranges at a 95% confidence level.

Our comparison of diagnosed soluble and total iron with surface concentration observations reveals several key findings. Firstly, both models effectively capture the global mean observational spatial distribution of total iron concentration with correlation coefficients of 0.7. However, on average, both models tend to overestimate the mean surface concentrations of both iron (Fe) and soluble iron (SFe). CAM6-MIMI demonstrates a greater overestimation in many regions compared to EC-Earth3-Iron in total Fe surface concentration in dust-dominated regions due to larger magnitude dust emissions in this model (Fig. A.42). Nonetheless, both models slightly overestimate SFe concentrations. In terms of solubility, lower regional average solubilities are shown in CAM6-MIMI compared to EC-Earth3-Iron (Fig. A.29). Additionally, EC-Earth3-Iron exhibits a greater spread in average solubilities than CAM6-MIMI, which might be due to its more

complex dissolution scheme.

Regionally, distinct patterns emerge. In certain areas of the SO, such as SADU, both models underestimate Fe and SFe surface concentrations. Conversely, in regions like A USP, SAPY, and SHOC, EC-Earth3-Iron underestimates Fe surface concentrations while CAM6-MIMI overestimates them, possibly due to higher dust surface concentrations in CAM6-MIMI (Fig. A.30). These regions also exhibit less correlation in both models, suggesting that future model improvements and observational campaigns can be focused here. Furthermore, in the NIND region, both models overestimate Fe and SFe surface concentrations, potentially linked to an overestimation of fossil fuel sources. Regions dominated by predominant dust sources, such as NACP, show overestimated SFe and Fe surface concentrations in both models, with CAM6-MIMI demonstrating a more pronounced overestimation. These regional variations highlight the complexities involved in modeling iron concentrations, influenced by factors such as dust sources, fossil fuel emissions, and regional dynamics. Understanding these nuances is crucial for improving the accuracy of global iron cycle models and their implications for biogeochemical processes.

Appendix A. Supplementary material

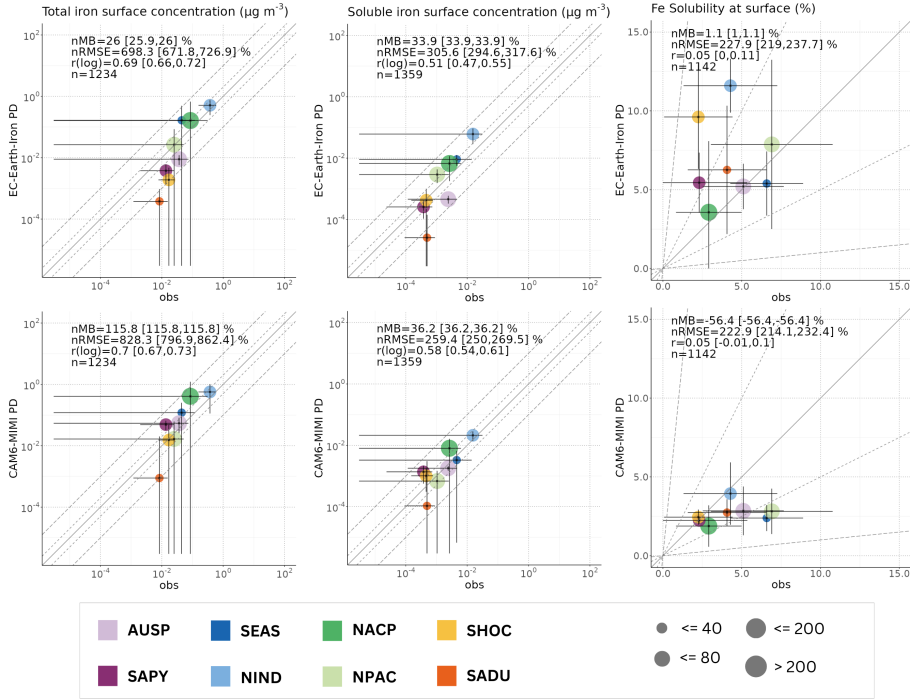


Figure A.29: **Evaluation of Fe surface concentrations.** Median value of surface concentrations of total iron (Fe) (left column), soluble iron (SFe) (middle column) and solubilities (right column) for model (EC-Earth3-Iron upper row, CAM6-MIMI lower row) and observations as compiled by Hamilton et al. 2022 Hamilton et al. (2022) for each region. Regions are depicted in Fig.4.1. The size of each coloured point shows number of observations corresponding to that region. Error bars indicate the interquartile range for each region. Global statistics are shown, where n is the number of total measurements, nRMSE is the normalized root mean square error, nMB is the normalized mean bias, and r is the correlation over all the points. The ranges for the nMB, nRMSE and r correspond to the 95% confidence level. Dashed lines represent differences of 2 times and 1 order of magnitude.

Reg	n	nMB	nMB _{min}	nMB _{max}	nRMSE	nRMSE _{min}	nRMSE _{max}	r(log)	r(log) _{min}	r(log) _{max}
AUSP	156	-0.82	-0.82	-0.82	1.84	1.66	2.07	0.46	0.33	0.58
SAPY	69	-0.44	-0.44	-0.44	1.74	1.57	1.96	0.67	0.57	0.75
SEAS	27	-0.38	-0.39	-0.38	1.72	1.47	2.06	-0.07	-0.3	0.17
		1.36	1.36	1.37	2.75	2.36	3.3	-0.08	-0.31	0.16
	27	-0.21	-0.23	-0.19	1.1	0.87	1.5	0.67	0.39	0.84
		-0.58	-0.6	-0.57	1.3	1.02	1.76	0.6	0.28	0.8
NIND	75	1.93	1.93	1.94	2.9	2.5	3.46	-0.34	-0.53	-0.13
		0.05	0.05	0.05	1.22	1.06	1.46	-0.43	-0.6	-0.23
NACP	784	0.08	0.08	0.08	2.43	2.32	2.56	0.6	0.56	0.64
		0.59	0.59	0.59	2.66	2.54	2.8	0.64	0.59	0.68
NPAC	160	0.45	0.45	0.45	1.4	1.26	1.57	0.32	0.17	0.45
		-0.47	-0.47	-0.47	1.21	1.09	1.36	0.59	0.47	0.68
SHOC	52	0.29	0.28	0.29	2.19	1.84	2.72	-0.09	-0.35	0.19
		1.36	1.36	1.37	2.75	2.36	3.3	-0.08	-0.31	0.16
SADU	36	-0.77	-0.78	-0.75	1.71	1.39	2.22	0.34	0.02	0.6
		-0.44	-0.44	-0.44	1.74	1.57	1.96	0.67	0.57	0.75

Table A-5: **Model evaluation statistics across regions of SFe surface concentrations.** Normalized Mean Bias (nMB), normalized Root Mean Square Error (nRMSE), and correlation in logarithmic base (r(log)) between monthly observations and model outputs of soluble iron (SFe) surface concentrations. The table presents estimates for each region (Reg), including the corresponding number of data points (n) and lower and upper 95% confidence intervals for each statistic. The first row of each region depicts results for EC-Earth3-Iron compared to observations, while the second row shows statistics for CAM6-MIM1.

Appendix A. Supplementary material

Reg	n	nMB	nMB _{min}	nMB _{max}	nRMSE	nRMSE _{min}	nRMSE _{max}	r(log)	r(log) _{min}	r(log) _{max}
AUSP	175	-0.46	-0.46	-0.46	1.71	1.55	1.91	0.63	0.53	0.71
SAPY	53	1.53	1.52	1.53	5.53	5.01	6.18	0.69	0.6	0.76
SEAS	33	-0.66	-0.66	-0.65	1.44	1.21	1.77	-0.01	-0.28	0.26
NIND	75	2.68	2.64	2.71	6.86	5.76	8.46	0.01	-0.26	0.28
NACP	634	1.64	1.61	1.66	2.98	2.4	3.92	0.69	0.46	0.84
NPAC	178	0.49	0.49	0.49	1.6	1.29	2.1	0.68	0.44	0.83
SHOC	55	0.15	0.15	0.15	0.86	0.74	1.02	0.49	0.3	0.65
SADU	31	1	0.99	1.01	2.68	2.31	3.19	0.42	0.22	0.59
		0.27	0.27	0.27	5.6	5.31	5.93	0.69	0.65	0.73
		1.17	1.17	1.17	6.62	6.28	7.01	0.7	0.66	0.74
		0.69	0.69	0.69	1.93	1.75	2.15	0.49	0.37	0.6
		0.08	0.08	0.08	1.49	1.35	1.66	0.48	0.36	0.59
		-0.78	-0.78	-0.77	1.11	0.94	1.37	0.36	0.11	0.57
		0.7	0.69	0.71	2.18	1.84	2.68	0.33	0.07	0.55
		0.07	0.05	0.09	2.05	1.65	2.73	0.51	0.19	0.73
		15.34	14.91	15.76	38.53	30.89	51.23	0.51	0.19	0.73

Table A.6: **Model evaluation statistics across regions of Fe surface concentrations.** Normalized Mean Bias (nMB), normalized Root Mean Square Error (nRMSE), and correlation in logarithmic base ($r(\log)$) between monthly observations and model outputs for total iron (Fe) surface observations. The table presents estimates for each region (Reg), including the corresponding number of data points (n) and lower and upper 95% confidence intervals for each statistic. The first row of each region depicts results for EC-Earth3-Iron compared to observations, while the second row shows statistics for CAM6-MIM1.

Table A.7: **Differences between CAM6-MIMI and EC-Earth3-Iron.** Summary of major key differences between the CAM6-MIMI and the EC-Earth3-Iron models.

	CAM6-MIM	EC-EARTH3-Iron
Horizontal resolution	1.25° x 0.9375°	3.0° x 2.0°
Vertical resolution	56 vertical levels	34 vertical levels
Atmospheric Reanalysis	MERRA2	ERA5
Aerosol Modes	modal aerosol	Modal size (lognormal) distribution, fine and coarse mode with mass median radii (lognormal standard deviation) of 0.34 μm (1.59) and 1.75 μm (2.00), respectively
Dust		
Mineralogy	Claquin et al. (1999)	Claquin et al. (1999) including the updates in Nickovic et al. (2012).
Fe content in minerals	Journet et al. (2008) as adopted by Ito and Xu (2014)	Nickovic et al. (2013)
OXL	Assumed oxalate concentration based on secondary organic carbon	Online chemical formation of OXL in cloud droplets and aerosol water in the fine and coarse modes, along with a low contribution of primary emissions from natural and anthropogenic wood-burning processes
Aerosol pH	Size dependent, estimated $[\text{H}^+]$ calculated from the ratio of sulfate to calcite, and temperature	Size dependent (fine and coarse modes) on-line calculated based on thermodynamic model ISORROPIA II (Fountoukis and Nenes, 2007) and kinetic limitations via mass transfer and transport between the gas and the particulate phases in accumulation and coarse modes (Pringle et al., 2010).

Appendix A. Supplementary material

fire Fe speciation	Fe:(BC) factors applied for combustion emissions (both for fires and fossil fuel combustion) Fossil fuels combustion follow Rathod et al. (2020) and Klimont et al (2017). Fire emissions follow Hamilton et al (2019)	Fe:(OC+BC) factors applied for combustion emissions (both for fires and fossil fuel combustion) following Ito et al. (2018) and Hajima et al. (2019) (Table S1 in Myriokefalitakis et al 2022).
fire Fe injection heights	Set fractional distribution of emissions heights for fires by biome (Dentener et al., 2006)	Distributed over model layers using the vertical profiles from Table A1 in van Noije et al. (2014).
fire Fe particle size distribution at emission	13.95% of emissions in the fine mode	21.505% of emissions in the fine mode
fire Fe solubility at emission	33% solubility in fine mode, 4% solubility in coarse mode	0% solubility
Fe dissolution pools	FeD: med and slow dissolution pools, fast dissolution pool is already soluble at emission, FeC	FeD: fast, med and slow dissolution pools, FeC
Dissolution scheme	proton- and organic-ligand-promoted iron dissolution mechanisms dependant on Temperature, pH proxy and OXL proxy	proton- , organic-ligand-promoted and photoreductive iron dissolution mechanisms dependant on Temperature, online computed pH and online computed OXL

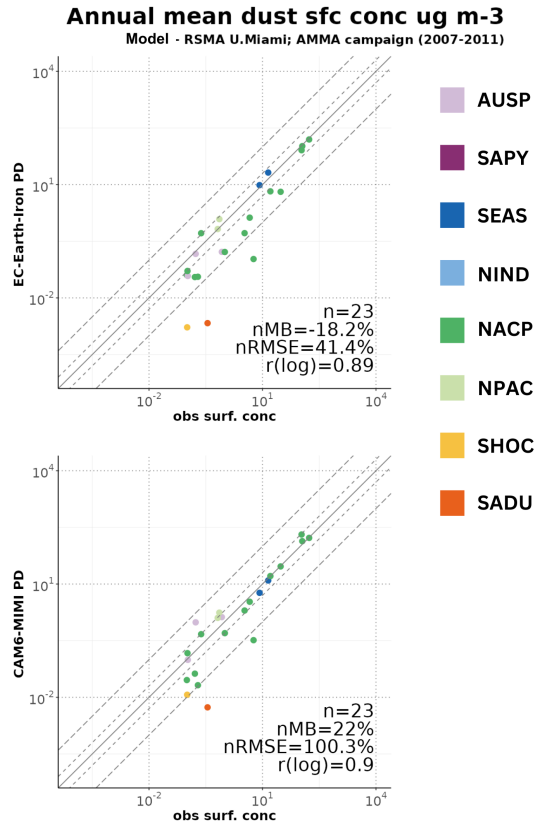


Figure A.30: **Modeled dust surface concentration against observations** Dust surface concentrations ($\mu\text{g m}^{-3}$) for EC-Earth3-Iron upper figure and CAM6-MIMI lower figure compared to observations from the RSMAS and AMMA databases. Colors indicate the observation point regions as defined in Fig.4.1. Where n is the number of measurements, nRMSE the normalized root mean square error, nMB the normalized mean bias, and r the correlation over all the points. The ranges for nMB, nRMSE and r correspond to the 95% confidence level

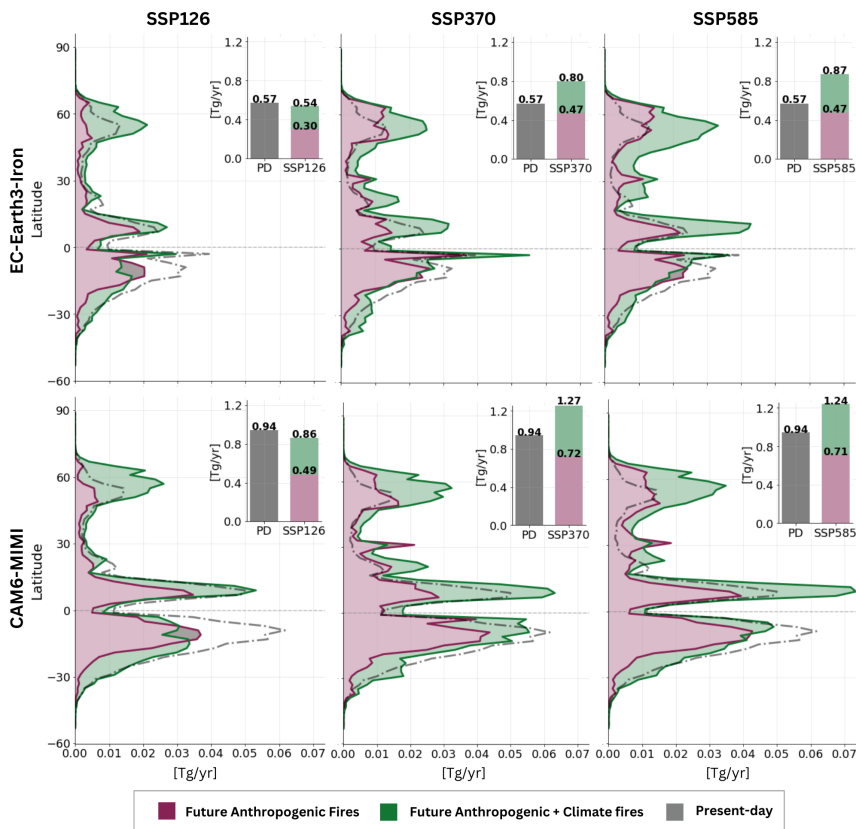


Figure A.31: **Fire-Fe emissions.** Fire iron (Fe) emissions by latitude for each scenario (SSP126, SSP370, SSP585, from left to right) and model (EC-Earth3-Iron and CAM6-MIMI from top to bottom). Purple-colored lines and shading represent emissions attributed to anthropogenic fires, while green-colored lines and shading represent emissions attributed to climate-driven fires. Present-day emissions are depicted in gray dashed lines. Bar plots illustrate the global emission budget of fire iron emissions.

		Emissions	Fire Emissions	Simulation Name
		SIMULATIONS Atmospheric nudging (2007-2011) EC-Earth3-Iron CAM6-MIMI		Present-day (2001-2010)
	GFED4s			PD
SSP1-2.6 (2091-2100)	no fires			SSP126-noFires
	CMIP6 fires			SSP126
	new Fires			SSP126-wNatFires
SSP3-7.0 (2091-2100)	no fires			SSP370-noFires
	CMIP6 fires			SSP370
	new Fires			SSP370-wNatFires
SSP5-8.5 (2091-2100)	no fires			SSP585-noFires
	CMIP6 fires			SSP585
	new Fires	SSP585-wNatFires		
AMIP-like meteo EC-Earth3-Iron		Emissions / SIC & SST	Fire Emissions	Simulation Name
		Present-day (2001-2010)	GFED4s	PD-AMIP
		SSP1-2.6 (2091-2100)	new Fires	SSP126-wNatFires-AMIP
		SSP3-7.0 (2091-2100)	new Fires	SSP370-wNatFires-AMIP
		SSP5-8.5 (2091-2100)	new Fires	SSP585-wNatFires-AMIP

Figure A.32: **Summary of simulations.** Model simulations conducted for this work, specifying the non-fire emission scenarios used, the time frame for the prescribed emissions, the fire emissions used, and the prescribed meteorological conditions.

Appendix A. Supplementary material

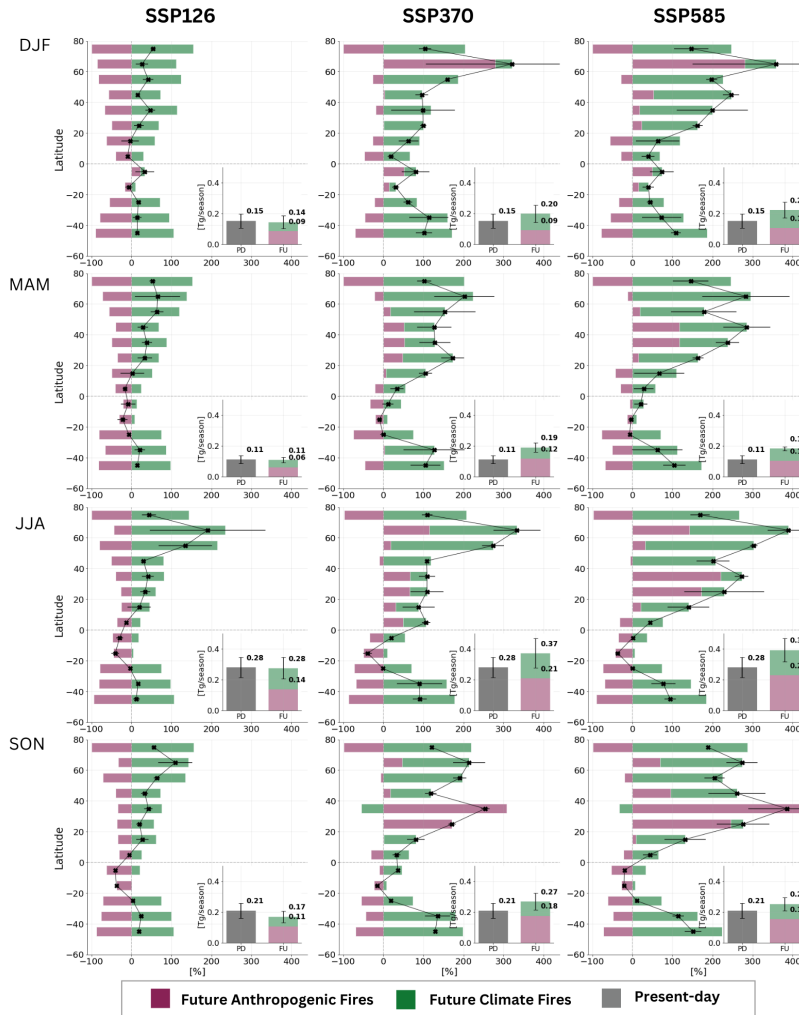


Figure A.33: **Future seasonal changes in fire Fe emissions.** Model-derived changes in fire iron (Fe) emissions relative to present-day estimates by 10° latitude bands for each season (DJF, MAM, JJA, SON, from top to bottom) and scenario (SSP126, SSP370, SSP585, from left to right) in black. Purple-colored bars denote the contribution of anthropogenic fires to future changes, while green bars illustrate the influence of climate-driven fires. Bar plots in the lower right corner display global emission budgets in Tg/yr of fire Fe emissions for present-day (depicted in gray) and end-of-the-century scenarios for each SSP. Black dots show the model mean and error bars indicate the model differences.

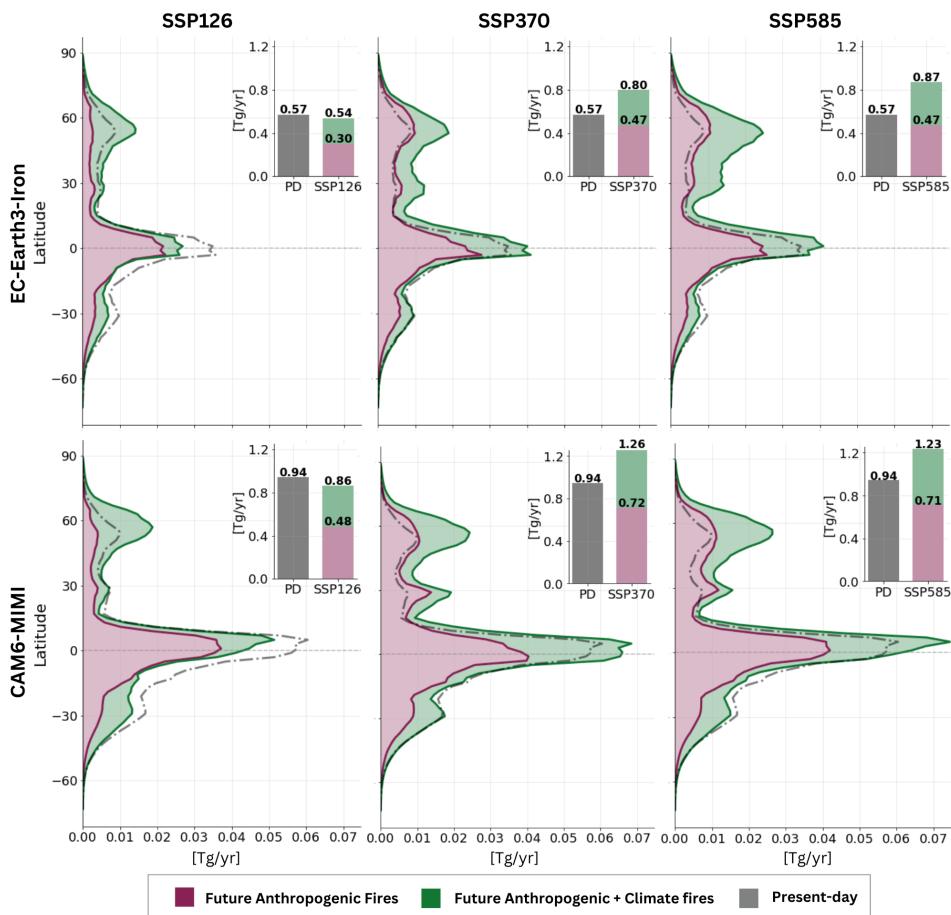


Figure A.34: **Fire Fe deposition.** Fire iron (Fe) deposition by latitude for each scenario (SSP126, SSP370, SSP585, from left to right) and model (EC-Earth3-Iron and CAM6-MIMI, from top to bottom). Purple-colored lines and shading represent deposition attributed to anthropogenic fires, while green-colored lines and shading represent deposition attributed to climate-driven fires. Present-day deposition are depicted in gray. Bar plots illustrate the global deposition budget of fire Fe.

Appendix A. Supplementary material

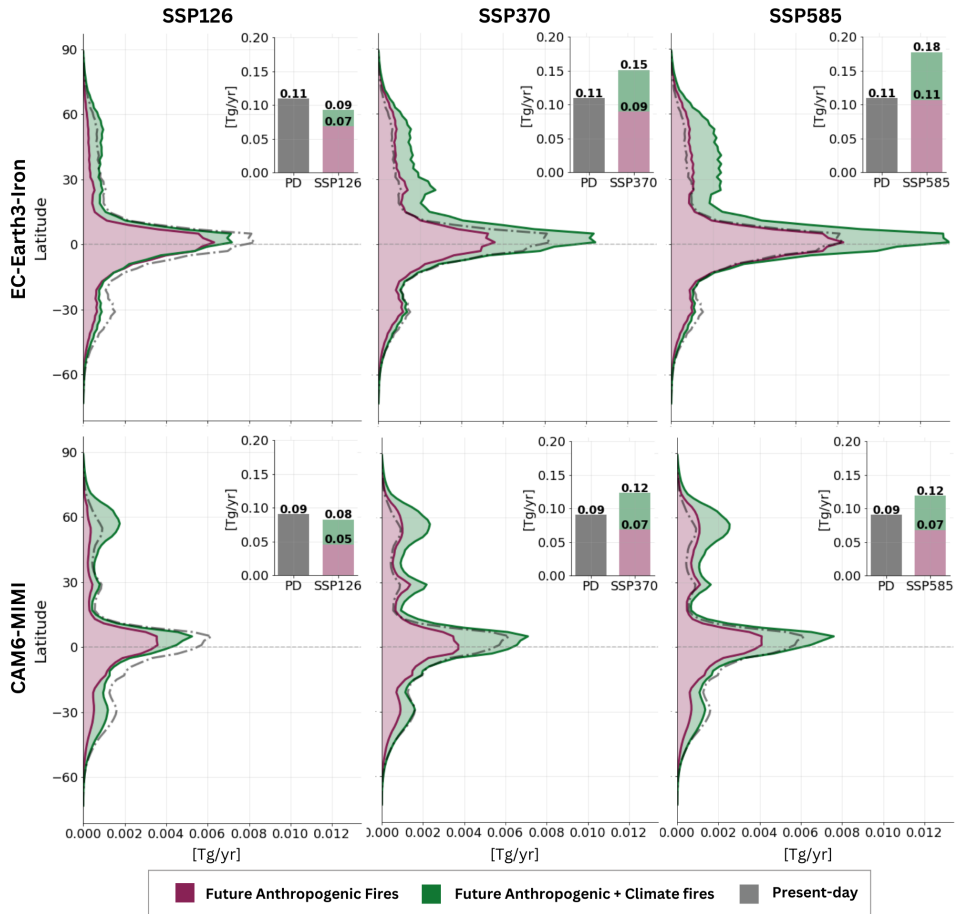


Figure A.35: **Fire SFe deposition.** Fire soluble iron (SFe) deposition by latitude for each scenario (SSP126, SSP370, SSP585 from left to right) and model (EC-Earth3-Iron and CAM6-MIMI, from top to bottom). Purple-colored lines and shading represent deposition attributed to anthropogenic fires, while green-colored lines and shading represent deposition attributed to climate-driven fires. Present-day deposition are depicted in gray. Bar plots illustrate the global deposition budget of fire SFe.

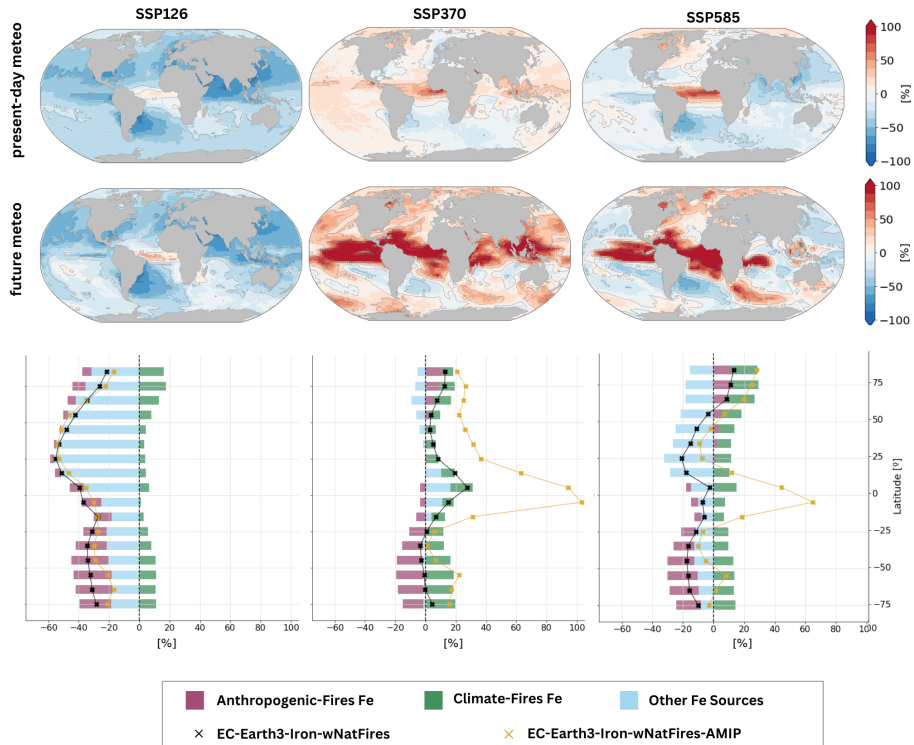


Figure A.36: **EC-Earth3-Iron projected future changes in SFe deposition compared to present-day by source.** Annual mean relative changes in soluble iron (SFe) deposition for future scenarios relative to the present-day scenario (SSP126, SSP370, and SSP585, from left to right) for EC-Earth3-Iron nudged towards present-day meteorology (upper panels) and with changes in future meteorology taken into account (bottom panels). Latitudinal relative changes are represented by black crosses (for nudged experiments) and yellow crosses (for AMIP-like experiments), accompanied by the relative contributions of changes due to anthropogenic fires (depicted in purple), climate-driven fires (depicted in green), and other (depicted in blue).

Appendix A. Supplementary material

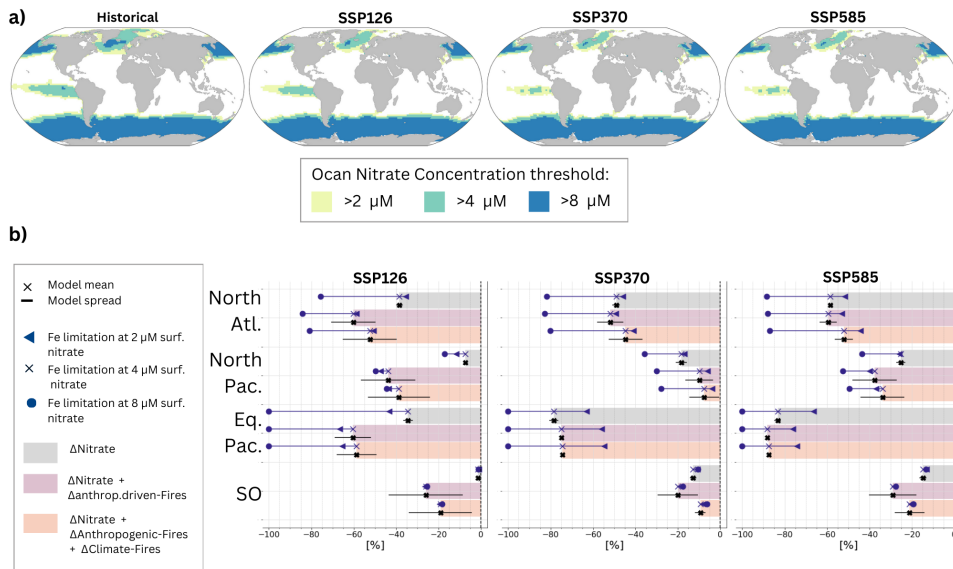


Figure A.37: **Changes in Fe limited areas.** (a) Ocean surface nitrate concentrations from CMIP6 models for the historical period and future scenarios SSP126, SSP370, and SSP585 (from top to bottom), adjusted to match World Ocean Atlas nitrate concentrations in the historical period. Areas are shown for three different nitrate concentrations thresholds ($2 \mu\text{M}$, $4 \mu\text{M}$, and $8 \mu\text{M}$). (b) Impacts of changing iron(Fe)-limited areas on future NPP_{iron} estimates for each scenario (SSP126, SSP370, and SSP585, from left to right) across Fe-limited regions (North Atlantic, North Pacific, Equatorial Pacific, and Southern Ocean, from top to bottom). Grey bars indicate NPP_{iron} changes when SFe deposition is held constant, accounting only for changes in ocean area limitation. Pink bars show the effects of both area limitation changes and projected anthropogenic SFe sources, while orange bars represent changes when both Fe-limited areas and all SFe sources, including climate-driven fire emissions, are projected to vary. Black crosses show the model mean projected change while black bars depict model differences. Blue triangles, crosses and circles show the changes when considering different nitrate thresholds to define Fe-limited areas ($2 \mu\text{M}$, $4 \mu\text{M}$, and $8 \mu\text{M}$, respectively).

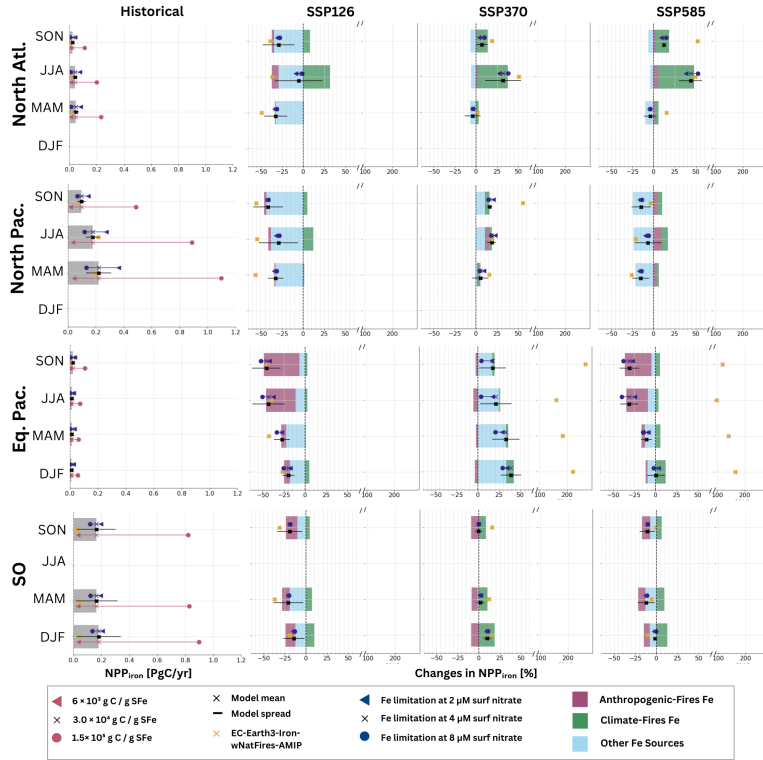


Figure A.38: **Future seasonal Fe-induced changes in NPP compared to present-day.** First column shows the historical (present-day) seasonal (SON, JJA, MAM, DJF) net primary productivity (NPP) induced by soluble iron (SFe) deposition (NPP_{iron}) for each Fe-limited region analyzed (high-latitude North Atlantic, North Pacific, Equatorial Pacific, Southern Ocean from top to bottom). Second, third and fourth columns show seasonal mean relative changes in NPP_{iron} for future scenarios relative to the present-day scenario (SSP126, SSP370, and SSP585, from left to right) in Fe-limited regions. Regional relative changes are represented by black crosses, accompanied by the contributions to the total change of changes due to anthropogenic fires (depicted in purple), climate-driven fires (depicted in green), and other (depicted in blue). Black dots show the model mean and error bars indicate the corresponding standard deviation. Red symbols show a range of C ratios observed in previous studies (triangle: 6×10^3 g C/g SFe, cross: 3×10^4 g C/g SFe, and circle: 1.4×10^5 g C/g SFe). Blue symbols denote different nitrate thresholds used to define Fe-limited regions (triangle: $2 \mu\text{M}$, cross: $4 \mu\text{M}$, and circle: $8 \mu\text{M}$). Yellow crosses show the EC-Earth3-Iron-wNatFires-AMIP simulations results.

Appendix A. Supplementary material

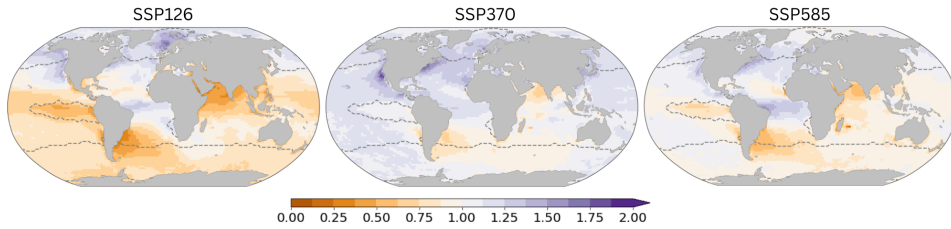


Figure A.39: **Fractional change in the Fe:N deposition ratio from 2010 to 2100.** Fractional change in the iron to nitrogen (Fe:N) deposition ratio from 2010 to 2100 for each scenario (SSP126, SSP370 and SSP585, from left to right) with the new fire dataset.

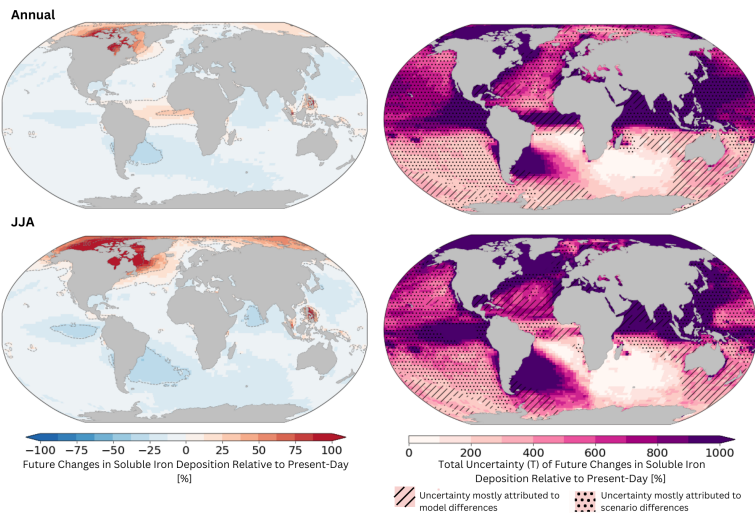


Figure A.40: **Mean and uncertainty in end-of-the-century SFe deposition changes.** Mean soluble iron (SFe) deposition changes across models and scenarios from the present day to the end of the century (left panels) and corresponding total uncertainty (right panels) for the annual mean (upper row) and summer (lower row). The attribution of uncertainty to model differences and scenario differences is shown with hashed and dotted masks, respectively. Areas without hashed or dotted masks correspond to regions where projected changes across models and scenarios are statistically significant with a 90% confidence interval after performing a two-tailed t-test

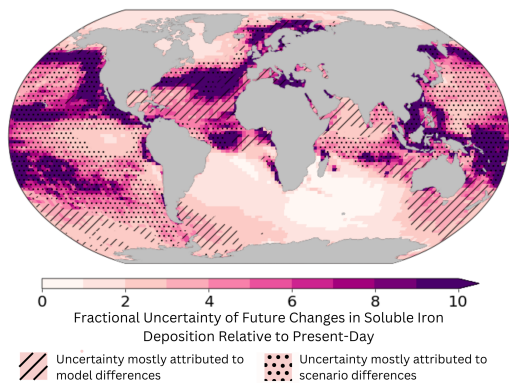


Figure A.41: **Model uncertainty versus socioeconomic scenarios in June, July, and August.** Estimated fractional uncertainty in NH summer soluble iron (SFe) changes from the present day to the end of the century, across scenarios and models (pink-shading). Uncertainty attribution to model and scenario differences is shown with hashed and dotted masks, respectively. Areas without masks indicate statistically significant projected changes (90% confidence) based on a two-tailed t-test.

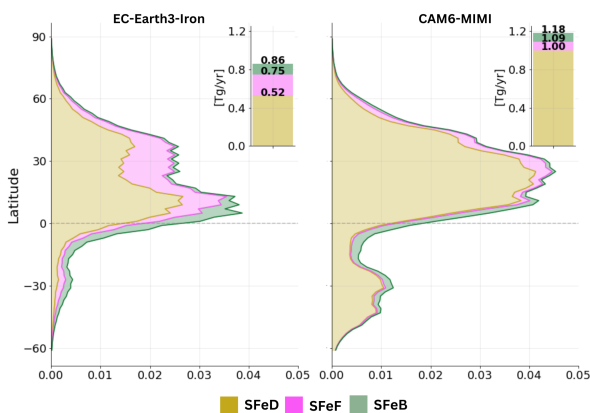


Figure A.42: **Latitudinal SFe deposition by source.** Soluble iron (SFe) deposition flux by latitude for EC-Earth3-Iron (left) and CAM6-MIMI (right) for present-day conditions. Colors indicate the iron source (yellow: dust-iron (FeD), pink: fossil fuels-iron (FeF), and green: fire-iron (FeB). Barplots indicate global yearly mean deposition flux in Tg/yr.

Appendix A. Supplementary material

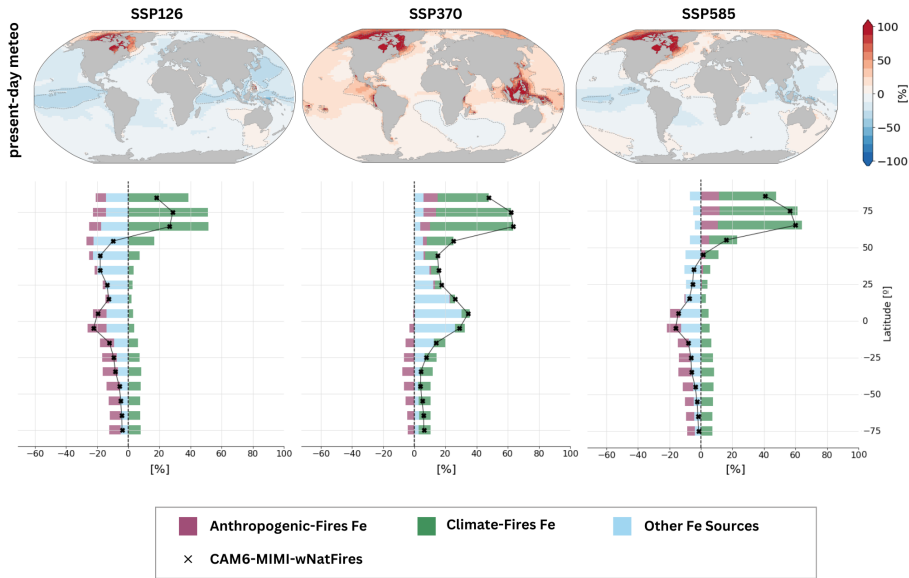


Figure A.43: **CAM6-MIMI projected future changes in SFe deposition compared to present-day.** Annual mean relative changes in soluble iron (SFe) deposition for future scenarios relative to the present-day scenario (SSP126, SSP370, and SSP585, from left to right) for CAM6-MIMI . Latitudinal relative changes are represented by black crosses, accompanied by the contributions to the total change of changes due to anthropogenic fires (depicted in purple), climate-driven fires (depicted in green), and other (depicted in blue).

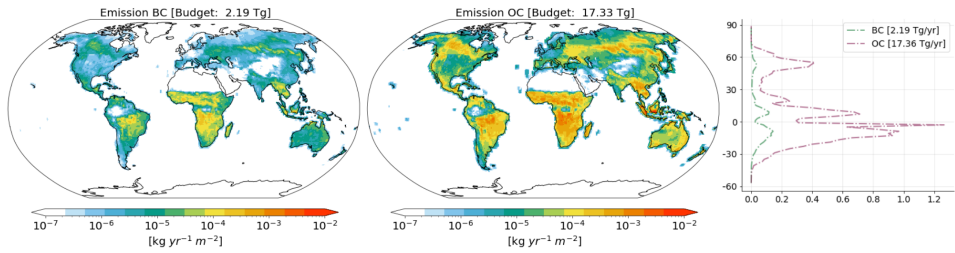


Figure A.44: **Present day BC and OC fire emissions.** Present-day annual mean emission flux [$\text{kg yr}^{-1} \text{m}^{-2}$] global distribution of Black Carbon (BC) (left panel) and Organic Carbon (OC) (middle panel) and corresponding annual emission budgets as in GFED4s. Latitudinal emission distribution of BC and OC emissions (right panel)

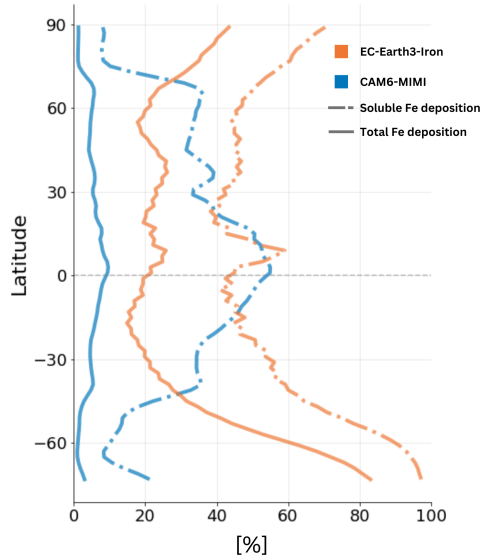


Figure A.45: **Fine vs coarse distribution of deposited fire Fe.** Percentage of iron (Fe) deposition in the fine mode for EC-Earth3-Iron in orange and CAM6-MIMI in blue for both soluble Fe deposition dashed-dot line and total Fe deposition (solid line) for present-day.

Appendix A. Supplementary material

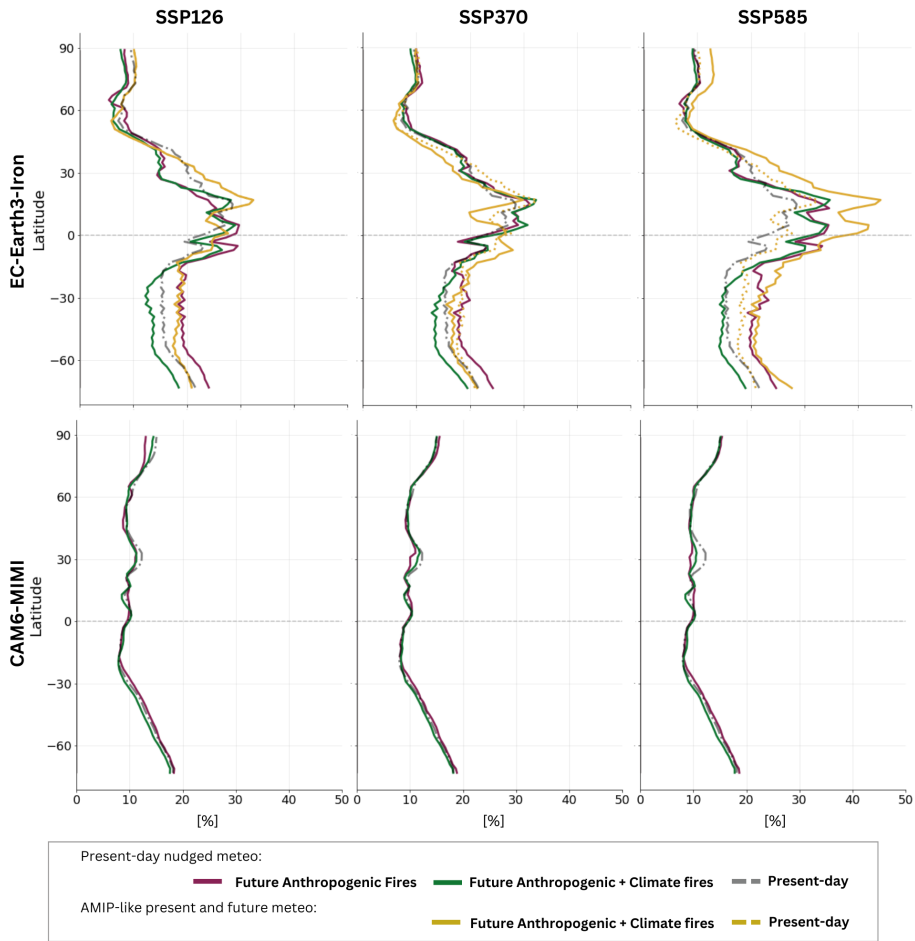


Figure A.46: **Fire Fe solubility at deposition.** Fire iron (Fe) solubility at deposition by latitude for each scenario [SSP126 (left column), SSP370 (middle column), SSP585 (right column)] and model [EC-Earth3-Iron (upper row), CAM6-MIMI (lower row)]. Purple lines show results when accounting for future anthropogenic fires only; green lines depict results when adding climate-driven fires. Present-day values are depicted in gray.

APPENDIX B

List of publications & Outreach activities

Articles in peer-review scientific journals

Publications included in this Thesis

1. **Bergas-Massó, E.**, Gonçalves Ageitos, M., Myriokefalitakis, S., Miller, R. L., van Noije, T., Le Sager, P., Montané Pinto, G., Pérez García-Pando, C.: Pre-Industrial, Present and Future Atmospheric Soluble Iron Deposition and the Role of Aerosol Acidity and Oxalate Under CMIP6 Emissions. *Earth's Future*, 11(6), e2022EF003353. doi: 10.1029/2022EF003353, 2023.
2. **Bergas-Massó, E.**, Hamilton D.S., Myriokefalitakis, S., Rathod, S., Gonçalves Ageitos, M., Pérez García-Pando, C.: Future Climate-Driven Fires Could Boost Oceanic Productivity over the Fe-limited North Atlantic. *in review*.

Co-author in other publications

1. Proestakis, E. and Amiridis, V. and García-Pando, C. P. and Tsyro, S. and Griesfeller, J. and Gkikas, A. and Georgiou, T. and Ageitos, M. G. and Escribano, J. and Myriokefalitakis, S. and **Bergas-Massó, E.** and Di Tomaso, E. and Basart, S. and Stuu, J.-B. W. and Benedetti, A.: Quantifying Dust Deposition over the Atlantic Ocean, *Earth System Science Data Discussions* [preprint], doi: <https://doi.org/10.5194/essd-2025-43>, in review, 2025.
2. Whaley, C. H., Butler, T., Adame, J. A., Ambulkar, R., Arnold, S. R., Buchholz, R. R., Gaubert, B., Hamilton, D. S., Huang, M., Hung, H., Kaiser, J. W., Kaminski, J. W., Knote, C., Koren, G., Kouassi, J.-L., Lin, M., Liu, T., Ma, J., Manomaiphiboon, K., **Bergas-Massó, E.**, McCarty, J. L., Mertens, M., Parrington, M., Peiro, H., Saxena, P., Sonwani, S., Surapipith, V., Tan, D., Tang, W., Tanpipat, V., Tsigaridis, K., Wiedinmyer, C., Wild, O., Xie, Y., and Zuidema, P.: HTAP3 Fires: Towards a multi-model, multi-pollutant study of fire impacts, *Geosci. Model Dev. Discuss.* [preprint], doi: [10.5194/gmd-2024-126](https://doi.org/10.5194/gmd-2024-126), in review, 2024.
3. Hamilton, D.S., Kasoar, M., **Bergas-Massó, E.**, Dalmonech, D., Hantson, S., Lasslop, G., Voulgarakis, A., and Wells C.: Global Warming Increases Fire Emissions but Resulting Aerosol Forcing is Uncertain. *Nature Geosciences.* [preprint], doi: [10.21203/rs.3.rs-4567012/v1](https://doi.org/10.21203/rs.3.rs-4567012/v1), in review, 2024.
4. Hamilton, D.S., Kelley, D., Perron, M.M.G., Llort, J., Burton, C., **Bergas-Massó, E.**, Ligouri-Bills, N., Barkley, A., Buchholz,

R., Diez, S., Dintwe, K., Forkel, M., Hall, J., Hanston, S., Hayman, G., Hebden, S., Jones, M.W., Kulkarni, C., Nowell, B., McCarty, J., Santin, C., Schneider, S.R., Shuman, J.K, Thoreson, J., Plummer, S., Poulter, B., Vanniere, B., Volker, C.: Igniting Progress: Results from the FLARE Workshop and 3 Challenges for the Future of Transdisciplinary Fire Science. [white paper], doi: 10.5281/zenodo.12634068, 2024.

5. Hamilton, D.S., Baker, A.R., Iwamoto, Y., Gassó, S., **Bergas-Massó, E.**, Deutch, S., Dinasquet, J., Kondo, Y., Llort, J., Myriokefalitakis, S., Perron, M.M.G., Wegmann, A., Yoon, J.: An aerosol odyssey: Navigating nutrient flux changes to marine ecosystems. *Elementa: Science of the Anthropocene*, 5 January 2023; 11 (1): 00037. doi: 10.1525/elementa.2023.00037, 2023
6. Myriokefalitakis, S., **Bergas-Massó, E.**, Gonçalves-Ageitos, M., Pérez García-Pando, C., van Noije, T., Le Sager, P., Ito, A., Athanasopoulou, E., Nenes, A., Kanakidou, M., Krol, M. C., and Gerasopoulos, E.: Multiphase processes in the EC-Earth model and their relevance to the atmospheric oxalate, sulfate, and iron cycles. *Geosci. Model Dev.*, 15, 3079–3120. doi: 10.5194/gmd-15-3079-2022, 2022.

Presentations in conferences and workshops

1. Hamilton, D.S., Kasoar, M., **Bergas-Massó, E.**, Dalmonech, D., Hantson, S., Lasslop, G., Voulgarakis, A., and Wells C.: “Exploring the Future of Fire and Aerosol Radiative Forcing”. In: *AGU Fall Meeting 2024*, Washington D.C. (USA), 13 December

Appendix B. List of publications & Outreach activities

2024. (Poster)
2. Llorc, J., **Bergas-Massó, E.**, Bernardello, R., Gonçalves Ageitos, M., Myriokefalitakis, S., and Pérez Garcçia-Pando, C.: “Evaluating the impact of a state-of-the-art iron atmospheric cycle in ocean biogeochemistry”. In: *SOLAS Open Science Conference 2024*, Goa (India), 11-15 November 2024. (Poster)
 3. **Bergas-Massó, E.**, Gonçalves Ageitos, M., Myriokefalitakis, S., Hamilton, D.S., Miller. R.L., and Pérez Garcçia-Pando, C.: “The atmospheric bioavailable iron delivery to the ocean across different climates”. In: *Fire science Learning AcRoss the Earth System (FLARE) Workshop*, online, 20 Setember 2023. (Oral presentation)
 4. **Bergas-Massó, E.**, Gonçalves Ageitos, M., Myriokefalitakis, S., Hamilton, D.S., Miller. R.L., and Pérez Garcçia-Pando, C.: “The atmospheric bioavailable iron delivery to the ocean across different climates ”. In: *SOLAS Summer School*, Mindelo (Cape Verde), 5-16 June 2023. (Oral presentation)
 5. **Bergas-Massó, E.**, Gonçalves Ageitos, M., Myriokefalitakis, S., Hamilton, D.S., Miller. R.L., and Pérez Garcçia-Pando, C.: “The iron cycle in a changing climate at the Barcelona Supercomputing Center”. In: *NCSU MEAS Symposium*, Raleigh (USA), 3rd April 2023. (Oral presentation)
 6. **Bergas-Massó, E.**, Gonçalves Ageitos, M., Myriokefalitakis, S., Miller. R.L., and Pérez Garcçia-Pando, C.: “Atmospheric Controls on Aerosol Iron Solubility under Different Climate

- Scenarios”. In: *AGU Fall Meeting 2022*, Chicago (USA), 12-16 December 2022, <https://ui.adsabs.harvard.edu/abs/2022AGUFM.B25A..03B/abstract>. (Presentation)
7. **Bergas-Massó, E.**, Gonçalves Ageitos, , M., Myriokefalitakis, S., Miller. R.L., and Pérez García-Pando, C.: “How does the use of different soil mineralogical atlases impact soluble iron deposition estimates?”. In: *International Technical Meeting On Air Pollution Modelling And Its Application (ITM)*, Barcelona (Spain), November 2021, https://doi.org/10.1007/978-3-031-12786-1_34. (Poster & Conference paper)
 8. **Bergas-Massó, E.**, Gonçalves Ageitos, , M., Myriokefalitakis, S., van Noije, T., Miller. R.L., and Pérez García-Pando, C.: “Soluble iron deposition under CMIP6 scenarios”. In: *Iron at the Air-Sea Interface Workshop*, online, 26-30 July 2021. (Poster)
 9. **Bergas-Massó, E.**, Gonçalves Ageitos, and Pérez García-Pando, C.: “Sensitivity of soluble iron deposition to soil mineralogy uncertainty”. In: *BSC Doctoral Symposium*, online, 11–13 May 2021, <http://hdl.handle.net/2117/346623>. (Poster & Extended abstract)
 10. **Bergas-Massó, E.**, Gonçalves Ageitos, Myriokefalitakis, S., van Noije, T., Miller, R.L., and Pérez García-Pando, C.: “Enhanced atmospheric solubilization of iron due to anthropogenic activities”. In: *EGU General Assembly 2021*, online, 19–30 April 2021, , EGU21-7519, <https://doi.org/10.5194/egusphere-egu21-7519>. (vPico

Appendix B. List of publications & Outreach activities

- presentation)
11. **Bergas-Massó, E.**, Gonçalves Ageitos, M., Myriokefalitakis, S., Miller. R.L., and Pérez Garcçia-Pando, C.: “Projections of atmospheric soluble iron deposition under CMIP6 emission scenarios”. In: *EC-Earth meeting 2021*, online, 8-11 February 2021. (Oral presentation)
 12. **Bergas-Massó, E.**, Gonçalves Ageitos, M., Myriokefalitakis, S., Miller. R.L., and Pérez Garcçia-Pando, C.: “Projections of atmospheric soluble iron deposition under CMIP6 emission scenarios”. In: *AGU Fall Meeting 2020*, online, December 2020. (Poster)
 13. Myriokefalitakis, S., **Bergas-Massó, E.**, Gonçalves Ageitos, S., and Pérez Garcçia-Pando, C.: “Description and evaluation of the atmospheric iron cycle in the EC-Earth earth system model”. In: *European Aerosol Conference 2020*, Aachen (online), August 2020. (Presentation)
 14. **Bergas-Massó, E.**, Gonçalves Ageitos, and Pérez Garcçia-Pando, C.: “The atmospheric iron cycle in EC-Earth”. In: *BSC Doctoral Symposium*, online, 23–27 May 2020, <http://hdl.handle.net/2117/331015>. (Poster & Extended abstract)
 15. **Bergas-Massó, E.**, Gonçalves Ageitos, M., Myriokefalitakis, S., and Pérez Garcçia-Pando, C.: “The atmospheric iron cycle in EC-Earth”. In: *EC-Earth meeting 2020*, online, 3-5 March 2020. (Poster)

APPENDIX C

List of contributions to projects

The outcomes and software developed within this PhD Thesis have contributed to several Spanish and European projects.

NUTRIENT

The QuaNtifying the present and fUTure atmospheric deliveRy of bioavailable iron to The ocean (**NUTRIENT**) project (CGL2017-88911-R), led by María Gonçalves Ageitos and Carlos Pérez García-Pando and funded by the Spanish Ministerio de Economía y Competitividad is the first of these projects that took place between 01/01/2018 and 31/12/2020. The project aimed to improve our understanding of the atmospheric delivery of bioavailable Fe to the ocean. Within the project scope, EC-Earth3-Iron was developed in strong collaboration with Stelios Myriokefalitakis.

The work presented in this Thesis was pivotal to the development of this project by tackling each of the objectives proposed in the project

Appendix C. List of contributions to projects

proposal:

- To implement and constrain a Fe processing mechanism in an ESM building upon previous work and taking into account recent experimental results.
- To improve and implement dust mineralogy in EC-Earth based on extensions of BFT and an updated soil mineralogy dataset.
- To advance in our understanding of the relative role of the natural versus anthropogenic sources of soluble Fe and of the different atmospheric dissolution mechanisms.
- To quantify present-day and project future changes (end of the century) in the soluble Fe deposition to the ocean.

DOMOS

The Dust-Ocean Modelling & Observing Study (**DOMOS**) project (ESA AO/1-10546/20/I-NB) funded by the European Space Agency (ESA), led by ECMWF took place between 01/09/2021 and 31/08/2023.

The project aimed to advance the understanding of dust and ocean interactions in the Atlantic in a changing climate through innovative use of model and observations.

This Thesis contributed to the project objectives of:

- Generating and evaluating state-of-the-art model reconstructions of the atmospheric iron cycle and of its impact upon ocean biogeochemistry, including the contribution of anthropogenic and natural dust and other sources of soluble iron deposition.

- Identifying any gaps in the observing system that need to be filled to have a complete picture of interactions between atmospheric dust and ocean.

BIOTA

The **BIOTA** project (PID2022-139362OB-I00) supported by *MICIU/AEI/10.13039/501100011033*, led by María Gonçalves Ageitos and Joan Llort, is a continuation of the successful NUTRIENT project above described. This project started in 01/09/2023 and will run until 31/08/2026.

The project aims to improve our understanding of the ocean biogeochemistry response to the varying atmospheric inputs of soluble iron under different climates. This Thesis has contributed to establishing the knowledge bases of the following project objectives:

- Assess the relative contribution of different sources and processes to the soluble iron deposition in the ocean in present climate.
- Evaluate the impact of future land use, vegetation and climate changes on soluble iron deposition in the ocean.
- Quantify the response of marine primary production and carbon export to atmospheric iron supply in the present and future climates.

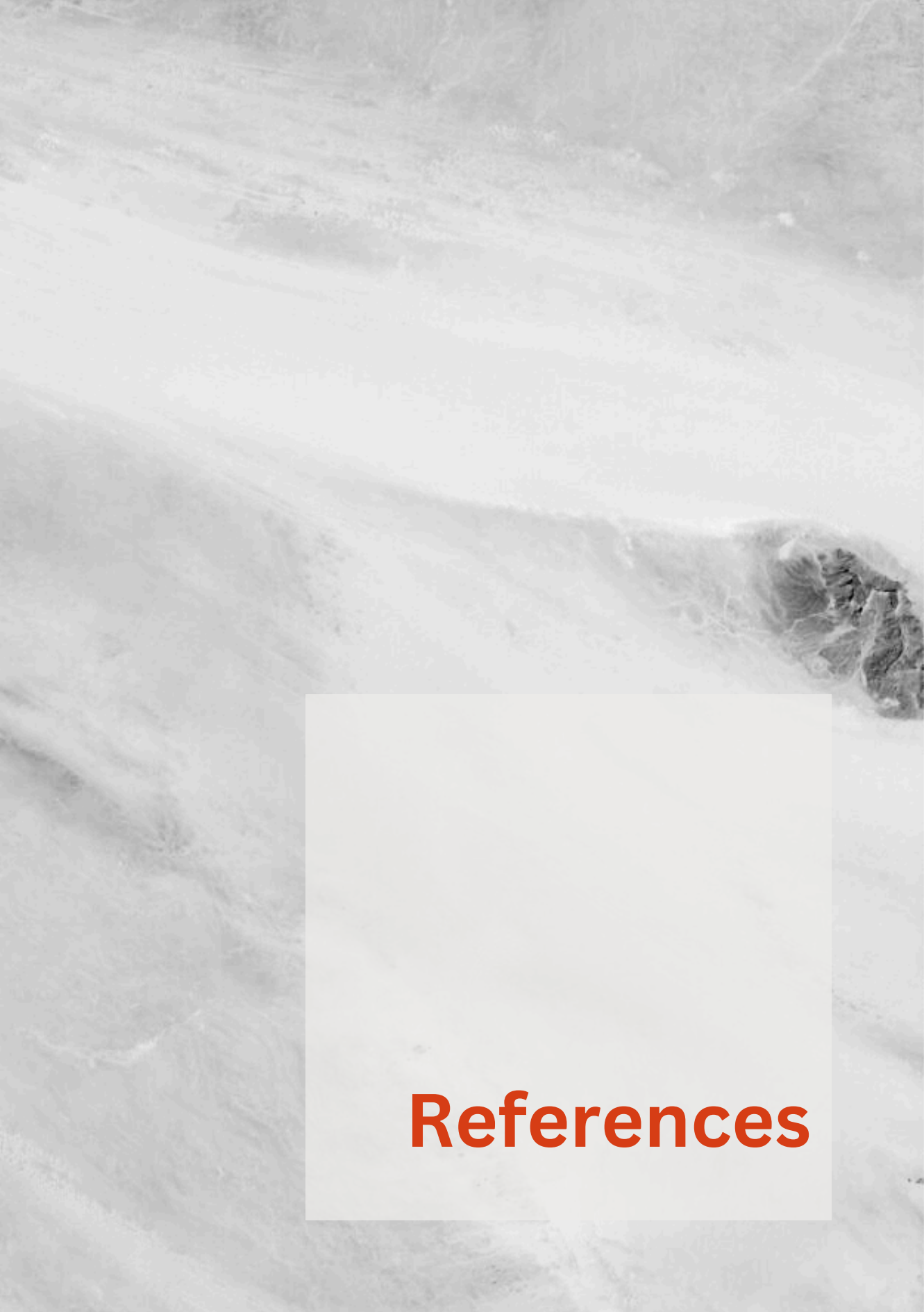
Other projects

This Thesis has also been supported by other projects, including the ERC Consolidator Grant **FRAGMENT** (grant agreement no. 773051) and the **AXA Chair on Sand and Dust Storms**, led by Carlos Pérez García-Pando, which aim to enhance our understanding of dust emissions and their impact on climate. In turn, this Thesis has contributed to these projects by advancing knowledge on the delivery of soluble iron (SFe) from dust to the ocean and exploring its implications for ocean biogeochemistry and climate. This work has also contributed to the H2020-**FORCeS** project, which aimed to understand and reduce the long-standing uncertainty in anthropogenic aerosol radiative forcing. It provided estimates of atmospheric iron (Fe) and supported the development of a comprehensive gas-phase chemistry model that incorporates Fe representation.

The work here has also benefited from other research initiatives or consortiums. As the main tool for iron-cycle modelling that has been used in this work is EC-Earth, I have been closely following the Aerosol Chemistry Model Intercomparison Project (**EC-Earth Consortium** activities and the **AerChemMIP**) initiative of CMIP6. All the themes worked during through this Thesis are of important interest to the global and multidisciplinary research project Surface Ocean - Lower Atmosphere Study **SOLAS** that aims at achieving a quantitative understanding of the key biogeochemical-physical interactions and feedbacks between the ocean and atmosphere, and of how this coupled system affects and is affected by climate and global change. I have been able to interact and be part of this scientific community.

Participating in a diverse array of projects involving international collaborations and transdisciplinary teams has significantly enriched my understanding of collaborative science. These experiences have demonstrated the value of integrating perspectives from various disciplines and cultures to address complex research questions effectively. Engaging with researchers from different backgrounds has not only broadened my knowledge but also honed my ability to communicate, adapt, and contribute meaningfully in dynamic, multi-faceted research environments. This exposure has strengthened my belief in building a science that is inclusive, equitable, and impactful for the betterment of all.



An aerial photograph of a coastline, showing a mix of dark and light terrain. A prominent white rectangular box is overlaid on the bottom right portion of the image, containing the word "References" in a bold, red, sans-serif font.

References

References

Achterberg, E. P., Moore, C. M., Henson, S. A., Steigenberger, S., Stohl, A., Eckhardt, S., Avendano, L. C., Cassidy, M., Hembury, D., Klar, J. K., Lucas, M. I., Macey, A. I., Marsay, C. M., and Ryan-Keogh, T. J. (2013). Natural iron fertilization by the eyjafjallajökull volcanic eruption. *Geophysical Research Letters*, 40(5):921–926.

Achterberg, E. P., Steigenberger, S., Marsay, C. M., Lemoigne, F. A., Painter, S. C., Baker, A. R., Connelly, D. P., Moore, C. M., Tagliabue, A., and Tanhua, T. (2018). Iron biogeochemistry in the high latitude north atlantic ocean. *Scientific Reports*, 8.

Adebisi, A., Kok, J. F., Murray, B. J., Ryder, C. L., Stuut, J.-B. W., Kahn, R. A., Knippertz, P., Formenti, P., Mahowald, N. M., Pérez García-Pando, C., Klose, M., Ansmann, A., Samset, B. H., Ito, A., Balkanski, Y., Di Biagio, C., Romanias, M. N., Huang, Y., and Meng, J. (2023). A review of coarse mineral dust in the earth system. *Aeolian Research*, 60:100849.

Adebisi, A. A. and Kok, J. F. (2020). Climate models miss most of the coarse dust in the atmosphere. *Science Advances*, 6(15):eaaz9507.

Adler, R., Gu, G., Sapiano, M., Wang, J.-J., and Huffman, G. (2017). Global precipitation: Means, variations and trends during the satellite era (1979–2014). *Surveys in Geophysics*, 38:1–21.

Akagi, S. K., Yokelson, R. J., Wiedinmyer, C., Alvarado, M. J., Reid,

References

- J. S., Karl, T., Crouse, J. D., and Wennberg, P. O. (2011). Emission factors for open and domestic biomass burning for use in atmospheric models. *Atmospheric Chemistry and Physics*, 11(9):4039–4072.
- Albani, S., Mahowald, N. M., Perry, A. T., Scanza, R. A., Zender, C. S., Heavens, N. G., Maggi, V., Kok, J. F., and Otto-Bliesner, B. L. (2014). Improved dust representation in the community atmosphere model. *Journal of Advances in Modeling Earth Systems*, 6(3):541–570.
- Andela, N., Morton, D. C., Giglio, L., Chen, Y., van der Werf, G. R., Kasibhatla, P. S., DeFries, R. S., Collatz, G. J., Hantson, S., Kloster, S., Bachelet, D., Forrest, M., Lasslop, G., Li, F., Mangeon, S., Melton, J. R., Yue, C., and Randerson, J. T. (2017). A human-driven decline in global burned area. *Science*, 356(6345):1356–1362.
- Anderson, N. J., Saros, J. E., Bullard, J. E., Cahoon, S. M. P., McGowan, S., Bagshaw, E. A., Barry, C. D., Bindler, R., Burpee, B. T., Carrivick, J. L., Fowler, R. A., Fox, A. D., Fritz, S. C., Giles, M. E., Hamerlik, L., Ingeman-Nielsen, T., Law, A. C., Mernild, S. H., Northington, R. M., Osburn, C. L., Pla-Rabès, S., Post, E., Telling, J., Stroud, D. A., Whiteford, E. J., Yallop, M. L., and Yde, J. C. (2017). The arctic in the twenty-first century: Changing biogeochemical linkages across a paraglacial landscape of greenland. *BioScience*, 67(2):118–133.
- Anderson, R. F., Cheng, H., Edwards, R. L., Fleisher, M. Q., Hayes, C. T., Huang, K.-F., Kadko, D., Lam, P. J., Landing, W. M., Lao, Y., Lu, Y., Measures, C. I., Moran, S. B., Morton, P. L., Ohnemus, D. C., Robinson, L. F., and Shelley, R. U. (2016). How well can we quantify dust deposition to the ocean? *Philosophical Transactions of*

the Royal Society A: Mathematical, Physical and Engineering Sciences, 374(2081):20150285.

Andreae, M. O. (2019). Emission of trace gases and aerosols from biomass burning – an updated assessment. *Atmospheric Chemistry and Physics*, 19(13):8523–8546.

Archibald, S., Staver, A. C., and Levin, S. A. (2012). Evolution of human-driven fire regimes in africa. *Proceedings of the National Academy of Sciences*, 109(3):847–852.

Ardyna, M., Claustre, H., Sallée, J.-B., D’Ovidio, F., Gentili, B., van Dijken, G., D’Ortenzio, F., and Arrigo, K. R. (2017). Delineating environmental control of phytoplankton biomass and phenology in the southern ocean. *Geophysical Research Letters*, 44(10):5016–5024.

Ardyna, M., Hamilton, D., Harmel, T., Lacour, L., Bernstein, D., Laliberte, J., Horvat, C., Laxenaire, R., Mills, M., van Dijken, G., Polyakov, I., Claustre, H., Mahowald, N., and Arrigo, K. (2022). Wildfire aerosol deposition likely amplified a summertime arctic phytoplankton bloom. *Communications Earth Environment*, page 1234567890.

Arimoto, R., Duce, R. A., Ray, B. J., Ellis Jr., W. G., Cullen, J. D., and Merrill, J. T. (1995). Trace elements in the atmosphere over the north atlantic. *Journal of Geophysical Research: Atmospheres*, 100(D1):1199–1213.

Atkins, P. (2010). *Shriver and Atkins’ Inorganic Chemistry*. OUP Oxford.

References

- Aumont, O. and Bopp, L. (2006). Globalizing results from ocean in situ iron fertilization studies. *Global Biogeochemical Cycles*, 20(2).
- Aumont, O., Bopp, L., and Schulz, M. (2008). What does temporal variability in aeolian dust deposition contribute to sea-surface iron and chlorophyll distributions? *Geophysical Research Letters*, 35(7).
- Aumont, O., Ethé, C., Tagliabue, A., Bopp, L., and Gehlen, M. (2015). Pisces-v2: an ocean biogeochemical model for carbon and ecosystem studies. *Geoscientific Model Development*, 8(8):2465–2513.
- Baddock, M. C., Mockford, T., Bullard, J. E., and Thorsteinsson, T. (2017). Pathways of high-latitude dust in the north atlantic. *Earth and Planetary Science Letters*, 459:170–182.
- Baker, A. and Croot, P. (2010). Atmospheric and marine controls on aerosol iron solubility in seawater. *Marine Chemistry*, 120(1):4–13. Aerosol chemistry and impacts on the ocean.
- Baker, A., Jickells, T., Witt, M., and Linge, K. (2006). Trends in the solubility of iron, aluminium, manganese and phosphorus in aerosol collected over the atlantic ocean. *Marine Chemistry*, 98(1):43–58.
- Baker, A., Weston, K., Kelly, S., Voss, M., Streu, P., and Cape, J. (2007). Dry and wet deposition of nutrients from the tropical atlantic atmosphere: Links to primary productivity and nitrogen fixation. *Deep Sea Research Part I: Oceanographic Research Papers*, 54(10):1704–1720.
- Baker, C. A., Martin, A. P., Yool, A., and Popova, E. (2022). Biological Carbon Pump Sequestration Efficiency in the North Atlantic: A Leaky or a Long-Term Sink? *Global Biogeochemical Cycles*, 36(6).

- Baldo, C., Formenti, P., Nowak, S., Chevaillier, S., Cazaunau, M., Pangui, E., Di Biagio, C., Doussin, J.-F., Ignatyev, K., Dagsson-Waldhauserova, P., Arnalds, O., MacKenzie, A. R., and Shi, Z. (2020). Distinct chemical and mineralogical composition of icelandic dust compared to northern african and asian dust. *Atmospheric Chemistry and Physics*, 20(21):13521–13539.
- Baldo, C., Ito, A., Krom, M. D., Li, W., Jones, T., Drake, N., Ignatyev, K., Davidson, N., and Shi, Z. (2022). Iron from coal combustion particles dissolves much faster than mineral dust under simulated atmospheric acidic conditions. *Atmospheric Chemistry and Physics*, 22(9):6045–6066.
- Balistrieri, L., Brewer, P., and Murray, J. (1981). Scavenging residence times of trace metals and surface chemistry of sinking particles in the deep ocean. *Deep Sea Research Part A. Oceanographic Research Papers*, 28(2):101–121.
- Ball, G., Regier, P., González-Pinzón, R., Reale, J., and Horn, D. V. (2021). Wildfires increasingly impact western us fluvial networks. *Nature Communications*, 12.
- Balsamo, G., Beljaars, A., Scipal, K., Viterbo, P., van den Hurk, B., Hirschi, M., and Betts, A. K. (2009). A revised hydrology for the ecmwf model: Verification from field site to terrestrial water storage and impact in the integrated forecast system. *Journal of Hydrometeorology*, 10(3):623 – 643.
- Barbeau, K., Rue, E., Bruland, K., and Butler, A. (2001). Photochemical cycling of iron in the surface ocean mediated by

References

microbial iron(iii)-binding ligands. *Nature*, 413:409–13.

Barkley, A., Prospero, J., Mahowald, N., Hamilton, D., Popendorf, K., Oehlert, A., Pourmand, A., Gatineau, A., Panechou-Pulcherie, K., Blackwelder, P., and Gaston, C. (2019). African biomass burning is a substantial source of phosphorus deposition to the amazon, tropical atlantic ocean, and southern ocean. *Proceedings of the National Academy of Sciences*, 116:201906091.

Behrenfeld, M., O'Malley, R., Boss, E., Westberry, T., Graff, J., Halsey, K., Milligan, A., Siegel, D., and Brown, M. (2016). Revaluating ocean warming impacts on global phytoplankton. *Nature Climate Change*, Advanced Online Access.

Behrenfeld, M. J., O'Malley, R. T., Siegel, D. A., McClain, C. R., Sarmiento, J. L., Feldman, G. C., Milligan, A. J., Falkowski, P. G., Letelier, R. M., and Boss, E. S. (2006). Climate-driven trends in contemporary ocean productivity. *Nature*, 444:752–755.

Belviso, S., Bopp, L., Mosseri, J., Tedetti, M., Garcia, N., Griffiths, B., Joux, F., Obernosterer, I., Uitz, J., and Veldhuis, M. J. (2008). Effect of natural iron fertilisation on the distribution of dms and dmsp in the indian sector of the southern ocean. *Deep Sea Research Part II: Topical Studies in Oceanography*, 55(5):893–900.

Bergametti, G. and Forêt, G. (2014). *Dust Deposition*, pages 179–200. Springer Netherlands, Dordrecht.

Bergas-Massó, E., Gonçalves Ageitos, M., Myriokefalitakis, S., Miller, R. L., van Noije, T., Le Sager, P., Montané Pinto, G., and Pérez García-Pando, C. (2023). Pre-industrial, present and future

- atmospheric soluble iron deposition and the role of aerosol acidity and oxalate under cmip6 emissions. *Earth's Future*, 11(6):e2022EF003353.
- Bibi, I., Singh, B., and Silvester, E. (2014). Dissolution kinetics of soil clays in sulfuric acid solutions: Ionic strength and temperature effects. *Applied Geochemistry*, 51:170–183.
- Bishop, J. K. B., Davis, R. E., and Sherman, J. T. (2002). Robotic observations of dust storm enhancement of carbon biomass in the north pacific. *Science*, 298(5594):817–821.
- Blott, S. J. and Pye, K. (2012). Particle size scales and classification of sediment types based on particle size distributions: Review and recommended procedures. *Sedimentology*, 59(7):2071–2096.
- Bond, T. C., Streets, D. G., Yarber, K. F., Nelson, S. M., Woo, J.-H., and Klimont, Z. (2004). A technology-based global inventory of black and organic carbon emissions from combustion. *Journal of Geophysical Research: Atmospheres*, 109(D14).
- Bond, W. J., Woodward, F. I., and Midgley, G. F. (2005). The global distribution of ecosystems in a world without fire. *New Phytologist*, 165(2):525–538.
- Bonneville, S., Van Cappellen, P., and Behrends, T. (2004). Microbial reduction of iron(III) oxyhydroxides: effects of mineral solubility and availability. *Chemical Geology*, 212(3):255–268. Bacteria and Geochemical Speciation of Metals.
- Bopp, L., Aumont, O., Belviso, S., and Blain, S. (2008). Modelling the effect of iron fertilization on dimethylsulphide emissions in the southern ocean. *Deep Sea Research Part II: Topical Studies in Oceanography*,

References

55(5):901–912. KEOPS: Kerguelen Ocean and Plateau compared Study.

Bowie, A. R., Lannuzel, D., Remenyi, T. A., Wagener, T., Lam, P. J., Boyd, P. W., Guieu, C., Townsend, A. T., and Trull, T. W. (2009). Biogeochemical iron budgets of the southern ocean south of australia: Decoupling of iron and nutrient cycles in the subantarctic zone by the summertime supply. *Global Biogeochemical Cycles*, 23(4).

Bowman, D. M. J. S., Balch, J., Artaxo, P., Bond, W. J., Cochrane, M. A., D'Antonio, C. M., DeFries, R., Johnston, F. H., Keeley, J. E., Krawchuk, M. A., Kull, C. A., Mack, M., Moritz, M. A., Pyne, S., Roos, C. I., Scott, A. C., Sodhi, N. S., and Swetnam, T. W. (2011). The human dimension of fire regimes on earth. *Journal of Biogeography*, 38(12):2223–2236.

Bowman, D. M. J. S., Balch, J. K., Artaxo, P., Bond, W. J., Carlson, J. M., Cochrane, M. A., D'Antonio, C. M., DeFries, R. S., Doyle, J. C., Harrison, S. P., Johnston, F. H., Keeley, J. E., Krawchuk, M. A., Kull, C. A., Marston, J. B., Moritz, M. A., Prentice, I. C., Roos, C. I., Scott, A. C., Swetnam, T. W., van der Werf, G. R., and Pyne, S. J. (2009). Fire in the earth system. *Science*, 324(5926):481–484.

Boyd, P. W., Arrigo, K. R., Strzepek, R., and Van Dijken, G. L. (2012). Mapping phytoplankton iron utilization: Insights into Southern Ocean supply mechanisms. *Journal of Geophysical Research: Oceans*, 117(6):1–18.

Boyd, P. W., Jickells, T., Law, C. S., Blain, S., Boyle, E. A., Buesseler, K. O., Coale, K. H., Cullen, J. J., de Baar, H. J. W., Follows, M.,

- Harvey, M., Lancelot, C., Levasseur, M., Owens, N. P. J., Pollard, R., Rivkin, R. B., Sarmiento, J., Schoemann, V., Smetacek, V., Takeda, S., Tsuda, A., Turner, S., and Watson, A. J. (2007). Mesoscale iron enrichment experiments 1993-2005: Synthesis and future directions. *Science*, 315(5812):612–617.
- Bressac, M., Guieu, C., Doxaran, D., Bourrin, F., Desboeufs, K., Leblond, N., and Ridame, C. (2014). Quantification of the lithogenic carbon pump following a simulated dust-deposition event in large mesocosms. *Biogeosciences*, 11(4):1007–1020.
- Browning, T. J. and Moore, C. M. (2023). Global analysis of ocean phytoplankton nutrient limitation reveals high prevalence of co-limitation. *Nature Communications*, 14(1):1–12.
- Bullard, J. E., Baddock, M., Bradwell, T., Crusius, J., Darlington, E., Gaiero, D., Gassó, S., Gisladottir, G., Hodgkins, R., McCulloch, R., McKenna-Neuman, C., Mockford, T., Stewart, H., and Thorsteinsson, T. (2016). High-latitude dust in the earth system. *Reviews of Geophysics*, 54(2):447–485.
- Byrne, B., Liu, J., Bowman, K. W., Pascolini-Campbell, M., Chatterjee, A., Pandey, S., Miyazaki, K., van der Werf, G. R., Wunch, D., Wennberg, P. O., Roehl, C. M., and Sinha, S. (2024). Carbon emissions from the 2023 canadian wildfires. *Nature*.
- Calewaert, J.-B., Sierra-Correa, P. C., de Boer, G., Crosman, K., Kågesten, G., Taconet, M., Busumprah, P. T., Alvarez-Fanjul, E., Shepherd, I., Schaap, D., Hall, S., Zinkann, A.-C., Haddad, T., Jegat, V., Smit, M., Sun, M., Suzuki, T., Visbeck, M., Xingyuan, R., and

References

McMeel, O. (2024). Ocean decade vision 2030 white papers – challenge 8: Create a digital representation of the ocean. *UNESCO-IOC, The Ocean Decade Series*, 51.8.

Calvin, K., Bond-Lamberty, B., Clarke, L., Edmonds, J., Eom, J., Hartin, C., Kim, S., Kyle, P., Link, R., Moss, R., McJeon, H., Patel, P., Smith, S., Waldhoff, S., and Wise, M. (2017). The ssp4: A world of deepening inequality. *Global Environmental Change*, 42:284–296.

Canadell, J., Monteiro, P., Costa, M., da Cunha, L. C., Cox, P., Eliseev, A., Henson, S., Ishii, M., Jaccard, S., Koven, C., et al. (2021). Climate change 2021: The physical science basis. contribution of working group i to the sixth assessment report of the intergovernmental panel on climate change. *Cambridge Univ. Press*.

Cao, F., Zhang, S.-C., Kawamura, K., Liu, X., Yang, C., Xu, Z., Fan, M., Zhang, W., Bao, M., Chang, Y., Song, W., Liu, S., Lee, X., Li, J., Zhang, G., and Zhang, Y.-L. (2017). Chemical characteristics of dicarboxylic acids and related organic compounds in pm2.5 during biomass-burning and non-biomass-burning seasons at a rural site of northeast china. *Environmental Pollution*, 231:654–662.

Carslaw, K., Boucher, O., Spracklen, D., Mann, G., Rae, J., Woodward, S., and Kulmala, M. (2010). A review of natural aerosol interactions and feedbacks within the earth system. *Atmospheric Chemistry and Physics*, 10(4):1701–1737.

Carter, T. S., Heald, C. L., Jimenez, J. L., Campuzano-Jost, P., Kondo, Y., Moteki, N., Schwarz, J. P., Wiedinmyer, C., Darmenov, A. S., Silva, A. M. D., and Kaiser, J. W. (2020). How emissions uncertainty

influences the distribution and radiative impacts of smoke from fires in north america. *Atmospheric Chemistry and Physics*, 20:2073–2097.

Chance, R., Jickells, T. D., and Baker, A. R. (2015). Atmospheric trace metal concentrations, solubility and deposition fluxes in remote marine air over the south-east atlantic. *Marine Chemistry*, 177:45–56. Biogeochemistry of trace elements and their isotopes.

Charlson, R. J., Warren, S. G., Lovelock, J. E., and Andreae, M. O. (1987). Oceanic phytoplankton, atmospheric sulphur, cloud albedo and climate. , 326:655–661.

Chen, H. and Grassian, V. H. (2013). Iron dissolution of dust source materials during simulated acidic processing: The effect of sulfuric, acetic, and oxalic acids. *Environmental Science and Technology*, 47(18):10312–10321.

Chen, H., Laskin, A., Baltrusaitis, J., Gorski, C. A., Scherer, M. M., and Grassian, V. H. (2012). Coal fly ash as a source of iron in atmospheric dust. *Environmental Science & Technology*, 46(4):2112–2120. PMID: 22260270.

Chen, R., Wu, B., Li, Z., and Wang, S. (2024). Impacts of enso on tropical pacific chlorophyll biomass under historical and rcp8.5 scenarios. *Journal of Geophysical Research: Oceans*, 129(4):e2023JC020720.

Chen, S., Huang, J., Li, J., Jia, R., Jiang, N., Kang, L., Ma, X., and Xie, T. (2017). Comparison of dust emissions, transport, and deposition between the taklimakan desert and gobi desert from 2007 to 2011. *Science China Earth Sciences*, pages 1–18.

References

- Chen, S., Jiang, N., Huang, J., Xu, X., Zhang, H., Zang, Z., Huang, K., Xu, X., Wei, Y., Guan, X., Zhang, X., Luo, Y., Hu, Z., and Feng, T. (2018). Quantifying contributions of natural and anthropogenic dust emission from different climatic regions. *Atmospheric Environment*, 191:94–104.
- Chen, Y., Romps, D. M., Seeley, J. T., Veraverbeke, S., Riley, W. J., Mekonnen, Z. A., and Randerson, J. T. (2021). Future increases in arctic lightning and fire risk for permafrost carbon. *Nature Climate Change*, 11:404–410.
- Cho, B. C. and Azam, F. (1990). Biogeochemical significance of bacterial biomass in the ocean’s euphotic zone. *Marine ecology progress series. Oldendorf*, 63(2):253–259.
- Chuang, P. Y., Duvall, R. M., Shafer, M. M., and Schauer, J. J. (2005). The origin of water soluble particulate iron in the asian atmospheric outflow. *Geophysical Research Letters*, 32(7).
- Chuvieco, E., Lizundia-Loiola, J., Pettinari, M. L., Ramo, R., Padilla, M., Tansey, K., Mouillot, F., Laurent, P., Storm, T., Heil, A., and Plummer, S. (2018). Generation and analysis of a new global burned area product based on modis 250 m reflectance bands and thermal anomalies. *Earth System Science Data*, 10(4):2015–2031.
- Claquin, T., Schulz, M., and Balkanski, Y. J. (1999). Modeling the mineralogy of atmospheric dust sources. *Journal of Geophysical Research: Atmospheres*, 104(D18):22243–22256.
- Clayton, D. (1983). *Principles of Stellar Evolution and Nucleosynthesis*. Astronomy / Astrophysics. University of Chicago Press.

- Coindreau, O., Hourdin, F., Haeffelin, M., Mathieu, A., and Rio, C. (2007). Assessment of physical parameterizations using a global climate model with stretchable grid and nudging. *Monthly Weather Review*, 135(4):1474 – 1489.
- Collins, M., Beverley, J. D., Bracegirdle, T. J., Catto, J., McCrystall, M., Dittus, A., Freychet, N., Grist, J., Hegerl, G. C., Holland, P. R., Holmes, C., Josey, S. A., Joshi, M., Hawkins, E., Lo, E., Lord, N., Mitchell, D., Monerie, P.-A., Priestley, M. D. K., Scaife, A., Screen, J., Senior, N., Sexton, D., Shuckburgh, E., Siegert, S., Simpson, C., Stephenson, D. B., Sutton, R., Thompson, V., Wilcox, L. J., and Woollings, T. (2024). Emerging signals of climate change from the equator to the poles: new insights into a warming world. *Frontiers in Science*, 2.
- Conway, T. M., Hamilton, D. S., Shelley, R. U., Aguilar-Islas, A. M., Landing, W. M., Mahowald, N. M., and John, S. G. (2019). Tracing and constraining anthropogenic aerosol iron fluxes to the north atlantic ocean using iron isotopes. *Nature Communications*, 10(1):2628.
- Cosentino, N. J., Ruiz-Etcheverry, L. A., Bia, G. L., Simonella, L. E., Coppo, R., Torre, G., Saraceno, M., Tur, V. M., and Gaiero, D. M. (2020). Does satellite chlorophyll-a respond to southernmost patagonian dust? a multi-year, event-based approach. *Journal of Geophysical Research: Biogeosciences*, 125(12):e2020JG006073.
- Craig, A., Valcke, S., and Coquart, L. (2017). Development and performance of a new version of the oasis coupler, oasis3-mct_3.0. *Geoscientific Model Development*, 10(9):3297–3308.

References

- Crusius, J., Sholkovitz, E., Bostick, B., and Schroth, A. (2009). Iron solubility driven by speciation in dust sources to the ocean. *Nature Geoscience - NAT GEOSCI*, 2:337–340.
- Cutter, G., Casciotti, K., Croot, P., Geibert, W., Heimbürger-Boavida, L.-E., Lohan, M., Planquette, H., and Flierdt, T. (2017). *Sampling and Sample-handling Protocols for GEOTRACES Cruises (Cookbook, version 3.0, 2017)*.
- Cwiertny, D. M., Baltrusaitis, J., Hunter, G. J., Laskin, A., Scherer, M. M., and Grassian, V. H. (2008). Characterization and acid-mobilization study of iron-containing mineral dust source materials. *Journal of Geophysical Research: Atmospheres*, 113(D5).
- Danabasoglu, G., Lamarque, J.-F., Bacmeister, J., Bailey, D. A., DuVivier, A. K., Edwards, J., Emmons, L. K., Fasullo, J., Garcia, R., Gettelman, A., Hannay, C., Holland, M. M., Large, W. G., Lauritzen, P. H., Lawrence, D. M., Lenaerts, J. T. M., Lindsay, K., Lipscomb, W. H., Mills, M. J., Neale, R., Oleson, K. W., Otto-Bliesner, B., Phillips, A. S., Sacks, W., Tilmes, S., van Kampenhout, L., Vertenstein, M., Bertini, A., Dennis, J., Deser, C., Fischer, C., Fox-Kemper, B., Kay, J. E., Kinnison, D., Kushner, P. J., Larson, V. E., Long, M. C., Mickelson, S., Moore, J. K., Nienhouse, E., Polvani, L., Rasch, P. J., and Strand, W. G. (2020). The community earth system model version 2 (cesm2). *Journal of Advances in Modeling Earth Systems*, 12(2):e2019MS001916.
- De Baar, H. (1994). von liebig's law of the minimum and plankton ecology (1899–1991). *Progress in oceanography*, 33(4):347–386.

- de Baar, H. J. W., Boyd, P. W., Coale, K. H., Landry, M. R., Tsuda, A., Assmy, P., Bakker, D. C. E., Bozec, Y., Barber, R. T., Brzezinski, M. A., Buesseler, K. O., Boyé, M., Croot, P. L., Gervais, F., Gorbunov, M. Y., Harrison, P. J., Hiscock, W. T., Laan, P., Lancelot, C., Law, C. S., Levasseur, M., Marchetti, A., Millero, F. J., Nishioka, J., Nojiri, Y., van Oijen, T., Riebesell, U., Rijkenberg, M. J. A., Saito, H., Takeda, S., Timmermans, K. R., Veldhuis, M. J. W., Waite, A. M., and Wong, C.-S. (2005). Synthesis of iron fertilization experiments: From the iron age in the age of enlightenment. *Journal of Geophysical Research: Oceans*, 110(C9).
- Deguillaume, L., Desboeufs, K. V., Leriche, M., Long, Y., and Chaumerliac, N. (2010). Effect of iron dissolution on cloud chemistry: from laboratory measurements to model results. *Atmospheric Pollution Research*, 1(4):220–228.
- Dennison, P. E., Brewer, S. C., Arnold, J. D., and Moritz, M. A. (2014). Large wildfire trends in the western united states, 1984–2011. *Geophysical Research Letters*, 41(8):2928–2933.
- Desboeufs, K., Sofikitis, A., Losno, R., Colin, J., and Ausset, P. (2005). Dissolution and solubility of trace metals from natural and anthropogenic aerosol particulate matter. *Chemosphere*, 58(2):195–203.
- Desboeufs, K. V., Losno, R., Vimeux, F., and Cholbi, S. (1999). The ph-dependent dissolution of wind-transported saharan dust. *Journal of Geophysical Research: Atmospheres*, 104.
- Di Biagio, C., Banks, J., and Gaetani, M. (2021). *Dust Atmospheric*

References

Transport Over Long Distances.

Doney, S. C., Lima, I., Feely, R. A., Glover, D. M., Lindsay, K., Mahowald, N., Moore, J. K., and Wanninkhof, R. (2009). Mechanisms governing interannual variability in upper-ocean inorganic carbon system and air–sea co₂ fluxes: Physical climate and atmospheric dust. *Deep Sea Research Part II: Topical Studies in Oceanography*, 56(8-10):640–655.

Döscher, R., Acosta, M., Alessandri, A., Anthoni, P., Arsouze, T., Bergman, T., Bernardello, R., Boussetta, S., Caron, L.-P., Carver, G., Castrillo, M., Catalano, F., Cvijanovic, I., Davini, P., Dekker, E., Doblas-Reyes, F. J., Docquier, D., Echevarria, P., Fladrich, U., Fuentes-Franco, R., Gröger, M., v. Hardenberg, J., Hieronymus, J., Karami, M. P., Keskinen, J.-P., Koenigk, T., Makkonen, R., Massonnet, F., Ménégos, M., Miller, P. A., Moreno-Chamarro, E., Nieradzick, L., van Noije, T., Nolan, P., O'Donnell, D., Ollinaho, P., van den Oord, G., Ortega, P., Prims, O. T., Ramos, A., Reerink, T., Rousset, C., Ruprich-Robert, Y., Le Sager, P., Schmith, T., Schrödner, R., Serva, F., Sicardi, V., Sloth Madsen, M., Smith, B., Tian, T., Tourigny, E., Uotila, P., Vancoppenolle, M., Wang, S., Wårlind, D., Willén, U., Wyser, K., Yang, S., Yepes-Arbós, X., and Zhang, Q. (2022). The ec-earth3 earth system model for the coupled model intercomparison project 6. *Geoscientific Model Development*, 15(7):2973–3020.

Drenkard, E. J., John, J. G., Stock, C. A., Lim, H.-G., Dunne, J. P., Ginoux, P., and Luo, J. Y. (2023). The importance of dynamic iron deposition in projecting climate change impacts on pacific ocean

biogeochemistry. *Geophysical Research Letters*, 50(21):e2022GL102058. e2022GL102058 2022GL102058.

Duan, Z. and Sun, R. (2003). An improved model calculating co₂ solubility in pure water and aqueous nacl solutions from 273 to 533 k and from 0 to 2000 bar. *Chemical Geology*, 193(3):257–271.

Duce, R. A., LaRoche, J., Altieri, K., Arrigo, K. R., Baker, A. R., Capone, D. G., Cornell, S., Dentener, F., Galloway, J., Ganeshram, R. S., Geider, R. J., Jickells, T., Kuypers, M. M., Langlois, R., Liss, P. S., Liu, S. M., Middelburg, J. J., Moore, C. M., Nickovic, S., Oschlies, A., Pedersen, T., Prospero, J., Schlitzer, R., Seitzinger, S., Sorensen, L. L., Uematsu, M., Ulloa, O., Voss, M., Ward, B., and Zamora, L. (2008). Impacts of atmospheric anthropogenic nitrogen on the open ocean. *Science*, 320(5878):893–897.

Duce, R. A. and Tindale, N. W. (1991). Atmospheric transport of iron and its deposition in the ocean. *Limnology and Oceanography*, 36.

Duggen, S., Croot, P., Schacht, U., and Hoffmann, L. (2007). Subduction zone volcanic ash can fertilize the surface ocean and stimulate phytoplankton growth: Evidence from biogeochemical experiments and satellite data. *Geophysical Research Letters*, 34(1).

Duggen, S., Olgun, N., Croot, P., Hoffmann, L., Dietze, H., Delmelle, P., and Teschner, C. (2010). The role of airborne volcanic ash for the surface ocean biogeochemical iron-cycle: a review. *Biogeosciences*, 7(3):827–844.

Emerson, S. and Hedges, J. (2008). *Chemical Oceanography and the Marine Carbon Cycle*. Cambridge University Press.

References

- Eppley, R. W. and Peterson, B. J. (1979). Particulate organic matter flux and planktonic new production in the deep ocean. *Nature*, 282(5740):677–680.
- Eyring, V., Bony, S., Meehl, G. A., Senior, C. A., Stevens, B., Stouffer, R. J., and Taylor, K. E. (2016). Overview of the coupled model intercomparison project phase 6 (cmip6) experimental design and organization. *Geoscientific Model Development*, 9(5):1937–1958.
- Eyring, V., Cox, P., Flato, G., Gleckler, P., Abramowitz, G., Caldwell, P., Collins, W., Gier, B., Hall, A., Hoffman, F., Hurtt, G., Jahn, A., Jones, C., Klein, S., Krasting, J., Kwiatkowski, L., Lorenz, R., Maloney, E., Meehl, G., and Williamson, M. (2019). Taking climate model evaluation to the next level. *Nature Climate Change*, 9:102–110.
- Falkowski, P., Scholes, R. J., Boyle, E., Canadell, J., Canfield, D., Elser, J., Gruber, N., Hibbard, K., Högberg, P., Linder, S., Mackenzie, F. T., III, B. M., Pedersen, T., Rosenthal, Y., Seitzinger, S., Smetacek, V., and Steffen, W. (2000). The global carbon cycle: A test of our knowledge of earth as a system. *Science*, 290(5490):291–296.
- Fan, S.-M., Moxim, W. J., and Levy II, H. (2006). Aeolian input of bioavailable iron to the ocean. *Geophysical Research Letters*, 33(7).
- Formenti, P., Rajot, J. L., Desboeufs, K., Caquineau, S., Chevaillier, S., Nava, S., Gaudichet, A., Journet, E., Triquet, S., Alfaro, S., Chiari, M., Haywood, J., Coe, H., and Highwood, E. (2008). Regional variability of the composition of mineral dust from western africa: Results from the amma sop0/dabex and dodo field campaigns. *Journal of Geophysical Research: Atmospheres*, 113(D23).

- Fountoukis, C. and Nenes, A. (2007). ISORROPIA II: a computationally efficient thermodynamic equilibrium model for K^+ - Ca^{2+} - Mg^{2+} - NH_4^+ - Na^+ - SO_4^2- - NO_3^- - Cl^- - H_2O aerosols. *Atmospheric Chemistry and Physics*, 7(17):4639–4659.
- Francois, R., Altabet, M. A., Yu, E.-F., Sigman, D. M., Bacon, M. P., Frank, M., Bohrmann, G., Bareille, G., and Labeyrie, L. D. (1997). Contribution of southern ocean surface-water stratification to low atmospheric CO_2 concentrations during the last glacial period. *Nature*, 389(6654):929–935.
- Frey, P. A. and Reed, G. H. (2012). The ubiquity of iron. *ACS Chemical Biology*, 7(9):1477–1481. PMID: 22845493.
- Fricko, O., Havlik, P., Rogelj, J., Klimont, Z., Gusti, M., Johnson, N., Kolp, P., Strubegger, M., Valin, H., Amann, M., Ermolieva, T., Forsell, N., Herrero, M., Heyes, C., Kindermann, G., Krey, V., McCollum, D. L., Obersteiner, M., Pachauri, S., Rao, S., Schmid, E., Schoepp, W., and Riahi, K. (2017). The marker quantification of the shared socioeconomic pathway 2: A middle-of-the-road scenario for the 21st century. *Global Environmental Change*, 42:251–267.
- Fu, H., Cwiertny, D. M., Carmichael, G. R., Scherer, M. M., and Grassian, V. H. (2010). Photoreductive dissolution of Fe-containing mineral dust particles in acidic media. *Journal of Geophysical Research: Atmospheres*, 115(D11).
- Fujimori, S., Hasegawa, T., Masui, T., Takahashi, K., Herran, D. S., Dai, H., Hijioka, Y., and Kainuma, M. (2017). Ssp3: Aim implementation of shared socioeconomic pathways. *Global*

References

Environmental Change, 42:268–283.

Gabric, A. J., Cropp, R. A., McTainsh, G. H., Johnston, B. M., Butler, H., Tilbrook, B., and Keywood, M. (2010). Australian dust storms in 2002–2003 and their impact on southern ocean biogeochemistry. *Global Biogeochemical Cycles*, 24(2).

Gao, Y., Fan, S.-M., and Sarmiento, J. L. (2003). Aeolian iron input to the ocean through precipitation scavenging: A modeling perspective and its implication for natural iron fertilization in the ocean. *Journal of Geophysical Research: Atmospheres*, 108(D7).

Gao, Y., Marsay, C. M., Yu, S., Fan, S., Mukherjee, P., Buck, C. S., and Landing, W. M. (2019). Particle-size variability of aerosol iron and impact on iron solubility and dry deposition fluxes to the arctic ocean. *Scientific Reports*, 9.

Gao, Y., Xu, G., Zhan, J., Zhang, J., Li, W., Lin, Q., Chen, L., and Lin, H. (2013). Spatial and particle size distributions of atmospheric dissolvable iron in aerosols and its input to the southern ocean and coastal east antarctica. *Journal of Geophysical Research: Atmospheres*, 118(22):12,634–12,648.

Garcia, H., Bouchard, C., Cross, S., Paver, C., Wang, Z., Reagan, J., Boyer, T., Locarnini, R., Mishonov, A., Baranova, O., Seidov, D., and Dukhovskoy, D. (2024). World ocean atlas 2023. vol. 4: Dissolved inorganic nutrients (phosphate, nitrate, silicate). Report.

Gates, W. L., Boyle, J. S., Covey, C., Dease, C. G., Doutriaux, C. M., Drach, R. S., Fiorino, M., Gleckler, P. J., Hnilo, J. J., Marlais, S. M., Phillips, T. J., Potter, G. L., Santer, B. D., Sperber, K. R., Taylor,

- K. E., and Williams, D. N. (1999). An overview of the results of the atmospheric model intercomparison project (amip i). *Bulletin of the American Meteorological Society*, 80:29–55.
- Geider, R. J., MacIntyre, H. L., and Kana, T. M. (1998). A dynamic regulatory model of phytoplanktonic acclimation to light, nutrients, and temperature. *Limnology and Oceanography*, 43(4):679–694.
- GESAMP (2010). Gesamp reports and studies. In *Proceedings of the GESAMP International Workshop on Plastic Particles as a Vector in Transporting Persistent, Bio-Accumulating and Toxic Substances in the Oceans*, volume 82, page 68.
- Gidden, M. J., Riahi, K., Smith, S. J., Fujimori, S., Luderer, G., Kriegler, E., van Vuuren, D. P., van den Berg, M., Feng, L., Klein, D., Calvin, K., Doelman, J. C., Frank, S., Fricko, O., Harmsen, M., Hasegawa, T., Havlik, P., Hilaire, J., Hoesly, R., Horing, J., Popp, A., Stehfest, E., and Takahashi, K. (2019). Global emissions pathways under different socioeconomic scenarios for use in cmip6: a dataset of harmonized emissions trajectories through the end of the century. *Geoscientific Model Development*, 12(4):1443–1475.
- Giles, D. M., Sinyuk, A., Sorokin, M. G., Schafer, J. S., Smirnov, A., Slutsker, I., Eck, T. F., Holben, B. N., Lewis, J. R., Campbell, J. R., Welton, E. J., Korkin, S. V., and Lyapustin, A. I. (2019). Advancements in the Aerosol Robotic Network (AERONET) Version 3 database – automated near-real-time quality control algorithm with improved cloud screening for Sun photometer aerosol optical depth (AOD) measurements. *Atmospheric Measurement Techniques*, 12(1):169–209.

References

- Ginoux, P., Prospero, J. M., Gill, T. E., Hsu, N. C., and Zhao, M. (2012). Global-scale attribution of anthropogenic and natural dust sources and their emission rates based on modis deep blue aerosol products. *Reviews of Geophysics*, 50.
- Gliß, J., Mortier, A., Schulz, M., Andrews, E., Balkanski, Y., Bauer, S. E., Benedictow, A. M. K., Bian, H., Checa-Garcia, R., Chin, M., Ginoux, P., Griesfeller, J. J., Heckel, A., Kipling, Z., Kirkevåg, A., Kokkola, H., Laj, P., Le Sager, P., Lund, M. T., Lund Myhre, C., Matsui, H., Myhre, G., Neubauer, D., van Noije, T., North, P., Olivie, D. J. L., Rémy, S., Sogacheva, L., Takemura, T., Tsigaridis, K., and Tsyro, S. G. (2021). AeroCom phase III multi-model evaluation of the aerosol life cycle and optical properties using ground- and space-based remote sensing as well as surface in situ observations. *Atmospheric Chemistry and Physics*, 21(1):87–128.
- Gnanadesikan, A., Sarmiento, J. L., and Slater, R. D. (2003). Effects of patchy ocean fertilization on atmospheric carbon dioxide and biological production. *Global Biogeochemical Cycles*, 17(2).
- Go, S., Lyapustin, A., Schuster, G. L., Choi, M., Ginoux, P., Chin, M., Kalashnikova, O., Dubovik, O., Kim, J., da Silva, A., Holben, B., and Reid, J. S. (2022). Inferring iron-oxide species content in atmospheric mineral dust from dscovr epic observations. *Atmospheric Chemistry and Physics*, 22(2):1395–1423.
- Gonçalves Ageitos, M., Obiso, V., Miller, R. L., Jorba, O., Klose, M., Dawson, M., Balkanski, Y., Perlwitz, J., Basart, S., Di Tomaso, E., Escribano, J., Macchia, F., Montané, G., Mahowald, N. M., Green, R. O., Thompson, D. R., and Pérez García-Pando, C. (2023). Modeling

dust mineralogical composition: sensitivity to soil mineralogy atlases and their expected climate impacts. *Atmospheric Chemistry and Physics*, 23(15):8623–8657.

González-Romero, A., González-Flórez, C., Panta, A., Yus-Díez, J., Córdoba, P., Alastuey, A., Moreno, N., Kandler, K., Klose, M., Clark, R. N., Ehlmann, B. L., Greenberger, R. N., Keebler, A. M., Brodrick, P., Green, R. O., Querol, X., and Pérez García-Pando, C. (2024). Probing iceland’s dust-emitting sediments: particle size distribution, mineralogy, cohesion, fe mode of occurrence, and reflectance spectra signatures. *Atmospheric Chemistry and Physics*, 24(11):6883–6910.

Graff, J. R., Westberry, T. K., Milligan, A. J., Brown, M. B., Dall’Olmo, G., van Dongen-Vogels, V., Reifel, K. M., and Behrenfeld, M. J. (2015). Analytical phytoplankton carbon measurements spanning diverse ecosystems. *Deep Sea Research Part I: Oceanographic Research Papers*, 102:16–25.

Green, R. O., Mahowald, N., Thompson, D. R., Ung, C., Brodrick, P., Pollock, R., Bennett, M., Lundeen, S., Joyce, M., Olson-Duvall, W., Oaida, B., Bradley, C., Diaz, E., Clark, R., Vannan, S., Swayze, G., Kokaly, R., Ginoux, P., Miller, R., Okin, G., Garcia-Pando, C. P., Ehlmann, B., Kalashnikova, O., Painter, T. H., Realmuto, V., Chadwick, D., Ben-Dor, E., Pearlshtien, D. H., Guanter, L., Phillips, B., Reath, K., Thorpe, A., Shaw, L., Keebler, A., Ochoa, F., Grant, K., Sen, A., Duren, R., Obiso, V., Gonçalves-Ageitos, M., and Huang, Y. (2023). Performance and early results from the earth surface mineral dust source investigation (emit) imaging spectroscopy mission. In *2023 IEEE Aerospace Conference*, pages 1–10.

References

- Gregg, W. W., Ginoux, P., Schopf, P. S., and Casey, N. W. (2003). Phytoplankton and iron: validation of a global three-dimensional ocean biogeochemical model. *Deep Sea Research Part II: Topical Studies in Oceanography*, 50(22):3143–3169. The US JGOFS Synthesis and Modeling Project: Phase II.
- Guieu, C., Aumont, O., Paytan, A., Bopp, L., Law, C. S., Mahowald, N., Achterberg, E. P., Marañón, E., Salihoglu, B., Crise, A., Wagener, T., Herut, B., Desboeufs, K., Kanakidou, M., Olgun, N., Peters, F., Pulido-Villena, E., Tovar-Sanchez, A., and Völker, C. (2014). The significance of the episodic nature of atmospheric deposition to low nutrient low chlorophyll regions. *Global Biogeochemical Cycles*, 28(11):1179–1198.
- Guieu, C., Bonnet, S., Wagener, T., and Loÿe-Pilot, M.-D. (2005). Biomass burning as a source of dissolved iron to the open ocean? *Geophysical Research Letters*, 32(19).
- Guieu, C., Dulac, F., Desboeufs, K., Wagener, T., Pulido-Villena, E., Grisoni, J.-M., Louis, F., Ridame, C., Blain, S., Brunet, C., Bon Nguyen, E., Tran, S., Labiadh, M., and Dominici, J.-M. (2010). Large clean mesocosms and simulated dust deposition: a new methodology to investigate responses of marine oligotrophic ecosystems to atmospheric inputs. *Biogeosciences*, 7(9):2765–2784.
- Guivarch, C. E., Kriegler, J., Portugal-Pereira, V., Bosetti, J., Edmonds, M., Fishedick, P., Havlík, P., Jaramillo, V., Krey, F., Lecocq, A., Lucena, M., Meinshausen, S., Mirasgedis, B., O’Neill, G., Peters, J., Rogelj, S., Rose, Y., Saheb, G., Strbac, A., Hammer Strømman, D., and van Vuuren, N. Z. e. (2023). *Ipcc, 2022:*

Annex iii: Scenarios and modelling methods. *IPCC, 2022: Climate Change 2022: Mitigation of Climate Change*, pages 1841–1908.

Gurvan, M., Bourdallé-Badie, R., Bouttier, P.-A., Bricaud, C., Bruciaferri, D., Calvert, D., Chanut, J., Clementi, E., Coward, A., Delrosso, D., Ethé, C., Flavoni, S., Graham, T., Harle, J., Iovino, D., Lea, D., Lévy, C., Lovato, T., Martin, N., Masson, S., Mocavero, S., Paul, J., Rousset, C., Storkey, D., Storto, A., and Vancoppenolle, M. (2019). Nemo ocean engine.

Hajima, T., Watanabe, M., Yamamoto, A., Tatebe, H., Noguchi, M., Abe, M., Ohgaito, R., Ito, A., Yamazaki, D., Okajima, H., Ito, A., Takata, K., Ogochi, K., Watanabe, S., and Kawamiya, M. (2019). Description of the MIROC-ES2L Earth system model and evaluation of its climate–biogeochemical processes and feedbacks.

Hamidi, M., Kavianpour, M., and Shao, Y. (2013). Synoptic analysis of dust storms in the middle east. *Asia-Pacific Journal of Atmospheric Sciences*, 49.

Hamilton, D. S., Baker, A. R., Iwamoto, Y., Gassó, S., Bergas-Masso, E., Deutch, S., Dinasquet, J., Kondo, Y., Llort, J., Myriokefalitakis, S., Perron, M. M., Wegmann, A., and Yoon, J. E. (2023). An aerosol odyssey: Navigating nutrient flux changes to marine ecosystems. *Elementa*, 11(1).

Hamilton, D. S., Hantson, S., Scott, C. E., Kaplan, J. O., Pringle, K. J., Nieradzik, L. P., Rap, A., Folberth, G. A., Spracklen, D. V., and Carslaw, K. S. (2018). Reassessment of pre-industrial fire emissions strongly affects anthropogenic aerosol forcing. *Nature Communications*,

References

9.

Hamilton, D. S., Kasoar, M., Bergas-Masso, E., Dalmonech, D., Hantson, S., Lasslop, G., Voulgarakis, A., and D. Wells, C. (2024a). Global warming increases fire emissions but resulting aerosol forcing remains uncertain.

Hamilton, D. S., Kelley, D., Perron, M. M., Llort, J., Burton, C., Bergas-Masso, E., Ligouri-Bills, N., Barkley, A., Buchholz, R., Diez, S., Dintwe, K., Forkel, M., Hall, J., Hantson, S., Hayman, G., Hebden, S., Jones, M. W., Kulkarni, C., Nowell, B., McCarty, J. L., Santin, C., Schneider, S. R., Shuman, J. K., Thoreson, J., Plummer, S., Poulter, B., Vanniere, B., and Volker, C. (2024b). Igniting Progress: Outcomes from the FLARE workshop and three challenges for the future of transdisciplinary fire science.

Hamilton, D. S., Moore, J. K., Arneth, A., Bond, T. C., Carslaw, K. S., Hantson, S., Ito, A., Kaplan, J. O., Lindsay, K., Nieradzick, L., Rathod, S. D., Scanza, R. A., and Mahowald, N. M. (2020a). Impact of changes to the atmospheric soluble iron deposition flux on ocean biogeochemical cycles in the anthropocene. *Global Biogeochemical Cycles*, 34.

Hamilton, D. S., Perron, M. M., Bond, T. C., Bowie, A. R., Buchholz, R. R., Guieu, C., Ito, A., Maenhaut, W., Myriokefalitakis, S., Olgun, N., Rathod, S. D., Schepanski, K., Tagliabue, A., Wagner, R., and Mahowald, N. M. (2022). Earth, wind, fire, and pollution: Aerosol nutrient sources and impacts on ocean biogeochemistry. *Annual Review of Marine Science*, 14(1):303–330.

- Hamilton, D. S., Scanza, R. A., Feng, Y., Guinness, J., Kok, J. F., Li, L., Liu, X., Rathod, S. D., Wan, J. S., Wu, M., and Mahowald, N. M. (2019). Improved methodologies for Earth system modelling of atmospheric soluble iron and observation comparisons using the Mechanism of Intermediate complexity for Modelling Iron (MIMI v1.0). *Geoscientific Model Development*, 12(9).
- Hamilton, D. S., Scanza, R. A., Rathod, S. D., Bond, T. C., Kok, J. F., Li, L., Matsui, H., and Mahowald, N. M. (2020b). Recent (1980 to 2015) Trends and Variability in Daily-to-Interannual Soluble Iron Deposition from Dust, Fire, and Anthropogenic Sources. *Geophysical Research Letters*, 47(17).
- Hamme, R. C., Webley, P. W., Crawford, W. R., Whitney, F. A., DeGrandpre, M. D., Emerson, S. R., Eriksen, C. C., Giesbrecht, K. E., Gower, J. F. R., Kavanaugh, M. T., Peña, M. A., Sabine, C. L., Batten, S. D., Coogan, L. A., Grundle, D. S., and Lockwood, D. (2010). Volcanic ash fuels anomalous plankton bloom in subarctic northeast pacific. *Geophysical Research Letters*, 37(19).
- Hammond, M., Beaulieu, C., Henson, S., and Sahu, S. (2020). Regional surface chlorophyll trends and uncertainties in the global ocean. *Scientific reports*, 10:15273.
- Han, Y., Zhao, T., Song, L., Fang, X., Yin, Y., Deng, Z., Wang, S., and Fan, S. (2011). A linkage between asian dust, dissolved iron and marine export production in the deep ocean. *Atmospheric Environment*, 45(25):4291–4298.
- Hand, J. L., Mahowald, N. M., Chen, Y., Siefert, R. L., Luo,

References

- C., Subramaniam, A., and Fung, I. (2004). Estimates of atmospheric-processed soluble iron from observations and a global mineral aerosol model: Biogeochemical implications. *Journal of Geophysical Research: Atmospheres*, 109(D17).
- Hand, J. L., Schichtel, B. A., Malm, W. C., and Pitchford, M. L. (2012). Particulate sulfate ion concentration and SO₂ emission trends in the United States from the early 1990s through 2010. *Atmospheric Chemistry and Physics*, 12(21):10353–10365.
- Harris, R. M., Remenyi, T. A., Williamson, G. J., Bindoff, N. L., and Bowman, D. M. (2016). Climate–vegetation–fire interactions and feedbacks: trivial detail or major barrier to projecting the future of the Earth system? *Wiley Interdisciplinary Reviews: Climate Change*, 7(6):910–931.
- Hauck, J., Völker, C., Wolf-Gladrow, D. A., Laufkötter, C., Vogt, M., Aumont, O., Bopp, L., Buitenhuis, E. T., Doney, S. C., Dunne, J., Gruber, N., Hashioka, T., John, J., Quéré, C. L., Lima, I. D., Nakano, H., Séférian, R., and Totterdell, I. (2015). On the southern ocean CO₂ uptake and the role of the biological carbon pump in the 21st century. *Global Biogeochemical Cycles*, 29(9):1451–1470.
- Hawkins, E. and Sutton, R. (2009). The potential to narrow uncertainty in regional climate predictions. *Bulletin of the American Meteorological Society*, 90(8):1095–1107.
- Henderson, R. (1916). Note on graduation by adjusted average. *Transactions of the actuarial society of America*, 17:43–48.
- Henson, S. A., Painter, S. C., Penny Holliday, N., Stinchcombe,

- M. C., and Giering, S. L. C. (2013). Unusual subpolar north atlantic phytoplankton bloom in 2010: Volcanic fertilization or north atlantic oscillation? *Journal of Geophysical Research: Oceans*, 118(10):4771–4780.
- Henson, S. A., Sarmiento, J. L., Dunne, J. P., Bopp, L., Lima, I., Doney, S. C., John, J., and Beaulieu, C. (2010). Detection of anthropogenic climate change in satellite records of ocean chlorophyll and productivity. *Biogeosciences*, 7(2):621–640.
- Hersbach, H., Bell, B., Berrisford, P., Hirahara, S., Horányi, A., Muñoz-Sabater, J., Nicolas, J., Peubey, C., Radu, R., Schepers, D., Simmons, A., Soci, C., Abdalla, S., Abellan, X., Balsamo, G., Bechtold, P., Biavati, G., Bidlot, J., Bonavita, M., De Chiara, G., Dahlgren, P., Dee, D., Diamantakis, M., Dragani, R., Flemming, J., Forbes, R., Fuentes, M., Geer, A., Haimberger, L., Healy, S., Hogan, R. J., Hólm, E., Janisková, M., Keeley, S., Laloyaux, P., Lopez, P., Lupu, C., Radnoti, G., de Rosnay, P., Rozum, I., Vamborg, F., Villaume, S., and Thépaut, J.-N. (2020). The era5 global reanalysis. *Quarterly Journal of the Royal Meteorological Society*, 146(730):1999–2049.
- Herut, B., Zohary, T., Krom, M., Mantoura, R. F. C., Pitta, P., Psarra, S., Rassoulzadegan, F., Tanaka, T., and Thingstad, T. F. (2005). Response of east mediterranean surface water to saharan dust: On-board microcosm experiment and field observations. *Deep Sea Research Part II: Topical Studies in Oceanography*, 52(22-23):3024–3040.
- Hessilt, T. D., Abatzoglou, J. T., Chen, Y., Randerson, J. T., Scholten, R. C., van der Werf, G., and Veraverbeke, S. (2022). Future increases

References

in lightning ignition efficiency and wildfire occurrence expected from drier fuels in boreal forest ecosystems of western north america. *Environmental Research Letters*, 17(5):054008.

Hieronymus, J., Hieronymus, M., Gröger, M., Schwinger, J., Bernadello, R., Tourigny, E., Sicardi, V., Ruvalcaba Baroni, I., and Wyser, K. (2024). Net primary production annual maxima in the north atlantic projected to shift in the 21st century. *Biogeosciences*, 21(9):2189–2206.

Hoesly, R. M., Smith, S. J., Feng, L., Klimont, Z., Janssens-Maenhout, G., Pitkanen, T., Seibert, J. J., Vu, L., Andres, R. J., Bolt, R. M., Bond, T. C., Dawidowski, L., Kholod, N., Ichi Kurokawa, J., Li, M., Liu, L., Lu, Z., Moura, M. C. P., O'Rourke, P. R., and Zhang, Q. (2018). Historical (1750–2014) anthropogenic emissions of reactive gases and aerosols from the community emissions data system (ceds). *Geoscientific Model Development*, 11.

Hoffmann, L., Breitbarth, E., Ardelan, M., Duggen, S., Olgun, N., Hassellöv, M., and Wängberg, S.- (2012). Influence of trace metal release from volcanic ash on growth of *thalassiosira pseudonana* and *emiliania huxleyi*. *Marine Chemistry*, 132-133:28–33.

Hofmann, M. and Schellnhuber, H.-J. (2009). Oceanic acidification affects marine carbon pump and triggers extended marine oxygen holes. *Proceedings of the National Academy of Sciences*, 106(9):3017–3022.

Hua, W., Lou, S., Huang, X., Xue, L., Ding, K., Wang, Z., and Ding, A. (2024). Diagnosing uncertainties in global biomass burning emission inventories and their impact on modeled air pollutants. *Atmospheric*

Chemistry and Physics, 24:6787–6807.

Huang, H., Gutjahr, M., Eisenhauer, A., and Kuhn, G. (2020). No detectable weddell sea antarctic bottom water export during the last and penultimate glacial maximum. *Nature Communications*, 11(1):424.

Huijnen, V., Williams, J., van Weele, M., van Noije, T., Krol, M., Dentener, F., Segers, A., Houweling, S., Peters, W., de Laat, J., Boersma, F., Bergamaschi, P., van Velthoven, P., Le Sager, P., Eskes, H., Alkemade, F., Scheele, R., Nédélec, P., and Pätz, H.-W. (2010). The global chemistry transport model tm5: description and evaluation of the tropospheric chemistry version 3.0. *Geoscientific Model Development*, 3(2):445–473.

Ilyina, T. and Friedlingstein, P. (2016). WCRP Grand Challenge: Carbon feedbacks in the climate system.

International Energy Agency (2008). *Energy statistics of OECD countries*. OECD.

International Energy Agency (2012). *Energy statistics of non-OECD countries*. OECD.

IPCC (2014). *Climate Change 2014: Synthesis Report. Contribution of Working Groups I, II and III to the Fifth Assessment Report of the Intergovernmental Panel on Climate Change*. IPCC, Geneva, Switzerland.

IPCC (2023a). *Climate Change 2022 - Mitigation of Climate Change: Working Group III Contribution to the Sixth Assessment Report of the Intergovernmental Panel on Climate Change*. Cambridge University Press.

References

- IPCC (2023b). *Global Carbon and Other Biogeochemical Cycles and Feedbacks*, page 673–816. Cambridge University Press.
- Ito, A. (2011). Mega fire emissions in Siberia: Potential supply of bioavailable iron from forests to the ocean. *Biogeosciences*, 8(6):1679–1697.
- Ito, A. (2012). Contrasting the effect of iron mobilization on soluble iron deposition to the ocean in the northern and southern hemispheres. *Journal of the Meteorological Society of Japan. Ser. II*, 90A:167–188.
- Ito, A. (2013). Global modeling study of potentially bioavailable iron input from shipboard aerosol sources to the ocean. *Global Biogeochemical Cycles*, 27(1):1–10.
- Ito, A. (2015). Atmospheric processing of combustion aerosols as a source of bioavailable iron. *Environmental Science and Technology Letters*, 2(3):70–75.
- Ito, A. and Feng, Y. (2010). Role of dust alkalinity in acid mobilization of iron. *Atmospheric Chemistry and Physics*, 10(19):9237–9250.
- Ito, A., Lin, G., and Penner, J. E. (2018). Radiative forcing by light-absorbing aerosols of pyrogenetic iron oxides. *Scientific Reports*, 8(1):1–11.
- Ito, A. and Miyakawa, T. (2023). Aerosol iron from metal production as a secondary source of bioaccessible iron. *Environmental Science & Technology*, 57(10):4091–4100.
- Ito, A., Myriokefalitakis, S., Kanakidou, M., Mahowald, N. M., Scanza, R. A., Hamilton, D. S., Baker, A. R., Jickells, T., Sarin, M., Bikkina,

- S., Gao, Y., Shelley, R. U., Buck, C. S., Landing, W. M., Bowie, A. R., Perron, M. M. G., Guieu, C., Meskhidze, N., Johnson, M. S., Feng, Y., Kok, J. F., Nenes, A., and Duce, R. A. (2019). Pyrogenic iron: The missing link to high iron solubility in aerosols. *Science Advances*, 5.
- Ito, A. and Shi, Z. (2016). Delivery of anthropogenic bioavailable iron from mineral dust and combustion aerosols to the ocean. *Atmospheric Chemistry and Physics*, 16(1):85–99.
- Ito, A. and Wagai, R. (2017). Data descriptor: Global distribution of clay-size minerals on land surface for biogeochemical and climatological studies. *Scientific Data*, 4.
- Ito, A. and Xu, L. (2014). Response of acid mobilization of iron-containing mineral dust to improvement of air quality projected in the future. *Atmospheric Chemistry and Physics*, 14(7).
- Ito, A., Ye, Y., Baldo, C., and Shi, Z. (2021). Ocean fertilization by pyrogenic aerosol iron. *npj Climate and Atmospheric Science*, in press:1–20.
- Ito, A., Ye, Y., Yamamoto, A., Watanabe, M., and Aita, M. N. (2020). Responses of ocean biogeochemistry to atmospheric supply of lithogenic and pyrogenic iron-containing aerosols. *Geological Magazine*, 157:741–756.
- Ito, T. and Follows, M. (2003). Upper ocean control on the solubility pump of co₂. *Journal of Marine Research - J MAR RES*, 61.
- Jaccard, S., Hayes, C. T., Martínez-García, A., Hodell, D., Anderson, R. F., Sigman, D., and Haug, G. (2013). Two modes of change in

References

southern ocean productivity over the past million years. *Science*, 339(6126):1419–1423.

Jacobson, M. C., Charlson, R. J., Rodhe, H., and Orians, G. H. (2000). *Earth system science : from biogeochemical cycles to global change*, volume 72. Academic Press, [2nd edition]. edition.

Jain, P., Barber, Q. E., Taylor, S. W., Whitman, E., Acuna, D. C., Boulanger, Y., Chavardès, R. D., Chen, J., Englefield, P., Flannigan, M., Girardin, M. P., Hanes, C. C., Little, J., Morrison, K., Skakun, R. S., Thompson, D. K., Wang, X., and Parisien, M. A. (2024). Drivers and impacts of the record-breaking 2023 wildfire season in canada. *Nature Communications*, 15.

Janssen, T. A., Jones, M. W., Finney, D., van der Werf, G. R., van Wees, D., Xu, W., and Veraverbeke, S. (2023). Extratropical forests increasingly at risk due to lightning fires. *Nature Geoscience*, 16(12):1136–1144.

Jeanneau, A. C., Ostendorf, B., and Herrmann, T. (2019). Relative spatial differences in sediment transport in fire-affected agricultural landscapes: A field study. *Aeolian Research*, 39:13–22.

Jeong, G. Y., Kim, J. Y., Seo, J., Kim, G. M., Jin, H. C., and Chun, Y. (2014). Long-range transport of giant particles in asian dust identified by physical, mineralogical, and meteorological analysis. *Atmospheric Chemistry and Physics*, 14(1):505–521.

Jickells, T., Buitenhuis, E., Altieri, K., Baker, A., Duce, R., Dentener, F., Fennel, K., Kanakidou, M., Laroche, J., Lee, K., Liss, P., Middelburg, J., Moore, J., Okin, G., Oschlies, A., Sarin, M., Seitzinger,

- S., Sharples, J., and Zamora, L. (2017). A re-evaluation of the magnitude and impacts of anthropogenic atmospheric nitrogen inputs on the ocean: Duce et al revisited. *Global Biogeochemical Cycles*, 31.
- Jickells, T. D., An, Z. S., Andersen, K. K., Baker, A. R., Bergametti, C., Brooks, N., Cao, J. J., Boyd, P. W., Duce, R. A., Hunter, K. A., Kawahata, H., Kubilay, N., LaRoche, J., Liss, P. S., Mahowald, N., Prospero, J. M., Ridgwell, A. J., Tegen, I., and Torres, R. (2005). Global iron connections between desert dust, ocean biogeochemistry, and climate.
- Johnson, K. S., Gordon, R. M., and Coale, K. H. (1997). What controls dissolved iron concentrations in the world ocean? *Marine Chemistry*, 57(3):137–161.
- Johnson, M. S. and Meskhidze, N. (2013). Atmospheric dissolved iron deposition to the global oceans: effects of oxalate-promoted Fe dissolution, photochemical redox cycling, and dust mineralogy. *Geoscientific Model Development*, 6.
- Johnson, M. S., Meskhidze, N., Kiliyanpilakkil, V. P., and Gassó, S. (2011). Understanding the transport of Patagonian dust and its influence on marine biological activity in the South Atlantic Ocean. *Atmospheric Chemistry and Physics*, 11(6):2487–2502.
- Jolly, W. M., Cochrane, M. A., Freeborn, P. H., Holden, Z. A., Brown, T. J., Williamson, G. J., and Bowman, D. M. J. S. (2015). Climate-induced variations in global wildfire danger from 1979 to 2013. *Nature Communications*, 6:7537.
- Jones, M. W., Abatzoglou, J. T., Veraverbeke, S., Andela, N., Lasslop,

References

G., Forkel, M., Smith, A. J. P., Burton, C., Betts, R. A., van der Werf, G. R., Sitch, S., Canadell, J. G., Santín, C., Kolden, C., Doerr, S. H., and Le Quéré, C. (2022). Global and regional trends and drivers of fire under climate change. *Reviews of Geophysics*, 60(3):e2020RG000726.

Jones, M. W., Veraverbeke, S., Andela, N., Doerr, S. H., Kolden, C., Mataveli, G., Pettinari, M. L., Quéré, C. L., Rosan, T. M., van der Werf, G. R., van Wees, D., and Abatzoglou, J. T. (2024). Global rise in forest fire emissions linked to climate change in the extratropics. *Science (New York, N.Y.)*, 386:eadl5889.

Journet, E., Balkanski, Y., and Harrison, S. P. (2014). A new data set of soil mineralogy for dust-cycle modeling. *Atmospheric Chemistry and Physics*, 14(8):3801–3816.

Journet, E., Desboeufs, K. V., Caquineau, S., and Colin, J. L. (2008). Mineralogy as a critical factor of dust iron solubility. *Geophysical Research Letters*, 35(7):3–7.

Kandler, K., Benker, N., Bundke, U., Cuevas, E., Ebert, M., Knippertz, P., Rodríguez, S., Schütz, L., and Weinbruch, S. (2007). Chemical composition and complex refractive index of saharan mineral dust at izaña, tenerife (spain) derived by electron microscopy. *Atmospheric Environment*, 41(37):8058–8074.

Karydis, V. A., Tsimpidi, A. P., Pozzer, A., and Lelieveld, J. (2021). How alkaline compounds control atmospheric aerosol particle acidity. *Atmospheric Chemistry and Physics*, 21(19):14983–15001.

Keerthi, M., Prend, C., Aumont, O., and Levy, M. (2022). Annual variations in phytoplankton biomass driven by small-scale physical

- processes. *Nature Geoscience*, 15:1–7.
- Keerthi, M. G., Levy, M., Aumont, O., Lengaigne, M., and Antoine, D. (2020). Contrasted contribution of intraseasonal time scales to surface chlorophyll variations in a bloom and an oligotrophic regime. *Journal of Geophysical Research: Oceans*, 125(5):e2019JC015701. e2019JC015701 2019JC015701.
- Khaykin, S., Legras, B., Bucci, S., Sellitto, P., Isaksen, L., Tencé, F., Bekki, S., Bourassa, A., Rieger, L., Zawada, D., Jumelet, J., and Godin-Beekmann, S. (2020). The 2019/20 Australian wildfires generated a persistent smoke-charged vortex rising up to 35 km altitude. *Communications Earth and Environment*, 1(1):22.
- Klimont, Z., Kupiainen, K., Heyes, C., Purohit, P., Cofala, J., Rafaj, P., Borken-Kleefeld, J., and Schöpp, W. (2017). Global anthropogenic emissions of particulate matter including black carbon. *Atmospheric Chemistry and Physics*, 17(14):8681–8723.
- Knippertz, P. and Stuut, J.-B. (2014). *Mineral Dust: A Key Player in the Earth System*.
- Knorr, W., Kaminski, T., Arneth, A., and Weber, U. (2014). Impact of human population density on fire frequency at the global scale. *Biogeosciences*, 11(4):1085–1102.
- Koffi, B., Dentener, F., Janssens-Maenhout, G., Guizzardi, D., Crippa, M., Diehl, T., and Galmarini, S. (2016). *Hemispheric Transport Air Pollution (HTAP): Specification of the HTAP2 experiments*.
- Kohfeld, K. E., Quere, C. L., Harrison, S. P., and Anderson, R. F. (2005). Role of marine biology in glacial-interglacial co₂ cycles. *Science*,

References

308(5718):74–78.

Kohfeld, K. E. and Ridgwell, A. (2009). *Glacial-Interglacial Variability in Atmospheric CO₂*, pages 251–286. American Geophysical Union (AGU).

Kok, J. F. (2011). A scaling theory for the size distribution of emitted dust aerosols suggests climate models underestimate the size of the global dust cycle. *Proceedings of the National Academy of Sciences*, 108(3):1016–1021.

Kok, J. F., Adebisi, A. A., Albani, S., Balkanski, Y., Checa-Garcia, R., Chin, M., Colarco, P. R., Hamilton, D. S., Huang, Y., Ito, A., Klose, M., Leung, D. M., Li, L., Mahowald, N. M., Miller, R. L., Obiso, V., Pérez García-Pando, C., Rocha-Lima, A., Wan, J. S., and Whicker, C. A. (2021a). Improved representation of the global dust cycle using observational constraints on dust properties and abundance. *Atmospheric Chemistry and Physics*, 21(10):8127–8167.

Kok, J. F., Adebisi, A. A., Albani, S., Balkanski, Y., Checa-Garcia, R., Chin, M., Colarco, P. R., Hamilton, D. S., Huang, Y., Ito, A., Klose, M., Li, L., Mahowald, N. M., Miller, R. L., Obiso, V., Pérez García-Pando, C., Rocha-Lima, A., and Wan, J. S. (2021b). Contribution of the world’s main dust source regions to the global cycle of desert dust. *Atmospheric Chemistry and Physics*, 21(10):8169–8193.

Kok, J. F., Storelvmo, T., Karydis, V. A., Adebisi, A. A., Mahowald, N. M., Evan, A. T., He, C., and Leung, D. M. (2023). Mineral dust aerosol impacts on global climate and climate change. *Nature Reviews Earth and Environment*, 4(2):71–86.

- Korte, L. F., Brummer, G.-J. A., van der Does, M., Guerreiro, C. V., Hennekam, R., van Hateren, J. A., Jong, D., Munday, C. I., Schouten, S., and Stuut, J.-B. W. (2017). Downward particle fluxes of biogenic matter and saharan dust across the equatorial north atlantic. *Atmospheric Chemistry and Physics*, 17(9):6023–6040.
- Kramer, S. J., Bisson, K. M., and Fischer, A. D. (2020). Observations of phytoplankton community composition in the santa barbara channel during the thomas fire. *Journal of Geophysical Research: Oceans*, 125(12):e2020JC016851.
- Krane, K. S. and Halliday, D. (1987). *Introductory nuclear physics*. Wiley, New York.
- Kriegler, E., Bauer, N., Popp, A., Humpenöder, F., Leimbach, M., Strefler, J., Baumstark, L., Bodirsky, B. L., Hilaire, J., Klein, D., Mouratiadou, I., Weindl, I., Bertram, C., Dietrich, J.-P., Luderer, G., Pehl, M., Pietzcker, R., Piontek, F., Lotze-Campen, H., Biewald, A., Bonsch, M., Giannousakis, A., Kreidenweis, U., Müller, C., Rolinski, S., Schultes, A., Schwanitz, J., Stevanovic, M., Calvin, K., Emmerling, J., Fujimori, S., and Edenhofer, O. (2017). Fossil-fueled development (ssp5): An energy and resource intensive scenario for the 21st century. *Global Environmental Change*, 42:297–315.
- Krishnamurthy, A., Moore, J. K., Mahowald, N., Luo, C., Doney, S. C., Lindsay, K., and Zender, C. S. (2009). Impacts of increasing anthropogenic soluble iron and nitrogen deposition on ocean biogeochemistry. *Global Biogeochemical Cycles*, 23(3).
- Krishnamurthy, A., Moore, J. K., Mahowald, N., Luo, C., and Zender,

References

- C. S. (2010). Impacts of atmospheric nutrient inputs on marine biogeochemistry. *Journal of Geophysical Research: Biogeosciences*, 115(G1).
- Krishnamurthy, A., Moore, J. K., Zender, C. S., and Luo, C. (2007). Effects of atmospheric inorganic nitrogen deposition on ocean biogeochemistry. *Journal of Geophysical Research: Biogeosciences*, 112(G2).
- Krishnapriya, M. S., Varikoden, H., Anjaneyan, P., and Kuttippurath, J. (2023). Marine heatwaves during the pre-monsoon season and their impact on chlorophyll-a in the north indian ocean in 1982-2021. *Marine Pollution Bulletin*, 197:115783–115783.
- Krol, M., Houweling, S., Bregman, B., van den Broek, M., Segers, A., van Velthoven, P., Peters, W., Dentener, F., and Bergamaschi, P. (2005). The two-way nested global chemistry-transport zoom model tm5: algorithm and applications. *Atmospheric Chemistry and Physics*, 5(2):417–432.
- Kruskal, W. H. and Wallis, W. A. (1952). Use of ranks in one-criterion variance analysis. *Journal of the American statistical Association*, 47(260):583–621.
- Kumar, N., Anderson, R., Mortlock, R., Froelich, P., Kubik, P., Dittrich-Hannen, B., and Suter, M. (1995). Increased biological productivity and export production in the glacial southern ocean. *Nature*, 378(6558):675–680.
- Kundu, S., Kawamura, K., Lee, M., Andreae, T. W., Hoffer, A., and Andreae, M. O. (2010). Comparison of amazonian biomass burning

and east asian marine aerosols: Bulk organics, diacids and related compounds, water-soluble inorganic ions, stable carbon and nitrogen isotope ratios. , 68:89–100.

Kurisu, M. and Takahashi, Y. (2019). Testing iron stable isotope ratios as a signature of biomass burning. *Atmosphere*, 10(2).

Kwiatkowski, L., Torres, O., Bopp, L., Aumont, O., Chamberlain, M., Christian, J. R., Dunne, J. P., Gehlen, M., Ilyina, T., John, J. G., Lenton, A., Li, H., Lovenduski, N. S., Orr, J. C., Palmieri, J., Santana-Falcón, Y., Schwinger, J., Séférian, R., Stock, C. A., Tagliabue, A., Takano, Y., Tjiputra, J., Toyama, K., Tsujino, H., Watanabe, M., Yamamoto, A., Yool, A., and Ziehn, T. (2020). Twenty-first century ocean warming, acidification, deoxygenation, and upper-ocean nutrient and primary production decline from cmip6 model projections. *Biogeosciences*, 17(13):3439–3470.

Lafon, S., Rajot, J.-L., Alfaro, S. C., and Gaudichet, A. (2004). Quantification of iron oxides in desert aerosol. *Atmospheric Environment*, 38(8):1211–1218.

Lam, P. J. and Bishop, J. K. B. (2008). The continental margin is a key source of iron to the hnlc north pacific ocean. *Geophysical Research Letters*, 35(7).

Lam, P. J., Ohnemus, D. C., and Marcus, M. A. (2012). The speciation of marine particulate iron adjacent to active and passive continental margins. *Geochimica et Cosmochimica Acta*, 80:108–124.

Lambert, F., Tagliabue, A., Shaffer, G., Lamy, F., Winckler, G., Farias, L., Gallardo, L., and De Pol-Holz, R. (2015). Dust fluxes

References

and iron fertilization in holocene and last glacial maximum climates. *Geophysical Research Letters*, 42(14):6014–6023.

Langmann, B. (2013). Volcanic ash versus mineral dust: Atmospheric processing and environmental and climate impacts. *International Scholarly Research Notices*, 2013(1):245076.

Lasaga, A. C., Soler, J. M., Ganor, J., Burch, T. E., and Nagy, K. L. (1994). Chemical weathering rate laws and global geochemical cycles. *Geochimica et Cosmochimica Acta*, 58(10):2361–2386.

Lawrence, D. M., Fisher, R. A., Koven, C. D., Oleson, K. W., Swenson, S. C., Bonan, G., Collier, N., Ghimire, B., van Kampenhout, L., Kennedy, D., Kluzek, E., Lawrence, P. J., Li, F., Li, H., Lombardozzi, D., Riley, W. J., Sacks, W. J., Shi, M., Vertenstein, M., Wieder, W. R., Xu, C., Ali, A. A., Badger, A. M., Bisht, G., van den Broeke, M., Brunke, M. A., Burns, S. P., Buzan, J., Clark, M., Craig, A., Dahlin, K., Drewniak, B., Fisher, J. B., Flanner, M., Fox, A. M., Gentine, P., Hoffman, F., Keppel-Aleks, G., Knox, R., Kumar, S., Lenaerts, J., Leung, L. R., Lipscomb, W. H., Lu, Y., Pandey, A., Pelletier, J. D., Perket, J., Randerson, J. T., Ricciuto, D. M., Sanderson, B. M., Slater, A., Subin, Z. M., Tang, J., Thomas, R. Q., Val Martin, M., and Zeng, X. (2019). The community land model version 5: Description of new features, benchmarking, and impact of forcing uncertainty. *Journal of Advances in Modeling Earth Systems*, 11(12):4245–4287.

Leung, D. M., Kok, J. F., Li, L., Lawrence, D. M., Mahowald, N. M., Tilmes, S., and Kluzek, E. (2024). A global dust emission dataset for estimating dust radiative forcings in climate models. *EGUsphere*, 2024:1–30.

- Li, F., Ginoux, P., and Ramaswamy, V. (2010). Transport of patagonian dust to antarctica. *Journal of Geophysical Research: Atmospheres*, 115(D18).
- Li, F., Val Martin, M., Andreae, M. O., Arneth, A., Hantson, S., Kaiser, J. W., Lasslop, G., Yue, C., Bachelet, D., Forrest, M., Kluzek, E., Liu, X., Mangeon, S., Melton, J. R., Ward, D. S., Darmenov, A., Hickler, T., Ichoku, C., Magi, B. I., Sitch, S., van der Werf, G. R., Wiedinmyer, C., and Rabin, S. S. (2019). Historical (1700–2012) global multi-model estimates of the fire emissions from the fire modeling intercomparison project (firemip). *Atmospheric Chemistry and Physics*, 19(19):12545–12567.
- Li, G., Cheng, L., Zhu, J., Trenberth, K. E., Mann, M. E., and Abraham, J. P. (2020). Increasing ocean stratification over the past half-century. *Nature Climate Change*, 10:1116–1123.
- Li, Z., Lin, Y., and Cassar, N. (2024). The influence of phytoplankton size fractions on the carbon export ratio in the surface ocean. *Ecological Modelling*, 495:110798.
- Lian, X., Piao, S., Chen, A., Huntingford, C., Fu, B., Li, L. Z., Huang, J., Sheffield, J., Berg, A. M., Keenan, T. F., McVicar, T. R., Wada, Y., Wang, X., Wang, T., Yang, Y., and Roderick, M. L. (2021). Multifaceted characteristics of dryland aridity changes in a warming world.
- Lin, G., Sillman, S., Penner, J. E., and Ito, A. (2014). Global modeling of soa: the use of different mechanisms for aqueous-phase formation. *Atmospheric Chemistry and Physics*, 14(11):5451–5475.

References

- Lis, H., Shaked, Y., Kranzler, C., Keren, N., and Morel, F. M. (2015). Iron bioavailability to phytoplankton: An empirical approach. *ISME Journal*, 9:1003–1013.
- Liu, J., Horowitz, L. W., Fan, S., Carlton, A. G., and Levy, H. (2012). Global in-cloud production of secondary organic aerosols: Implementation of a detailed chemical mechanism in the GFDL atmospheric model AM3. *Journal of Geophysical Research Atmospheres*, 117(15):1–15.
- Liu, L., Li, W., Lin, Q., Wang, Y., Zhang, J., Zhu, Y., Yuan, Q., Zhou, S., Zhang, D., Baldo, C., and Shi, Z. (2022a). Size-dependent aerosol iron solubility in an urban atmosphere. *npj Climate and Atmospheric Science*, 5(1). Funding Information: This work was funded by the National Natural Science Foundation of China (42075096, 42107108, and 41907186), China Postdoctoral Science Foundation (2020M681823), and Zhejiang Provincial Natural Science Foundation of China (LZ19D050001 and LY21D050002). Publisher Copyright: © 2022, The Author(s).
- Liu, M., Matsui, H., Hamilton, D. S., Lamb, K. D., Rathod, S. D., Schwarz, J. P., and Mahowald, N. M. (2022b). The underappreciated role of anthropogenic sources in atmospheric soluble iron flux to the southern ocean. *npj Climate and Atmospheric Science*, 5(1).
- Liu, T., Mickley, L. J., Marlier, M. E., DeFries, R. S., Khan, M. F., Latif, M. T., and Karambelas, A. (2020). Diagnosing spatial biases and uncertainties in global fire emissions inventories: Indonesia as regional case study. *Remote Sensing of Environment*, 237:111557.

- Liu, X., Ma, P.-L., Wang, H., Tilmes, S., Singh, B., Easter, R. C., Ghan, S. J., and Rasch, P. J. (2016). Description and evaluation of a new four-mode version of the modal aerosol module (mam4) within version 5.3 of the community atmosphere model. *Geoscientific Model Development*, 9(2):505–522.
- Liu, X. and Millero, F. J. (2002). The solubility of iron in seawater. *Marine Chemistry*, 77(1):43–54.
- Llort, J., Lévy, M., Sallée, J. B., and Tagliabue, A. (2019). Nonmonotonic response of primary production and export to changes in mixed-layer depth in the southern ocean. *Geophysical Research Letters*, 46(6):3368–3377.
- Longo, A. F., Feng, Y., Lai, B., Landing, W. M., Shelley, R. U., Nenes, A., Mihalopoulos, N., Violaki, K., and Ingall, E. D. (2016). Influence of atmospheric processes on the solubility and composition of iron in saharan dust.
- Luo, C. and Gao, Y. (2010). Aeolian iron mobilisation by dust-acid interactions and their implications for soluble iron deposition to the ocean: A test involving potential anthropogenic organic acidic species. *Environmental Chemistry*, 7(2):153–161.
- Luo, C., Mahowald, N., Bond, T., Chuang, P. Y., Artaxo, P., Siefert, R., Chen, Y., and Schauer, J. (2008). Combustion iron distribution and deposition. *Global Biogeochemical Cycles*, 22(1).
- Luo, C., Mahowald, N. M., and del Corral, J. (2003). Sensitivity study of meteorological parameters on mineral aerosol mobilization,

References

transport, and distribution. *Journal of Geophysical Research: Atmospheres*, 108(D15).

Luo, C., Mahowald, N. M., Meskhidze, N., Chen, Y., Siefert, R. L., Baker, A. R., and Johansen, A. M. (2005). Estimation of iron solubility from observations and a global aerosol model. *Journal of Geophysical Research: Atmospheres*, 110(D23).

Mackie, D. S. (2005). Simulating the cloud processing of iron in australian dust: ph and dust concentration. *Geophysical Research Letters*, 32.

Mahowald, N., Albani, S., Kok, J. F., Engelstaeder, S., Scanza, R., Ward, D. S., and Flanner, M. G. (2014). The size distribution of desert dust aerosols and its impact on the earth system. *Aeolian Research*, 15:53–71.

Mahowald, N., Luo, C., del Corral, J., and Zender, C. S. (2003). Interannual variability in atmospheric mineral aerosols from a 22-year model simulation and observational data. *Journal of Geophysical Research: Atmospheres*, 108(D12).

Mahowald, N. M. (2007). Anthropocene changes in desert area: Sensitivity to climate model predictions. *Geophysical Research Letters*, 34(18).

Mahowald, N. M., Baker, A. R., Bergametti, G., Brooks, N., Duce, R. A., Jickells, T. D., Kubilay, N., Prospero, J. M., and Tegen, I. (2005). Atmospheric global dust cycle and iron inputs to the ocean. *Global Biogeochemical Cycles*, 19.

- Mahowald, N. M., Engelstaedter, S., Luo, C., Sealy, A., Artaxo, P., Benitez-Nelson, C., Bonnet, S., Chen, Y., Chuang, P. Y., Cohen, D. D., Dulac, F., Herut, B., Johansen, A. M., Kubilay, N., Losno, R., Maenhaut, W., Paytan, A., Prospero, J. M., Shank, L. M., and Siefert, R. L. (2009). Atmospheric iron deposition: Global distribution, variability, and human perturbations. *Annual Review of Marine Science*, 1:245–278.
- Mahowald, N. M., Hamilton, D. S., Mackey, K. R., Moore, J. K., Baker, A. R., Scanza, R. A., and Zhang, Y. (2018). Aerosol trace metal leaching and impacts on marine microorganisms. *Nature Communications*, 9(1).
- Mahowald, N. M., Kloster, S., Engelstaedter, S., Moore, J. K., Mukhopadhyay, S., McConnell, J. R., Albani, S., Doney, S. C., Bhattacharya, A., Curran, M. A. J., Flanner, M. G., Hoffman, F. M., Lawrence, D. M., Lindsay, K., Mayewski, P. A., Neff, J., Rothenberg, D., Thomas, E., Thornton, P. E., and Zender, C. S. (2010). Observed 20th century desert dust variability: impact on climate and biogeochemistry. *Atmospheric Chemistry and Physics*, 10(22):10875–10893.
- Mahowald, N. M. and Luo, C. (2003). A less dusty future? *Geophysical Research Letters*, 30(17).
- Mahowald, N. M., Muhs, D. R., Levis, S., Rasch, P. J., Yoshioka, M., Zender, C. S., and Luo, C. (2006). Change in atmospheric mineral aerosols in response to climate: Last glacial period, preindustrial, modern, and doubled carbon dioxide climates. *Journal of Geophysical Research: Atmospheres*, 111(D10).

References

- Manubens-Gil, D., Vegas-Regidor, J., Prodhomme, C., Mula-Valls, O., and Doblás-Reyes, F. J. (2016). Seamless management of ensemble climate prediction experiments on hpc platforms. In *2016 International Conference on High Performance Computing Simulation (HPCS)*, pages 895–900.
- Marañón, E., Fernández, A., Mouriño-Carballido, B., Martínez-García, S., Teira, E., Cermeño, P., Chouciño, P., Huete-Ortega, M., Fernández, E., Calvo-Díaz, A., Morán, X. A. G., Bode, A., Moreno-Ostos, E., Varela, M. M., Patey, M. D., and Achterberg, E. P. (2010). Degree of oligotrophy controls the response of microbial plankton to saharan dust. *Limnology and Oceanography*, 55(6):2339–2352.
- Marticorena, B., Chatenet, B., Rajot, J. L., Traoré, S., Coulibaly, M., Diallo, A., Koné, I., Maman, A., NDiaye, T., and Zakou, A. (2010). Temporal variability of mineral dust concentrations over west africa: analyses of a pluriannual monitoring from the amma sahelian dust transect. *Atmospheric Chemistry and Physics*, 10(18):8899–8915.
- Martin, J. H. (1990). Glacial-interglacial co₂ change: The iron hypothesis. *Paleoceanography*, 5(1):1–13.
- Martinez-Vicente, V., Dall’Olmo, G., Tarran, G., Boss, E., and Sathyendranath, S. (2013). Optical backscattering is correlated with phytoplankton carbon across the atlantic ocean. *Geophysical Research Letters*, 40(6):1154–1158.
- Matsui, H., Mahowald, N., Moteki, N., Hamilton, D., Ohata, S., Yoshida, A., Koike, M., Scanza, R., and Flanner, M. (2018). Anthropogenic combustion iron as a complex climate forcer. *Nature*

Communications, 9.

Mauritsen, T., Bader, J., Becker, T., Behrens, J., Bittner, M., Brokopf, R., Brovkin, V., Claussen, M., Crueger, T., Esch, M., Fast, I., Fiedler, S., Fläschner, D., Gayler, V., Giorgetta, M., Goll, D. S., Haak, H., Hagemann, S., Hedemann, C., Hohenegger, C., Ilyina, T., Jahns, T., Jimenéz-de-la Cuesta, D., Jungclaus, J., Kleinen, T., Kloster, S., Kracher, D., Kinne, S., Kleberg, D., Lasslop, G., Kornblueh, L., Marotzke, J., Matei, D., Meraner, K., Mikolajewicz, U., Modali, K., Möbis, B., Müller, W. A., Nabel, J. E. M. S., Nam, C. C. W., Notz, D., Nyawira, S.-S., Paulsen, H., Peters, K., Pincus, R., Pohlmann, H., Pongratz, J., Popp, M., Raddatz, T. J., Rast, S., Redler, R., Reick, C. H., Rohrschneider, T., Schemann, V., Schmidt, H., Schnur, R., Schulzweida, U., Six, K. D., Stein, L., Stemmler, I., Stevens, B., von Storch, J.-S., Tian, F., Voigt, A., Vrese, P., Wieners, K.-H., Wilkenskjaeld, S., Winkler, A., and Roeckner, E. (2019). Developments in the mpi-m earth system model version 1.2 (mpi-esm1.2) and its response to increasing co2. *Journal of Advances in Modeling Earth Systems*, 11(4):998–1038.

McCarty, J. L., Aalto, J., Paunu, V.-V., Arnold, S. R., Eckhardt, S., Klimont, Z., Fain, J. J., Evangelidou, N., Venäläinen, A., Tchepakova, N. M., Parfenova, E. I., Kupiainen, K., Soja, A. J., Huang, L., and Wilson, S. (2021). Reviews and syntheses: Arctic fire regimes and emissions in the 21st century. *Biogeosciences*, 18(18):5053–5083.

McDonough, W. and s. Sun, S. (1995). The composition of the earth. *Chemical Geology*, 120(3):223–253. Chemical Evolution of the Mantle.

Meinander, O., Dagsson-Waldhauserova, P., Amosov, P., Aseyeva, E.,

References

- Atkins, C., Baklanov, A., Baldo, C., Barr, S. L., Barzycka, B., Benning, L. G., Cvetkovic, B., Enchilik, P., Frolov, D., Gassó, S., Kandler, K., Kasimov, N., Kavan, J., King, J., Koroleva, T., Krupskaya, V., Kulmala, M., Kusiak, M., Lappalainen, H. K., Laska, M., Lasne, J., Lewandowski, M., Luks, B., McQuaid, J. B., Moroni, B., Murray, B., Möhler, O., Nawrot, A., Nickovic, S., O'Neill, N. T., Pejanovic, G., Popovicheva, O., Ranjbar, K., Romanias, M., Samonova, O., Sanchez-Marroquin, A., Schepanski, K., Semenov, I., Sharapova, A., Shevnina, E., Shi, Z., Sofiev, M., Thevenet, F., Thorsteinsson, T., Timofeev, M., Umo, N. S., Uppstu, A., Urupina, D., Varga, G., Werner, T., Arnalds, O., and Vukovic Vimic, A. (2022). Newly identified climatically and environmentally significant high-latitude dust sources. *Atmospheric Chemistry and Physics*, 22(17):11889–11930.
- Meskhidze, N., Chameides, W. L., and Nenes, A. (2005). Dust and pollution: A recipe for enhanced ocean fertilization? *Journal of Geophysical Research: Atmospheres*, 110(D3).
- Meskhidze, N., Johnson, M. S., Hurley, D., and Dawson, K. (2016). Influence of measurement uncertainties on fractional solubility of iron in mineral aerosols over the oceans. *Aeolian Research*, 22:85–92.
- Miyakawa, T., Ito, A., Zhu, C., Shimizu, A., Matsumoto, E., Mizuno, Y., and Kanaya, Y. (2023). Trace elements in pm_{2.5} aerosols in east asian outflow in the spring of 2018: emission, transport, and source apportionment. *Atmospheric Chemistry and Physics*, 23(22):14609–14626.
- Moore, C. M., Mills, M. M., Arrigo, K. R., Berman-Frank, I., Bopp, L., Boyd, P. W., Galbraith, E. D., Geider, R. J., Guieu, C., Jaccard,

- S. L., Jickells, T. D., La Roche, J., Lenton, T. M., Mahowald, N. M., Marañón, E., Marinov, I., Moore, J. K., Nakatsuka, T., Oschlies, A., Saito, M. A., Thingstad, T. F., Tsuda, A., and Ulloa, O. (2013). Processes and patterns of oceanic nutrient limitation. *Nature Geoscience*, 6(9):701–710.
- Moore, J., Doney, S. C., Glover, D. M., and Fung, I. Y. (2001). Iron cycling and nutrient-limitation patterns in surface waters of the world ocean. *Deep Sea Research Part II: Topical Studies in Oceanography*, 49.
- Moore, J. K. and Doney, S. C. (2007). Iron availability limits the ocean nitrogen inventory stabilizing feedbacks between marine denitrification and nitrogen fixation. *Global Biogeochemical Cycles*, 21(2):0–12.
- Moore, J. K., Doney, S. C., and Lindsay, K. (2004). Upper ocean ecosystem dynamics and iron cycling in a global three-dimensional model. *Global Biogeochemical Cycles*, 18(4).
- Mortlock, R., Charles, C., Froelich, P., Zibello, M., Saltzman, J., Hays, J., and Burckle, L. (1991). Evidence for lower productivity in the antarctic ocean during the last glaciation. *Nature*, 351(6323):220–223.
- Moss, R., Edmonds, J., Hibbard, K., Manning, M., Rose, S., Vuuren, D., Carter, T., Emori, S., Kainuma, M., Kram, T., Meehl, G., Mitchell, J., Nakicenovic, N., Riahi, K., Smith, S., Ronald, S., Thomson, A., Weyant, J., and Wilbanks, T. (2010). The next generation of scenarios for climate change research and assessment. *Nature*, 463:747–56.
- Moxim, W. J., Fan, S.-M., and Levy, H. (2011). The meteorological nature of variable soluble iron transport and deposition within

References

the north atlantic ocean basin. *Journal of Geophysical Research: Atmospheres*, 116(D3).

Muhs, D. R., Budahn, J., Reheis, M., Beann, J., Skipp, G., and Fisher, E. (2007). Airborne dust transport to the eastern pacific ocean off southern california: Evidence from san clemente island. *Journal of Geophysical Research: Atmospheres*, 112(D13).

Muller-Karger, F. E., Tan, A. S. H., Allcock, L., Appeltans, W., Barón Aguilar, C., Blanco, A., Bograd, S. J., Buttigieg, P., Costello, M. J., Darnaude, A., Dupuis, B., Evaux, L. M., Friedman, K., Goodwin, K., Jungbluth, S., Leinen, M., Levin, L., Mahapatra, P., Martone, R., Mtwana Nordlund, L., Ndah, A. B., Pante, E., Pearlman, J., Pelletier, D., Pendleton, L., Relano, V., Rogers, A. D., San Diego-McGlone, M. L., Seeyave, S., Sequeira, A., Soares, J., Stiasny, M., Taylor, S., and Vavia, A. (2024). Ocean decade vision 2030 white papers – challenge 2: Protect and restore ecosystems and biodiversity. *UNESCO-IOC, The Ocean Decade Series*, 51.2.

Myriokefalitakis, S., Bergas-Massó, E., Gonçalves-Ageitos, M., Pérez García-Pando, C., van Noije, T., Le Sager, P., Ito, A., Athanasopoulou, E., Nenes, A., Kanakidou, M., Krol, M. C., and Gerasopoulos, E. (2022). Multiphase processes in the ec-earth model and their relevance to the atmospheric oxalate, sulfate, and iron cycles. *Geoscientific Model Development*, 15(7):3079–3120.

Myriokefalitakis, S., Daskalakis, N., Gkouvousis, A., Hilboll, A., van Noije, T., Williams, J. E., Le Sager, P., Huijnen, V., Houweling, S., Bergman, T., Nüß, J. R., Vrekoussis, M., Kanakidou, M., and Krol, M. C. (2020). Description and evaluation of a detailed gas-phase

chemistry scheme in the tm5-mp global chemistry transport model (r112). *Geoscientific Model Development*, 13(11):5507–5548.

Myriokefalitakis, S., Daskalakis, N., Mihalopoulos, N., Baker, A. R., Nenes, A., and Kanakidou, M. (2015). Changes in dissolved iron deposition to the oceans driven by human activity: a 3-d global modelling study. *Biogeosciences*, 12(13):3973–3992.

Myriokefalitakis, S., Ito, A., Kanakidou, M., Nenes, A., Krol, M. C., Mahowald, N. M., Scanza, R. A., Hamilton, D. S., Johnson, M. S., Meskhidze, N., Kok, J. F., Guieu, C., Baker, A. R., Jickells, T. D., Sarin, M. M., Bikkina, S., Shelley, R., Bowie, A., Perron, M. M., and Duce, R. A. (2018). Reviews and syntheses: The gesamp atmospheric iron deposition model intercomparison study.

Myriokefalitakis, S., Tsigaridis, K., Mihalopoulos, N., Sciare, J., Nenes, A., Kawamura, K., Segers, A., and Kanakidou, M. (2011). In-cloud oxalate formation in the global troposphere: a 3-d modeling study. *Atmospheric Chemistry and Physics*, 11(12):5761–5782.

NASA (1986). *Earth System Science: Overview: A Program for Global Change*. The National Academies Press, Washington, DC.

Neuer, S., Torres-Padrón, M., Gelado-Caballero, M., Rueda, M., Hernández-Brito, J., Davenport, R., and Wefer, G. (2004). Dust deposition pulses to the eastern subtropical north atlantic gyre: Does ocean’s biogeochemistry respond? *Global Biogeochemical Cycles*, 18(4).

Neukermans, G., Bach, L., Butterley, A., Sun, Q., Claustre, H., and Fournier, G. (2023). Quantitative and mechanistic understanding of

References

the open ocean carbonate pump-perspectives for remote sensing and autonomous in situ observation. *Earth-Science Reviews*, 239:104359.

Nguyen, H. D., Leys, J., Riley, M., White, S., Azzi, M., Trieu, T., Salter, D., Ji, F., Nguyen, H., Chang, L. T.-C., Monk, K., Firth, J., Fuchs, D., and Barthelemy, X. (2024). Effects of dust storm and wildfire events on phytoplankton growth and carbon sequestration in the tasman sea, southeast australia. *Atmosphere*, 15(3).

Nicholson, S. E. (2018). The itcz and the seasonal cycle over equatorial africa. *Bulletin of the American Meteorological Society*, 99(2):337 – 348.

Nickovic, S., Vukovic, A., and Vujadinovic, M. (2013). Atmospheric processing of iron carried by mineral dust. *Atmospheric Chemistry and Physics*, 13(18):9169–9181.

Nickovic, S., Vukovic, A., Vujadinovic, M., Djurdjevic, V., and Pejanovic, G. (2012). Technical Note: High-resolution mineralogical database of dust-productive soils for atmospheric dust modeling. *Atmospheric Chemistry and Physics*, 12(2):845–855.

Nissimov, J. I., Vandzura, R., Johns, C. T., Natale, F., Haramaty, L., and Bidle, K. D. (2018). Dynamics of transparent exopolymer particle production and aggregation during viral infection of the coccolithophore, *emiliana huxleyi*. *Environmental Microbiology*, 20(8):2880–2897.

Oakes, M., Ingall, E. D., Lai, B., Shafer, M. M., Hays, M. D., Liu, Z. G., Russell, A. G., and Weber, R. J. (2012). Iron solubility related to particle sulfur content in source emission and ambient

fine particles. *Environmental Science & Technology*, 46(12):6637–6644. PMID: 22621615.

Okin, G. S., Baker, A. R., Tegen, I., Mahowald, N. M., Dentener, F. J., Duce, R. A., Galloway, J. N., Hunter, K., Kanakidou, M., Kubilay, N., Prospero, J. M., Sarin, M., Surapipith, V., Uematsu, M., and Zhu, T. (2011). Impacts of atmospheric nutrient deposition on marine productivity: Roles of nitrogen, phosphorus, and iron. *Global Biogeochemical Cycles*, 25(2):1–10.

Olgun, N., Duggen, S., Andronico, D., Kutterolf, S., Croot, P. L., Giammanco, S., Censi, P., and Randazzo, L. (2013). Possible impacts of volcanic ash emissions of mount etna on the primary productivity in the oligotrophic mediterranean sea: Results from nutrient-release experiments in seawater. *Marine Chemistry*, 152:32–42.

Olgun, N., Duggen, S., Croot, P. L., Delmelle, P., Dietze, H., Schacht, U., Óskarsson, N., Siebe, C., Auer, A., and Garbe-Schönberg, D. (2011). Surface ocean iron fertilization: The role of airborne volcanic ash from subduction zone and hot spot volcanoes and related iron fluxes into the pacific ocean. *Global Biogeochemical Cycles*, 25(4).

O’Neill, B. C., Kriegler, E., Ebi, K. L., Kemp-Benedict, E., Riahi, K., Rothman, D. S., van Ruijven, B. J., van Vuuren, D. P., Birkmann, J., Kok, K., Levy, M., and Solecki, W. (2017). The roads ahead: Narratives for shared socioeconomic pathways describing world futures in the 21st century. *Global Environmental Change*, 42:169–180.

Oschlies, A., Koeve, W., Rickels, W., and Rehdanz, K. (2010). Side effects and accounting aspects of hypothetical large-scale southern

References

- ocean iron fertilization. *Biogeosciences*, 7(12):4017–4035.
- Pan, X., Ichoku, C., Chin, M., Bian, H., Darmenov, A., Colarco, P., Ellison, L., Kucsera, T., Silva, A. D., Wang, J., Oda, T., and Cui, G. (2020). Six global biomass burning emission datasets: Intercomparison and application in one global aerosol model. *Atmospheric Chemistry and Physics*, 20:969–994.
- Panias, D., Taxiarchou, M., Paspaliaris, I., and Kontopoulos, A. (1996). Mechanisms of dissolution of iron oxides in aqueous oxalic acid solutions. *Hydrometallurgy*, 42.
- Panta, A., Kandler, K., Alastuey, A., González-Flórez, C., González-Romero, A., Klose, M., Querol, X., Reche, C., Yus-Díez, J., and Pérez García-Pando, C. (2023). Insights into the single-particle composition, size, mixing state, and aspect ratio of freshly emitted mineral dust from field measurements in the moroccan sahara using electron microscopy. *Atmospheric Chemistry and Physics*, 23(6):3861–3885.
- Paris, R. and Desboeufs, K. V. (2013). Effect of atmospheric organic complexation on iron-bearing dust solubility. *Atmospheric Chemistry and Physics*, 13(9):4895–4905.
- Paris, R., Desboeufs, K. V., Formenti, P., Nava, S., and Chou, C. (2010). Chemical characterisation of iron in dust and biomass burning aerosols during amma-sop0/dabex: implication for iron solubility. *Atmospheric Chemistry and Physics*, 10(9):4273–4282.
- Pausas, J. G. and Keeley, J. E. (2019). Wildfires as an ecosystem service. *Frontiers in Ecology and the Environment*, 17:289–295.

- Paytan, A., Mackey, K. R. M., Chen, Y., Lima, I. D., Doney, S. C., Mahowald, N., Labiosa, R., and Post, A. F. (2009). Toxicity of atmospheric aerosols on marine phytoplankton. *Proceedings of the National Academy of Sciences*, 106(12):4601–4605.
- Pease, P. P., Tchakerian, V. P., and Tindale, N. W. (1998). Aerosols over the arabian sea: geochemistry and source areas for aeolian desert dust. *Journal of Arid Environments*, 39(3):477–496.
- Pechony, O. and Shindell, D. T. (2010). Driving forces of global wildfires over the past millennium and the forthcoming century. *Proc. Natl. Acad. Sci.*, 107:19167–19170.
- Perlwitz, J. P., Pérez García-Pando, C., and Miller, R. L. (2015a). Predicting the mineral composition of dust aerosols – part 1: Representing key processes. *Atmospheric Chemistry and Physics*, 15(20):11593–11627.
- Perlwitz, J. P., Pérez García-Pando, C., and Miller, R. L. (2015b). Predicting the mineral composition of dust aerosols – part 2: Model evaluation and identification of key processes with observations. *Atmospheric Chemistry and Physics*, 15(20):11629–11652.
- Perron, M. M., Meyerink, S., Corkill, M., Strzelec, M., Proemse, B. C., Gault-Ringold, M., Sanz Rodriguez, E., Chase, Z., and Bowie, A. R. (2022). Trace elements and nutrients in wildfire plumes to the southeast of australia. *Atmospheric Research*, 270:106084.
- Pezzulli, S., Stephenson, D. B., and Hannachi, A. (2005). The variability of seasonality. *Journal of Climate*, 18(1):71 – 88.

References

Prospero, J. M. (1996). *Saharan Dust Transport Over the North Atlantic Ocean and Mediterranean: An Overview*, pages 133–151. Springer Netherlands, Dordrecht.

Prospero, J. M. (1999). Long-term measurements of the transport of african mineral dust to the southeastern united states: Implications for regional air quality. *Journal of Geophysical Research: Atmospheres*, 104(D13):15917–15927.

Prospero, J. M., Ginoux, P., Torres, O., Nicholson, S. E., and Gill, T. E. (2002). Environmental characterization of global sources of atmospheric soil dust identified with the nimbus 7 total ozone mapping spectrometer (toms) absorbing aerosol product. *Reviews of Geophysics*, 40(1):2–1–2–31.

Prospero, J. M. and Lamb, P. J. (2003). African droughts and dust transport to the caribbean: Climate change implications. *Science*, 302(5647):1024–1027.

Pérez García-Pando, C., Miller, R. L., Perlwitz, J. P., Rodríguez, S., and Prospero, J. M. (2016). Predicting the mineral composition of dust aerosols: Insights from elemental composition measured at the izaña observatory. *Geophysical Research Letters*, 43(19):10,520–10,529.

Randerson, J., Van der Werf, G., Giglio, L., Collatz, G., and Kasibhatla, P. (2017). Global Fire Emissions Database, Version 4.1 (GFEDv4).

Rathod, S. D., Hamilton, D. S., Li, L., Mahowald, N. M., Matsui, H., Pierce, J. R., and Bond, T. C. (2022). Atmospheric radiative and oceanic biological productivity responses to increasing

anthropogenic combustion-iron emission in the 1850–2010 period. *Geophysical Research Letters*, 49(16):e2022GL099323. e2022GL099323 2022GL099323.

Rathod, S. D., Hamilton, D. S., Mahowald, N. M., Klimont, Z., Corbett, J. J., and Bond, T. C. (2020). A Mineralogy-Based Anthropogenic Combustion-Iron Emission Inventory. *Journal of Geophysical Research: Atmospheres*, 125(17):1–35.

Rathod, S. D., Hamilton, D. S., Nino, L., Kreidenweis, S. M., Bian, Q., Mahowald, N. M., Alastuey, A., Querol, X., Paytan, A., Artaxo, P., Herut, B., Gaston, C., Prospero, J., Chellam, S., Hueglin, C., Varrica, D., Dongarra, G., Cohen, D. D., Smichowski, P., Gomez, D., Lambert, F., Barraza, F., Bergametti, G., Rodríguez, S., Gonzalez-Ramos, Y., Hand, J., Kyllönen, K., Hakola, H., Chuang, P., Hopke, P. K., Harrison, R. M., Martin, R. V., Walsh, B., Weagle, C., Maenhaut, W., Morera-Gómez, Y., Chen, Y.-C., Pierce, J. R., and Bond, T. C. (2024). Constraining present-day anthropogenic total iron emissions using model and observations. *Journal of Geophysical Research: Atmospheres*, 129(17):e2023JD040332.

Raven, J. A., Evans, M. C. W., and Korb, R. E. (1999). The role of trace metals in photosynthetic electron transport in o₂-evolving organisms. *Photosynthesis Research*, 60:111–150.

Riahi, K., van Vuuren, D. P., Kriegler, E., Edmonds, J., O'Neill, B. C., Fujimori, S., Bauer, N., Calvin, K., Dellink, R., Fricko, O., Lutz, W., Popp, A., Cuaresma, J. C., KC, S., Leimbach, M., Jiang, L., Kram, T., Rao, S., Emmerling, J., Ebi, K., Hasegawa, T., Havlik, P., Humpenöder, F., Da Silva, L. A., Smith, S., Stehfest, E., Bosetti, V.,

References

Eom, J., Gernaat, D., Masui, T., Rogelj, J., Strefler, J., Drouet, L., Krey, V., Luderer, G., Harmsen, M., Takahashi, K., Baumstark, L., Doelman, J. C., Kainuma, M., Klimont, Z., Marangoni, G., Lotze-Campen, H., Obersteiner, M., Tabeau, A., and Tavoni, M. (2017). The shared socioeconomic pathways and their energy, land use, and greenhouse gas emissions implications: An overview. *Global Environmental Change*, 42:153–168.

Rickly, P. S., Guo, H., Campuzano-Jost, P., Jimenez, J. L., Wolfe, G. M., Bennett, R., Bourgeois, I., Crouse, J. D., Dibb, J. E., Digangi, J. P., Diskin, G. S., Dollner, M., Gargulinski, E. M., Hall, S. R., Halliday, H. S., Hanisco, T. F., Hannun, R. A., Liao, J., Moore, R., Nault, B. A., Nowak, J. B., Peischl, J., Robinson, C. E., Ryerson, T., Sanchez, K. J., Schöberl, M., Soja, A. J., Clair, J. M. S., Thornhill, K. L., Ullmann, K., Wennberg, P. O., Weinzierl, B., Wiggins, E. B., Winstead, E. L., and Rollins, A. W. (2022). Emission factors and evolution of so₂ measured from biomass burning in wildfires and agricultural fires. *Atmospheric Chemistry and Physics*, 22:15603–15620.

Ricour, F., Guidi, L., Gehlen, M., DeVries, T., and Legendre, L. (2023). Century-scale carbon sequestration flux throughout the ocean by the biological pump. *Nature Geoscience*, 16(12):1105–1113.

Rienecker, M. M., Suarez, M. J., Gelaro, R., Todling, R., Bacmeister, J., Liu, E., Bosilovich, M. G., Schubert, S. D., Takacs, L., Kim, G.-K., Bloom, S., Chen, J., Collins, D., Conaty, A., da Silva, A., Gu, W., Joiner, J., Koster, R. D., Lucchesi, R., Molod, A., Owens, T., Pawson, S., Pegion, P., Redder, C. R., Reichle, R., Robertson,

- F. R., Ruddick, A. G., Sienkiewicz, M., and Woollen, J. (2011). Merra: Nasa's modern-era retrospective analysis for research and applications. *Journal of Climate*, 24(14):3624 – 3648.
- Riera, R. and Pausas, J. G. (2023). Fire ecology in marine systems. *Trends in Ecology Evolution*.
- Rizzolo, J. A., Barbosa, C. G. G., Borillo, G. C., Godoi, A. F. L., Souza, R. A. F., Andreoli, R. V., Manzi, A. O., Sá, M. O., Alves, E. G., Pöhlker, C., Angelis, I. H., Ditas, F., Saturno, J., Moran-Zuloaga, D., Rizzo, L. V., Rosário, N. E., Pauliquevis, T., Santos, R. M. N., Yamamoto, C. I., Andreae, M. O., Artaxo, P., Taylor, P. E., and Godoi, R. H. M. (2017). Soluble iron nutrients in saharan dust over the central amazon rainforest. *Atmospheric Chemistry and Physics*, 17(4):2673–2687.
- Rodriguez-Caballero, E., Stanelle, T., Egerer, S., Cheng, Y., Su, H., Canton, Y., Belnap, J., Andreae, M. O., Tegen, I., Reick, C. H., Pöschl, U., and Weber, B. (2022). Global cycling and climate effects of aeolian dust controlled by biological soil crusts. *Nature Geoscience*, 15:458–463.
- Rodríguez, S., Prospero, J. M., López-Darias, J., García-Alvarez, M.-I., Zuidema, P., Nava, S., Lucarelli, F., Gaston, C. J., Galindo, L., and Sosa, E. (2021). Tracking the changes of iron solubility and air pollutants traces as african dust transits the atlantic in the saharan dust outbreaks. *Atmospheric Environment*, 246:118092.
- Rousset, C., Vancoppenolle, M., Madec, G., Fichet, T., Flavoni, S., Barthélemy, A., Benschila, R., Chanut, J., Levy, C., Masson, S.,

References

and Vivier, F. (2015). The louvain-la-neuve sea ice model lim3.6: global and regional capabilities. *Geoscientific Model Development*, 8(10):2991–3005.

Ryan-Keogh, T. J., Macey, A. I., Nielsdóttir, M. C., Lucas, M. I., Steigenberger, S. S., Stinchcombe, M. C., Achterberg, E. P., Bibby, T. S., and Moore, C. M. (2013). Spatial and temporal development of phytoplankton iron stress in relation to bloom dynamics in the high-latitude North Atlantic Ocean. *Limnology and Oceanography*, 58(2):533–545.

Sanders, R., Henson, S. A., Koski, M., Rocha, C. L. D. L., Painter, S. C., Poulton, A. J., Riley, J., Salihoglu, B., Visser, A., Yool, A., Bellerby, R., and Martin, A. P. (2014). The biological carbon pump in the north atlantic. *Progress in Oceanography*, 129:200–218.

Sarma, V. V. S. S., Krishna, M. S., Srinivas, T. N. R., Kumari, V. R., Yadav, K., and Kumar, M. D. (2021). Elevated acidification rates due to deposition of atmospheric pollutants in the coastal bay of bengal. *Geophysical Research Letters*, 48(16):e2021GL095159.

Sasaoka, K., Chiba, S., and Saino, T. (2011). Climatic forcing and phytoplankton phenology over the subarctic north pacific from 1998 to 2006, as observed from ocean color data. *Geophysical Research Letters*, 38(15).

Sathyendranath, S., Jackson, T., Brockmann, C., Brotas, V., Calton, B., Chuprin, A., Clements, O., Cipollini, P., Danne, O., Dingle, J., Donlon, C., Grant, M., Groom, S., Krasemann, H., Lavender, S., Mazeran, C., Mélin, F., Müller, D., Steinmetz, F., Valente, A., Zühlke,

- M., Feldman, G., Franz, B., Frouin, R., Werdell, P. J., and Platt, T. (2023). ESA Ocean Colour Climate Change Initiative: Version 6.0, 4km resolution data. 08 August 2023.
- Scanza, R. A., Hamilton, D. S., Perez Garcia-Pando, C., Buck, C., Baker, A., and Mahowald, N. M. (2018). Atmospheric processing of iron in mineral and combustion aerosols: development of an intermediate-complexity mechanism suitable for earth system models. *Atmospheric Chemistry and Physics*, 18(19):14175–14196.
- Scheuvens, D., Schütz, L., Kandler, K., Ebert, M., and Weinbruch, S. (2013). Bulk composition of northern african dust and its source sediments — a compilation. *Earth-Science Reviews*, 116:170–194.
- Schlesinger, W. and Bernhardt, E. (2013). *Biogeochemistry: An Analysis of Global Change*. Elsevier Science.
- Schlosser, J. S., Braun, R. A., Bradley, T., Dadashazar, H., MacDonald, A. B., Aldhaif, A. A., Aghdam, M. A., Mardi, A. H., Xian, P., and Sorooshian, A. (2017). Analysis of aerosol composition data for western united states wildfires between 2005 and 2015: Dust emissions, chloride depletion, and most enhanced aerosol constituents. *Journal of Geophysical Research: Atmospheres*, 122(16):8951–8966.
- Schmidl, C., Marr, I. L., Caseiro, A., Kotianová, P., Berner, A., Bauer, H., Kasper-Giebl, A., and Puxbaum, H. (2008). Chemical characterisation of fine particle emissions from wood stove combustion of common woods growing in mid-european alpine regions. *Atmospheric Environment*, 42(1):126–141.
- Schulz, M., Prospero, J. M., Baker, A. R., Dentener, F., Ickes, L., Liss,

References

- P. S., Mahowald, N. M., Nickovic, S., García-Pando, C. P., Rodríguez, S., et al. (2012). Atmospheric transport and deposition of mineral dust to the ocean: Implications for research needs. *Environmental science & technology*, 46(19):10390–10404.
- Sedwick, P. N., Sholkovitz, E. R., and Church, T. M. (2007). Impact of anthropogenic combustion emissions on the fractional solubility of aerosol iron: Evidence from the sargasso sea. *Geochemistry, Geophysics, Geosystems*, 8(10).
- Seinfeld, J. and Pandis, S. (2016). *Atmospheric Chemistry and Physics: From Air Pollution to Climate Change*. Wiley.
- Seland, Ø., Bentsen, M., Olivié, D., Toniazzo, T., Gjermundsen, A., Graff, L. S., Debernard, J. B., Gupta, A. K., He, Y.-C., Kirkevåg, A., Schwinger, J., Tjiputra, J., Aas, K. S., Bethke, I., Fan, Y., Griesfeller, J., Grini, A., Guo, C., Ilicak, M., Karset, I. H. H., Landgren, O., Liakka, J., Moseid, K. O., Nummelin, A., Spensberger, C., Tang, H., Zhang, Z., Heinze, C., Iversen, T., and Schulz, M. (2020). Overview of the Norwegian Earth System Model (NorESM2) and key climate response of CMIP6 DECK, historical, and scenario simulations. *Geoscientific Model Development*, 13(12):6165–6200.
- Senf, F., Heinold, B., Kubin, A., Müller, J., Schrödner, R., and Tegen, I. (2023). How the extreme 2019–2020 Australian wildfires affected global circulation and adjustments. *Atmospheric Chemistry and Physics*, 23(15):8939–8958.
- Shakun, J., Clark, P., He, F., Marcott, S., Mix, A., Liu, Z., Otto-Bliesner, B., Schmittner, A., and Bard, E. (2012). Global

warming preceded by increasing carbon dioxide concentrations during the last deglaciation. *Nature*, 484:49–54.

Shao, Y., Wyrwoll, K.-H., Chappell, A., Huang, J., Lin, Z., McTainsh, G. H., Mikami, M., Tanaka, T. Y., Wang, X., and Yoon, S. (2011). Dust cycle: An emerging core theme in earth system science. *Aeolian Research*, 2(4):181–204.

Shi, D., Kranz, S. A., Kim, J.-M., and Morel, F. M. M. (2012a). Ocean acidification slows nitrogen fixation and growth in the dominant diazotroph *trichodesmium* under low-iron conditions. *Proceedings of the National Academy of Sciences*, 109(45):E3094–E3100.

Shi, Z. and Baldo, C. (2023). Key role of iron oxyhydroxides in dust aerosol from high and low latitudes. In *EGU General Assembly 2023*, Vienna, Austria.

Shi, Z., Bonneville, S., Krom, M. D., Carslaw, K. S., Jickells, T. D., Baker, A. R., and Benning, L. G. (2011a). Iron dissolution kinetics of mineral dust at low pH during simulated atmospheric processing. *Atmospheric Chemistry and Physics*, 11(3):995–1007.

Shi, Z., Krom, M. D., Bonneville, S., Baker, A. R., Jickells, T. D., and Benning, L. G. (2009). Formation of iron nanoparticles and increase in iron reactivity in mineral dust during simulated cloud processing. *Environmental Science & Technology*, 43(17):6592–6596.

Shi, Z., Krom, M. D., Jickells, T. D., Bonneville, S., Carslaw, K. S., Mihalopoulos, N., Baker, A. R., and Benning, L. G. (2012b). Impacts

References

on iron solubility in the mineral dust by processes in the source region and the atmosphere: A review. *Aeolian Research*, 5:21–42.

Shi, Z. B., Woodhouse, M. T., Carslaw, K. S., Krom, M. D., Mann, G. W., Baker, A. R., Savov, I., Fones, G. R., Brooks, B., Drake, N., Jickells, T. D., and Benning, L. G. (2011b). Minor effect of physical size sorting on iron solubility of transported mineral dust. *Atmospheric Chemistry and Physics*, 11(16):8459–8469.

Shutler, J. D., Land, P. E., Brown, C. W., Findlay, H. S., Donlon, C. J., Medland, M., Snooke, R., and Blackford, J. C. (2013). Coccolithophore surface distributions in the north atlantic and their modulation of the air-sea flux of CO_2 from 10 years of satellite earth observation data. *Biogeosciences*, 10(4):2699–2709.

Siefert, R. L., Johansen, A. M., and Hoffmann, M. R. (1999). Chemical characterization of ambient aerosol collected during the southwest monsoon and intermonsoon seasons over the arabian sea: Labile-Fe(II) and other trace metals. *Journal of Geophysical Research: Atmospheres*, 104(D3):3511–3526.

Siegel, D., Behrenfeld, M., Maritorena, S., McClain, C., Antoine, D., Bailey, S., Bontempi, P., Boss, E., Dierssen, H., Doney, S., Eplee, R., Evans, R., Feldman, G., Fields, E., Franz, B., Kuring, N., Mengelt, C., Nelson, N., Patt, F., Robinson, W., Sarmiento, J., Swan, C., Werdell, P., Westberry, T., Wilding, J., and Yoder, J. (2013). Regional to global assessments of phytoplankton dynamics from the seawifs mission. *Remote Sensing of Environment*, 135:77–91.

Siegel, D. A., Devries, T., Cetinić, I., and Bisson, K. M. (2023).

- Quantifying the Ocean's Biological Pump and Its Carbon Cycle Impacts on Global Scales. *Annual Review of Marine Science*, 15:329–356.
- Sigman, D. M. and Hain, M. P. (2012). The biological productivity of the ocean. *Nature Education Knowledge*, 3(10):21.
- Simó, R. (2011). The role of marine microbiota in short-term climate regulation.
- Smith, B., Prentice, I. C., and Sykes, M. T. (2001). Representation of vegetation dynamics in the modelling of terrestrial ecosystems: comparing two contrasting approaches within european climate space. *Global Ecology and Biogeography*, 10(6):621–637.
- Smith, B., Wårlind, D., Arneeth, A., Hickler, T., Leadley, P., Siltberg, J., and Zaehle, S. (2014). Implications of incorporating n cycling and n limitations on primary production in an individual-based dynamic vegetation model. *Biogeosciences*, 11(7):2027–2054.
- Smith, M. B., Mahowald, N. M., Albani, S., Perry, A., Losno, R., Qu, Z., Marticorena, B., Ridley, D. A., and Heald, C. L. (2017). Sensitivity of the interannual variability of mineral aerosol simulations to meteorological forcing dataset. *Atmospheric Chemistry and Physics*, 17(5):3253–3278.
- Smith, S. J., Andres, R., Conception, E., and Lurz, J. (2004). Historical Sulfur Dioxide Emissions 1850-2000 : Methods and Results. *Methods*, (January).
- Smith, S. V. and Key, G. S. (1975). Carbon dioxide and metabolism in marine environments. *Limnology and Oceanography*, 20(3):493–495.

References

- Solmon, F., Chuang, P., Meskhidze, N., and Chen, Y. (2009). Acidic processing of mineral dust iron by anthropogenic compounds over the north pacific ocean. *Journal of Geophysical Research: Atmospheres*, 114(D2).
- Spokes, L. J. and Jickells, T. D. (1996). Factors controlling the solubility of aerosol trace metals in the atmosphere and on mixing into seawater. *Aquatic Geochemistry*, 1.
- Spokes, L. J., Jickells, T. D., and Lim, B. (1994). Solubilisation of aerosol trace metals by cloud processing: A laboratory study. *Geochimica et Cosmochimica Acta*, 58:3281–3287.
- Stephens, B. B. and Keeling, R. F. (2000). The influence of antarctic sea ice on glacial–interglacial co₂ variations. *Nature*, 404(6774):171–174.
- Stockdale, A., Tipping, E., Lofts, S., and Mortimer, R. J. G. (2016). Effect of ocean acidification on organic and inorganic speciation of trace metals. *Environmental Science & Technology*, 50(4):1906–1913. PMID: 26807813.
- Stohl, A., Prata, A. J., Eckhardt, S., Clarisse, L., Durant, A., Henne, S., Kristiansen, N. I., Minikin, A., Schumann, U., Seibert, P., Stebel, K., Thomas, H. E., Thorsteinsson, T., Tørseth, K., and Weinzierl, B. (2011). Determination of time- and height-resolved volcanic ash emissions and their use for quantitative ash dispersion modeling: the 2010 eyjafjallajökull eruption. *Atmospheric Chemistry and Physics*, 11(9):4333–4351.

Student (1908). The probable error of a mean. *Biometrika*, pages 1–25.

Stumm, W. and Morgan, J. (2012). *Aquatic Chemistry: Chemical Equilibria and Rates in Natural Waters*. Environmental Science and Technology: A Wiley-Interscience Series of Texts and Monographs. Wiley.

Séférian, R., Nabat, P., Michou, M., Saint-Martin, D., Voldoire, A., Colin, J., Decharme, B., Delire, C., Berthet, S., Chevallier, M., Sénési, S., Franchisteguy, L., Vial, J., Mallet, M., Joetzjer, E., Geoffroy, O., Guérémy, J.-F., Moine, M.-P., Msadek, R., Ribes, A., Rocher, M., Roehrig, R., Salas-y Mélia, D., Sanchez, E., Terray, L., Valcke, S., Waldman, R., Aumont, O., Bopp, L., Deshayes, J., Éthé, C., and Madec, G. (2019). Evaluation of cnrm earth system model, cnrm-esm2-1: Role of earth system processes in present-day and future climate. *Journal of Advances in Modeling Earth Systems*, 11(12):4182–4227.

Tagliabue, A., Kwiatkowski, L., Bopp, L., Butenschön, M., Cheung, W., Lengaigne, M., and Vialard, J. (2021). Persistent uncertainties in ocean net primary production climate change projections at regional scales raise challenges for assessing impacts on ecosystem services. *Frontiers in Climate*, 3.

Tagliabue, A., Twining, B. S., Barrier, N., Maury, O., Berger, M., and Bopp, L. (2023). Ocean iron fertilization may amplify climate change pressures on marine animal biomass for limited climate benefit. *Global Change Biology*, 29(18):5250–5260.

References

- Tang, W., Llort, J., Weis, J., Perron, M., Basart, S., Li, Z., Sathyendranath, S., Jackson, T., Sanz Rodriguez, E., Proemse, B., Bowie, A., Schallenberg, C., Strutton, P., Matear, R., and Cassar, N. (2021). Widespread phytoplankton blooms triggered by 2019–2020 australian wildfires. *Nature*, 597:370–375.
- Tebaldi, C., Debeire, K., Eyring, V., Fischer, E., Fyfe, J., Friedlingstein, P., Knutti, R., Lowe, J., O’Neill, B., Sanderson, B., Vuuren, D., Riahi, K., Meinshausen, M., Nicholls, Z., Tokarska, K., Hurtt, G., Kriegler, E., Lamarque, J.-F., Meehl, G., and Ziehn, T. (2021). Climate model projections from the scenario model intercomparison project (scenariomip) of cmip6. *Earth System Dynamics*, 12:253–293.
- Tegen, I., Harrison, S. P., Kohfeld, K., Prentice, I. C., Coe, M., and Heimann, M. (2002). Impact of vegetation and preferential source areas on global dust aerosol: Results from a model study. *Journal of Geophysical Research: Atmospheres*, 107(D21):AAC 14–1–AAC 14–27.
- Tegen, I., Werner, M., Harrison, S. P., and Kohfeld, K. E. (2004). Relative importance of climate and land use in determining present and future global soil dust emission. *Geophysical Research Letters*, 31(5).
- Textor, C., Schulz, M., Guibert, S., Kinne, S., Balkanski, Y., Bauer, S., Berntsen, T., Berglen, T., Boucher, O., Chin, M., Dentener, F., Diehl, T., Easter, R., Feichter, H., Fillmore, D., Ghan, S., Ginoux, P., Gong, S., Grini, A., Hendricks, J., Horowitz, L., Huang, P., Isaksen, I., Iversen, I., Kloster, S., Koch, D., Kirkevåg, A., Kristjansson, J. E., Krol, M., Lauer, A., Lamarque, J. F., Liu, X., Montanaro, V., Myhre,

- G., Penner, J., Pitari, G., Reddy, S., Seland, Ø., Stier, P., Takemura, T., and Tie, X. (2006). Analysis and quantification of the diversities of aerosol life cycles within aerocom. *Atmospheric Chemistry and Physics*, 6(7):1777–1813.
- Theodosi, C., Markaki, Z., and Mihalopoulos, N. (2010). Iron speciation, solubility and temporal variability in wet and dry deposition in the eastern mediterranean. *Marine Chemistry*, 120:100–107.
- Thomalla, S. J., Nicholson, S. A., Ryan-Keogh, T. J., and Smith, M. E. (2023). Widespread changes in southern ocean phytoplankton blooms linked to climate drivers. *Nature Climate Change*, 13:975–984.
- Turekian, K. K. (1977). The fate of metals in the oceans. *Geochimica et Cosmochimica Acta*, 41(8):1139–1144.
- Turner, S. M., Harvey, M. J., Law, C. S., Nightingale, P. D., and Liss, P. S. (2004). Iron-induced changes in oceanic sulfur biogeochemistry. *Geophysical Research Letters*, 31(14).
- Turner, S. M., Nightingale, P. D., Spokes, L. J., Liddicoat, M. I., and Liss, P. S. (1996). Increased dimethyl sulphide concentrations in sea water from in situ iron enrichment. *Nature*, 383(6600):513–517.
- Twining, B. S. and Baines, S. B. (2013). The trace metal composition of marine phytoplankton. *Annual Review of Marine Science*, 5:191–215.
- Uitz, J., Claustre, H., Gentili, B., and Stramski, D. (2010). Phytoplankton class-specific primary production in the world’s oceans: Seasonal and interannual variability from satellite observations. *Global Biogeochemical Cycles*, 24(3).

References

United Nations Department of Economic and Social Affairs, Lang, Y., and Moeini-Meybodi, H. (2021). Wildfires – a growing concern for sustainable development.

United Nations Environment Programme (2022). Spreading like wildfire – the rising threat of extraordinary landscape fires. a unep rapid response assessment. Technical report, United Nations Environment Programme.

Uruchi, W., Castrillo, M., and Beltrán, D. (2021). Autosubmit gui: A javascript-based graphical user interface to monitor experiments workflow execution. *Journal of Open Source Software*, 6:3049.

van Marle, M. J. E., Kloster, S., Magi, B. I., Marlon, J. R., Daniau, A.-L., Field, R. D., Arneth, A., Forrest, M., Hantson, S., Kehrwald, N. M., Knorr, W., Lasslop, G., Li, F., Mangeon, S., Yue, C., Kaiser, J. W., and van der Werf, G. R. (2017). Historic global biomass burning emissions for CMIP6 (BB4CMIP) based on merging satellite observations with proxies and fire models (1750–2015). *Geoscientific Model Development*, 10(9):3329–3357.

van Noije, T., Bergman, T., Le Sager, P., O'Donnell, D., Makkonen, R., Gonçalves-Ageitos, M., Döscher, R., Fladrich, U., von Hardenberg, J., Keskinen, J.-P., Korhonen, H., Laakso, A., Myriokefalitakis, S., Ollinaho, P., Pérez García-Pando, C., Reerink, T., Schrödner, R., Wyser, K., and Yang, S. (2021). Ec-earth3-aerchem: a global climate model with interactive aerosols and atmospheric chemistry participating in cmip6. *Geoscientific Model Development*, 14(9):5637–5668.

- van Oostende, M., Hieronymi, M., Krasemann, H., Baschek, B., and Röttgers, R. (2022). Correction of inter-mission inconsistencies in merged ocean colour satellite data. *Frontiers in Remote Sensing*, 3.
- van Vuuren, D. P., Stehfest, E., Gernaat, D. E., Doelman, J. C., van den Berg, M., Harmsen, M., de Boer, H. S., Bouwman, L. F., Daioglou, V., Edelenbosch, O. Y., Girod, B., Kram, T., Lassaletta, L., Lucas, P. L., van Meijl, H., Müller, C., van Ruijven, B. J., van der Sluis, S., and Tabeau, A. (2017). Energy, land-use and greenhouse gas emissions trajectories under a green growth paradigm. *Global Environmental Change*, 42:237–250.
- Vancoppenolle, M., Fichefet, T., Goosse, H., Bouillon, S., Madec, G., and Maqueda, M. A. M. (2009). Simulating the mass balance and salinity of arctic and antarctic sea ice. 1. model description and validation. *Ocean Modelling*, 27(1–2):33 – 53.
- Vignati, E., Wilson, J., and Stier, P. (2004). M7: An efficient size-resolved aerosol microphysics module for large-scale aerosol transport models. *Journal of Geophysical Research: Atmospheres*, 109(D22).
- Visser, F., Gerringa, L. J. A., Van der gaast, S. J., De baar, H. J. W., and Timmermans, K. R. (2003). The role of the reactivity and content of iron of aerosol dust on growth rates of two antarctic diatom species. *Journal of Phycology*, 39(6):1085–1094.
- Volk, T. and Hoffert, M. I. (1985). *Ocean Carbon Pumps: Analysis of Relative Strengths and Efficiencies in Ocean-Driven Atmospheric CO₂ Changes*, pages 99–110. American Geophysical Union (AGU).

References

- Vollmer, T. D., Ito, T., and Lynch-Stieglitz, J. (2022). Proxy-based preformed phosphate estimates point to increased biological pump efficiency as primary cause of last glacial maximum co2 drawdown. *Paleoceanography and Paleoclimatology*, 37(11):e2021PA004339.
- Volpe, G., Banzon, V. F., Evans, R. H., Santoleri, R., Mariano, A. J., and Sciarra, R. (2009). Satellite observations of the impact of dust in a low-nutrient, low-chlorophyll region: Fertilization or artifact? *Global Biogeochemical Cycles*, 23(3).
- Voulgarakis, A. and Field, R. D. (2015). Fire Influences on Atmospheric Composition, Air Quality and Climate. *Current Pollution Reports*, 1(2):70–81.
- Wadham, J. L., Hawkings, J. R., Tarasov, L., Gregoire, L. J., Spencer, R. G. M., Gutjahr, M., Ridgwell, A., and Kohfeld, K. E. (2019). Ice sheets matter for the global carbon cycle. *Nature Communications*, 10:3567.
- Wagenbrenner, N. S., Chung, S. H., and Lamb, B. K. (2017). A large source of dust missing in particulate matter emission inventories? wind erosion of post-fire landscapes. *Elementa: Science of the Anthropocene*, 5:2.
- Wagenbrenner, N. S., Germino, M. J., Lamb, B. K., Robichaud, P. R., and Foltz, R. B. (2013). Wind erosion from a sagebrush steppe burned by wildfire: Measurements of pm10 and total horizontal sediment flux. *Aeolian Research*, 10:25–36.
- Wagner, R., Jähn, M., and Schepanski, K. (2018). Wildfires as a source of airborne mineral dust – revisiting a conceptual model using

- large-eddy simulation (les). *Atmospheric Chemistry and Physics*, 18(16):11863–11884.
- Wagner, R., Schepanski, K., and Klose, M. (2021). The dust emission potential of agricultural-like fires—theoretical estimates from two conceptually different dust emission parameterizations. *Journal of Geophysical Research: Atmospheres*, 126(18):e2020JD034355. e2020JD034355 2020JD034355.
- Wang, B., Chen, M., Zheng, M., and Qiu, Y. (2022a). The biological uptake of dissolved iron in the changing daya bay, south china sea: Effect of ph and do. *Marine Pollution Bulletin*, 178:113635.
- Wang, R., Balkanski, Y., Boucher, O., Bopp, L., Chappell, A., Ciais, P., Hauglustaine, D., Peñuelas, J., and Tao, S. (2015). Sources, transport and deposition of iron in the global atmosphere. *Atmospheric Chemistry and Physics*, 15:6247–6270.
- Wang, Y., Chen, H.-H., Tang, R., He, D., Lee, Z., Xue, H., Wells, M., Boss, E., and Chai, F. (2022b). Australian fire nourishes ocean phytoplankton bloom. *Science of The Total Environment*, 807:150775.
- Ward, D. S., Kloster, S., Mahowald, N. M., Rogers, B. M., Randerson, J. T., and Hess, P. G. (2012). The changing radiative forcing of fires: Global model estimates for past, present and future. *Atmospheric Chemistry and Physics*, 12(22):10857–10886.
- Warneck, P. (1999). *Chemistry of the Natural Atmosphere*. International Geophysics. Academic Press.
- Weber, M. E., Bailey, I., Hemming, S. R., Martos, Y. M., Reilly, B. T., Ronge, T. A., Brachfeld, S., Williams, T., Raymo, M., Belt, S. T., et al.

References

(2022). Antiphased dust deposition and productivity in the antarctic zone over 1.5 million years. *Nature Communications*, 13(1):2044.

Werf, G. R. V. D., Randerson, J. T., Giglio, L., Collatz, G. J., Kasibhatla, P. S., and Arellano, A. F. (2006). Interannual variability in global biomass burning emissions from 1997 to 2004. *Atmospheric Chemistry and Physics*, 6:3423–3441.

Werner, M., Tegen, I., Harrison, S. P., Kohfeld, K. E., Prentice, I. C., Balkanski, Y., Rodhe, H., and Roelandt, C. (2002). Seasonal and interannual variability of the mineral dust cycle under present and glacial climate conditions. *Journal of Geophysical Research: Atmospheres*, 107(D24):AAC 2–1–AAC 2–19.

Westberry, T., Shi, Y., Yu, H., Behrenfeld, M., and Remer, L. (2019). Satellite-detected ocean ecosystem response to volcanic eruptions in the subarctic northeast pacific ocean. *Geophysical Research Letters*, 46(20):11270–11280.

Westberry, T. K., Behrenfeld, M. J., Shi, Y. R., Yu, H., Remer, L. A., and Bian, H. (2023). Atmospheric nourishment of global ocean ecosystems. *Science*, 380(6644):515–519.

Westerling, A. L., Hidalgo, H. G., Cayan, D. R., and Swetnam, T. W. (2006). Warming and earlier spring increase western u.s. forest wildfire activity. *Science*, 313(5789):940–943.

Winton, V. H. L., Edwards, R., Bowie, A. R., Keywood, M., Williams, A. G., Chambers, S. D., Selleck, P. W., Desservettaz, M., Mallet, M. D., and Paton-Walsh, C. (2016). Dry season aerosol iron solubility

in tropical northern australia. *Atmospheric Chemistry and Physics*, 16(19):12829–12848.

Wu, C., Lin, Z., and Liu, X. (2020). The global dust cycle and uncertainty in cmip5 (coupled model intercomparison project phase 5) models. *Atmospheric Chemistry and Physics*, 20(17):10401–10425.

Xi, H., Bretagnon, M., Losa, S. N., Brotas, V., Gomes, M., Peeken, I., Alvarado, L. M. A., Mangin, A., and Bracher, A. (2023). Satellite monitoring of surface phytoplankton functional types in the atlantic ocean over 20 years (2002–2021). *State of the Planet*, 1-osr7:5.

Xi, H., Losa, S. N., Mangin, A., Garnesson, P., Bretagnon, M., Demaria, J., Soppa, M. A., Hembise Fanton d’Andon, O., and Bracher, A. (2021). Global chlorophyll a concentrations of phytoplankton functional types with detailed uncertainty assessment using multisensor ocean color and sea surface temperature satellite products. *Journal of Geophysical Research: Oceans*, 126(5):e2020JC017127.

Yamaguchi, R., Rodgers, K. B., Timmermann, A., Stein, K., Schlunegger, S., Bianchi, D., Dunne, J. P., and Slater, R. D. (2022). Trophic level decoupling drives future changes in phytoplankton bloom phenology. *Nature Climate Change*, 12:469–476.

Yamasoe, M. A., Artaxo, P., Miguel, A. H., and Allen, A. G. (2000). Chemical composition of aerosol particles from direct emissions of vegetation fires in the amazon basin: water-soluble species and trace elements. *Atmospheric Environment*, 34(10):1641–1653.

Yarwood, G., Rao, S., Yocke, M., and Whitten, G. (2005). Updates to the carbon bond chemical mechanism: Cb05. Technical report,

References

Final report to the U.S. EPA, RT-0400675. Available online at <http://www.camx.com>.

Yoon, J.-E., Lim, J.-H., Shim, J.-M., Kwon, J.-I., and Kim, I.-N. (2019). Spring 2018 asian dust events: Sources, transportation, and potential biogeochemical implications. *Atmosphere*, 10(5).

Yoshioka, M., Grosvenor, D. P., Booth, B. B. B., Morice, C. P., and Carslaw, K. S. (2024). Warming effects of reduced sulfur emissions from shipping. *EGUsphere*, 2024:1–19.

Yu, Y. and Ginoux, P. (2022). Enhanced dust emission following large wildfires due to vegetation disturbance. *Nature Geoscience*, 15:878–884.

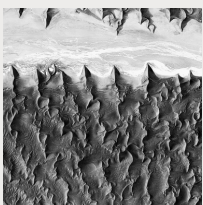
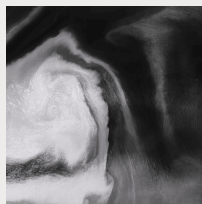
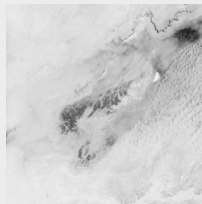
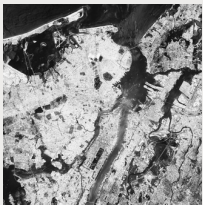
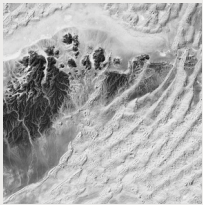
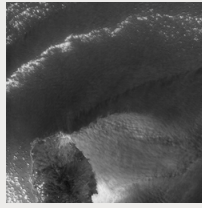
Yu, Y., Kalashnikova, O. V., Garay, M. J., and Notaro, M. (2019). Climatology of asian dust activation and transport potential based on misr satellite observations and trajectory analysis. *Atmospheric Chemistry and Physics*, 19(1):363–378.

Yuan, Z., Achterberg, E. P., Engel, A., Wen, Z., Zhou, L., Zhu, X., Dai, M., and Browning, T. J. (2023). Phytoplankton community response to episodic wet and dry aerosol deposition in the subtropical north atlantic. *Limnology and Oceanography*, 68(9):2126–2140.

Zellner, A. (1978). Seasonal analysis of economic time series. *NBER Books*.

Zender, C. S., Bian, H., and Newman, D. (2003). Mineral dust entrainment and deposition (dead) model: Description and 1990s dust climatology. *Journal of Geophysical Research: Atmospheres*, 108(D14).

- Zhang, Y. G., Pagani, M., Liu, Z., Bohaty, S. M., and DeConto, R. (2013). A 40-million-year history of atmospheric CO_2 . *Philosophical Transactions of the Royal Society A: Mathematical, Physical and Engineering Sciences*, 371(2001):20130096.
- Zheng, B., Ciais, P., Chevallier, F., Chuvieco, E., Chen, Y., and Yang, H. (2021). Increasing forest fire emissions despite the decline in global burned area. *Science Advances*, 7(39):eabh2646.
- Zhou, Y., Huang, X. H., Bian, Q., Griffith, S. M., Louie, P. K. K., and Yu, J. Z. (2015). Sources and atmospheric processes impacting oxalate at a suburban coastal site in hong kong: Insights inferred from 1year hourly measurements. *Journal of Geophysical Research: Atmospheres*, 120(18):9772–9788.
- Zhu, X., Prospero, J. M., Millero, F. J., Savoie, D. L., and Brass, G. W. (1992). The solubility of ferric ion in marine mineral aerosol solutions at ambient relative humidities. *Marine Chemistry*, 38(1):91–107.
- Zhuang, G., Yi, Z., Duce, R. A., and Brown, P. R. (1992a). Correction to “chemistry of iron in marine aerosols”. *Global Biogeochemical Cycles*, 6.
- Zhuang, G., Yi, Z., Duce, R. A., and Brown, P. R. (1992b). Link between iron and sulphur cycles suggested by detection of $Fe(n)$ in remote marine aerosols. *Nature*, 355.



Iron is an essential micronutrient for vital processes in organisms. Its bioavailability is crucial in the open ocean, where one-third of waters face iron limitation. This limitation impacts ocean productivity and the ocean's ability to capture atmospheric carbon dioxide.

In this PhD Thesis, the journey of iron from land to the ocean is traced. This work seeks to address uncertainties in the atmospheric supply of iron to the ocean and the processes that influence its bioavailability. Using a modeling framework, the research quantifies changes in bioavailable iron deposition from the pre-industrial era to the end of the 21st century, accounting for the effects of human-induced changes on global climate, aerosol emissions, and atmospheric chemistry. Additionally, it examines how these changes could affect ocean biogeochemistry.

By advancing our understanding of the Earth system, this work offers not only a more precise comprehension of the subject but also a deeper appreciation of the intricate relationships between science, society, and the environment.

Supervisors:

Maria Gonçalves Ageitos

Carlos Pérez García Pando